COMPUTATIONAL MODELING AND STRUCTURE-ACTIVITY RELATIONSHIPS OF CYTOCHROME P450 1A1: AN APPROACH TO CYP1A1 GENE DIRECTED ENZYME PRODRUG THERAPY

Thesis submitted to the School of Medicine, Faculty of Health Science, Flinders University, Adelaide, Australia, in fulfilling the requirements for the degree of Doctor of Philosophy

August 2010

BENJAMIN C LEWIS

Supervisors: Professor John O Miners, Professor Peter I Mackenzie

TABLE OF CONTENTS

COMPUTATIONAL MODELING AND STRUCTURE-ACTIVITY RELATIONSHIPS OF CYTOCHROME P450 1A1: AN APPROACH TO CYP1A1 GENE DIRECTED ENZYME PRODRUG THERAPY

LIST OF FIGURES

LIST OF TABLES

DECLARATION

"I certify that this thesis does not incorporate without acknowledgement any material previously submitted for a degree or diploma in any university; and that to the best of my knowledge and belief it does not contain any material previously published or written by another person except where due reference is made in the text."

Benjamin C Lewis

Dated:

ACKNOWLEDGEMENTS

I would like to thank those people who have endured or are suffering with cancer for inspiring me throughout this study.

I sincerely thank my supervisors, Professor John O Miners and Professor Peter I Mackenzie for their guidance, phenomenal expertise, and patience. Their perpetual enthusiasm for research motivates me to be a better scientist; I shall never forget you.

I dedicate this thesis to the two people who know me best, my wonderful wife Emily and my dear daughter May; you complete me.

PEER-REVIEWED WORK RESULTING FROM THIS THESIS

Refereed journal articles

1. **Lewis BC**, Mackenzie PI, Miners JO. Comparative homology modeling of human cytochrome P4501A1 (CYP1A1) and confirmation of residues involved in 7-ethoxyresorufin *O*-deethylation by site-directed mutagenesis and enzyme kinetic analysis. *Archives of Biochemistry and Biophysics*. 2007 Dec 1; 468(1): 58-69.

Conference proceedings

1. Homology modeling of Cytochrome P4501A1 (CYP1A1). **B.C. Lewis**, P.I. Mackenzie, and J.O. Miners. Joint meeting of the Australasian Society of Experimental and Clinical Pharmacologists and Toxicologists and the Australasian Pharmaceutical Sciences Association; Melbourne, Australia (2005).
2. Homology modeling of Cytochrome P4501A1 (CYP1A1). **B.C. Lewis**, P.I. Mackenzie, and J.O. Miners. International Conference on Pharmacogenetics; Changsha, China (2006).
3. Identification of the cytochrome P4501A1 (CYP1A1) residues involved in 7-ethoxyresorufin *O*-deethylation. **B.C. Lewis**, P.I. Mackenzie, and J.O. Miners. Joint meeting of the Australasian Society of Clinical and Experimental Pharmacologists and Toxicologists, and the South East Asian, Western Pacific Regional Meeting of Pharmacologists; Adelaide, Australia (2007).

4. Structure-function relationships of cytochrome P4501A1 (CYP1A1). **B.C. Lewis**, P.I. Mackenzie, and J.O. Miners. Adelaide Pharmacology Group meeting; National Wine Centre of Australia, Adelaide, Australia (2008).

5. Homology modeling guided mutagenesis of cytochrome P4501A1 (CYP1A1) to identify residues involved in 7-ethoxyresorufin *O*-deethylation. **B.C. Lewis**, P.I. Mackenzie, and J.O. Miners. Joint meeting of the Australian Society for Biochemistry and Molecular Biology, and the Australia and New Zealand Society for Cell and Developmental Biology; (ComBio), Canberra, Australia (2008).

Invited lectures and presentations

1. Adelaide Pharmacology Group meeting, National Wine Centre of Australia, Adelaide, Australia (2008).

2. Combio2008. The Annual Conferences of the Australian Society for Biochemistry and Molecular Biology, the Australian Society of Plant Scientists and the Australia and New Zealand Society for Cell and Developmental Biology; Canberra, Australia (21^{st}-25^{th} September, 2008).

Scientific awards

1. **2007 ASCEPT Oral Prize**. The ASCEPT Oral Prize is awarded annually for the best oral communication by a Higher Degree student member of the Australasian Society of Clinical and Experimental Pharmacologists and Toxicologists.

2. **2007 Percy Prize finalist.** In memory of Dr Neville Percy, the Percy prize is awarded to a higher degree student for a poster presentation.

ABSTRACT

Given the paucity of data relating to the structure of human CYP1A1, an enzyme of considerable toxicological significance, the initial aim of this thesis was to generate a chemically and structurally valid CYP1A1 homology model. CYP1A1 homology models based on the CYP2C5 X-ray crystal structure and a composite of the CYP2C5, CYP2C8, and CYP2C9 X-ray crystal structures were compared to a model generated using the crystal coordinates of CYP1A2. The model using the CYP1A2 coordinates gave near ideal stereochemical quality and was favored energetically. Automated *in silico* docking studies identified active-site residues potentially involved in the orientation and binding of the prototypic CYP1A1 substrate, 7-ethoxyresorufin. The most energetically favorable pose placed the carbon atom adjacent to the ether oxygen of 7-ethoxyresorufin at 4.4Å from the heme iron, at an angle of 106.4º to the plane of the heme. The CYP1A1 mutants S122A, F123A, F224A, A317Y, T321G, and I386G were generated to explore the roles of these residues in 7-ethoxyresorufin binding and turnover, and generally confirmed the importance of aromatic interactions over hydrogen bonding in orientating 7-ethoxyresorufin in a catalytically favorable orientation.

The validated 3-dimensional structure of CYP1A1 was subsequently employed to elucidate structure-activity relationships with the anticancer prodrug, dacarbazine (DTIC). *In silico* docking experiments demonstrated that DTIC orientates in close proximity to S122, F123, D313, A317, I386, Y259, and L496. Docking located the site of metabolism of DTIC at 5.6Å from the heme iron at an angle of 105.3º to the plane of the heme. Binding of DTIC in the active-site was stabilized by H-bonding between Y259 and the N2 position of the imidazole ring. Structural modification of

the CYP1A1 enzyme to increase its catalytic efficiency (V_{max}/K_m) for *N*-demethylation and the subsequent activation of DTIC was facilitated by the CYP1A1 homology model. Twenty-nine CYP1A1 mutants were generated and expressed in *E. coli*. DTIC *N*-demethylation by the CYP1A1 E161K, E256K, and I458V mutants exhibited Michaelis-Menten kinetics, with decreases in K_m that doubled the catalytic efficiency relative to wild-type ($P<0.05$). The kinetics of DTIC *N*-demethylation by the CYP1A1*2C and CYP1A1*4 polymorphic variants was additionally characterized. There was an approximate 30% reduction in catalytic efficiency of the CYP1A1*2C and CYP1A1*4 variants relative to wild-type. Thus, patients with malignancies who carry either polymorphism may not respond as well to DTIC treatment compared to those expressing the wild-type enzyme.

As a chemotherapeutic agent, DTIC has relatively poor clinical activity in human malignancies and exhibits numerous serious adverse effects, which presumably arise from bioactivation in the liver and other tissues resulting in systemic exposure to the cytotoxic metabolite. Gene directed enzyme prodrug therapy (GDEPT) provides a means to enhance the efficacy and reduce the systemic toxicities associated with conventional chemotherapy. Thus, COS-7 and SK-MEL-28 cells were transfected with cDNA encoding an open reading frame (ORF) comprising the CYP1A1 (wild-type or mutant) coding sequence (CDS), a picornaviral 2A cleavage peptide, followed by the cytochrome P450 oxidoreductase (OxR) CDS. Cell line sensitization assays using the wild-type, E161K, E256K, and I458V CYP1A1-2A-OxR constructs were attempted, but the generation of stable cell lines was not successful. However, data obtained from transiently expressed CYP1A1-2A-OxR motifs in COS-7 and SK-MEL-28 cells revealed the synthesis of both holo-CYP1A1 and OxR proteins.

This study elucidated important structural characteristics of human CYP1A1 and how manipulation of protein tertiary structure can enhance enzyme function. Combination of kinetic analyses with *in silico* docking data has allowed interpretation of the structure-activity relationships of CYP1A1 and DTIC. Moreover, the successful generation of CYP1A1 enzymes with catalytically enhanced DTIC activation highlights their potential use as a strategy for P450-based GDEPT in the treatment of metastatic malignant melanoma.

ABBREVIATIONS AND SYMBOLS

±	plus or minus
17α	P45017A hydroxylase leader sequence
4-MU	4-methylumbeliferone
Å	angstroms (1.0×10^{-10} m)
AFM	atomic force microscopy
AhR	aromatic hydrocarbon receptor
AIC	Amino-imidazole-carboxamide
Amp^R	ampicillin resistance
bp	basepairs
°C	degrees Celsius
cDNA	complementary deoxyribonucleic acid
CDS	coding sequence
$Chlor^R$	chloramphenicol resistance
cm	centimetre
CYP	cytochrome P450
CYP1A1	cytochrome P4501A1
Cα	alpha-carbon atom
Da	Daltons
DTIC	dacarbazine
DTT	dithiothreitol
E. coli	*Escherichia coli*
Eres	7-ethoxyresorufin
EROD	ethoxyresorufin *O*-deethylase
FAD	flavin adenine dinucleotide
FF	atomic force field
FMN	flavin mononucleotide
FxR	ferrodoxin reductase
g	gram
g	gravitational force
GDEPT	gene-directed enzyme prodrug therapy
h	hour(s)
HLM	human liver microsomes
HMM	hidden Markov model
HMMTIC	hydroxy-dimethyl-triazenyl-imidazole-carboxamide
HPLC	high performance liquid chromatography
HRP	horseradish peroxidase
HTE	high transformation efficiency
IU	international units
kb	kilobases
kcal	kilocalorie
kDa	kilodaltons
K_m	Michaelis constant
K_{si}	reversible inhibition

	constant
L	litre
LB	Lauria-Bertani broth or agar
M	Moles per litre
mA	milliamps
mg	milligram
min	minute(s)
mL	millilitre
μL	microlitre
mM	millimolar
mm	millimetre
μM	micromolar
μm	micrometer
MOPS	3-morpholino propane sulfonic acid
mRNA	messenger ribonucleic acid
MTIC	methyl-triazenyl-imidazole-carboxamide
n	Hill coefficient
$NADP^+$	nicotinamide dinucleotide phosphate
NADPH	nicotinamide dinucleotide phosphate, reduced form
nd	not detected
ng	nanogram
nM	nanomolar
nmole	nanomole
NMR	nuclear magnetic resonance
OD	optical density
OmpA	outer membrane protein-A
OxR	cytochrome P450 oxidoreductase
P450	cytochrome P450
PAH	polycyclic aromatic hydrocarbon
PDB	RCSB protein databank
pmol	picomole
PMSF	phenylmethylsulfonyl fluoride
r^2	coefficient of determination
Res	resorufin
RMSD	root mean square deviation
rpm	revolutions per minute
R-value	statistical measure of fit
[S]	substrate concentration
S_{50}	substrate concentration at half V_{max} in the Hill equation
SCR	sequence conserved region
SD	standard deviation
SDS PAGE	sodium dodecyl sulfate polyacrylamide gel electrophoresis
sec	second(s)

SNP	single nucleotide polymorphism
SRS	substrate recognition site
TBS	tris-buffered saline
TBST	TBS + tween-20
TEA	triethylamine
UV	Ultraviolet
V	volts
v	enzymatic rate of product formation
V	volume (L)
v/v	volume per volume
vdW	van der Waals force
Vis	visible
V_{max}	maximal velocity of enzyme reaction rate
W	watts
w/v	weight per volume
w/w	weight per weight
ϕ	phi torsional angle
ψ	psi torsional angle

CHAPTER 1
INTRODUCTION

1.1 Overview

The concept of overexpression of individual cytochrome P450 enzymes in tumor cells is now becoming well recognized as a means to develop novel targets for anticancer therapy. The outcome in terms of cytotoxicity or lack of response to an anticancer drug is dependant on both the relative amount and the activity of the individual P450(s) within the tumor. Clearly, enhanced expression of individual P450s in tumor cells increases the potential for activation of anticancer prodrugs by the tumor cells directly.

For successful anticancer treatment using a prodrug, it is important to establish whether activation occurs at the tumor site, in the liver (or other 'non-target' tissues), or a combination of both. Extensive activation of a chemotherapeutic agent by an organ remote to the tumor site can lead to undesirable systemic exposure to the cytotoxic drug metabolites that kill host cells as opposed to the tumor cell target. In an attempt to combat this problem, several "next generation" selective cytotoxic agents entering clinical-trial have been designed around P450s, e.g. aminophenylbenzothiazoles and aliphatic amine N-oxides (Patterson & Murray 2002). However, these leads still appear to be inferior since most of the drugs are subject to more complex metabolic activation pathways than many conventional drugs.

Since the activation of many prodrugs used in clinical practice is dependant on the intrinsic ability of the liver to metabolize the drug, activation is sensitive to changes in hepatic enzyme activity. Despite this, few studies examine the metabolic activation of anticancer agents in patients carrying variant P450 alleles. Interindividual variation in P450-mediated metabolism, resulting from genetic polymorphism, effectively renders each patient unique with respect to prodrug activation, as well as drug dosage and kinetics. An area that potentially improves tumor/drug selectivity and one which minimises problems associated with interindividual variation is gene directed enzyme prodrug therapy (GDEPT).

Chemotherapy has long been the sole treatment for metastatic melanoma. In Australia and the United States the prodrug dacarbazine (DTIC) is currently the only approved chemotherapeutic agent targeted specifically to the treatment of metastatic melanoma. However, treatment with DTIC is generally associated with relatively poor outcomes and the co-administration of other therapies offers minimal clinical advantages. DTIC is primarily activated by the cytochromes P450 CYP1A1 and CYP1A2. To date, no studies have characterized the kinetics of DTIC metabolism in patients carrying wild-type or polymorphic CYP1A alleles, or their cellular response after bioactivation. However, numerous studies have investigated the substrate selectivity of the CYP1A enzymes (Lewis et al. 1999; Liu et al. 2003; Liu et al. 2004; Taly et al. 2007). Therefore, an opportunity exists to examine the structure-activity relationships between CYP1A1 and DTIC, however, the chemical structure of CYP1A1 has not been elucidated. Thus, a valid 3-dimensional structure of CYP1A1 would not only aid our understanding of the mechanism(s) involved in DTIC activation, but also aid our understanding of interactions with numerous other CYP1A1 drug substrates.

The purpose of this thesis was to identify important chemical and structural characteristics of human CYP1A1 and how manipulation of the enzyme's tertiary structure may be used to enhance the activation of DTIC. Molecular modeling of CYP1A1 elucidated a valid homology model that was utilized in the successful generation of a range of catalytically altered enzymes. By increasing enzyme-substrate affinity these enzymes doubled the catalytic efficiency of DTIC activation. The CYP1A1 mutants described are potential leads for use in P450-based GDEPT for the treatment of metastatic malignant melanoma.

Despite ongoing attempts by the pharmaceutical industry to discover and develop novel anti-cancer therapies, there have been no new approved therapies for metastatic melanoma use since 1998 (Proleukin, recombinant form of interleukin-2; FDA Center for Drug Evaluation and Research; last updated: July 2010; http://www.centerwatch.com/drug-information/fda-approvals/). The subsequent chapters of this thesis highlight that specialized and focused *in vitro* studies may potentially result in tailoring the activity of a preexisting drug to one with enhanced capabilities that may ultimately be employed in the clinic by means of gene therapy.

1.2 Rationale for the study

The research described in this thesis proceeded from the following broad concepts:

Little chemical or structural information is known regarding human CYP1A1, a key enzyme involved in the activation of the widely used chemotherapeutic agent DTIC. DTIC is currently the only approved non-biologic chemotherapy drug for metastatic melanoma. While it is the best available treatment and the standard against which new melanoma drugs are evaluated, it is unfortunately not particularly effective with

an average response of only 19% with no significant improvement in overall patient survival. Furthermore, DTIC is associated with severe adverse reactions, including liver damage. An improved understanding of the enzyme-substrate interactions and the kinetics of DTIC activation may provide a more targeted approach to cancer treatment.

1.3 Cytochromes P450

1.3.1 Background

P450s are represented by 781 gene families and constitute a superfamily of cysteinato-heme enzymes. These enzymes are present in all forms of life, with fungi being the largest contributor (310 families), followed by bacteria (205 families, including 10 Archaeal), animals (110 families), plants (95 families), and protists (61 families). Excluding variants and pseudogenes, there are approximately 8128 uniquely named P450 amino acid sequences. Of these, 2565 are found in animals (last updated: July 2010; http://drnelson.uthsc.edu/P450.statsfile.html).

Individual P450 enzymes are discrete gene products with molecular masses of approximately 57,000 Daltons (Da) (~500 amino acid residues). All P450s are related but differ from one-another in amino acid sequence and the mechanism by which each gene is regulated. Coding sequence (CDS) variations give rise to differences in secondary- and tertiary-structure (and ultimately quaternary structure), and subsequently determine the chemistry of the protein active-site. It is the chemistry of the protein active-site that establishes P450 substrate and inhibitor selectivities. Different members of the P450 superfamily have distinct, but often

overlapping substrate selectivities, with some enzymes acting on the same substrates, but possessing different stereo-selectivity or different kinetic mechanisms.

P450s are classified according to the electron-transfer protein each enzyme requires for catalysis. Electrons can be supplied to the P450 enzyme from either NADH/FAD (class I), NADPH/FAD-FMN (class II), no electron donor (class III), or NADPH directly (class IV) (Meunier, de Visser & Shaik 2004; Werck-Reichhart & Feyereisen 2000). Mammalian class I P450s are located in the inner mitochondrial membrane and are involved in steroid synthesis. The mitochondrial mammalian P450s, along with the soluble bacterial P450s, utilize the class I electron transport chain which involves the reduction of a flavin adenine dinucleotide (FAD)-containing reductase by NADH. Two electrons are then transferred from FAD to ferrodoxin reductase (FxR; Fe_2-S_2). The FxR protein subsequently acts as an electron shuttle by transferring each electron to the P450 enzyme for catalysis. Class II P450s are involved in the metabolism of drugs and other xenobiotics and are localized in the endoplasmic reticulum (ER) membrane (Peterson & Prough 1986). The electron transport chain of class II P450s, which are found in most eukaryotic cell types, is composed of a complex oxidoreductase (OxR) flavoprotein which has both FAD and flavin mononucleotide (FMN) domains (Meunier, de Visser & Shaik 2004; Peterson & Prough 1986). Potentiometric studies have shown that FAD serves as the initial electron acceptor from NADPH, while FMN serves to reduce the P450 holoenzyme (Figure 1.1) (Fleming et al. 2003). The electron flow to the heme iron is presumed to be regulated by a substrate dependant increase in the redox potential of the heme (Johnson et al. 2005b). An additional COOH-terminally anchored electron donor, cytochrome b_5, which also utilizes electrons from NADPH, has been found to enhance the activity of some class II P450 enzymes (Werck-Reichhart & Feyereisen

2000). Class III enzymes are self-sufficient and require no electron donor. They are involved in the synthesis of endogenous mediators, such as prostaglandins, in mammals. P450s that receive electrons directly from NADPH belong to class IV. Unique to fungi, these soluble P450s have the ability to reduce nitric oxide (NO) to nitrous oxide (N_2O) (Werck-Reichhart & Feyereisen 2000).

This thesis focuses on the mammalian microsomal class II P450 enzymes. Further classification of the class II P450 enzymes is achieved on the basis of their catalytic activity. Activities may be classified in three distinct groups: (i) monooxygenase activity, where an oxygen atom is incorporated into a substrate; (ii) oxidase activity, resulting in the formation of superoxide anion radicals or hydrogenperoxide (uncoupling of the catalytic cycle); and (iii) the production of free radical intermediates from substrate/reductase activity (under anaerobic conditions).

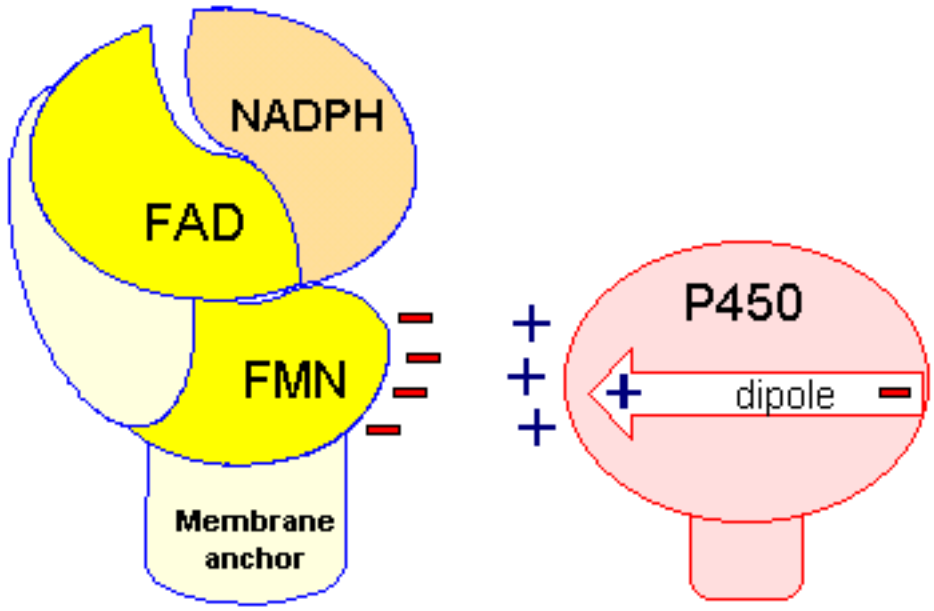

Figure 1.1 The P450 oxidoreductase, flavin adenine dinucleotide and flavin mononucleotide complex. Electrons from the membrane bound NADPH-OxR complex migrate from NADPH to FAD, to FMN, and then finally to the P450 heme Fe^{3+}.

The primary reaction catalyzed by class II P450s is the hydroxylation of a carbon atom, according to the catalytic cycle represented in Figure 1.2. For hydroxylation to proceed, the activation of molecular oxygen (O_2) is required. This is achieved by the heme prosthetic group situated within the active-site of the P450 holoenzyme, which utilizes electrons donated from the NADPH-OxR complex (Fleming et al. 2003). The heme group is comprised of an Fe^{3+} protoporphyrin-IX-complex covalently linked to an atom of sulfur provided by a highly conserved cysteine residue within the carboxy-terminal domain of the P450 enzyme (Figure 1.3). In the non-catalytic state, the sixth coordination site of the Fe^{3+} atom is stabilized by a single water molecule (de Graaf, Vermeulen & Feenstra 2005). In the presence of a substrate, the reductive activation of oxygen occurs from two one-electron donations, and is targeted toward the sixth coordination position. The first electron reduces the substrate-bound ferric heme (Fe^{3+}--R), facilitating the rapid binding of dioxygen and the formation of a ferrous-dioxygen intermediate (Fe^{2+}--O_2--R). It is at this point that other lone pair electron donors, particularly carbon monoxide (CO), can compete with O_2 for the iron electron pair acceptor site (Omura & Sato 1964b). The second electron donation forms a ferric hydroperoxy complex that is subsequently protonated (Fe^{3+}--H_2O_2--R). The O--O bond is then cleaved leaving one atom of oxygen incorporated into the substrate (R) with the remaining atom of oxygen reduced to form water (eq 1.1) (Fleming et al. 2003; Guengerich 2001; Guengerich et al. 2000; Meunier, de Visser & Shaik 2004).

$$R\text{-}H + O_2 + 2\acute{e} + 2H^+ \xrightarrow{\text{cytochrome P450}} ROH + H_2O \qquad (1.1)$$

where R is the C-H bond of any P450 substrate and é is a single electron.

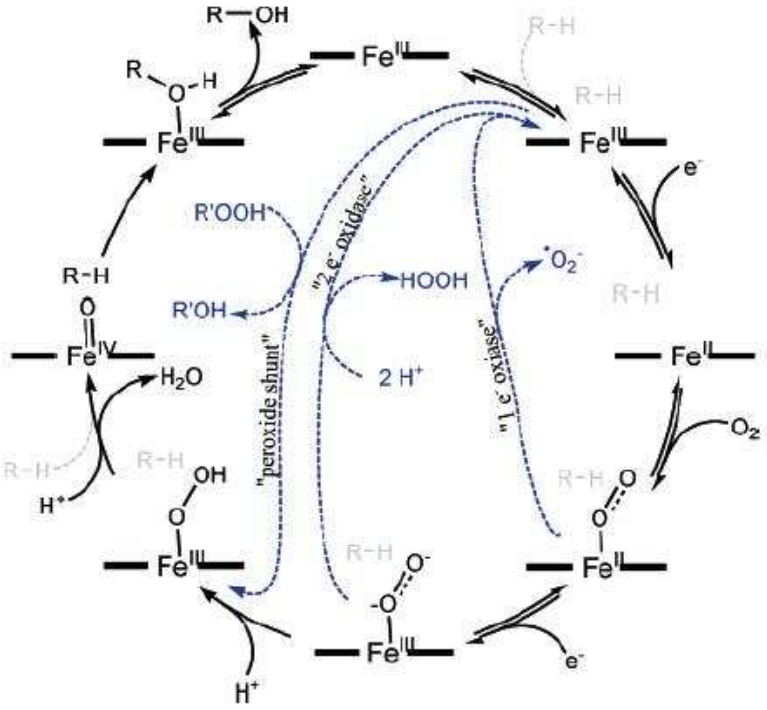

Figure 1.2 Schematic representation of the catalytic cycle of class II P450 enzymes. The main reaction is the monooxygenation pathway used in hydroxylation (black). Three alternative pathways are shown (blue) corresponding to the one- and two-electron oxidase uncoupling reactions and the peroxide shunt. The one-electron oxidase produces a superoxide radical, which can subsequently generate a radical derivative of the substrate. The peroxide shunt is the pathway used in generating an activated iron-oxygen species. Taken from de Graaf, Vermeulen & Feenstra (2005).

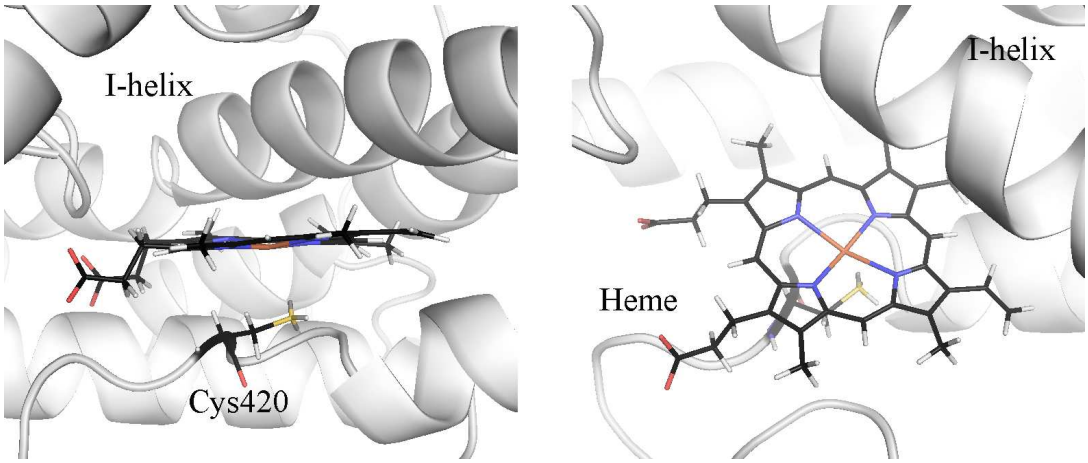

Figure 1.3 The heme prosthetic group of the cytochromes P450. Orthogonal views of the Fe^{3+} protoporphyrin-IX-complex covalently linked to the highly conserved cysteine residue (labeled Cys420). Sulfur atoms are colored yellow. For simplification, the 6^{th} co-ordination site of the octahedral Fe^{3+} atom is not included.

1.3.2 Orientation and membrane topology of cytochromes P450

The membrane topology of P450s has been extensively studied by numerous chemical and computational approaches (Szczesna-Skorupa et al. 1995). Class II P450s reside on the cytosolic face of the ER and do not undergo recycling through the pre-Golgi compartment (Szczesna-Skorupa et al. 1998). Initial data suggested that P450s of the ER contained four to eight transmembrane helical domains, with the active-site positioned within the membrane itself. Subsequent findings identified microsomal P450s as being bound to the ER by a single 'anchor' site located at the NH_2-terminus. Moreover, the active-site was shown to be part of a large cytoplasmic domain that potentially contains one or two additional membrane contact sites. The presence of an NH_2-terminal signal peptide is strong evidence for targeting microsomal P450s to the ER membrane. The apparent signal peptide is not proteolytically cleaved, but is actually retained and utilized as the membrane anchor (Black 1992; Szczesna-Skorupa et al. 1998). Once associated with the ER membrane, the mobility of the membrane bound P450 has been likened to that of Golgi and plasma-membrane proteins ($2\text{-}6x10^{-10}cm^2/s$) (Werck-Reichhart & Feyereisen 2000). However, P450s are thought to be hindered from traversing the membrane surface. Szczesna-Skorupa *et al.* (1998) hypothesized that the mechanism of P450 retention in the ER membrane may be related to the formation of protein-protein aggregates. Since P450s are known to closely associate with their redox partners, this appears highly probable.

The orientation of microsomal P450s in the ER membrane is clearly dependant on the location of the insertion signal, NH_2-terminal anchor, and the halt-transfer signal that serves to arrest polypeptide translocation through the membrane. In addition, the heme-containing domain may utilize amphipathic helices in binding to the cytosolic

side of the membrane. Black (1992) hypothesized that the plane of the active-site heme is likely positioned at an angle somewhat greater than parallel to the membrane surface. Likewise, research conducted by Bayburt & Sligar (2002) and Edwards et al. (1991) concluded that P450s are most likely orientated with the heme positioned perpendicular to the membrane. However, the exact nature of the peripheral membrane interactions of P450s remain incompletely characterized (Edwards et al. 1991; Szczesna-Skorupa et al. 1998).

Due to the challenges associated with crystallizing membrane-bound proteins, mammalian P450 X-ray crystal structures have become available only in the last decade. Crystallization of mammalian CYP1A2 (Sansen et al. 2007), CYP2A6 (Yano et al. 2005), CYP2C8 (Schoch et al. 2004), CYP2C9 (Wester et al. 2004; Williams et al. 2003), CYP3A4 (Yano et al. 2005), CYP2B4 (Scott et al. 2004b), CYP2C5 (Wester et al. 2003a; Wester et al. 2003b; Williams et al. 2000b), and CYP2D6 (Rowland et al. 2006) was accomplished by truncating the NH_2-terminus, thus generating a soluble form of the enzyme. Additionally, atomic force microscopy (AMF) has been employed to directly investigate the topography of membrane-bound proteins. To determine the position of the native membrane-bound enzyme relative to the membrane itself, rabbit CYP2B4 was incorporated into nanometer-scale phospholipids bilayer disks and visualized by AFM (Bayburt & Sligar 2002; Black 1992). Protein insertion occurred to a depth of 3.5nm. The orientation of the heme was estimated from results of anisotropy decay measurements after flash photolysis. Angles of 41º, 55º, or 71º between the heme and membrane were observed for purified CYP2B4 from phenobarbital-induced rabbits. For CYP2B4 from 3-methylcholanthrene induced animals, angles of 48º or 62º were observed, therefore suggesting orientation of the heme lays more perpendicular to the

membrane than parallel to it. Bayburt and Sligar (2002) additionally investigated the orientation of the redox transfer complexes. This was accomplished by overlaying the known structure of bacterial CYP102 with rabbit CYP2B4. They suggested that the overall fold of the CYP102-FMN domain resembles that of the mammalian reductase FMN domain. If the CYP102-FMN domain is positioned on the membrane surface analogous to that proposed for mammalian P450 reductase, then the heme domain is orientated perpendicular to the membrane and the hydrophobic tip of CYP2B4 is inserted into the membrane surface (Figure 1.4).

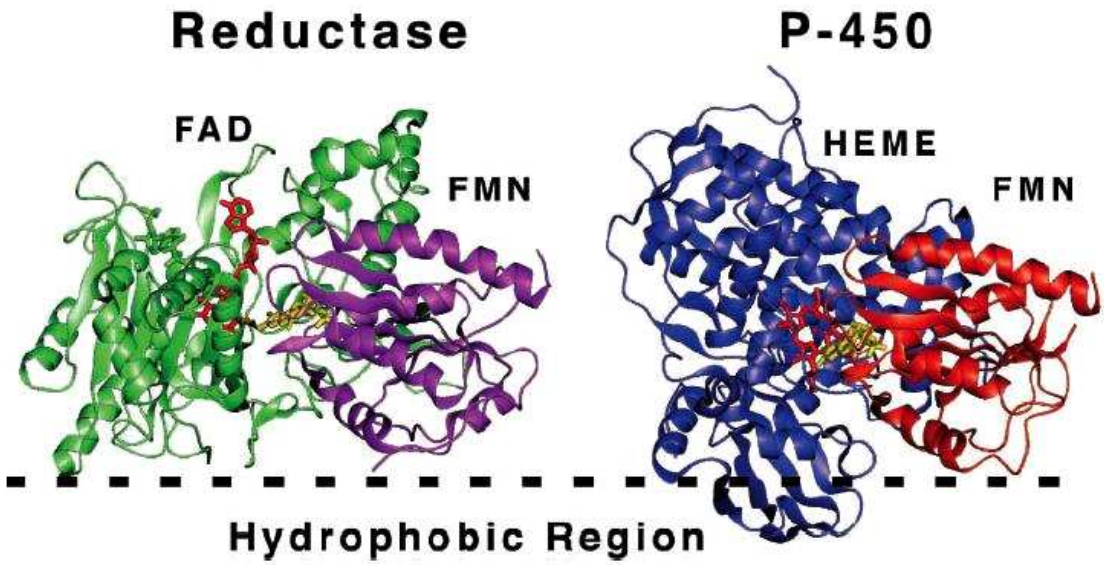

Figure 1.4 Orientation of mammalian OxR and P450 relative to the membrane surface. Cytochrome P450 (blue) is orientated with the heme (red) perpendicular to the ER membrane. Note the position (yellow) where FMN (purple) accepts electrons from FAD (green); in the P450 this position (FMN red) is in close proximity to the heme cofactor.

1.3.3 Human cytochromes P450

Human P450s are integral in regulating the steady-state levels of endogenous hormones and the numerous physiological substrates required for cell proliferation and differentiation (Guengerich 2001; Nebert & Nelson 1991). In addition, human P450s are the major catalysts involved in the biotransformation of pharmaceuticals and are therefore of considerable interest in terms of drug therapy. Notably, the class II P450 enzymes typically insert an atom of atmospheric molecular oxygen (O_2) into a substrate which results in the hydroxylation, epoxidation, and dealkylation of substrates to name a few.

Due to the large number of human P450s, individual enzymes require naming on the basis of evolutionary relatedness to their primary amino acid sequence (Figure 1.5). Members in a given gene family generally have more than 40% identity with other members of the same family, while members of the same human P450 subfamily have greater than 55% amino acid sequence identity and appear to lie on the same chromosome cluster (Nelson et al. 1996).

P450s can be categorized as either xenobiotic-metabolizing enzymes comprising CYP1, CYP2, and CYP3 with some involvement from CYP4, or as P450s involved in the synthesis of endogenous substrates such as steroids, fatty acids, and prostaglandins, namely CYP11, CYP17, CYP19, and CYP21 families (Daly 2003; McFadyen, Melvin & Murray 2004; Petushkova et al. 2006; Rendic 2002). The principal human P450s in CYP1, CYP2, and CYP3 families contribute primarily to the conversion of exogenous lipophilic molecules to water-soluble forms for excretion from the body (eq 1.2).

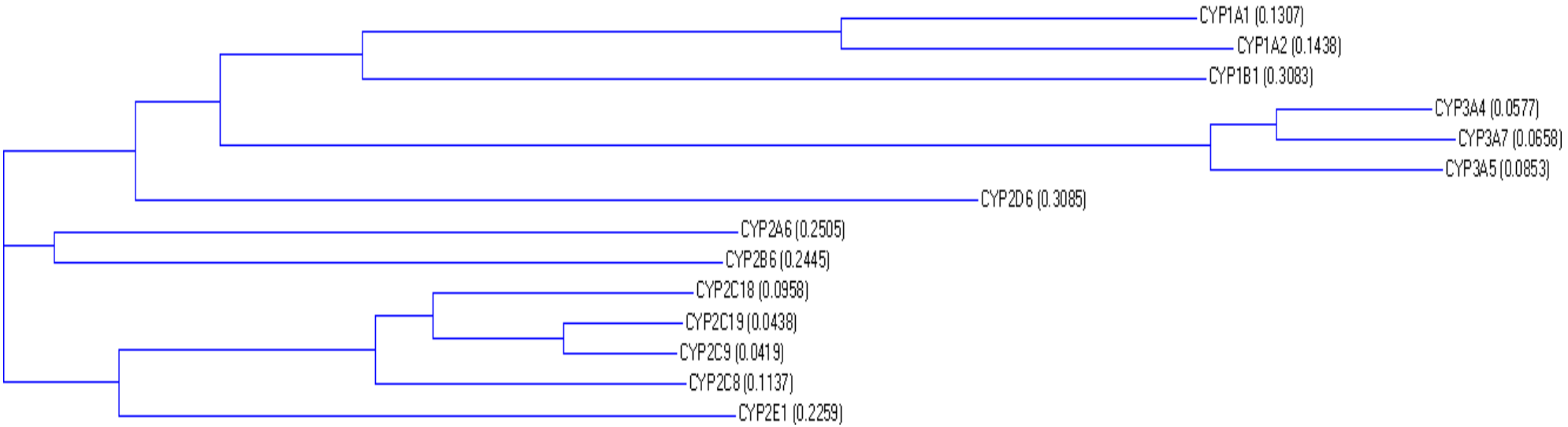

Figure 1.5 Evolutionary tree showing the relatedness of the main human P450s involved in the clearance of hydrophobic compounds. The Tree was built using the Neighbor Joining method (NJ) of Saitou and Nei (Saitou & Nei 1987). The NJ method utilizes a matrix of distances between all pairs of sequence to be analyzed. These distances are related to the degree of divergence between each gene. The Tree is calculated after the sequences are aligned. Distance values are in parenthesis.

$$\text{R-H} + O_2 + 2\text{é} + \text{NADPH} + H^+ \xrightarrow[(\textit{oxidation})]{\text{cytochrome P450}} \text{R-OH} + H_2O + \text{NADP}^+$$

$$\text{R-OH} \xrightarrow[(\textit{conjugation})]{\text{transferases}} \text{R-OX} \dashrightarrow \text{Renal excretion} \qquad (1.2)$$

where R is any P450 substrate and X is any conjugation molecule (e.g. glucuronic acid).

The CYP1 family is comprised of enzymes involved in the metabolism of polycyclic aromatic hydrocarbons, heterocyclic compounds, methylxanthines, and aromatic amines. CYP1 is comprised of two subfamilies; CYP1A and CYP1B. The CYP2 family includes enzymes that metabolize numerous organic compounds, namely drugs, non-drug xenobiotics, and steroids, and consists of eight subfamilies comprising mammalian genes CYP2A through CYP2G and CYP2J. The CYP3 family similarly metabolizes drugs and other xenobiotics as well as being responsible for the 6β-hydroxylation of testosterone (Levy et al. 2000). Family CYP3 currently consists of one subfamily, CYP3A, which includes 27 genes. Examples of drug substrates of mammalian P450 enzymes are given in Table 1.1.

Human P450s are expressed in varying amounts throughout many tissues, with the highest levels found in the liver. The relative abundance of P450s in human liver can be seen in Figure 1.6a (Yeo, Rostami-Hodjegan & Tucker 2004). Some 57 different P450 genes (plus 58 pseudogenes) are present in the human genome, with eight accounting for more than 90% of drug oxidations (1A2, 2A6, 2C8, 2C9, 2C19, 2D6, 3A4, 3A5) (Figure 1.6b) (Code et al. 1997).

Table 1.1 Representative substrates of the principal P450 enzymes from families CYP1, CYP2, and CYP3.

P450 Enzyme	Drug Substrate
CYP1A1	phenacetin, dacarbazine, pregnenolone
CYP1A2	caffeine, clozapine, phenacetin, tacrine, theophylline
CYP2A6	nicotine
CYP2C8	cerivastatin, paclitaxel, repaglinide
CYP2C9	ibuprofen, phenytoin, tolbutamide, *S*-warfarin
CYP2C19	omeprazole, proguanil, *S*-mephenytoin
CYP2D6	codeine, debrisoquine, fluoxetine, metoprolol, perhexiline, tamoxifen
CYP2E1	ethanol, enflurane, halothane
CYP3A4/5	Ca-channel antagonists, cyclosporine, HIV-protease inhibitors, midazolam, nifedipine, simvastatin, tacrolimus

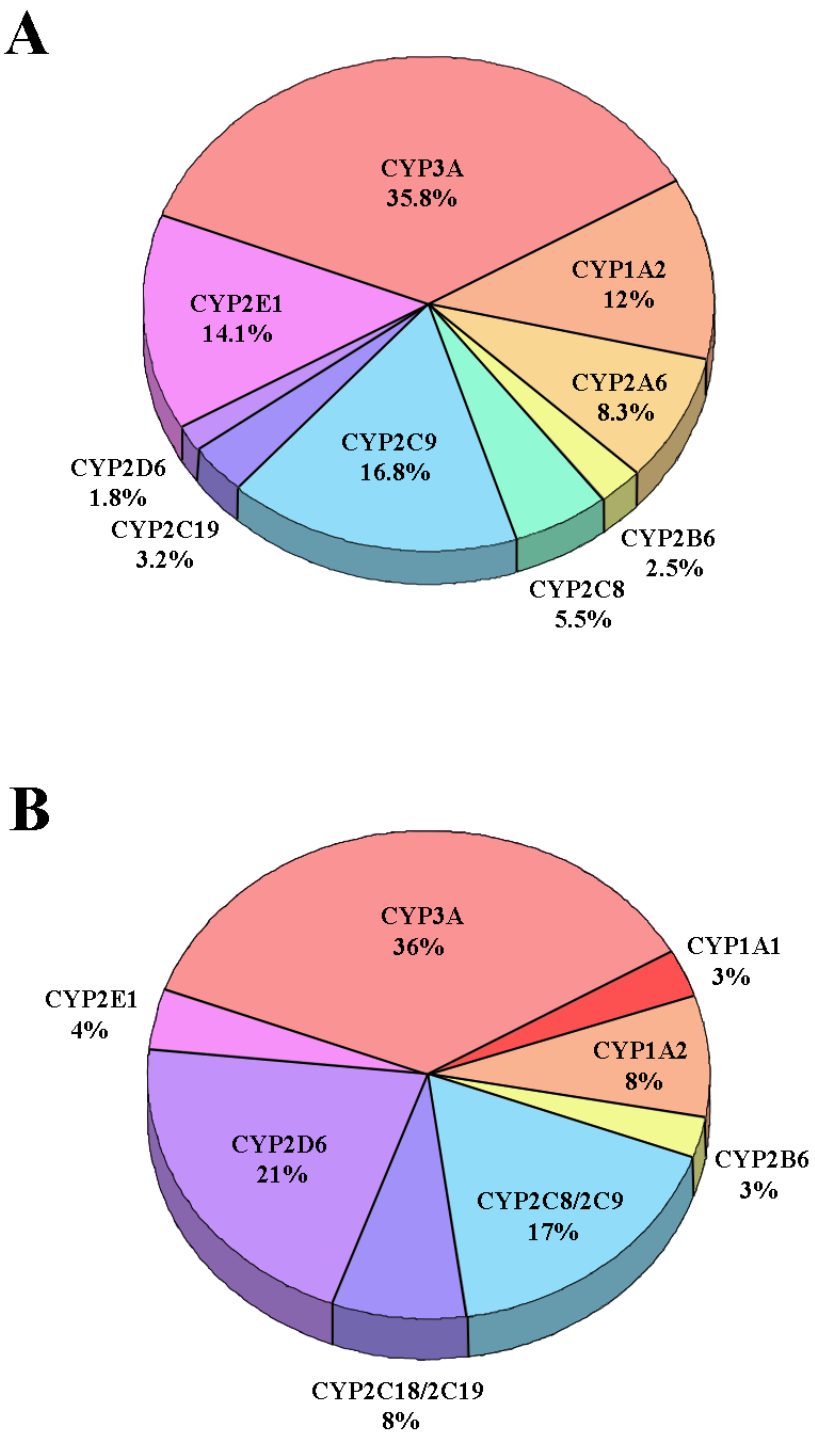

Figure 1.6 The relative abundance of human P450 enzymes in the liver (a); and the percentage of pharmaceuticals metabolized by respective P450 enzymes (b).

1.3.4 Human cytochrome P4501A subfamily

Human CYP1A1 and CYP1A2 share 72% amino acid sequence identity, but display differing substrate and inhibitor profiles, although some substrates can be metabolized by both enzymes. For example, 7-ethoxyresorufin is *O*-deethylated by both enzymes, albeit more effectively by CYP1A1 than CYP1A2, whereas CYP1A2 exhibits a preference for 7-methoxyresorufin (Burke et al. 1994; Hanioka et al. 2000). The basis of this overlapping substrate selectivity was investigated by Liu et al. (2004) whereby five reciprocal active-site mutations between CYP1A1 and CYP1A2 (viz. residues 122/124, 221/223, 225/227, 312, and 382) were used to identify key residues involved in alkoxyresorufin metabolism (Figure 1.7). Residue substitution led to loss of 7-methoxy- and 7-ethoxyresorufin *O*-deethylation activity compared to wild-type, except for the CYP1A1 S122T mutation which increased both activities. In addition, it was shown that mutations at position 382 in both CYP1A1 and CYP1A2 shifted the substrate selectivity from one enzyme to the other, confirming the importance of this residue. Interestingly, the CYP1A1 G225V mutant gave rise to a significant loss of heme and high levels of apoenzyme. Notably, mutagenesis of the CYP1A1 active-site residues involved in the stabilization and orientations of DTIC have not been reported.

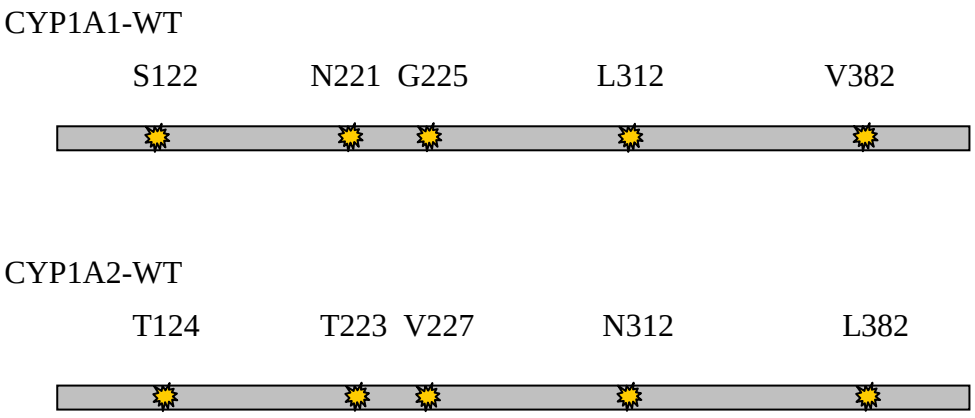

Figure 1.7 Location of the reciprocal mutation sites in CYP1A1 and CYP1A2 employed in the study of Liu *et al.* (2004).

1.3.5 Human cytochrome P4501A1

1.3.5.1 Background

CYP1A1 is the focus of this thesis. The *CYP1A1* (P1-450) gene, located at 15q22-q24, comprises seven exons and six introns and spans 5810 base pairs (Jaiswal, Gonzalez & Nebert 1985; Kawajiri et al. 1986). Human CYP1A1 (EC:1.14.14.1) is mainly present in the skin, lungs, placenta, and lymphocytes, and plays an important role in the metabolic activation of chemical carcinogens. Basal CYP1A1 protein expression in all tissues is thought to be low (Nebert et al. 2004), but varying levels of CYP1A1 mRNA have been detected following induction by polycyclic aromatic hydrocarbons (PAH's). Table A1.1 (Appendix 1) lists most substrates, inhibitors, and exogenous inducers of CYP1A1. CYP1A1 is capable of oxidizing benzo[a]pyrene and other PAH's to carcinogenic species (Chua et al. 2000; Chun, Shimada & Guengerich 1996; Liu et al. 2003; Sparfel et al. 2004). This enzyme is strongly induced by cigarette smoke and potentially associated with lung cancer (Han, Pentecost & Spivack 2003; Patterson & Murray 2002). Like many other P450s,

CYP1A1 is polymorphic and genetic variation is thought to play a role in determining cancer susceptibility (Balasubramanian et al. 2004; Han, Pentecost & Spivack 2003; Miyoshi et al. 2002).

1.3.5.2 Interindividual variability in human CYP1A1 expression

Nine CDS polymorphic alleles of the *CYP1A1* gene have been identified (Table 1.2). The frequencies of the four most common variant alleles, CYP1A1*2A, CYP1A1*2C, CYP1A1*3, and CYP1A1*4, vary between different populations: 2.7-5.1% in Caucasians; 10-15% in Japanese; 13.6-25.5% in Africans; and 2.7-22% in African-Americans (Garte et al. 2001). CYP1A1*2A and CYP1A1*2B are in linkage disequilibrium. Some polymorphisms in the mRNA and protein coding sequences of CYP1A1 have been hypothesized to be responsible for interindividual differences in the susceptibility to chemically induced disease, but have not been extensively studied in terms of both functional and clinical consequences. Of the polymorphisms reported in the coding region of CYP1A1, only a few have measurable functional consequences (Han, Pentecost & Spivack 2003). Han, Pentecost and Spivack (2003) examined 1.5kb of the promoter region of *CYP1A1*. Thirteen single nucleotide polymorphisms (SNP's) were identified, with the majority occurring as multi-SNP combinations in individual patients. The majority of CYP1A1 haplotypes were shown to have no functional effects compared to the wild-type promoter sequences. In contrast, two constructs of composite polymorphisms (C2923T-G2875A-T3777G and C2923T-T3777G-G4335A) appeared to result in a significant increase in basal promoter activity (1.38- and 1.50-fold, respectively).

Table 1.2 *CYP1A1* polymorphisms.

Data were obtained from http://www.imm.ki.se/CYPalleles/.

Allele	Protein	Nucleotide Changes	Trivial Name	Effect
CYP1A1*1A	CYP1A1.1	None	Wild-type	-
CYP1A1*1B	CYP1A1.1	C-3219T	-	-
CYP1A1*1C	CYP1A1.1	G-3229A	-	-
[a]**CYP1A1*2A**	CYP1A1.1	T3801C (MspI)	m1	-
[a]CYP1A1*2B	CYP1A1.2	A2455G; T3801C (MspI)	-	I462V
CYP1A1*2C	CYP1A1.2	A2455G	m2	I462V
CYP1A1*3	CYP1A1.1	T3205C	m3	-
CYP1A1*4	CYP1A1.4	C2453A	m4	T461N
CYP1A1*5	CYP1A1.5	C2461A	-	R464S
CYP1A1*6	CYP1A1.6	G1636T	-	M331I
CYP1A1*7		2346_2347 T insertion	-	Frame shift
CYP1A1*8	CYP1A1.8	T2414A	-	I448N
CYP1A1*9	CYP1A1.9	C2461T	-	R464C
CYP1A1*10	CYP1A1.10	C2500T	-	R477W
CYP1A1*11	CYP1A1.11	C2546G	-	P492R

[a]Denotes linkage disequilibrium.

1.3.5.3 Regulation of human CYP1A1

CYP1A1 (along with CYP1A2 and CYP1B1) is regulated by the aromatic hydrocarbon receptor (AhR). The AhR is a ligand activated transcription factor that mediates a toxic response toward specific chemical pollutants, including PAH's and polychlorinated dioxins, most notably benzo[a]pyrene (BaP), 3-methylcholanthrene (3-MC), 2,3,7,8-tetrachlorodibenzo-*p*-dioxin (TCDD), and β-naphthoflavone (βNF) (Denison & Nagy 2003; Nebert et al. 2004; Shimada & Fujii-Kuriyama 2004). The AhR is a member of the basic helix loop, helix (bHLH/PAS) protein superfamily (Galijatovic et al. 2004), whose members play an important part in facilitating intercellular signaling via sensory pathways (Roblin, Okey & Harper 2004). The AhR is a critical mediator of a cell signaling system, whereby its activation gives rise to the altered regulation of numerous genes. AhR is a soluble cytosolic protein which forms a complex with the chaperone proteins hsp90 and hsp23 and an immunophillin-like protein (involved in its immunosuppressive behavior) (Figure 1.8). Upon ligand activation, the AhR translocates to the nucleus, dissociates from the hsp proteins, and forms a heterodimer with another bHLH/PAS protein, the AhR nuclear translocator (ARNT). The ligand-AhR-ARNT complex then interacts with a 5′-GCGCT-3′ DNA core binding motif, commonly termed the xenobiotic (or drug) response element (XRE; DRE), present in multiple copies upstream of the *CYP1A1* gene promoter (Le Ferrec et al. 2002). The DNA bound AhR-ARNT dimer then recruits cofactors, allowing the complex to regulate expression of *CYP1A1* (Levine-Fridman, Chen & Elferink 2004; Roblin, Okey & Harper 2004). Interestingly, the human *CYP1A1* gene also contains a negative regulatory domain about -800 bases from the transcriptional start site (Galijatovic et al. 2004). This is not evident in other species.

Research conducted by Harper *et al* (2004) shows that CYP1A2 and CYP1B1 are constitutively expressed in the liver of AhR-null mice. In addition, CYP1A2 and CYP1B1 are induced in AhR-null mice by phenobarbitone, indicating that the expression of CYP1A2 and CYP1B1 can be regulated by factors other than the AhR (e.g. the constitutive androstane receptor, CAR). In contrast, CYP1A1 expression appears to be highly dependent on the AhR. Transfection of the full-length human AhR cDNA into BP8 rat hepatoma cells (AhR deficient) was sufficient to induce substantial CYP1A1 mRNA levels without the presence of an exogenous AhR ligand. This was achieved using the human elongation factor 1α-subunit promoter (hEF-1α). Additionally, the AhR antagonist, 3,4-dimethoxyflavone, is known to inhibit CYP1A1 expression in a concentration dependent manner (Roblin, Okey & Harper 2004).

The AhR transcription factor is additionally involved in cell cycle regulation (Levine-Fridman, Chen & Elferink 2004). This suggests that in the absence of an exogenous ligand, the AhR functions to promote cell growth. Studies with 5L rat hepatoma cells (AhR-positive) demonstrated that TCDD induces a G_1 phase cell cycle arrest not detected in BP8 cells. Other findings suggest that some endogenous AhR agonists may also be substrates for the CYP1A1 enzyme (Chang & Puga 1998). CYP1A1-mediated depletion of the endogenous AhR agonist therefore creates a negative feedback mechanism which suppresses prolonged AhR activity under normal physiological conditions. Evidence presented by Levine-Fridman, Chen and Elferink (2004) further suggests that the duration of AhR activity can dramatically impact on the cell cycle response to growth factors and other extra-cellular signals (consistent with the hypothesis that the AhR functions as a regulator of cell cycle progression through G_1 phase) and that growth factor-stimulated CYP1A1 induction

during the G1-to-S phase transition inactivates the AhR by rapidly depleting the endogenous ligand. In addition, failure to inhibit AhR activity resulted in cell cycle arrest.

Differences in the susceptibility of individuals to the adverse actions of PAH's may be due to differing CYP1A1 expression and genetic variations in *CYP1A1*. The same can be said for interindividual differences in the levels of expression of the AhR, and the occurrence of AhR polymorphism. In addition to the multiplicity of genotypic transcriptional malfunctions, further exogenous compounds can account for the disruption of post-transcriptional inhibition. For example, fluasterone (16α-fluoro-5-androsten-17-one), a synthetic analogue of the chemo-preventative hormone dehydroepiandrosterone (DHEA), has been shown to inhibit the rate of CYP1A1 promoter-controlled transcription. Fluasterone moderately inhibited TCDD-induced transcription of CYP1A1 by hindering the XRE binding motif, as measured by ethoxyresorufin *O*-deethylase (EROD) activity. In the presence of the RNA polymerase II inhibitor actinomycin D, fluasterone caused an increase in the degradation of CYP1A1 mRNA (Ciolino, MacDonald & Yeh 2002). In contrast, CYP1B1 mRNA remained unaffected, further indicating that the expression of the CYP1A1 gene is regulated by unique factors.

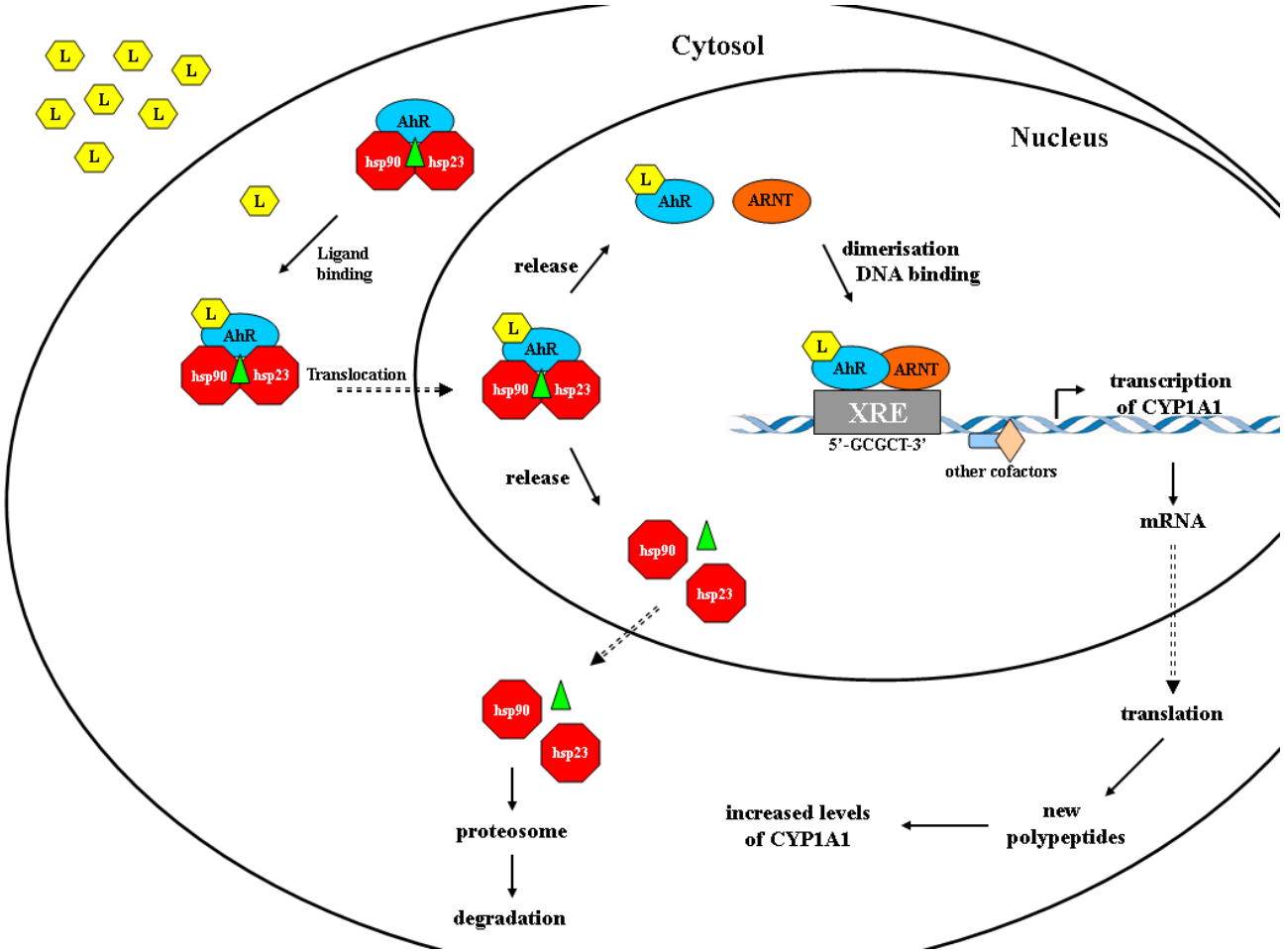

Figure 1.8 The molecular mechanism of activation of gene expression by the Aromatic Hydrocarbon Receptor (AhR).

L; ligand, hsp90; heat shock protein 90, hsp23; heat shock protein 23, ARNT; AhR nuclear translocator, XRE; xenobiotic response element.

1.3.5.4 Inhibition of human CYP1A1

Many chemicals including α-naphthoflavone, 7-hydroxyflavone, synthetic chemo-preventative organoselenium compounds such as 1,2-, 1,3-, and 1,4-phenylenebis(methylene)selenocyanate, vinylic and acetylenic PAH's such as 1-(1-propynyl)pyrene, and 4-(1-propynyl)biphenyl have been identified as inhibitors of CYP1A1 (Appendix 1, Table A1.1). Recently, Chun, Kim and Guengerich (1999) reported that the natural products resveratrol and rhapontigenin are also inhibitors of human CYP1A1. For example, the IC_{50} value for rhapontigenin (3,3′,5-trihydroxy-4′methyl-thoxystilbene) inhibition of CYP1A1 was 0.4 μM. As a mechanism-based inhibitor, rhapontigenin showed a 400-fold selectivity for CYP1A1 over CYP1A2 and a 23-fold selectivity over CYP1B1. In addition, rhapontigenin did not show any significant inhibition of EROD activity in human liver microsomes which contain negligible amounts of CYP1A1 (Chun et al. 2001). With respect to resveratrol (*trans*-3,4′,5-trihydrostilbene), there was a 50-fold selectivity in its inhibition of CYP1A1 over CYP1A2, with an IC_{50} value of 23μM. Prior to this study, resveratrol was perceived to be a potential cancer chemo-preventative agent due to its ability to inhibit oxidation/reduction enzymes and induce conjugation enzymes. However, the mechanism-based inactivation of CYP1A1 with rhapontigenin suggests that this compound would be a more potent and selective chemo-preventative agent.

1.3.6 Heterologous expression of human P450 enzymes

1.3.6.1 Background

The heterologous expression of recombinant proteins provides a means of obtaining higher yields of a target protein compared to those levels found endogenously in cells. Mammalian expression systems are routinely used for a variety of recombinant proteins, however the over-expression of P450s in mammalian cell lines has been less successful (McManus et al. 1990). Greater success has been achieved using yeast (Ikushiro et al. 2004), insect (Ong et al. 1998), and bacterial expression systems, with bacteria being the simplest and most cost effective (Boye et al. 2004; Gonzalez & Korzekwa 1995). Bacteria also has the advantage of accommodating foreign genetic material (Fujita & Kamataki 2002) and producing very high yields of protein in a relatively short amount of time due to competent cell replication (Baneyx & Mujacic 2004). However, the production of functional proteins in *E. coli*, especially from eukaryotic origin, can be problematic due to differences in codon usage and the formation of inclusion bodies (Jana & Deb 2005). Table 1.3 summarizes some of the molecular tools used to increase expression yields of functional recombinant proteins.

Table 1.3 Molecular tools and techniques used for optimizing heterologous protein expression in *Escherichia coli.* Modified from Jana & Deb (2005).

Component	Remarks
Host strain	Choice of host strain can impact expression via the host's genotype. Sufficient cellular machinery is required for correct protein translation and folding.
Plasmid copy number	Gene dosage, as manipulated through plasmid copy number, can greatly affect protein expression.
Antibiotic selection	Choice of antibiotic resistance on the expression plasmid can influence heterologous expression.
Promoter	Strong or weak, inducible or constitutive; promoter and regulation are major influences on protein expression, which is also affected by relative orientation and strength of promoters on the plasmid.
Transcription termination	Effectiveness and spacing of transcription terminators affect expression.
mRNA stability	The stability of the mRNA affects yield. Secondary structure at the 5' end of the message often plays a critical role.
Translation signal	The ribosome binding-site affects the amount of ribosome loading and clearance, and hence, expression. Secondary structure at the 5' end can affect the accessibility of the ribosome binding-site.
Codon usage (*E. coli*)	Numerous differences occur between human and bacterial codon usage. Utilizing the optimal *E. coli* codons often improves yield.
Signal peptide	An amino signal peptide, used for targeting a protein to a specific region of the bacterial cell, can greatly enhance the expression yield through protein folding and stability.
Temperature	Temperature has a profound affect on protein folding and stability. Improves yields of soluble proteins.
Growth conditions	Growth conditions, oxygen levels, growth rate, carbon source and fermentor configuration all affect yield.
Media and supplements	Supplementation with rare elements can aid the correct folding of recombinant proteins and stabilization during transport across membranes.

1.3.6.2 Expression of modified P450s in Escherichia coli

Unlike most eukaryotes and many bacteria, enterobacteria such as *E. coli* lack P450s, which makes them a useful organism for recombinant expression. Successful synthesis of P450s in *E. coli* requires the nucleotide CDS of the desired protein to be cloned downstream of an efficient promoter and ribosome binding-site in a high copy number plasmid. Transcriptional activation of the promoter gives rise to mRNA molecules that await ribosome-mRNA complexation for efficient translation. As described by Barnes (1996), the nascent polypeptide then associates with the *E. coli* membrane, binds a molecule of heme, and folds into its final tertiary structure.

The bacterial plasmid of choice for many laboratories expressing P450s is pCW ori(+) (Figure 1.9), a derivative of the pHSe5 plasmid backbone. pCW ori(+) contains a pBR322 origin of replication, the *lac* I^q gene that encodes a repressor protein which binds to the *lac* operator and blocks transcription down-stream, the β-lactamase gene for conferring ampicillin resistance, and a bacterophage origin of replication. Transcription and translation of pCW ori(+) is controlled by a *lac*UV5 promoter and two copies of the *tac* promoter cassette with translation initiation coming from the phage T4 lysozyme gene. A trpA transcription termination cassette is located down-stream of the multiple cloning site (MCS). Protein synthesis is induced with isopropyl β-D-thiogalactopyranoside (IPTG), a molecular mimic of allolactose, a lactose metabolite that triggers transcription of the *lac* operon. The modified CheW chemotaxis gene of *E. coli* and the β-galactosidase gene aid insert selection.

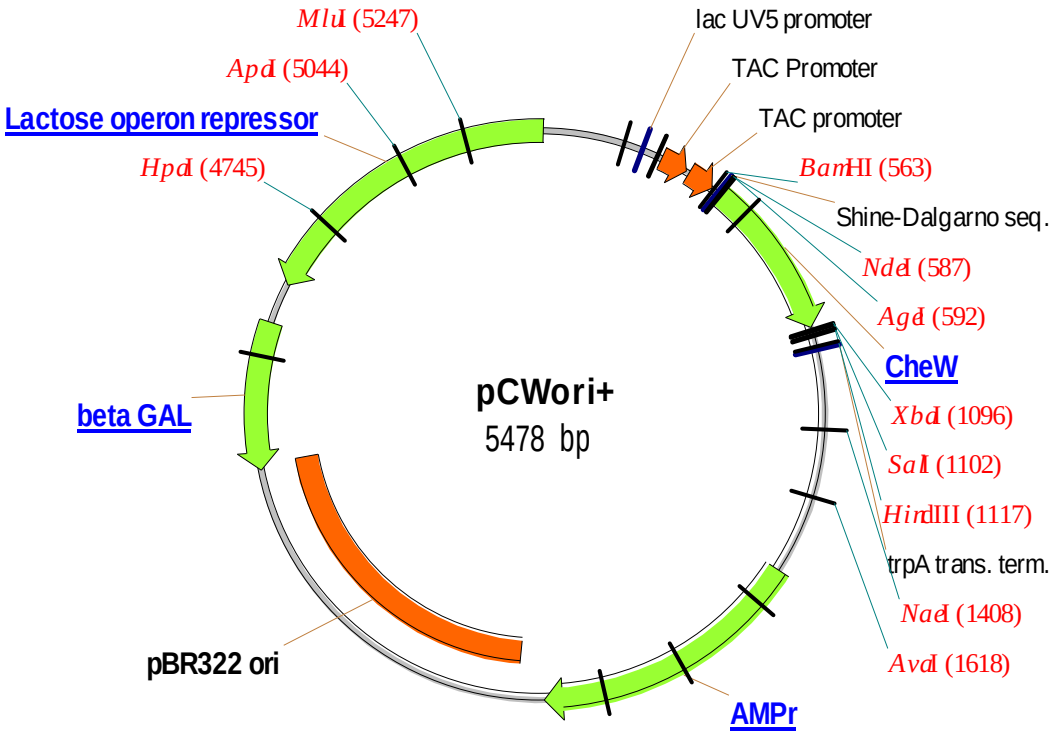

Figure 1.9 Plasmid map of the pCW ori(+) bacterial expression plasmid. Elements are drawn to scale.

Due to the fact that all class II P450s bind to the ER membrane, truncation of the 5' terminus of the CDS to remove the hydrophobic transmembrane domain typically increases the yield of many P450s in bacteria. This has been observed by several investigators, primarily utilizing CYP2C family proteins (Boye et al. 2004; Guo et al. 1994; Iwata et al. 1998; Sandhu, Baba & Guengerich 1993). Additionally, the NH_2-terminus can be modified to target expression of a P450 to a desired *E. coli* organelle (Luirink et al. 2005), which in turn decreases the likelihood of secondary-structure formation of message around the ribosome assembly site (and the ATG). Table 1.4 lists several signal sequences used for targeting message to different locations within the gram-negative bacterial cell (Figure 1.10). In addition, the leader sequence

obtained from the bovine microsomal 17α-hydroxylase cytochrome P450, P45017A is required. In an attempt to optimize bacterial expression, Barnes, Arlotto and Waterman (1991) showed that modification to the first seven residues of P45017A greatly enhanced holoenzyme formation. Specifically, the second codon was changed from TGG (Trp) to GCT (Ala), the preferred second codon for expression of the bacterial *lac*Z gene. In addition, amending the DNA CDS of residues 4, 5, 6 and 7 of P45017A to utilize the bacterial codon usage reduced the Gibbs free energy (ΔG) of mRNA self-hybridization. Use of the P45017A-signal peptide (17α-leader sequence) has a profound effect on the yield of functional P45017A in *E. coli* and has subsequently been used by numerous groups to successfully express large amounts of mammalian P450s in *E. coli* (Boye et al. 2004; Fisher et al. 1992; Gillam et al. 1997; Lewis, Mackenzie & Miners 2007; Pritchard et al. 1997; Richardson et al. 1995; Shet et al. 1994).

The heterologous expression of P450s in *E. coli* is usually conducted in K-12 strains where heme is impermeable to the gram-negative phenotype. This makes holoenzyme P450 expression somewhat limited in addition to the fact that heme is potentially toxic to the cells (Harnastai, Gilep & Usanov 2006). The ability of most bacteria to produce the heme precursor 5-aminolevulinic acid (δ-ALA) via ALA synthase (C-4 path) is not shared by *E. coli*, which synthesize δ-ALA from glutamate (C-5 path) (Avissar & Beale 1989). Since cellular heme content plays a role in the regulation of δ-ALA production, endogenous heme biosynthesis is tightly controlled with almost no free heme present under normal culture conditions (Woodard & Dailey 1995). Moreover, heme has a relatively low affinity for the nascent P450 polypeptide. To combat this problem bacterial cultures are commonly supplemented with exogenous δ-ALA.

Table 1.4 Common signal peptides used in the expression of eukaryotic proteins in bacteria. Basic amino acids, blue; hydrophobic amino acids, yellow. Red stars represent cleavage sites that mark the end of each signal peptide. Refer to Figure 1.10 for a schematic representation of gram-negative bacteria.

Inner Membrane Proteins	**Signal Peptide**
Phage fd, major coat protein	MKKSLVLKASVAVATLVPMLSFA*AE
Phage fd, minor coat protein	MKKLLFAIPLVVPFYSHS*AE
Periplasmic Proteins	**Signal Peptide**
Alkaline phosphatase	MKQSTIALALLPLLFTPVTKA*RT
Leucine-specific binding protein	MKANAKTIIAGMIALAISHTAMA*DD
β-lactamase of pBR322	MSIQHFRVALIPFFAAFCLPVFA*HP
Outer Membrane Proteins	**Signal Peptide**
Lipoprotein	MKATKLVLGAVILGSTLLAG*CS
LamB	LRKLPLAVAVAAGVMSAQAMA*VD
OmpA	MMITMKKTAIAIAVALAGFATVAQA*AP

In the bacterial heterologous system used for P450s, it is not uncommon for overexpressed proteins to form insoluble aggregates called ‘inclusion bodies’. Inclusion bodies usually result from proteins that fail to fold correctly and tend to accumulate in the cytoplasm or periplasm (Figure 1.10) depending on the signal peptide used (Table 1.4). The recombinant protein usually accounts for 80-95% of the inclusion body and is contaminated with outer membrane proteins, ribosomal components, and a small amount of phospholipids and nucleic acids (Baneyx &

Mujacic 2004). In the case of P450s, heme incorporation is critical for obtaining the correct folding conformation.

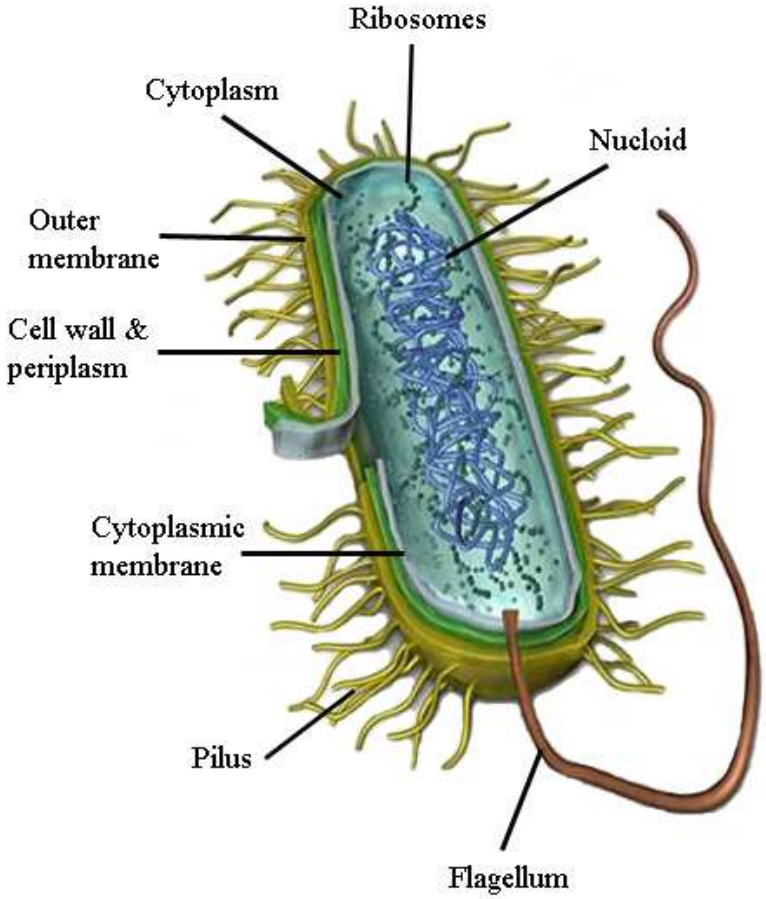

Figure 1.10 Schematic representation of the structural organisation of gram-negative bacteria. Amended from Pugsley (1993).

Once successful expression of P450 has been achieved, membranous extracts usually undergo spectral analysis to determine the functional holoenzyme concentration. This is achieved by reducing the protein preparation containing the oxidized P450 with sodium dithionite ($Na_2S_2O_4$) followed by exposure to $CO_{(g)}$ to uncouple the P450 catalytic cycle (Figure 1.2). The initial oxidized P450 present in the native protein preparation gives a Soret band at 414nm (extinction coefficient; $124mM^{-1}cm^{-1}$). Reduction of the heme Fe^{3+} to Fe^{2+} shifts the Soret band to 427nm ($149mM^{-1}cm^{-1}$). Treatment with $CO_{(g)}$ also displaces any $O_{2(g)}$ bound to the Fe^{2+} allowing the absorption spectra to be determined for both apo- and holo-enzyme forms (Figure 1.11). In the reduced apo- form bound with $CO_{(g)}$, a shift in the Soret band to 420nm is observed along with a marked increase in absorbance intensity ($213mM^{-1}cm^{-1}$). The reduced P450 with bound $CO_{(g)}$ gives rise to an absorbance peak at 450nm ($91mM^{-1}cm^{-1}$) characteristic of the holo- form of the enzyme (Miyake & Takayama 1975; Omura & Sato 1964a; Omura & Sato 1964b).

To generate an active system *in vitro*, P450s require the donation of electrons, utilized for reducing the heme Fe^{3+}, from the redox partner (section 1.3.1). Bacteria, however, do not contain a suitable endogenous redox partner, hence, the heterologous expression of P450s additionally requires expression of OxR. Dual expression may be achieved by a number of methods: (i) a CYP-OxR fusion construct (Deeni et al. 2001; Fisher et al. 1992; Fisher, Shet & Estabrook 1996; Shet et al. 1994; Shet et al. 1993), (ii) a bicistronic plasmid (Boye et al. 2004; Gillam et al. 1997; Parikh, Gillam & Guengerich 1997), or (iii) the simultaneous co-transformation of different P450 and OxR plasmids (Dong & Porter 1996; Fujita & Kamataki 2002; Iwata et al. 1998; Lewis, Mackenzie & Miners 2007; Pritchard et al. 1998). It should be noted that mixing of bacterial membrane preparations generated

from separate P450 and OxR expressions can reconstitute enzymatic activity (Boye et al. 2004). However, the generation of an active mixed-membrane system is not successful with those P450 enzymes that contain a hydrophobic signal peptide, but is feasible for those P450s expressed with a truncated NH_2-terminus (e.g. CYP2C9 Δ3-20 truncation) (unpublished observation). It appears that the more hydrophilic nature of the truncated P450 allows greater flexibility in the bacterial membrane and can therefore align and couple more freely with the supplemented OxR.

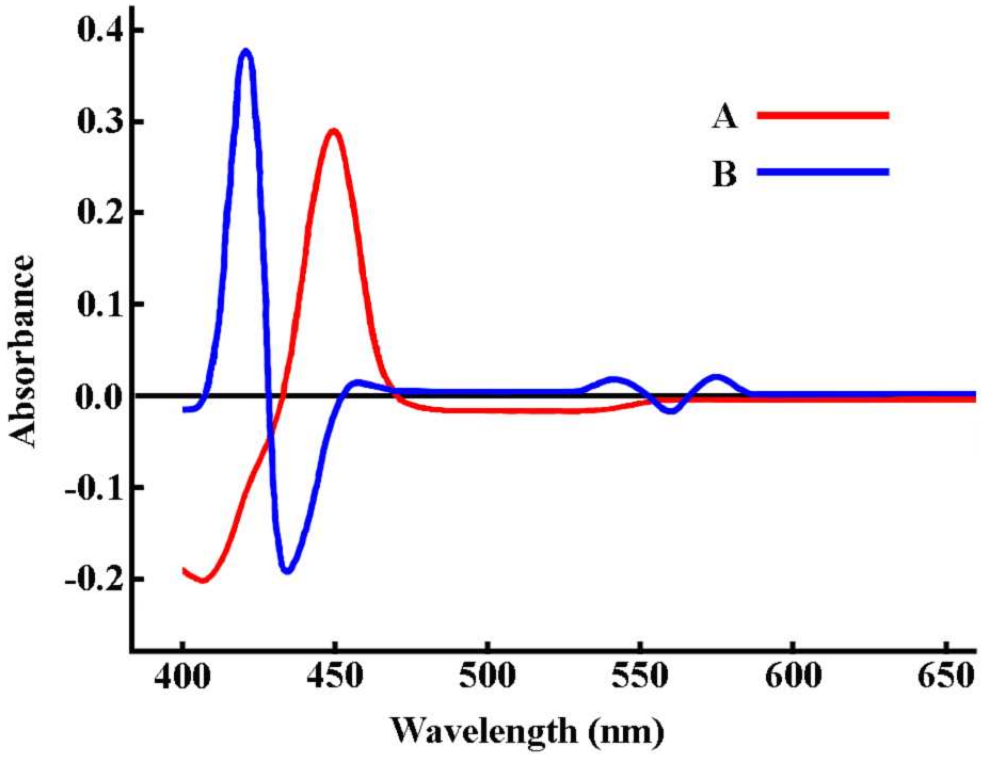

Figure 1.11 P450 CO difference spectra. Spectrum A (red) shows the formation of the ferrous Fe^{2+}-CO complex of a typical holo-P450 after reduction with sodium dithionate and bubbling with $CO_{(g)}$ (450 peak). Spectrum B (blue) shows the inactive reduced apo-enzyme peak at 420nm with a deep trough at 435nm, two small peaks at 540nm and 575nm, and a trough at 560nm. The P420 species has a substantially larger Soret molar absorption coefficient than the holo- form.

Like P450, the measurement of OxR concentration is equally important and is commonly attained by the method outlined by Yasukochi & Masters (1976). NADPH-dependent reduction of cytochrome *c* is monitored by the increase of absorbance at 550nm. The rate of reduction of cytochrome *c* (nmol/mg protein/min) is used as a measure of OxR activity in expressed membrane fractions. The OxR:P450 ratio can be critical for the derivation of kinetic parameters for a drug substrate, whereby an excess of OxR over P450 can enhance catalytic activity (Venkatakrishnan et al. 2000; Yamazaki et al. 1999). Additionally, many P450-dependant reactions have been shown to be stimulated by cytochrome b_5. This possibly occurs via direct electron transfer to the P450 from cytochrome b_5 (holo-b_5) or through a conformational effect on the P450 in the absence of electron transfer (apo-b_5) (Yamazaki et al. 1997; Yamazaki et al. 2001).

1.3.6.3 Recombinant expression of human CYP1A1

Guo et al. (1994) were the first to express the full-length cDNA encoding human CYP1A1, along with several modified constructs, including one carrying the 17α-leader sequence, in *E. coli*. Little expression was observed with the native sequence and several modified constructs, but successful expression (20-25nmol P450 L^{-1} culture) was achieved with a construct in which the Ala codon GCT was placed in the second position and the 5′-terminal codons were maximized for AT content and minimized for potential secondary structure formation of the message transcript. α-Naphthoflavone was found to protect against denaturation by detergents during the solubilization of membranes and was therefore added to all buffers used for purification. The recombinant CYP1A1 catalyzed 7-ethoxyresorufin *O*-deethylation and benzo[a]pyrene 3-hydroxylation with K_m (V_{max}) values of 0.58μM (8.3 nmol

min^{-1}/nmol P450) and 15μM (2.5 nmol min^{-1}/nmol P450), respectively. To further optimize expression, Chun, Shimada and Guengerich (1996) utilized the pCW ori(+) plasmid to code for a fusion protein consisting of the complete CYP1A1 coding sequence (with second amino acid change, Ala) connected by a Ser-Thr linker to rat OxR (beginning at amino acid 57). Expression was typically 150nmol P450 L^{-1} culture, similar to the levels observed with CYP1B1 (Shimada et al. 1998). The favorable difference in CYP1A1 expression compared to that of Guo *et al* (1994) was thought to be due to the addition of the heme precursor δ-ALA to cultures.

The purified fusion protein was shown to catalyze benzo[a]pyrene 3-hydroxylation, 7-ethoxyresorufin *O*-deethylation, and zoxazolamine 6-hydroxylation according to Michaelis-Menten kinetics. However, the catalytic activity of the fusion protein was markedly lower than that of a similar fusion protein constructed with rat CYP1A1. This was thought to reflect the inherently lower activity of human CYP1A1 compared to the rat enzyme, reflecting structural differences arising from the differing coding sequences in each species (Figure 1.12). Notably, no increase in turnover was observed when purified OxR or cytochrome b_5 was added. Furthermore, the authors found that the catalytic activity of the enzyme was considerably higher within purified fractions in contrast to enzyme still localized in membranes.

```
                1                                                  50
human CYP1A1    M....LFPIS MSATEFLLAS VIFCLVFWVI RASRPQVPKG KNPPGPWGW
  rat CYP1A1    MPSVYGFPAF TSATELLLAV TTFCLGFWVV RVTRTWVPKG KSPPGPWGL
               51                                                 100
human CYP1A1    PLIGHMLTLG KNPHLALSRM SQQYGDVLQI RIGSTPVVVL GLDTIRQAL
  rat CYP1A1    PFIGHVLTLG KNPHLSLTKL SQQYGDVLQI RIGSTPVVVL GLNTIKQAL
               101                                                150
human CYP1A1    VRQGDDFKGR PDLYTFTLIS NGQSMSFSPD SGPVWAARRR AQNGLKSFS
  rat CYP1A1    VKQGDDFKGR PDLYSFTLIA NGQSMTFNPD SGPLWAARRR AQNALKSFS
               151                                                200
human CYP1A1    IASDPASSTS CYLEEHVSKE AEVLISTLQE LMAGPGHFNP RYVVVSVTN
  rat CYP1A1    IASDPTLASS CYLEEHVSKE AEYLISKFQK LMAEVGHFDP KYLVVSVAN
               201                                                250
human CYP1A1    VICAICFGRR YDHNHQELLS LVNLNNNFGE VVGSGNPADF PILRYLPNP
  rat CYP1A1    VICAICFGRR YDHDDQELLS IVNLSNEFGE VTGSGYPADF PILRYLPNS
               251                                                300
human CYP1A1    SLNAFKDLNE KFYSFMQKMV KEHYKTFEKG HIRDITDSLI HCQEKQLDE
  rat CYP1A1    SLDAFKDLNK KFYSFMKKLI KEHYRTFEKG HIRDITDSLI HCQDRRLDE
               301                                                350
human CYP1A1    NANVQLSDEK IINIVLDLFG AGFDTVTTAI SWSLMYLVMN RVQRKIQEE
  rat CYP1A1    NANVQLSDDK VITIVFDLFG AGFDTITTAI SWSLMYLVTN RIQRKIQEE
               351                                                400
human CYP1A1    LDTVIGRSRR PRLSDRSHLP YMEAFILETF RHSSFVPFTI HSTTRDTSL
  rat CYP1A1    LDTVIGRDRQ PRLSDRPQLP YLEAFILETF RHSSFVPFTI HSTIRDTSL
               401                                                450
human CYP1A1    KGFYIPKGRC VFVNQWQINH DQKLWVNPSE FLPERFLTPD AIDKVLSEK
  rat CYP1A1    NGFYIPKGHC VFVNQWQVNH DQELWGDPNE FRPERFLTSS TLDKHLSEK
               451                                                500
human CYP1A1    VIIFGMGKRK CIGETIARWE VFLFLAILLQ RVEFSVPLGV VDMTPIYGL
  rat CYP1A1    VILFGLGKRK CIGETIGRLE VFLFLAILLQ QMEFNVSPGE VDMTPAYGL
               501                 524
human CYP1A1    TMKHACCEHF QMQLRS.... ....
  rat CYP1A1    TLKHARCEHF QVQMRSSGPQ HLQA
```

Figure 1.12 Sequence alignment of human CYP1A1 and rat CYP1A1. Alignment similarity is 85.1% (red and green) while identity is 77.7% (red only).

1.4 Cytochromes P450 and neoplastic disease

1.4.1 Metabolic conversion of anti-cancer drugs

P450s are responsible for the metabolism of most prescribed cancer chemotherapeutic agents (Guengerich et al. 2000) by generating inactive or metabolically activated products, or both. While P450 enzymes are predominantly located in the liver, there is substantial evidence that individual P450s are also expressed in other tissues such as the brain, lung, kidney, and the gastrointestinal tract (Guengerich 2000; Murray et al. 1992; Patterson & Murray 2002; Rooney et al. 2004). In addition, there is also evidence showing P450 expression in resected human tumors. Of particular interest is expression in a variety of solid tumors including breast, colon, lung, esophagus, ovarian, bladder, prostate, stomach, and soft tissue sarcomas (Lord, Bongiovanni & Bralley 2002; McFadyen, Melvin & Murray 2004; Miyoshi et al. 2002; Rooney et al. 2004). Indeed CYP1A1, CYP1B1, and CYP3A4 are known to be over-expressed in tumors (Murray et al. 1992; Patterson & Murray 2002; Rooney et al. 2004; Schwartz, Chen & Waxman 2002) and may influence the fate of certain cytotoxic drugs within the tumor.

1.4.2 Cytochrome P450-based prodrug cancer therapy

One promising area for the improvement of tumor/drug selectivity, and one which escapes the problems associated with inter-individual variation, is Gene-Directed Enzyme Prodrug Therapy (GDEPT) (Aghi, Hochberg & Breakefield 2000; Cass et al. 2001; Daly 2003; Denny 2002; Hughes et al. 2002; Johnson 2003; Xu & McLeod 2001). GDEPT is a two step approach. In the first step a drug-activating enzyme is targeted and expressed in the tumor tissue. The gene(s) encoding the enzyme(s)

should be of either non-human origin or human protein that is deficient or expressed in low concentrations in normal tissue (Denny 2002). The protein must achieve sufficient expression in the tumors and have high catalytic activity (Daly 2003). In the second step a non-toxic prodrug, which is a substrate of the exogenous enzyme that is now expressed in the tumor, is administered systemically (Xu & McLeod 2001). The net gain is that the prodrug can be activated within the tumor, producing high local concentrations of the active moiety.

Although GDEPT is susceptible to the same technical challenges as other areas of medicine utilizing gene therapy, it has several advantages over other cancer gene therapies due to its ability to not only reduce systemic exposure, but also transiently replace a polymorphic gene that may confer a 'poor (or extensive) metabolizer' phenotype. In addition, GDEPT is known to produce a 'bystander effect', which extends the cytotoxic response beyond those cells transfected with the prodrug-activating P450. A limitation of GDEPT, however, is that only a small proportion of tumor cells become activated using current enzyme prodrug combinations. In an effort to overcome this problem, the approach of many researchers is to generate new activation competent drugs, i.e. prodrugs that are efficiently activated and effective at killing neighboring cells via a bystander effect (Xu & McLeod 2001). Since recombinant DNA technology can be utilized in GDEPT, an alternative solution is to design specific P450 enzymes with enhanced prodrug activating abilities. Thus, mutant forms of human enzymes can be generated by site-directed mutagenesis and, in doing so, avoid the expected immune response seen with the use of non-human proteins [e.g. rat CYP2B1 (Kan, Kingsman & Naylor 2002)].

Much remains unknown about the use of P450 enzymes in GDEPT, with the majority of questions relating to the design of novel substrates. An increased

understanding of the metabolism of antineoplastic agents within the body is also essential in order to develop more highly specialized and directed therapies. As such, enhanced tumor mediated metabolism by P450s requires further investigation to utilize the specific activation of prodrugs by enzymes, whose expression, or kinetic activity is limited to, or can be enhanced in, cancer cells. GDEPT utilizing P450's may offer the possibility of a truly targeted chemotherapy so long as overproduction of the toxic metabolite is constrained to the tumor environment, thereby minimizing systemic toxicity.

1.5 Structure and function of the mammalian cytochromes P450

1.5.1 Background

Structure-activity analyses in P450s have been essential in understanding the mechanisms responsible for substrate selectivity, regioselectivity, stereoselectivity, and substrate orientation (Lewis 2003; Lewis, Modi & Dickins 2002; Lewis, Lake & Dickins 2004; Miles et al. 2000; Ridderstrom et al. 2001). Using various experimental and analytical approaches, links between structure and function have elucidated numerous relationships, from the substrate recognition sites (SRS) proposed by Gotoh (1992) to the interactions affecting flexibility of the heme prosthetic group by Hudecek et al. (2007). Technical advances in structural and computational techniques, such as nuclear magnetic resonance (NMR), X-ray diffraction, and computational modeling, have substantially increased the P450 knowledge base at the molecular level. Of further importance was the development of site-directed mutagenesis, which allows the targeted substitution of active-site

amino acids and hence a better understanding of the chemistry of substrate access, catalysis, product egress, and enzyme inhibition.

1.5.2 Crystal structure determination

Due to the large molecular size of P450s, application of NMR for structure determination has been somewhat limited. In contrast, the use of X-ray diffraction has proved to be a more powerful method for elucidating the structures of P450s, including those with bound substrate. The generation of mammalian P450 structures has been challenging largely due to the difficulty in obtaining large quantities of protein in a homogeneous state for growing diffraction quality crystals (Zhao & Halpert 2007). The first P450 crystal structure solved was that of CYP101 ($P450_{cam}$) from *Pseudomonos putida* in 1985 (Poulos et al. 1985). The structure of CYP101 was bound with the bicyclic terpene, camphor, which was located in a buried pocket adjacent to the oxygen binding site of the heme. The CYP101 structure was refined to an R-value (statistical measure of fit) of 0.23 at a resolution of 2.6Å. Availability of the CYP101 crystal structure was particularly useful for resolving the topology and secondary structure in the region surrounding the heme. Furthermore, elucidation of the CYP101 crystal structure was an important milestone allowing researchers to make comparisons with the eukaryotic P450s. However, extrapolation of the CYP101 structural data to eukaryotic P450s proved difficult, primarily due to the membrane binding of mammalian P450s and the limited sequence identity among P450 enzymes (generally 10-30%) (Lewis 2002a). In addition, as a class I P450 the residues responsible for the alignment of CYP101 and its redox partner (FAD) are

markedly different to that of the mammalian class II proteins (FAD-FMN; section 1.3.1).

Hasemann et al. (1995) proposed that regions of functional significance among P450s should be conserved at the secondary structure level despite differences in the primary sequence. To this end, they published structures of the class I P450 enzyme CYP108 ($P450_{terp}$; *Pseudomonas sp.*) and the first structure of a soluble class II P450 enzyme, CYP505 ($P450_{BM-3}$; *Bacillus magaterium*). The comparison between all three P450 crystal structures (CYP101, CYP108, and CYP505) revealed a tertiary arrangement with a highly conserved core of secondary-structure elements. The substrate recognition regions exhibited the greatest differences, with large shifts in the B', F and G helices (Figure 1.13).

The first mammalian P450 to be crystallized was rabbit CYP2C5 (Williams et al. 2000a). CYP2C5 was modified to increase its solubility and aid crystallization. The crystallized form of CYP2C5 differed from the native enzyme by deletion of the transmembrane domain (residues 3-21), in addition to incorporating D2A, Q22K, N23T, G25S, and R26K mutations that were introduced to improve heterologous expression. A further five substitutions were made: N202H, R206E, I207L, S209G, and S210T, to reduce membrane association, phospholipid dependence for catalysis, and protein aggregation (Cosme & Johnson 2000). Cosme and Johnson's (2000) results identified that the residues of the F and G helix, and the F-G loop were responsible for the membrane interaction of CYP2C5 and the aggregation state of truncated CYP2C5 in solution. Structurally, the CYP2C5 crystal revealed that attachment to the ER membrane occurs through a broad hydrophobic surface that neighbors the N-terminal transmembrane anchor, and that orientation of the electrostatic dipole in the membrane bound enzyme appears optimal for maximizing

OxR alignment and electron transfer (section 1.3.1). In addition, the entrance to the putative substrate access channel between the F-G loop and the N-terminal β-sheet system was also shown to be located in the membrane attachment surface (Figure 1.14a).

The CYP2C5 crystal structure shows the enzyme in a closed conformation. It is also clear that significant structural differences occur between the mammalian CYP2C5 compared to the soluble microbial CYP101, CYP108, and CYP505 structures (Figures 1.13 and 1.14), particularly in the active-site. In a subsequent study, Wester et al. (2003a) co-crystallized CYP2C5 with the sulfaphenazole analogue, 4-methyl-*N*-methyl-*N*-(2-phenyl-2*H*-pyrazol-3-yl)benzenesulfonamide (DMZ), at 2.3Å resolution (Figure 1.14b).

Like rabbit CYP2C5, the crystallization of rabbit CYP2B4 was achieved in both the presence and absence of substrate. The initial CYP2B4 structure was obtained by (Scott et al. 2004a) at 1.6Å resolution (R-value 0.217), the most accurate mammalian structure at that time. The crystallized protein differed from the native enzyme by truncation of the N-terminus (3-21) and mutation of residues E2A, G22K, H23K, P24T, K25S, A26S, H27K, and R29K to facilitate protein expression. The structure of CYP2B4 revealed an open cleft, formed by the B', C, F, and G helices, which extends from the protein surface toward the heme Fe. This structure is representative of an open enzyme conformation (Figure 1.15a).

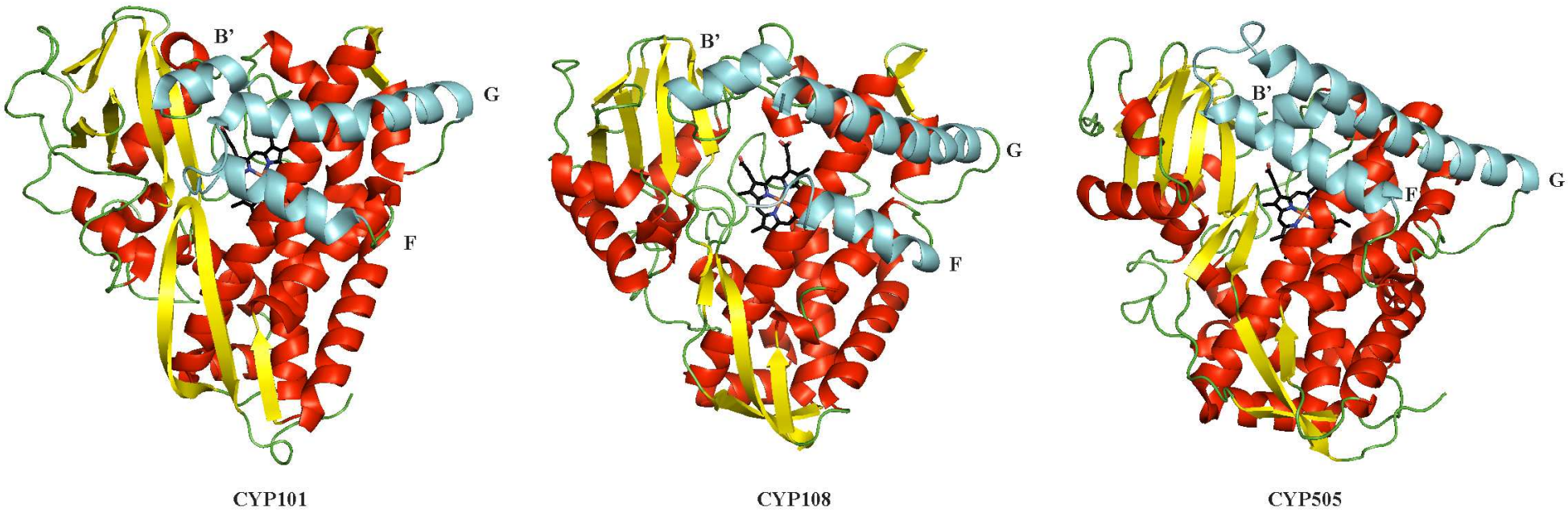

Figure 1.13 Crystal structures of CYP101 ($P450_{cam}$), CYP108 ($P450_{terp}$), and CYP505 ($P450_{BM-3}$). The largest differences occur in the B', F, and G helicies (cyan).

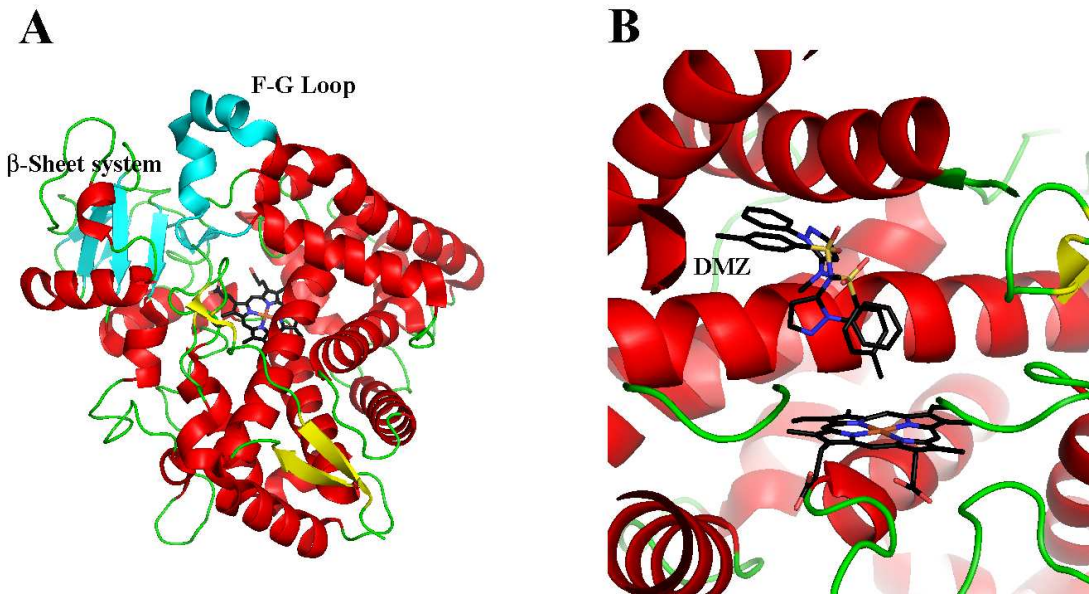

Figure 1.14 The tertiary structure of rabbit CYP2C5 crystalized with and without substrate. (a) The overall fold of rabbit CYP2C5 (pdb; 1NR6) highlighting the F-G loop and the N-terminal β-sheet system shown in cyan. The F-G loop was omitted from the final crystal structure and is subsequently not represented as a loop using the model viewer, PyMOL (seen as a helix). (b) The recrystallized structure (pdb; 1N6B) bound with 4-methyl-N-methyl-N-(2-phenyl-2H-pyrazol-3-yl)benzenesulfonamide (DMZ) in two different catalytic orientations.

Scott et al. (2004a) found that, compared to the CYP2C5 structure, the open cleft in CYP2B4 is generated by the repositioning of highly conserved secondary structures. Interestingly, CYP2B4 crystallized as a dimer, with the F' and G' helices of one molecule filling the open cleft of a second molecule, therefore trapping the enzyme in the open conformation. The structure of CYP2B4 co-crystallized with the specific inhibitor, 4-(4-chloro-phenyl)imidazole (CPI) (1.9Å resolution; R-value 0.215), adopted a closed conformation similar to that seen for mammalian CYP2C5 (Figure 1.15b). The differences between the open and closed structures of CYP2B4 were primarily due to the relocation of the B', C, and F through G helices. Collectively, this was termed the ‘lid’ domain (Scott et al. 2004b).

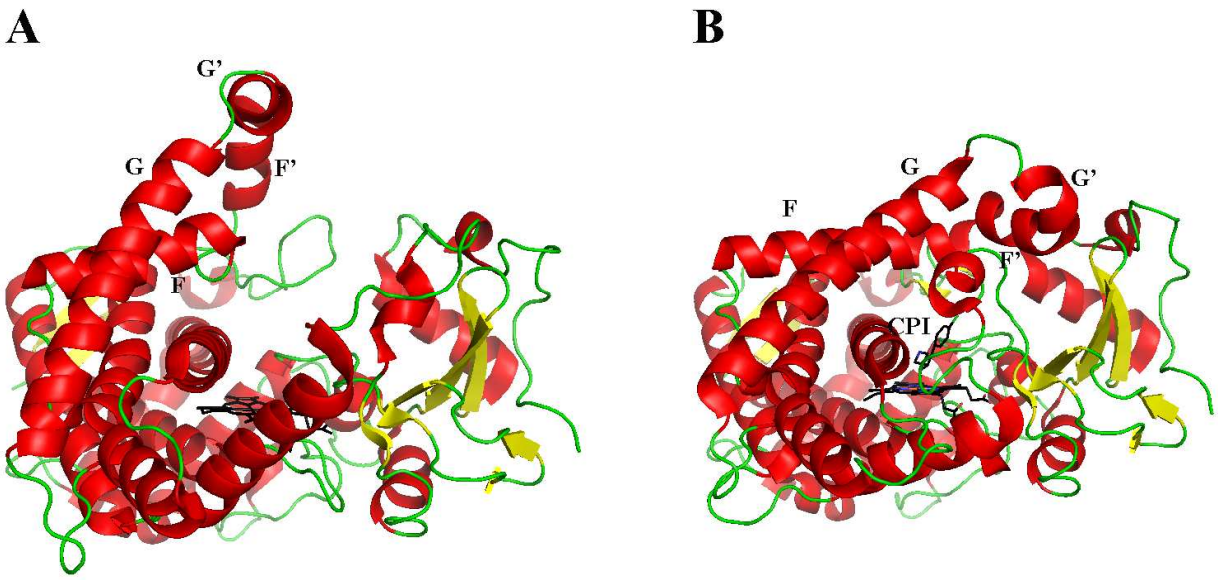

Figure 1.15 The open and closed conformations of rabbit CYP2B4. (a) The open conformation of CYP2B4 (pdb; 1PO5). (b) CYP2B4 (pdb; 1SUO) co-crystallized with 4-(4-chloro-phenyl)imidazole (CPI) highlighting the orgasnization of the F-G loop 'lid'.

Elucidation of the structures of the human drug metabolizing P450s CYP2A6, CYP2C9, CYP2C8, CYP3A4, and CYP2D6 followed in reasonably quick succession. All CDS required truncation of the membrane bound N-terminal domain in addition to mutations necessary for protein solubilization. Three structures of CYP2C9 have been solved; the first structure was unliganded (pdb; 1OG2, 2.6Å) (Figure 1.16a) and the second was co-crystallized with the anti-coagulant drug warfarin (pdb; 1OG5, 2.55Å) (Figure 1.16b) (Williams et al. 2003). The third CYP2C9 structure solved by Wester et al. (2004) showed significant differences compared to the 1OG5 crystal (RMSD 0.74Å). The crystal structure of Wester *et al.* (2003) (pdb; 1R9O, 2Å) (Figures 1.16c and 1.16d) was complexed with flurbiprofen and contained fewer modifications to the CYP2C9 CDS. The 1OG5 structure reported by Williams *et al.* (2003) was essentially CYP2C5-like, with extensive modifications in residues 30-53, 97-121, 196-233, and 467-478. Specifically, the

K206E, I215V, C216Y, S220P, P221A, I223L, and I234L substitutions all corresponded to residues found in CYP2C5. In addition, the location of the bound warfarin in the 1OG5 structure was positioned at the distal end of the active-site cavity with the site of hydroxylation in an unproductive orientation some 10Å from the heme Fe (Figure 1.16b). The refined 1R9O CYP2C9 structure displays the native conformation of the F to G helix region and exhibits an extra turn at the N-terminus of the A helix. In addition, the distinct conformation of the B to C helix region allows R108 to hydrogen bond with D293 and N289 on the I-helix. Furthermore, the 1R9O structure described by Wester *et al.* (2003) highlights the role of R108 and its importance in stabilizing and orientating the binding of the acidic flurbiprofen in the CYP2C9 active-site for productive catalysis (Figure 1.16d).

Like CYP2B4, human CYP2C8 was crystallized as a symmetric dimer formed by the interaction of the F, F', G', and G helices (Schoch et al. 2004). Interestingly, two palmitic acid molecules were bound at the dimer interface, suggesting a peripheral binding site that may contribute to drug interactions during CYP2C8 catalyzed biotransformation (Figure 1.17). The 2.7Å (R-value 0.248) structure of CYP2C8 (pdb; 1PQ2) additionally identified an active-site volume almost twice that of rabbit CYP2C5, which is consistent with the large size of its preferred substrate paclitaxel (853.9 $gmol^{-1}$) (Kerdpin et al. 2004). The increased volume of the CYP2C8 active-site reveals a shift in the F' helix which establishes a cavity above β-sheet 1. However, flexibility in the F-G helix region is likely to be reduced in CYP2C8 dimers (Schoch et al. 2004).

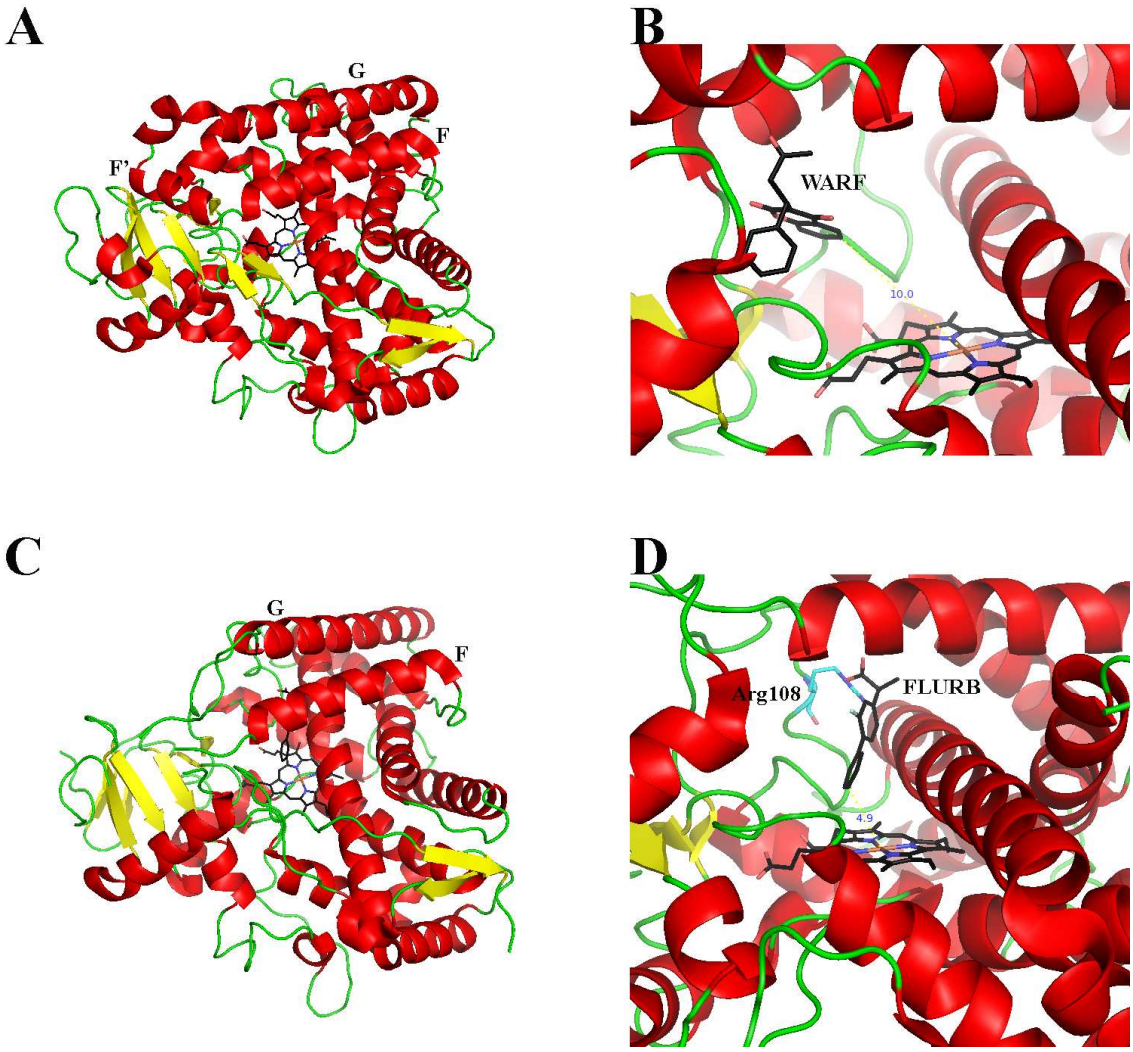

Figure 1.16 Bound and unbound crystal structures of human CYP2C9. (a) The crystal strucuture of CYP2C9 in the absence of ligand (pdb; 1OG2, 2.6Å) and (b) cocrystallized with warfarin (WARF) located 10Å from the site of catalysis (pdb; 1OG5, 2.55Å). (c) The refined crystal structure of CYP2C9 generated by Wester *et al.* (2003) (pdb; 1R9O, 2Å), (d) 1R9O complexed with flurbiprofen (FLURB), the site of catalysis positioned 4.9Å from the heme Fe.

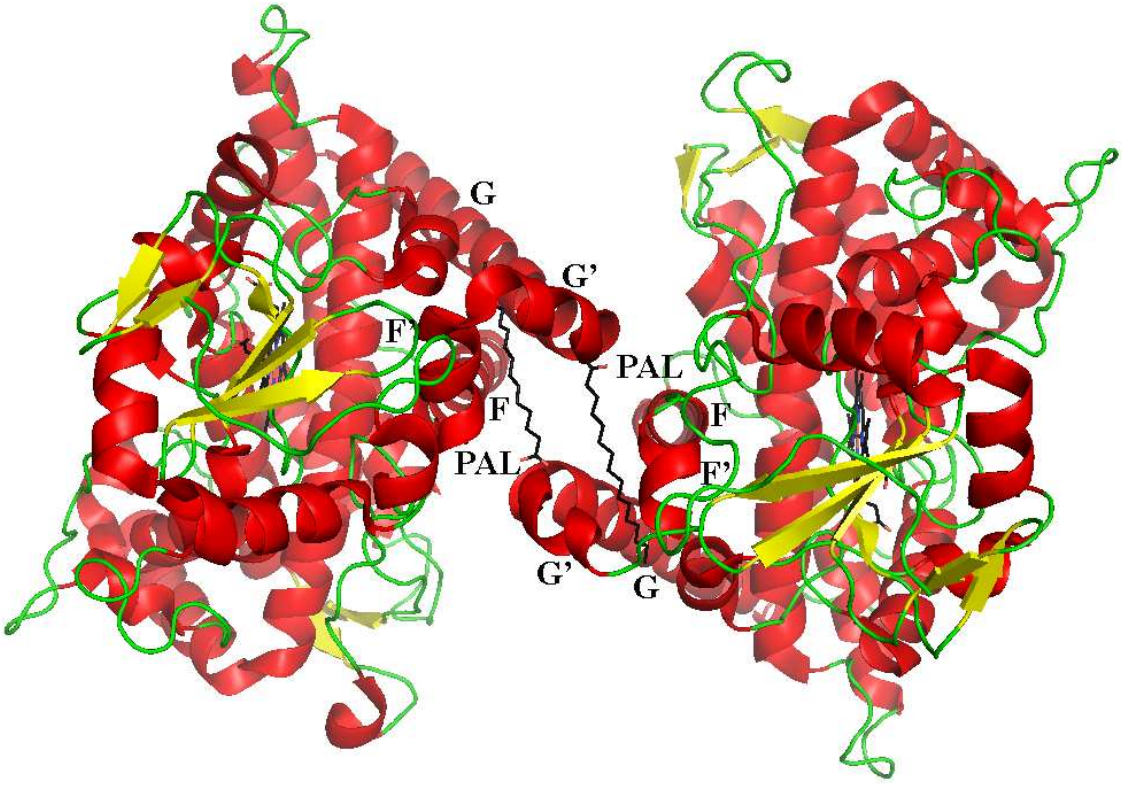

Figure 1.17 The crystal strucuture of CYP2C8 shown as a symmetric dimer. The fatty acid binding site is located at the dimerization interface. Palmitic acid (PAL).

The first crystal structure of a CYP3A enzyme was achieved by Yano et al. (2005) in the presence of the substrate erythromycin. However, electron density maps did not reveal the location of the substrate molecule and therefore could not be resolved in the final crystal structure. The CYP3A4 crystal (pdb; 1TQN) was determined to 2.05Å resolution (R-value 0.241) and, like CYP2C8 (1438Å^3), it revealed a large active-site volume (1386 Å^3), which is not surprising considering CYP3A4 oxidizes some of the largest P450 substrates (e.g. macrolide antibiotics, cyclosporin) (Polasek & Miners 2006). However, the shapes of their cavities differ markedly, due to differences in secondary and tertiary structure rearrangement. The major differences are seen in the F to G helix region that passes over the heme, creating a large cavity in CYP3A4. Close inspection of the CYP3A4 structure reveals helices F and G do

not extend over the active-site cavity (Figure 1.18) as they do in the CYP2C structures (Figures 1.16 and 1.17). In fact, the F-F' and G'-G loops are markedly elongated in the CYP3A4 structure and are comprised of residues 209-217 and 237-242, respectively. The replacement of helices (in the CYP2C proteins) with loops in CYP3A4 introduces the desired flexibility required to accommodate large or multiple substrates. Docking studies conducted by Yano et al. (2005) revealed that 7,8-benzoflavone and testosterone could bind simultaneously within the CYP3A4 active-site. Interestingly, several possible combinations of locations were observed. Similar to CYP2C9, R106 (corresponding to R108 in CYP2C9) resides at the distal end of the active-site cavity and participates in a network of hydrogen bonds linking Y53, D61, D76, R372, and E374 (Figure 1.18).

The first CYP2A enzyme to be crystallized was CYP2A6 (Yano et al. 2005). CYP2A6 is not considered a major drug metabolizing enzyme (section 1.3.3; Figure 1.6), however, this enzyme contributes to nicotine metabolism and is able to activate tobacco-specific procarcinogens (Tyndale & Sellers 2001). To better understand the mechanism of substrate and inhibitor binding in CYP2A6, Yano *et al.* (2005) generated crystal structures in both the presence of coumarin (substrate) at 1.9Å resolution (pdb; 1Z10, R-value 0.23) (Figure 1.19a), and in the presence of methoxsalen (inhibitor) at 2.05Å resolution (pdb; 1Z11, R-value 0.261) (Figure 1.19b). The volume of the CYP2A6 cavity is approximately one quarter that of CYP2C8, CYP2C9, and CYP3A4 and is well suited for small planar substrates that fit within the narrow, hydrophobic active-site. The CYP2A6 active-site shows features in common with CYP101.

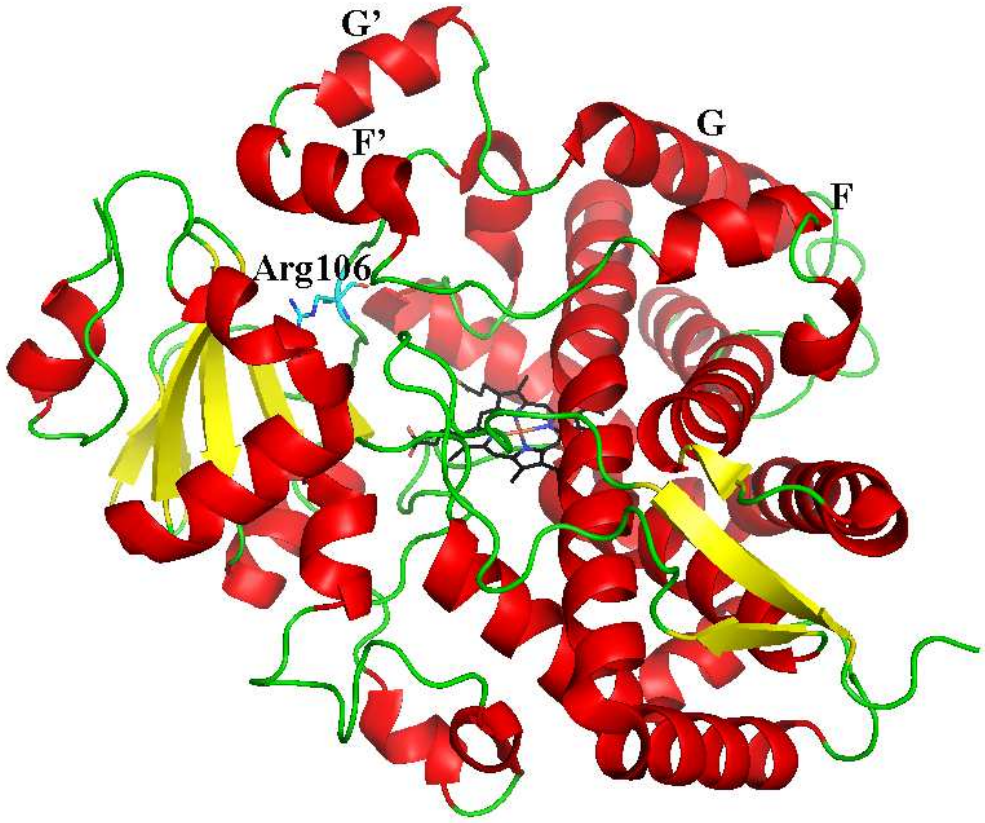

Figure 1.18 The crystal strucuture of human CYP3A4. The CYP3A4 structure identifies greater flexibility is achieved in the F through G helix region by minimizing the rigid helix strucutre. This allows the accommodation of large substrate molecules and may also contribute to heterotrophic cooperativity by allowing multiple binding sites for smaller substrate molecules. Through hydrogen bonding, R106 (cyan) is important for the orientation and stabilization of substrates in the distal end the CYP3A4 active-site.

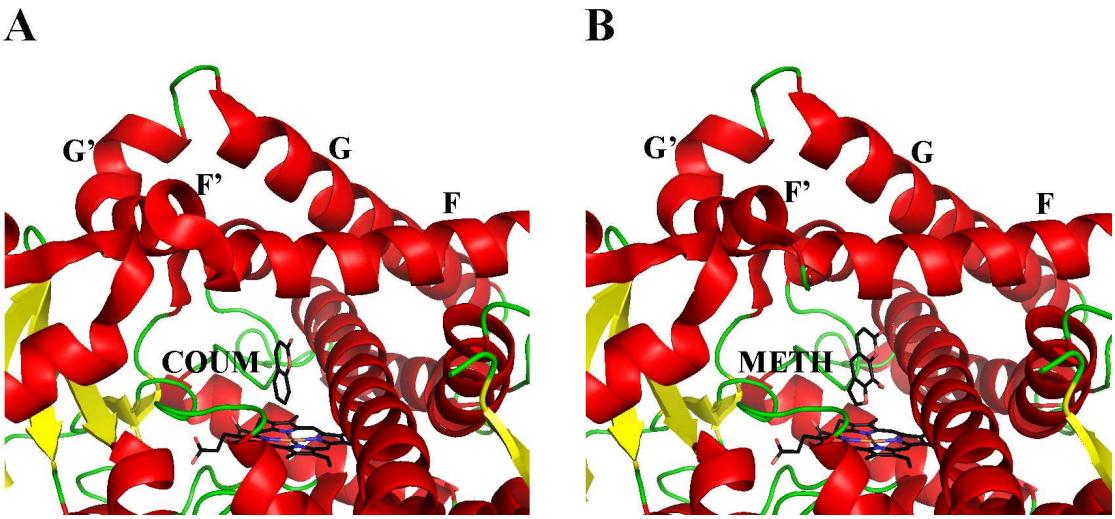

Figure 1.19 The bound and unbound crystal structures of CYP2A6. The crystal strucuture of CYP2A6 comparing the binding sites for (a) coumarin (COUM) and (b) methoxsalen (METH).

Human CYP2D6 is responsible for the metabolism of many clinical drugs (section 1.3.3; Figure 1.6) particularly those containing (protonated) basic nitrogen's and planar aromatic rings. CYP2D6 was crystallized recently by Rowland et al. (2006). The CYP2D6 structure was solved to 3.0Å (pdb; 2F9Q, R-value 0.232) and was solubilized using mutations based on its homology with CYP505 ($P450_{BM-3}$). The CYP2D6 structure (Figure 1.20) shows similarities to that of CYP2C9 (RMSD 1.16Å), but important differences occur in the F through G helix region. The F helix in CYP2D6 is two turns larger and arcs down toward the heme, thereby decreasing the active-site volume (540$Å^3$). There is no evidence of an F' helix, although a small G' helix was reported by the authors. However, Rowland *et al.* (2006) acknowledge that the quality of electron density maps in the F-G loop region is unsatisfactory. The crystal structure suggests that F120 is used to control the orientation of substrates relative to the heme.

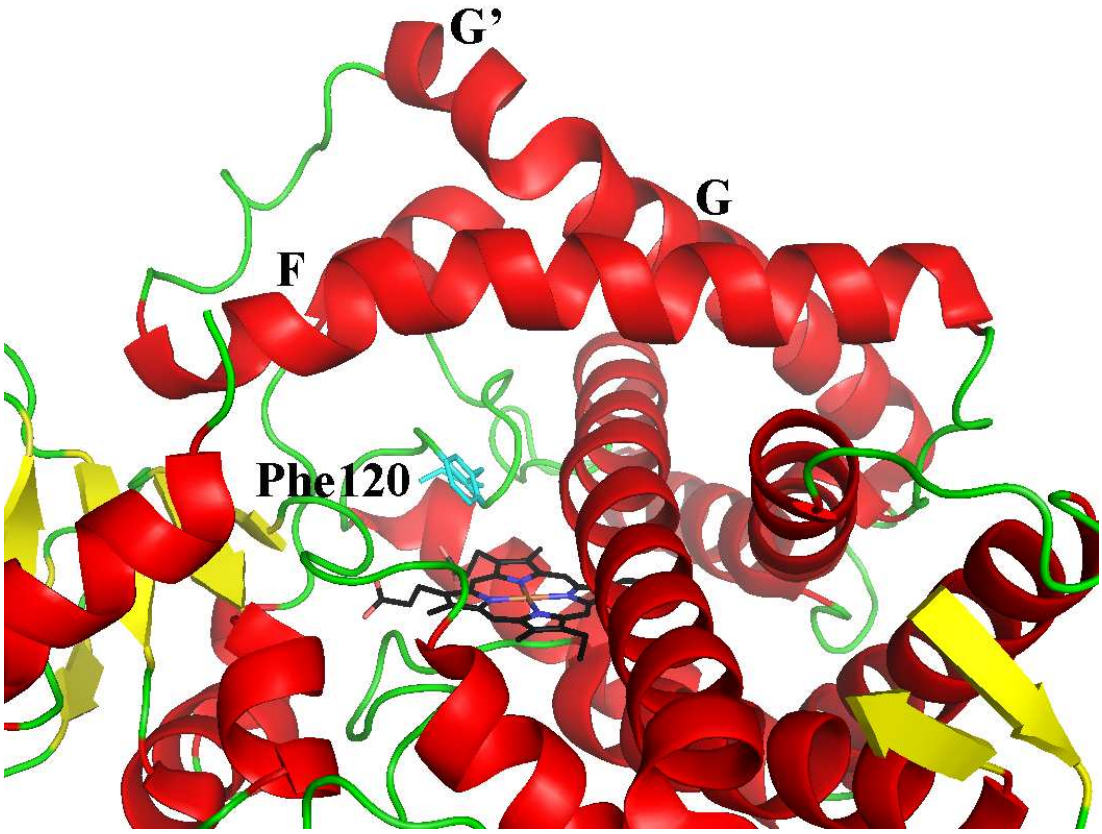

Figure 1.20 The crystal structure of CYP2D6 (2F9Q). The inward arching of the F helix is responsible for the small active-site cavity. F120 (cyan) is located in SRS1 and aids the productive alignment of aromatic substrates for catalysis.

During the course of this thesis, the human CYP1A2 crystal structure was elucidated by Sansen et al. (2007). Determination of the first CYP1 family enzyme was achieved at 1.95Å resolution (pdb; 2HI4, R-value 0.223) as a complex with the inhibitor, α-naphthoflavone. As for CYP2C5 (Wester et al. 2003b), CYP2C8 (Schoch et al. 2004), CYP2B4 (Scott et al. 2004a), and CYP2A6 (Yano et al. 2005), the N-terminal transmembrane domain of CYP1A2 was removed (at residue 42) and modified to encode the MAKKTSSKGKL (G1 construct) terminus. In addition, a further CYP1A2 3-26 deletion construct was crystallized. Both constructs were

designed to reduce protein aggregation and increase solubility. The final model comprises residues 34-513 refined from the superimposition of the derived structures. No mutations were made to increase expression yields, although the pCW-CYP1A2 expression construct was coexpressed with plasmids containing the chaperone proteins GroEL and GroES in an attempt to improve protein folding and yield (Baneyx & Mujacic 2004). Analogous with other crystallized P450 structures, the most conserved regions are the heme binding site and the proximal surface of the protein where OxR, NADPH, and cytochrome b_5 bind. Similarly, the most divergent regions appear in the substrate active-site, the B-C helix, and F-G helix regions. One notable difference in CYP1A2 is the 3^{10} F' and G' helices rather than α-helices. Even though CYP1A2 shares <29% sequence identity with CYP2A6, CYP2B4, CYP2C5, CYP2C8, CYP2C9, and CYP3A4, the secondary structure is clearly maintained (Figure 1.21a). In the presence of α-naphthoflavone the CYP1A2 structure appears in a closed conformation with the active-site cavity calculated at 363$Å^3$, slightly larger than CYP2A6 (260 $Å^3$) (Figure 1.21b). Interestingly, Sansen et al. (2007) reported the absence of water in the CYP1A2 active-site when complexed with α-naphthoflavone, which may describe the predominantly high-spin Fe state in the substrate free ferric enzyme (i.e. no water at the sixth coordination site on the heme Fe).

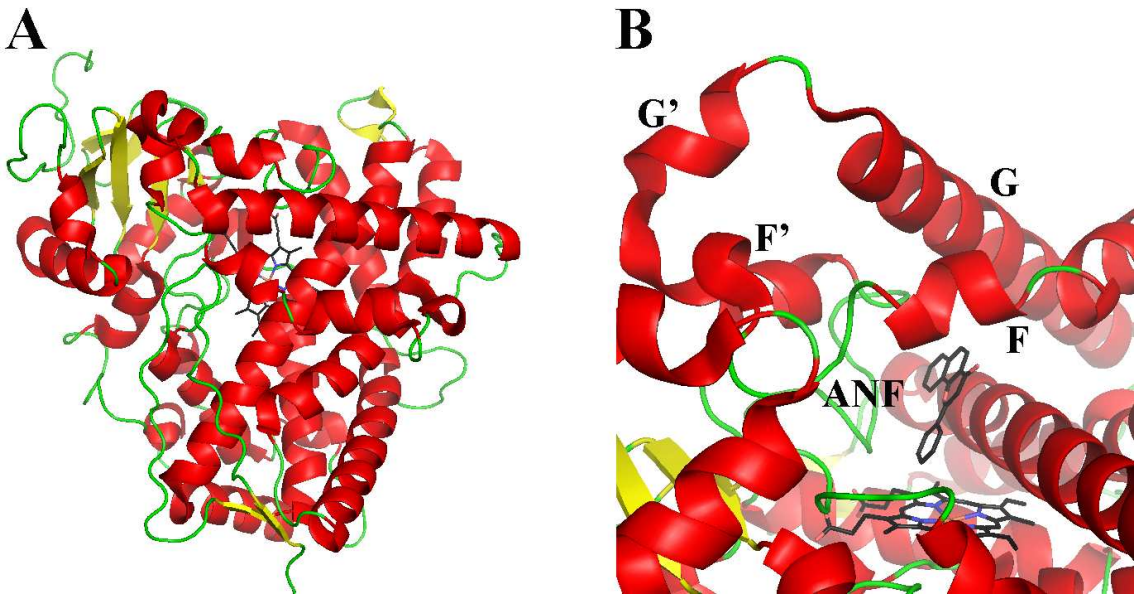

Figure 1.21 The bound and unbound crystal structures of human CYP1A2. (a) The secondary and tertiary structure of human CYP1A2 (2HI4) closely resembles that of other crystallised P450s. (b) The CYP1A2 inhibitor α-naphthoflavone (ANF) is positioned in the active-site cavity in close approximation to the heme Fe. The CYP1A2 active-site is well adapted for planar aromatic compounds.

1.5.3 Three-dimensional molecular modeling

1.5.3.1 Background

Protein modeling may be used to predict protein structure. The structure and function of a protein are interconnected through the amino acid residues that determine the tertiary structure. Thus, based on an understanding of a protein's function and its primary sequence, predictions relating to protein structure can be made. Modeling is necessary when the structure of a protein cannot be determined experimentally, or if poor resolution is obtained with the crystallized protein. In the case of the class II P450s, their hydrophobic and membranous nature greatly limits the solubility required for trouble-free crystallization, highlighting the need to elucidate P450 structures by molecular modeling.

Currently, protein modeling is classified into three general categories (Krane & Raymer 2003):

(i) *ab initio* modeling, where a protein structure is generated by utilizing the primary sequence of the protein in question with no direct use of known structure(s). This is achieved by predictors that use potentials derived from distance data between atoms, rather than physical descriptors (e.g. electrostatic potential, hydrophobic contacts, etc.).

(ii) Fold recognition modeling or 'threading', where there is little similarity in the primary sequence but the target protein contains a fold that is already known. These techniques exploit the differences in the distribution of inter-residue distances for different combinations of amino acid residues.

(iii) Comparative or 'knowledge-based' modeling, where the data derived from nuclear magnetic resonance (NMR) or the X-ray crystallography of related protein structures are utilized to guide the modeling process. For comparative modeling to be successful, significant amino acid sequence homology must exist between the query and template protein(s).

Although considerable progress has been made in *ab initio* and fold recognition protein structure prediction (Lazaridis & Karplus 2000; Teodorescu et al. 2004), comparative protein modeling remains the most accurate prediction method available (Moult 1999). However, the accuracy of a protein structure derived from comparative modeling is still highly dependant on both the crystal template quality and sequence homology (Acharya & Lloyd 2005; Sippl 1993). For the purpose of this thesis, only comparative modeling will be discussed.

There are many variations in comparative modeling techniques (Wallner & Elofsson 2005). The most common technique involves the breakdown of the structure into conserved core regions and the loops that interlock them. Rigid templates that represent the conserved regions are obtained from homologous proteins of known structure and are usually found within the Brookhaven Protein Data Bank (PDB). There are currently 66478 structures in the PDB archive (last updated July, 2010). If more than one homologous template is available, then the atomic coordinates of all homologous residues (dependant on alignment) are usually averaged. All variable loop regions of the model are then searched within the PBD to resolve those fragments whose anchor regions have a good geometric fit to the template. Loop analysis usually provides a geometric tool whereby the retrieved fragment (and subsequent tertiary structure) is scored on the basis of 'fit quality' to the anchor regions sequence homology, steric interactions, and stereochemistry.

1.5.3.2 Model refinement through molecular mechanics

Homology models generated from comparative modeling usually begin as 'off-lattice' homology models, meaning that all originate as high energy protein structures that require geometry optimization and energy minimization. The potential energy functions used to relieve high energy conformations, termed Force Fields (FF), need to consider both dominant and subtle factors associated with protein stability in order to manipulate the energy of each amino acid within the protein structure. The objective of a FF is to derive an approximated energy function for which known crystallized proteins are represented in their energy minimized state. At the atomic level, a FF acts on individual residues by using statistically significant side-chain conformations (rotomers) to represent the flexibility of each amino acid

(Gordon, Marshall & Mayo 1999). A variety of stochastic and deterministic search algorithms are then used to find the combination of amino acid side-chain rotomers that complement the neighboring residue fold as ranked by a potential energy function. The potential energy terms commonly used in FFs describe the packing among non-covalently bound atoms (e.g. van der Waals forces), electrostatic interactions (e.g. distance attenuated charge), internal coordinate energies (e.g. torsional strain, dihedral angle), hydrophobic contacts, hydrogen bonding (e.g. angle dependant potential), and solvent (e.g. octanol/gas-water free energy of transfer) and entropic factors (e.g. conformational freedom) (Gordon, Marshall & Mayo 1999; Krane & Raymer 2003). A simple example of a FF is seen in equation 1.3.

$$\Delta G = \Delta G_{\text{van der Waals}} + \Delta G_{\text{H-bond}} + \Delta G_{\text{solvent}} + \Delta G_{\text{Coulomb}} \quad \text{(eq. 1.3)}$$

where ΔG is the Gibbs free energy, with van der Waals, H-bond, solvent, and Coulomb potentials describing atom packing, sidechain-sidechain/sidechain-backbone interactions, solvation, and electrostatic energies, respectively.

In most cases, energy minimization leads to the optimization of the static atomic structure and therefore only establishes a local energy minimum for those residues in a specific configurational space (Lesyng & McCammon 1993). Hence, there is no guarantee that the local energy minimum represents that of the global minimum of the protein. Additionally, the relative weights of those descriptors making up the FF need to be correctly balanced in order to provide a more realistic refinement. However, the unrealistic weighting of electrostatic and van der Waals interactions

can generate non-optimal atom packing and unsatisfied hydrogen bond donor or acceptor sites (Linge et al. 2003).

1.5.3.3 CYP1A1 model construction

Extensive structure analysis of CYP1A1 has been accomplished by Lewis and his colleagues (Lewis, Modi & Dickins 2002; Lewis 2002a; Lewis 2002b; Lewis, Ioannides & Parke 1994a,1994b; Lewis, Ito & Lake 2006; Lewis & Lake 1996; Lewis, Lake & Dickins 2004; Lewis et al. 1999). The Lewis laboratory has primarily focused on the molecular modeling and quantitative structure-activity relationships of CYP1A enzymes and their interaction with drugs and other chemicals, particularly those associated with human drug metabolism. Utilizing the substrate bound CYP101 structure (Poulos et al. 1985), the first homology model of rat CYP1A1 was elucidated by Lewis, Ioannides & Parke (1994b) to investigate the selectivity and species differences between CYP1A1 and CYP1A2 (Lewis & Lake 1996; Lewis et al. 1999).

Using the SwissProt database sequence of CYP1A1 (accession P04798), Szklarz and Paulsen (2002) constructed the first homology model of CYP1A1 based on the coordinates of crystallized rabbit CYP2C5 (pdb entry 1DT6). In order to evaluate whether the CYP2C5 structure was the best available template, the CYP1A1 sequence was additionally aligned with those of the bacterial crystal templates CYP505 ($P450_{BM3}$), CYP101 ($P450_{cam}$), CYP108 ($P450_{terp}$), and CYP107A1 ($P450_{eryF}$). Based on this alignment, CYP1A1 showed greatest identity with CYP2C5 (28.8%) (Figure 1.22). The model was used to manually dock three substrates, 7-methoxy-, 7-ethoxy-, and 7-pentoxyresorufin into the active-site of CYP1A1. The compounds were docked in productive binding orientations, leading to their *O*-

dealkylation using the docking module of Insight-II. The docked resorufins, along with benzo[a]pyrene, were shown to be stabilized mainly by hydrophobic interactions. The key amino acids that potentially interact within 5Å of these substrates were documented as residues 111 of helix B; 122 and 123 of the B′-C loop; 224 and 228 of helix F; 312, 313, 316, 317, 320, and 321 of helix I; 381 and 382 of the loop between the K helix and sheet 1-4; 386 of sheet 1-4; 497 and 498 of sheet 4-2. These residues therefore provide candidate sites for mutagenesis as their replacement with other amino acids can be expected to alter catalytic activity. In this regard, V382 was identified computationally to affect CYP1A1's activity towards 7-methoxy- and 7-ethoxyresorufin through its interaction with the alkoxy chain of each substrate (Szklarz & Paulsen 2002). This was later confirmed by Liu et al. (2003) who showed that activity of the wild-type CYP1A1 enzyme was highest with 7-ethoxyresorufin and lowest with 7-pentoxyresorfin. Upon substitution of V382 with alanine, the activities toward 7-methoxy- and 7-ethoxyresorufin fell 10-fold, although little change in K_m values were observed (Table 1.5). The V382A mutant displayed the highest catalytic efficiency with 7-pentoxyresorufin, suggesting that replacement of Val with Ala at position 382 increases the active-site volume and allows better oxidation of the larger substrate (Figure 1.23). In contrast, generation of a V382L mutant significantly decreased oxidation of all alkoxyresorufin substrates.

```
             1                                                  50
human CYP1A1  MLFPISMSAT EFLLASVIFC LVFWVIRASR PQVPKGLKNP PGPWGWPLIG
rabbit CYP2C5 ....MDPVVV LVLGLCCLLL LSIWKQNSGR G......KLP PGPTPFPIIG

              51                                                 100
human CYP1A1  HMLTLG.KNP HLALSRMSQQ YGDVLQIRIG STPVVVLSGL DTIRQALVRQ
rabbit CYP2C5 NILQIDAKDI SKSLTKFSEC YGPVFTVYLG MKPTVVLHGY EAVKEALVDL

             101                                                150
human CYP1A1  GDDFKGRPDL YTFTLISNGQ SMSFSPDSGP VWAARRRLAQ NGLKSFSIAS
rabbit CYP2C5 GEEFAGRGSV PILEKVSKGL GIAFS..NAK TWKEMRRFSL MTLRNFGMGK

             151                                                200
human CYP1A1  DPASSTSCYL EEHVSKEAEV LISTLQELMA GPGHFNPYRY VVVSVTNVIC
rabbit CYP2C5 R.......SI EDRIQEEARC LVEELRKTNA SP..CDPTFI LGCAPCNVIC

             201                                                250
human CYP1A1  AICFGRRYDH NHQELLSLVN .LNNNFGEVV GS..GNPADF IPILRYLPNP
rabbit CYP2C5 SVIFHNRFDY KDEEFLKLME SLNENVRILS SPWLQVYNNF PALLDYFPG.

             251                                                300
human CYP1A1  SLNAFKDLNE KFYSFMQKMV KEHYKTFEKG HIRDITDSLI EHCQEKQLDE
rabbit CYP2C5 IHKTLLKNAD YIKNFIMEKV KEHQKLLDVN NPRDFIDCFL IKMEQE....

             301                                                350
human CYP1A1  NANVQLSDEK IINIVLDLFG AGFDTVTTAI SWSLMYLVMN PRVQRKIQEE
rabbit CYP2C5 .NNLEFTLES LVIAVSDLFG AGTETTSTTL RYSLLLLLKH PEVAARVQEE

             351                                                400
human CYP1A1  LDTVIGRSRR PRLSDRSHLP YMEAFILETF RHSSFVPFTI PHSTTRDTSL
rabbit CYP2C5 IERVIGRHRS PCMQDRSRMP YTDAVIHEIQ RFIDLLPTNL PHAVTRDVRF

             401                                                450
human CYP1A1  KGFYIPKGRC VFVNQWQINH DQKLWVNPSE FLPERFLTPD GAIDKVLSEK
rabbit CYP2C5 RNYFIPKGTD IITSLTSVLH DEKAFPNPKV FDPGHFLDES G..NFKKSDY

             451                                                500
human CYP1A1  VIIFGMGKRK CIGETIARWE VFLFLAILLQ RVEFSVPLGV KVDMTPIYGL
rabbit CYP2C5 FMPFSAGKRM CVGEGLARME LFLFLTSILQ NFKLQS.LVE PKDLDITAVV

             501            517
human CYP1A1  TMKHACCEHF QMQLRS.
rabbit CYP2C5 NGFVSVPPSY QLCFIPI
```

Figure 1.22 Sequence alignment between human CYP1A1 and rabbit CYP2C5. Initial alignment gave 44.3% similarity (red & green) and 28.8% identity (red only).

Table 1.5 Comparison of kinetic parameters of CYP1A1 (WT) and the V382A and V382L mutants. Taken from Liu et al. (2003).

Variant	Substrate	K_m (μM)	V_{max} (nmol. min^{-1}/nmol P450)	V_{max}/K_m
CYP1A1 (WT)	7-methoxyresorufin	1.3	2.4	1.9
	7-ethoxyresorufin	0.60	11	17.9
	7-pentoxyresorufin	0.3	0.4	1.33
CYP1A1 V382A	7-methoxyresorufin	0.8	0.2	0.23
	7-ethoxyresorufin	0.55	1.1	2.0
	7-pentoxyresorufin	0.15	0.6	4.5
CYP1A1 V382L	7-methoxyresorufin	2.0	0.15	0.07
	7-ethoxyresorufin	2.3	0.15	0.07
	7-pentoxyresorufin	1.8	0.01	0.004

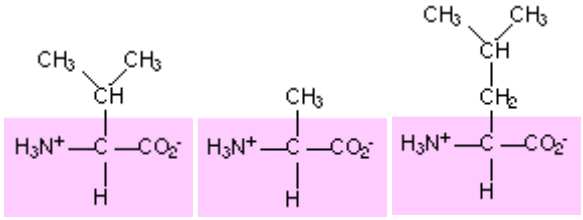

Valine Alanine Leucine

Figure 1.23 The amino acid substitutions made by Szklarz *et al.* (2003). Variablity in side-chain volume affects the kinetics of 7-methoxy-, 7-ethoxy-, and 7-pentoxyresorufin dealkylation by CYP1A1. The smaller molecular volume of alanine increases the void volume of the P450 active-site, potentially accommodating larger substrates.

One important approach to studying the structure-activity relationship of CYP1A1 for enhanced DTIC metabolism involves a combination of molecular modeling and computational chemistry. Prior to the commencement of this thesis no CYP1A1 homology model had been generated using human P450 templates. Importantly, the ways in which X-ray diffraction data are collected and refined have a strong impact on the final quality of the homology model. This being the case, the current published models might be considered inherently inaccurate, not only based on the template used, in some cases chimeras (CYP2C5; 1NR6, CYP2C9; 1OG5), but additionally in the resolution of the structural templates. By generating a model based on human templates, with inclusion of the largely homologous CYP1A2 (~80%), increased accuracy of secondary and tertiary structure organization would be achieved, therefore enabling the key residues involved in CYP1A1 substrate selectivity to be identified. From this, accurate predictions can be made as to what amino acid substitutions would enhance or inhibit enzyme/substrate affinity and DTIC activation.

1.6 Research aims

The primary aim of the *in silico* studies presented in this thesis was to generate a CYP1A1 homology model with the greatest possible accuracy. The CYP1A1 structure could then be utilized to generate modified enzymes, capable of enhanced DTIC bioactivation *in vitro*.

Specific aims were:

1. Generate a chemically and structurally valid CYP1A1 homology model based on crystallized human P450 homologs – **Chapter 3**.
2. Validate the CYP1A1 homology model by utilizing structure-activity analysis with the prototypical CYP1A1 substrate, 7-ethoxyresorufin – **Chapter 4**.
3. Characterize those residues that are critical for the alignment and orientation of DTIC in the CYP1A1 active-site and elucidate which protein mutations will enhance DTIC activation – **Chapter 5**.
4. Evaluate the bioactivation and cytotoxicity of selected CYP1A1 mutants with enhanced DTIC activation kinetics in the mammalian cell lines SK-MEL-28 and COS-7 – **Chapter 6**.

CHAPTER 2
MATERIALS AND METHODS

2.1 Materials

2.1.1 Equipment

Table 2.1 Equipment used in the experimental procedures.

Equipment Model	Manufacturer
Microfuge® 18 bench top centrifuge	Beckman Instruments, Germany
J2-21M/E centrifuge, L8-70M Ultracentrifuge	Beckman Instruments, Germany
Innova™ 4330 refrigerated incubator shaker	New Brunswick Scientific, NJ, USA
Thermomixer Comfort 96-well plate shaker	Eppendorf, Australia
Plate incubator (agar; 37°C)	Scientific Equipment Manufacturers, Australia
Inverted microscope (CK2)	OLYMPUS, NSW, Australia
Hy-Lite Haemocytometer	Hausser Scientific, USA
Gene Genius Bio Imaging System	SYNGENE, USA

Equipment Model	Manufacturer
LAS-400 Imager (chemiluminescence)	Fuji film, NSW, Australia
Cary 300 UV-VIS spectrophotometer	Varian Australia Pty. Ltd.
ABI 3130-XL DNA sequencer	Applied Biosystems VIC, Australia
DTX 880 Multimode Detector	Beckman Coulter NSW, Australia
Mini-Protean® III Cell (PAGE), Mini-Sub® Cell GT (AGE)	BIO-RAD Life Science NSW, Australia
Robocycler® Gradient 96 PCR machine	Stratagene, CA, USA
DNA Thermal Cycler 480	Perkin Elmer Massachusetts, USA
VC505 Ultrasonic processor	SONICS & MATERIALS Inc., CT, USA
Series 1100 HPLC; autosampler, degasser, quaternary pump, thermostated column compartment, fluorescence detector	HEWLETT PACKARD, VIC, Australia
Series 1200 HPLC; autosampler, degasser, quaternary pump, thermostated column compartment, UV detector	Agilent Technologies, VIC, Australia

2.1.2 Chemicals and reagents

All chemicals and reagents used in this thesis were of the highest analytical grade available. Table 2.2 lists major chemicals and reagents, and their respective suppliers.

Table 2.2 Sources of chemicals and reagents used in the experimental procedures.

Chemical/Reagent	Supplier
1kb DNA Ladder	New England Biolabs United Kingdom
4-methylumbelliferone, 7-ethoxyresorufin, amino-imidazole-carboxamide, ammonium persulphate, β-mercaptoethanol, bovine serum albumin, ColorBurst™ protein marker, δ-aminolevulinic acid, 5-3,3-dimethyltriazine-1-imidazole-4-carboxamide, dithiothreitol, ethidium bromide, isopropyl β-D-1-thiogalactopyranoside, 4-morpholinepropanesulfonic acid, NZ-Amine (casein hydrolysate), sodium-1-heptane sulfonate, resorufin, sodium dithionite, triethylamine, Tris-base, triton X-100, trypan blue, tween-20, chloramphenicol, G418 sulfate, BioMax Light Chemiluminescence Film	Sigma-Aldrich NSW, Australia
30% acrylamide/bis solution 19:1 (5% C), bromophenol blue, Trans-Blot® Transfer nitrocellulose	BIO-RAD Life Science NSW, Australia
acetonitrile (HPLC grade)	Optigen Scientific SA, Australia
agar, tryptone, yeast extract	US Biologicals MA, USA
Dulbecco's Modified Eagle Medium	Invitrogen VIC, Australia

Chemical/Reagent	Supplier
dimethyl sulfoxide, ethylenediaminetetraacetic, sodium dodecyl sulfate	Merck (BDH) VIC, Australia
foetal bovine serum	TRACE Bioscience NSW, Australia
Lipofectamine 2000, Lipofectamine LTX, MEM non-essential amino acids, MEM sodium pyruvate, penicillin/streptomycin solution, peptone, trypsin-EDTA solution 0.25%, , Opti-MEM, PLUS reagent	Invitrogen VIC, Australia
protease inhibitor cocktail, EDTA-free	Roche Diagnostics NSW, Australia
rubidium chloride (RbCl), tetramethylethylenediamine, ampicillin	Amresco OH, USA
sucrose	Chem Supply SA, Australia
xylene cyanol FF	Pharmacia NSW, Australia
neomycin sulfate (G418)	Astral-Scientific NSW, Australia

2.1.3 Analytical and preparative kits

Table 2.3 shows the analytical and preparative kits used in this thesis, and their respective suppliers.

Table 2.3 Analytical and preparative kits used in the experimental procedures.

Kit	Supplier
QIAprep® Spin Miniprep Kit, QIAquick® Gel extraction kit, QIAquick® PCR purification kit, QIAexpress® Detection kit (tetra-HIS)	QIAGEN, VIC, Australia
Fast-Link™ DNA Ligation kit	Epicentre, WI, USA
MultiTox-Fluor Multiplex Cytotoxicity kit	Promega, NSW, Australia
QuikChange® II Site-Directed Mutagenesis kit	Stratagene, CA, USA

2.1.4 Enzymes

Table 2.4 shows all enzymes used and their respective suppliers. All enzymes were supplied free of nucleases.

Table 2.4 Enzymes used in the experimental procedures.

Enzyme	Buffer	Supplier
Antarctic phosphatase	AP unique	New England Biolabs United Kingdom
KpnI	#1	
EcoRI, XbaI	#2	
BamHI, SalI	#3	
NdeI	#4	
Lysozyme (chicken egg)	-	Sigma-Aldrich, NSW, Australia
Pfu HS Polymerase	Ultra II	Stratagene, CA, USA

2.1.5 Antibodies for immunochemical detection of proteins

Table 2.5 shows all antibodies used in this thesis and their respective suppliers.

Table 2.5 Primary and secondary antibodies used in the experimental procedures.

Antibody	Supplier
Anti-human CYP1A1 IgG	CHEMICON International, MA, USA
QIAexpress® Tetra-His HRP-conjugate	QIAGEN, VIC, Australia
ZyMax™ Goat anti-rabbit IgG (H+L) HRP-conjugate	ZYMED Laboratories, CA, USA

2.1.6 Software for *in silico* chemistry and data analysis

Table 2.6 shows all software programs used in this thesis and their respective suppliers. All molecular modeling and cheminformatic software was licensed according to the conditions relating to use by an academic institution.

Table 2.6 Molecular modeling, stochastic, and cheminformatic software used in the experimental procedures.

Program	Developer
JPRED	University of Dundee, United Kingdom
INFOALIGN	EMBOSS, Cambridge, United Kingdom
Vector NTi v9.0	Invitrogen, Victoria, Australia
HMMER-2.3.2	Janelia Farm Research, Virginia, USA
PROCHECK v3.5.4	European Bioinformatics Institute, Cambridge, United Kingdom
SYBYL 7.3-8.1	TRIPOS, MO, USA
ProSa2003 v4.0	Center of Applied Molecular Engineering, Salzburg, Austria
ClustalW, ClustalX-1.8	University College Dublin, Dublin, Ireland
EnzFitter®	Biosoft, Cambridge, United Kingdom
SPSS v12.0.1	SPSS Inc., IL, USA

2.2 Methods

2.2.1 Buffers and solutions

All buffers and solutions were prepared from molecular biology grade solutions using the methods outlined by Sambrook and Russell (2001). Sterilization was achieved either by autoclaving (121ºC) or ultra filtration (0.2-0.45μm).

2.2.2 Molecular biology techniques

2.2.2.1 Bacterial strains

DH5α cells, a K-12 strain of *E. coli*, were used for all routine DNA manipulations and for the heterologous expression of OmpA-rOxR, 17α-CYP1A1 wild-type, and mutant constructs. DH5α chemically competent cells were freshly prepared using the method outlined by Hanahan (1985). Briefly, DH5α cells were streaked from a 40% glycerol stock onto a Lauria-Bertani (LB) agar plate and incubated overnight at 37ºC. A single colony was isolated and subcultured in LB broth with orbital shaking (225 rpm; New Brunswick Scientific, Innova 4330) at 37ºC for 16hr. The subculture was then used to inoculate prewarmed LB broth (2x 100mL) at 1:100 dilution in 500mL conical flasks. Cultures were grown to an optical density of 0.3-0.5 AU at 600nm, transferred to sterile Falcon® tubes and placed on ice for 10min prior to centrifugation at 1,912x *g* (3,000 rpm; Sigma laboratory 4K15) for 10min at 4ºC. The supernatant fraction was decanted and the cell pellet resuspended in 30mL of RF1 buffer (100mM rubidium chloride, 50mM manganese chloride, 30mM potassium chloride, 10mM calcium chloride, 15% w/v glycerol), followed by incubation on ice for 45min. Cells were then pelleted at 5,311x *g* (5,000 rpm; Sigma laboratory 4K15) for 10min at 4ºC, the supernatant fraction decanted, and the cell pellets resuspended

in RF2 buffer (10mM MOPS, 10mM rubidium chloride, 75mM calcium chloride, 15% w/v glycerol) to a final volume of 8mL. The cell suspension was subsequently incubated on ice for 10min and aliquoted (100μL) into sterile 1.5mL tubes. All tubes were snap frozen in a Dewar flask containing dry ice and ethanol and stored at -80ºC.

2.2.2.2 CYP1A1 and OxR cDNA

N-Terminus modifications previously shown to promote high levels of bacterial expression of human P450s were made to the wild-type CYP1A1 cDNA (GenBank accession no. NM_000499). The CYP1A1 cDNA was modified for bacterial expression by replacing the first 18 codons with those of the bovine CYP17A leader sequence (MALLLAVFL) (Figure 2.1). To facilitate detection, a 6xHis tag was added to the C-terminus of CYP1A1 by PCR using 3′ oligonucleotides containing the desired additions. *NdeI* and *XbaI* restriction sites (shown in italics) were additionally incorporated for cloning purposes: forward primer, 5′ AT***CATATG***ATCATGGCTCTGTTATTAGCAGTTTTTCTGTTCTGTCTGG 3′; reverse primer, 5′ TA***TCTAGA***ACCTAGTGATGGTGATGGTGATGAGAG CGCAGCTGCATTTGG 3′. The 1551bp PCR product was digested with *NdeI* and *XbaI* and ligated into the pCW ori(+) plasmid (Figure 2.2a). The pCW 17α-CYP1A1 construct was transformed into DH5α *E. coli* cells and colonies screened for the CYP1A1 insert by restriction enzyme analysis. The DNA sequence was confirmed on both strands by sequencing (ABI 3130-XL DNA sequencer; Applied Biosystems, Victoria, Australia). The OxR expression construct, generated using the bacterial plasmid pACYC, comprised the OmpA signal sequence fused upstream of the full length native rat OxR sequence (Shen et al. 1989) (Figure 2.2b; Table 1.4).

```
   CYP1A1  MLFPISMSAT EFLLASVIFC LVFWVIRASR PQVPKGKNPP…
17αCYP1A1  M-------A- --LLAVFLFC LVFWVIRASR PQVPKGKNPP…
```

Figure 2.1 Amino acid alignment showing the 5' N-terminal domain of the native CYP1A1 and the 17α-CYP1A1 CDS.

2.2.2.3 Transformation of competent E. coli

Competent cells (section 2.2.2.1) were thawed on ice and a 50µL aliquot transferred to a pre-chilled sterile 1.5mL tube. Whole plasmids (0.5µL; ~25ng), ligation reaction products (2.5µL), or nicked plasmids (2.5µL; <250ng) were added to the cells, which were then incubated on ice for 30min. Uptake of plasmid DNA was induced by heating the chemically competent cell/DNA solution to 42ºC for 50 sec. The transformation stock was cooled on ice (2min), then transferred into a 13mL round bottom aerobic subculture tube containing 400µL of pre-warmed (42ºC) NZY$^+$ amine broth. Transformations were subsequently incubated at 37ºC with shaking (225 rpm) for 1h. A 200µL aliquot of the transformation stock was plated onto LB agar plates containing the desired antibiotic and incubated overnight at 37ºC.

In the event that plasmid cloning was not efficient using DH5α cells, XL10-Gold® Ultracompetant cells (Stratagene, La Jolla, CA, USA) activated with β-mercaptoethanol were utilized. The high transformation efficiency (HTE) phenotype of XL10-Gold® cells improves competent cell performance and allows the transformation of large plasmids and ligated DNA. Regardless of cell type, all transformations were conducted in NZY$^+$ amine broth, plated onto LB agar plates, and subsequently subcultured in LB broth.

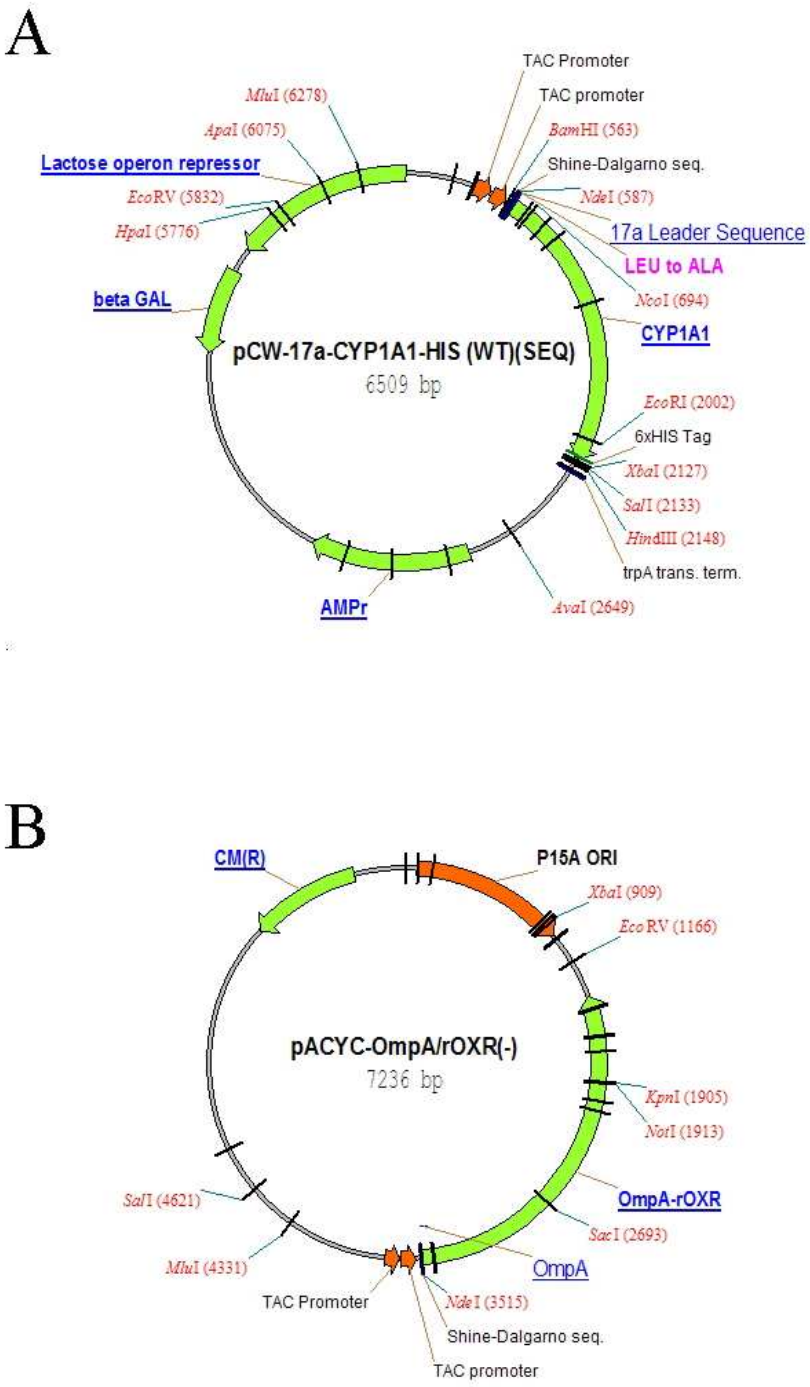

Figure 2.2 Circularised pCW 17α-CYP1A1 and pACYC OmpA-rOxR plasmids. (a) the CYP1A1 coding sequence was ligated into the pCW backbone using the *NdeI* and *XbaI* restriction sites. (b) The OxR expression construct contains the bacterial OmpA leader sequence and was generated using the expression plasmid, pACYC.

2.2.2.4 Plasmid amplification by bacterial subculture

pCW 17α-CYP1A1 and pACYC OmpA-rOxR plasmids were subcultured individually to amplify the number of plasmid particles. Single colonies were isolated from agar plates containing DH5α cells transformed with the desired plasmid or ligation product. Colonies were individually used to inoculate 5mL LB subcultures containing the desired antibiotic for plasmid selection; selection for pCW and pACYC required ampicillin (Amp^R, 100μg/mL) and chloramphenicol ($Chlor^R$, 50μg/mL), respectively. Subcultures were incubated at 37ºC with shaking (200 rpm) for 16h.

2.2.2.5 Identification of plasmid DNA

Purification of plasmid DNA was achieved using the QIAprep Spin Miniprep kit according to the manufacturer's instructions (Table 2.3). Plasmid DNA was digested with type II restriction enzymes to resolve the fragmentation pattern specific to the size of each plasmid containing P450 or OxR CDS. The restriction digests were prepared by mixing 1μL of plasmid DNA (~50-200ng), 1x NEB Buffer, BSA, 0.25μL of restriction enzyme(s) and water to a final volume of 10μL. Digests were incubated for 60min at 37ºC, followed by agarose gel electrophoresis to visualize plasmid fragmentation.

2.2.2.6 Agarose gel electrophoresis of restriction digests

Digestion products (10μL) were routinely resolved by mixing samples with 2μL of 6x DNA loading buffer (0.25% (w/v) bromophenol blue, 0.25% (w/v) xylene cyanol, 30% (w/v) glycerol), with electrophoresis through 1%(w/v) agarose gels in Tris-

acetate EDTA buffer (40mM Tris-acetate, 1mM EDTA) containing 250ng/mL of ethidium bromide at 100V for 20min. DNA bands were examined by exposing the gel to UV light (245nm; transilluminator). The sizes of the bands in each lane were estimated by comparison with a set of DNA molecular weight markers (1kb DNA ladder; NEB, cat. no. N3232L).

2.2.2.7 Extraction of DNA from agarose gel

Preparative gels were run at 100V for 20min, or until the desired band was isolated, and subsequently excised from the gel under UV light (365nm). Exposure to UV radiation was minimized to limit the formation of pyrimidine dimers. The gel slice was then transferred into a microcentrifuge tube and the DNA extracted using the QIAquick gel extraction kit, using a modified version of the manufacturer's instructions (Table 2.3). Briefly, the gel slice was dissolved by adding 3x volume of QG™ buffer (v/w) to the gel with subsequent heating at 42ºC for ~5min. After the gel had completely dissolved, 1x gel volume of isopropanol (v/w) was added and the sample loaded on the purification spin column provided. The column was centrifuged for 1min and the eluate discarded. The DNA was washed with PE™ buffer (750µL; 2x 1min) and then eluted in water (30µL).

2.2.2.8 Ligation of DNA fragments

Fast-Link™ DNA ligase (Epicentre®) was used for most ligation reactions. Fast-Link™ catalyzes the formation of phosphodiester bonds between terminal 5'-phosphate and 3'-hydroxyl groups of adjacent nucleotides. The ratio of the vector and insert varied depending on the type of 'ends' (cohesive; 1:2, or blunt; 1:5) generated

during restriction digestion. All ligation reactions were conducted at 25ºC for 30min followed by heat inactivation of the enzyme at 70ºC for 15min prior to transformation (section 2.2.2.3).

2.2.3 Mutagenesis

2.2.3.1 Generation of CYP1A1 mutants

The CYP1A1 residues S116, S122, F123, E161, E166, V191, F224, V228, E256, Y259, N309, L312, D313, G316, A317, D320, T321, V322, I386, I458, T461, I462, and T497 were mutated to generate 116A, 122A, 122T, 123A, 161K, 166Q, 191M, 224A, 228T, 256K, 259F, 309T, 312F, 313A, 313N, 316V, 317G, 317Y, 320A, 321G, 321P, 321S, 322A, 386G, 386V, 458P, 458V, 461N, 462V, and 497S variants. This method employed the QuickChange® II Site-Directed Mutagenesis kit (Table 2.3), but due to the high GC content of the CYP1A1 cDNA the primer design method described by Zheng *et al.* (2004) was used to minimize primer hetero-dimerization. The partially overlapping primers used for mutagenesis are given in Chapters 4 and 5. Mutations were confirmed by nucleotide sequencing on both strands (ABI 3130-XL DNA sequencer, Applied Biosystems, Victoria, Australia).

2.2.3.2 Mutagenesis primer design

All oligonucleotides were prepared using a partial overlapping primer design. This method overcomes the problems associated with primer pair self-annealing and hetero-dimerization and reduces the formation of hairpin loops. The following criteria were applied to primer design: at least eight non-overlapping bases should be introduced at the 3' terminus of the primer, the targeted mutation(s) should be

included in both primers, and at least one G or C should be placed at the end of each terminus. All oligonucleotides were synthesized by Sigma-Genosys (Sigma-Aldrich; Sydney, Australia) and purified by PAGE.

2.2.3.3 Mutagenesis polymerase chain reaction (PCR) conditions

All PCR mutagenesis reactions were carried out in sterile 0.2mL microfuge tubes. Reaction mixtures (50μL) contained: parental plasmid template (50-100ng), primers (0.2mM each), pfuUltra® II Fusion HS DNA polymerase buffer (1x), deoxyribonucleotide triphosphates (10mM each), pfuUltra® II Fusion HS DNA polymerase (Stratagene® cat. no. 600672; 2.5U), DMSO (5% v/v), and sterile water. A 'master mix' of all reagents (template DNA and polymerase omitted) was used to eliminate the likelihood of reaction variation. An aliquot (47μL) of the 'master mix' was delivered into each reaction vessel containing template (0-2μL) and the contents vortex mixed. Finally, polymerase (1μL) was delivered to each tube and reactions covered with mineral oil (2 drops) to inhibit evaporation during thermal cycling. Negative control reactions without DNA template were included to assess whether template or reaction component contamination occurred.

2.2.3.4 PCR cycling parameters

All reactions were carried out for a total of 16 cycles using a Robocycler® Gradient 96 PCR machine (Stratagene, CA, USA) thermal cycler, unless stated otherwise. The PCR reaction consisted of three stages: template DNA denaturation, primer annealing, and chain extension. During the first cycle, *Pfu* HS Ultra II Polymerase (Stratagene, CA, USA) was activated by incubation at 95ºC for 2min. All subsequent

cycles consisted of denaturation of the template at 95ºC for 1min, primer annealing at 52ºC for 1min, polymerization and extension at 68ºC for 5min (1 kb/min plasmid length), and in the final cycle, a conclusive strand extension at 68ºC for 10min.

2.2.3.5 Parental template removal from mutagenesis products

Mutagenesis products were purified using the QIAquick PCR Purification Kit according to the manufacturer's instructions (Table 2.3). The eluted products (30μL) were digested with DpnI restriction enzyme (1μL, NEB buffer # 4). Since the DpnI enzyme requires its cut-site to be methylated, only the parental template is digested, leaving the mutagenesis PCR product unaltered. Finally, DpnI enzyme was heat inactivated (65ºC, 15min) and 1μL of each mutant construct transformed into 50μL of DH5α cells (section 2.2.2.3).

2.2.3.6 Agarose gel electrophoresis of mutagenesis products

Mutagenesis products (6μL) were routinely resolved by mixing samples with 2μL of sterile water and 2μL 6x DNA loading buffer (0.25% (w/v) bromophenol blue, 0.25% (w/v) xylene cyanol, 30% (w/v) glycerol) prior to agarose gel electrophoresis (section 2.2.2.6). The desired mutation products exhibit an intense band at the size of the entire plasmid (i.e. insert + vector backbone) when estimated against a set of DNA molecular weight markers (1kb DNA Ladder; NEB). Gels were run at 100V for 20min.

2.2.4 Protein preparation and quantification

2.2.4.1 Preparation of human liver microsomes (HLM)

Human liver tissue was obtained from the human liver 'bank' of the Department of Clinical Pharmacology, Flinders Medical Centre. Approval for the harvesting of human liver tissue and its use in xenobiotic metabolism studies was obtained from the Flinders Medical Centre Research Ethics Committee and from the donor next-of-kin.

HLM were prepared by the differential centrifugation method described by Bowalgaha et al. (2005) using five human livers (H7, H10, H15, H29 and H40). All steps involved in the preparation of HLM were carried out between 0ºC and 4ºC. Briefly, frozen liver tissue samples (~1g) were suspended in polycarbonate centrifuge tubes containing 5ml of ice cold phosphate buffer (0.1M, pH 7.4) and 1.15% (w/v) KCl. Tissue was coarsely minced prior to homogenization (Ultra Turrax T25 tissue grinder, 2x 20,500 rpm for 30sec, with 30sec cooling). Homogenates were transferred to a 30mL Potter-Elvehjam homogeniser (mechanical drive at 1480 rpm) and homogenized over 8x strokes at full speed. Homogenates were centrifuged at 700x *g* (3,000 rpm; Beckman J2-21M/E centrifuge, JA-20 rotor) for 10min followed by a second spin at 10,000x *g* (11,000 rpm; Beckman® J2-21 M/E centrifuge, JA-20 rotor) for 10min. The supernatant fraction was decanted and then centrifuged at 105,000x *g* (34,000 rpm; Beckman® L8-70M ultracentrifuge) for 75min at 4ºC. The resulting pellet was resuspended in ice cold phosphate buffer (5mL; 0.1M, pH 7.4) containing 1.15% (w/v) KCl and again centrifuged at 105,000x g (34,000 rpm; Beckman® L8-70M ultracentrifuge) for 60min at 4ºC. The microsomal pellet was resuspended in 1mL of ice cold phosphate buffer (0.1M, pH 7.4) containing 20% (v/v) glycerol. Total P450 content was determined for all HLM preparations (section

2.2.4.5) prior to storage at -80ºC. The mean P450 content of HLM preparations used throughout this thesis was 589nmol/mg total protein.

Pooled HLM were prepared by mixing equal protein amounts of microsomes from H7, H10, H15, H29, and H40.

2.2.4.2 Expression of heterologous CYP1A1 and OxR

pCW 17α-CYP1A1 (wild-type and mutants) and pACYC OmpA-OxR were co-transformed into DH5α *E. coli* cells. Cells were cultured using a modification of the protocol of Boye et al. (2004). Briefly, overnight cultures (5mL) grown in LB broth with ampicillin (100μg/mL) and chloramphenicol (50μg/mL) at 37ºC were used to inoculate a 100mL culture of Terrific broth containing 100μg/mL ampicillin and 50μg/mL chloramphenicol. Cultures were grown at 37ºC with shaking (160 rpm) for 4h, or until reaching an optical density of 0.7 to 0.9 AU at 600nm. Cultures were cooled to 30ºC and isopropyl-1-thio-β-D-galactopyranoside (IPTG; 1mM) and δ-aminolevulinic acid (δ-ALA; 1.0mM) added. The cultures were subsequently grown at 30ºC with shaking (160 rpm) for an additional 40h in <1% dissolved oxygen.

2.2.4.3 Harvesting of bacterial cultures and preparation of membranes

Bacterial cells used for the heterologous expression of 17α-CYP1A1 and OxR constructs (section 2.2.4.2) were harvested and membranes prepared according to Gillam et al. (1993). Briefly, cultures were chilled on ice (10min) and centrifuged at 5,000x *g* (6,500 rpm; JA-20 rotor, Beckman J2-21M/E centrifuge) for 10min at 4ºC. The supernatant fraction was discarded and the cell pellet resuspended in TES buffer (100mm Tris-base, 0.5mM EDTA, 500mM sucrose, pH 7.6; 15mL/g wet-weight of

cells). Following the addition of lysozyme (300µg/g cells) to digest the outer bacterial membrane, cell suspensions were diluted (1:1) with pre-chilled (4ºC) sterile water and incubated on ice for 30min with gentle shaking. The resulting spheroplasts were sedimented at 10,000x *g* (9500 rpm; JA20 rotor, Beckman J2-21M/E centrifuge) for 10min at 4ºC, the supernatant fraction discarded, and the pellet resuspended in SRB (100mM phosphate buffer, pH 7.6, 6mM $Mg(OAc)_2$, 0.1mM DTT, 20% (v/v) glycerol; 5mL SRB per 50mL culture). Spheroplast preparations were stored overnight at -80ºC. The following day, spheroplasts were thawed on ice and supplemented with PMSF (50µL of 100mM stock per 5mL SRB) and protease inhibitors (200µL of 30mg/mL stock per 5mL SRB). Suspensions were sonicated (8sec bursts separated by 60sec cooling) 10 times on a salted ice-bath with the sonicator set to continuous with 45% duty cycle, and then centrifuged at 10,000x *g* (9000 rpm; JA20 rotor, Beckman J2-21M/E centrifuge) for 20min at 4ºC. The resulting supernatant fraction was carefully removed and centrifuged at 180,000x *g* (45000 rpm; 60Ti rotor, Beckman L8-70M ultracentrifuge) for 100min at 4ºC. The supernatant fraction was discarded and membrane fractions resuspended in TES/water (1:1; 300µL per 50mL culture) by gentle pipetting. Expressed membrane bound protein was stored at -80ºC until use.

2.2.4.4 Lowry estimation of total protein content

All protein estimations were performed in triplicate using the method described by Lowry et al. (1951). Total protein content was determined in glass tubes at room temperature in a total volume of 2.75mL. Mixtures contained the protein source (25µL of 1:10 dilution in sterile water) and 475µL of sterile water. Two mL of the alkaline Lowry ABC solution (98% A, 1% B, 1% C; v/v) was delivered to each tube

and incubated for 10min at room temperature. Under alkaline conditions the Cu^{2+} ions in the Lowry ABC solution form a complex with each peptide bond and are subsequently reduced to Cu^{1+} ions. Folin-Ciocalteu's Phenol reagent (250µL of 1:1 dilution in sterile water; Sigma-Aldrich cat. # F9252) was then delivered to each tube and the mixture incubated for 15min at room temperature. During incubation the Cu^{1+} ions interact with radicals present in tyrosine, tryptophan, and cysteine residues and react with the Folins to produce an unstable product which is quickly reduced forming molybdenum/tungsten blue. Absorbance was read at 660nm (Cary 300 conc; Varian Inc., Melbourne, Australia) and the concentration of total protein calculated by comparison to a calibration curve prepared with BSA (0-100µg) using equation 2.1.

$$\text{Total protein conc.} = \frac{\left(\dfrac{\text{OD}_{660}\ \text{sample}}{\text{slope of calibration curve}}\right)}{\text{sample volume}\ (\mu\text{L})} \times \text{dilution factor} \qquad (2.1)$$

2.2.4.5 Cytochrome P450 reduced difference spectroscopy

Total P450 content was determined by the method of Omura and Sato (1964) at a protein concentration of 2mg/mL. Sodium dithionite (~20mg) was added to membrane preparations, which were mixed by inversion and then aliquoted into two quartz cuvettes at room temperature. Cuvettes were placed in both the sample and reference positions of the spectrophotometer (Cary 300; Varian Inc., Melbourne, Australia) and the background absorbance zeroed. Spectra were recorded between 520nm to 400nm at a scan rate of 600nm/min and a spectral bandwidth of 1nm. Once the baseline was recorded, carbon monoxide was bubbled through the sample cuvette

for 1min (~1.5 bubbles/sec) and the carbon monoxide difference spectra recorded. P450 content and concentrations were calculated using equations 2.2 and 2.3 respectively.

$$\text{CYP content (nmol/mL)} = \left(\frac{(\text{Abs}_{450} - \text{Abs}_{490}) \times \text{dilution factor} \times 1000}{91\text{mM}^{-1}.\text{cm}^{-1}} \right) \quad (2.2)$$

$$\text{CYP concentration (nmol/mg)} = \left(\frac{\text{P450 content (nmol/mL)}}{\text{protein concentration (mg/mL)}} \right) \quad (2.3)$$

2.2.4.6 Determination of P450 oxidoreductase content

Oxidoreductase activity was measured indirectly using the method of Yasukochi and Masters (1976). In order to estimate the rate of reduction of cytochrome *c*, the reaction mixture contained 1mM KCN, 52.5μM cytochrome *c*, expressed protein (100μg), and 0.3mM NADPH in 0.3M potassium phosphate buffer (pH7.7). The reaction mixture was gently mixed by inversion and then aliquoted into two quartz cuvettes at room temperature. Cuvettes were placed in both the sample and reference positions of the spectrophotometer (Cary 300; Varian Inc., Melbourne, Australia) and zeroed against background. The reaction was initiated by the addition of NADPH (25μL) to the sample cuvette. Spectral data were obtained by observing the reduction of cytochrome *c* measured over 1min at 550nm. Since NADPH was limiting in the reduction of cytochrome *c*, the linear region of the kinetic curve was used to extrapolate the OxR activity of membrane preparations over 1min. The nmol cytochrome *c* reduced/min/mg protein was determined using equation 2.4 with an

extinction coefficient of $19.1 mM^{-1}cm^{-1}$. OxR content (nmol/mg protein) was calculated using a specific activity of 3000nmol cytochrome *c* reduced/nmol OxR/min (equation 2.5) (Li et al. 1999; Nadler & Strobel 1991).

$$\text{nmol/min/mg protein} = \left(\frac{OD_{550}/\text{min} \times 1000 \times \text{total volume (mL)}}{19.1 mM^{-1}cm^{-1} \times 1cm \times \text{protein conc (mg/mL)}} \right) \quad (2.4)$$

$$\text{OxR concentration (nmol/mg)} = \left(\frac{\text{nmol cytochrome c reduced/min/mg}}{3000} \right) \quad (2.5)$$

2.2.5 Tissue culture

2.2.5.1 Counting of cells

Cells were counted using a hemocytometer. Equal volumes of cells and 0.4% Trypan blue solution (25µl) were mixed together in a sterile microfuge. The chamber of the hemocytometer was filled with the homogenous stained cell suspension (25µl) by capillary action beneath a coverslip. Each chamber is divided into nine 1.0mm squares (Figure 2.3). The total number of cells in the five central 1.0mm squares was counted using a Clay Adams (BD, NSW, Australia) cell counter and averaged. The coverslip supported over the hemocytometer ensured the total volume over each 1.0mm square is $1x10^{-4}$ cm^3 (length x width x height; 0.1cm x 0.1cm x 0.01cm). The cell concentration per milliliter was determined using equation 2.6.

$$\text{number of cells per mL} = \left((\text{average number cells in } 1\times10^{-4}\text{ mL})(\text{dilution factor})\right)\left(1\times10^{4}\text{ mL}\right) \quad (2.6)$$

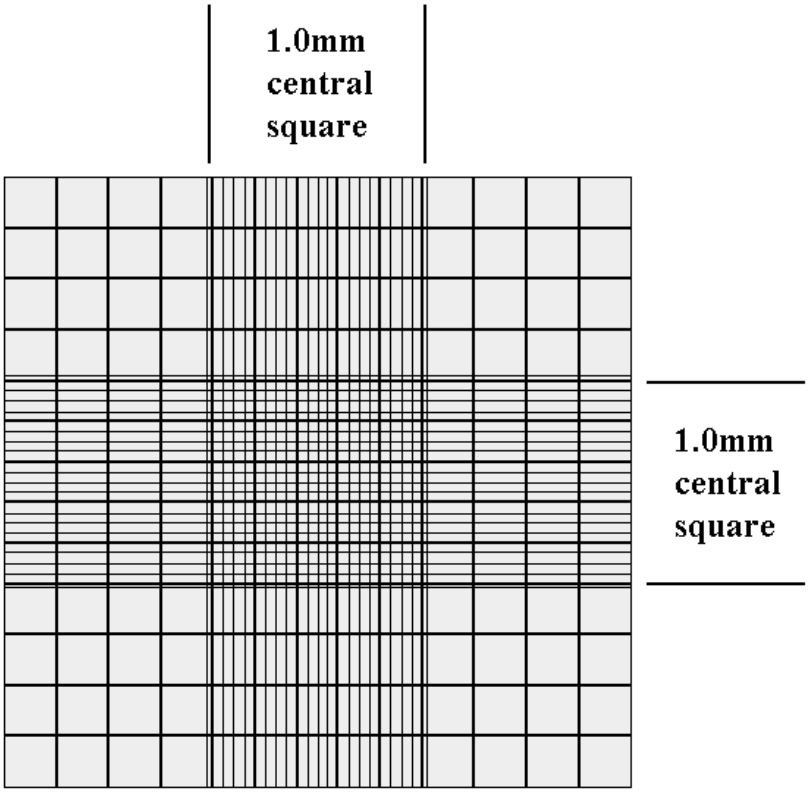

Figure 2.3 Counting of cells with a hemocytometer. Cells stained with trypan blue were loaded onto the hemocytometer and the average number of cells in each 1.0mm square counted. The number of cells/mL of cell suspension is then calculated as described in equation 2.6.

2.2.6 Western blotting

2.2.6.1 Polyacrylamide gel electrophoresis (PAGE)

Equal amounts of total protein from each recombinant enzyme preparation were subjected separately to SDS PAGE (Laemmli 1970). Protein extracts (25-100µg) were combined with 5x denaturing sample buffer (5µL; 250mM Tris-base; pH 6.8, 50% (v/v) glycerol, 5% (w/v) SDS, 0.2% (w/v) bromophenol blue, 250mM DTT) and made up to a final volume of 25µL with sterile water. Samples were denatured by heating at 95ºC for 5min, loaded (25µL) onto 4% stacking gels, and electrophoresed at 100V (150W/150mA) until the samples passed through the

stacking gel (~30min). Samples were then separated on 10% polyacrylamide running gels at 170V (150W/150mA) until the solvent front eluted from the base of the gel (~60min). SDS PAGE was conducted in running buffer (25mM Tris-base, 192mM glycine, 3.5mM SDS) using the BIORAD Mini-PROTEAN® III Electrophoresis Cell.

2.2.6.2 Protein transfer

Following PAGE, proteins were rectilinearly transferred to Trans-Blot® Transfer Medium pure nitrocellulose membrane (BIORAD; 0.45μm) using the BIORAD Mini-PROTEAN® III Electrophoresis Cell at 90V (150W/150mA). Transfer occurred at 4ºC with stirring for 2h in pre-chilled (4ºC) transfer buffer (25mM Tris-base, 192mM glycine, 20% (v/v) methanol). Membranes were initially washed in TBST (3x 2min; 60mL; 50mM Tris-base, 37.5mM NaCl, 0.2% (v/v) tween-20) to remove any residual methanol that contributes to background staining, followed by a rinse in TBS (2x 30sec; 60mL; 50mM Tris-base, 37.5mM NaCl). Immunodetection of P450 proteins was achieved by sequential incubations at room temperature with gentle agitation on a reciprocal shaker. Incubations were performed as follows:

- Membrane blocking was achieved in 3% blocking solution (25mL; TBS, 3% (w/v) skim milk powder) overnight at 4ºC (without shaking) followed by rinsing in TBS (2x 60mL).
- Incubation of rabbit anti-human CYP1A1 (polyclonal) primary antisera (Hakkola et al. 1996) (CHEMICON® INTERNATIONAL) diluted 1:3000 in 1% antibody incubation solution (25mL; TBST, 1% (w/v) skim milk powder)

was performed for 2h at room temperature with shaking followed by washing in TBST (3x 10 min; 60mL).

- Membranes were gently washed in 1.5% blocking solution (2x 10min; 25mL; TBS, 1.5% (w/v) skim milk powder) followed by rinsing in TBS (2x 60mL).
- Incubation of ZyMax™ Goat anti-Rabbit IgG (H+L) secondary HRP-conjugated IgG (ZYMED, Invitrogen) diluted 1:4000 (9.375pg) in 1% antibody incubation solution for 1h at room temperature with shaking, followed by washing in TBST (3x 15min; 60mL).
- Membranes were placed in TBS (60mL) until exposure to chemiluminescence substrates.

2.2.6.3 Immunodetection detection of proteins

Immunoreactivity was detected using the BM Chemiluminescence Blotting Substrate (POD; Figure 2.4) (Roche Diagnostics GmbH, Mannheim Germany) according to the manufacturer's instructions and recorded on either Omat autoradiographic detection film (Kodak) or digitally, using the FUJIFILM LAS-400 image reader (version 2.0; FUJIFILM Life Science Corporation; Tokyo, Japan) in conjunction with Multi Gauge image viewer (version 3.0; FUJIFILM Life Science Corporation). The autoradiographic film was processed manually, using Kodak GBX developer and Kodak GBX fixer and replenisher reagents (2min).

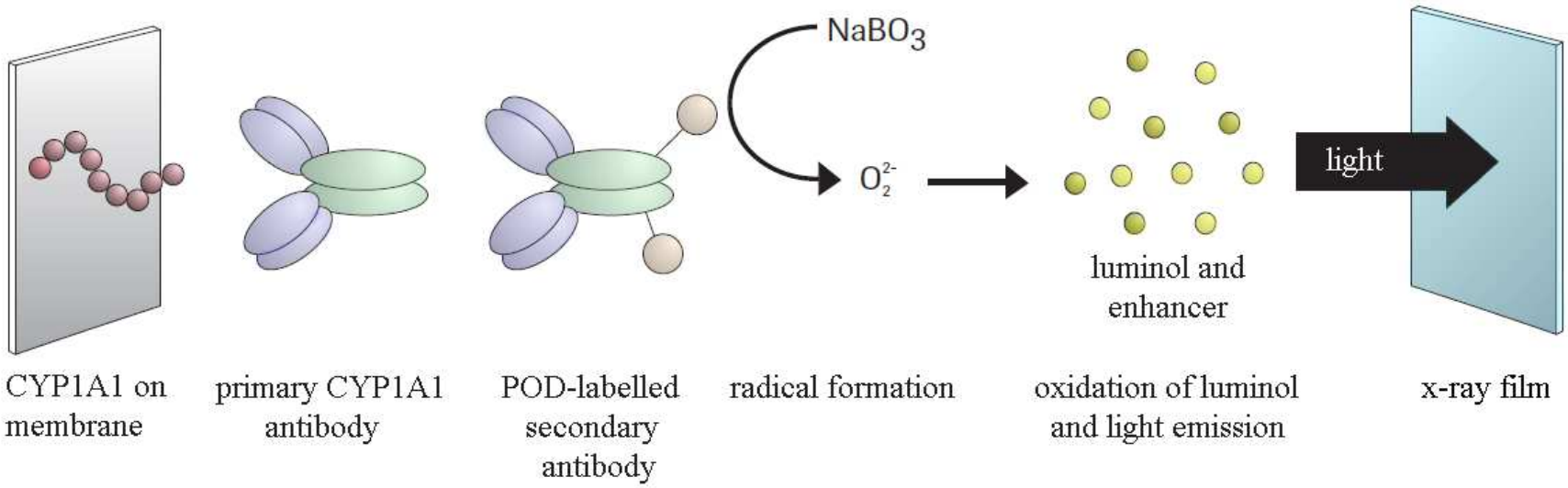

Figure 2.4 Schematic representation of the immuno-detection of CYP1A1. The BM Chemiluminescence Blotting System is based on HRP-labeled secondary reagents and the substrate luminol. In the presence of hydrogen peroxide (H_2O_2), HRP catalyzes the oxidation of luminol generating an activated intermediate which decays by emitting light.

Electrophoresis of ColorBurst electrophoresis molecular weight markers (8,000-220,000 Da; Sigma-Aldrich) was used to estimate the molecular mass of individual P450 proteins separated on Western blots. The relative migration of the known molecular weight of each protein standard (myosin-violet; 220kDa, BSA-red; 100kDa, GDH-blue; 60kDa, ADH-red; 45kDa, carbonic-anhydrase-orange; 30 kDa, trypsin inhibitor-blue; 20kDa, lysozyme-red; 12kDa, and aprotinin-blue; 8kDa) in Tris-glycine (4-20% gel) could not be used as standards for quantitative molecular mass determinations, but only as a qualitative tool.

2.2.6.4 CYP1A1 isolation

The molecular masses of protein bands detected using the CYP1A1 primary antisera were determined by comparison with the known protein standards (section 2.2.6.3). The mass of each protein band under investigation was compared with the expected molecular mass to confirm the presence of CYP1A1 in protein extracts. Several controls were included to verify the specificity of the protein-antibody interactions:

- Purified bacterially expressed 17α-CYP1A1 was electrophoresed with all mammalian cell extracts as a positive control.
- Specificity of the immunoreactive bands detected by the CYP1A1 antibody was determined by pre-absorption of the antibody with an immunogenic peptide. A 20-fold excess of peptide was combined with the antibody in 1mL of sterile PBS supplemented with rabbit serum (1%) and incubated at 4ºC overnight. The peptide/antibody complex was then used in place of the primary antibody.

- The specificity of primary antibody binding was determined by electrophoresis of 400ng of CYP1A1 antisera on an SDS-PAGE gel.
- The specificity of secondary antibody binding and chemiluminescence was determined by omission of the primary antisera.

2.2.7 Enzyme kinetics

Under the reaction conditions employed, rates of Res and AIC formation were required to be linear with respect to both incubation time and holo-CYP1A1 concentration. Furthermore, all kinetic experiments were undertaken with protein stored for less than four weeks and which had been subjected to only one freeze-thaw cycle.

2.2.7.1 Incubation conditions

All incubations containing recombinant CYP1A1 presented in this thesis were performed in phosphate buffer (0.1M, pH 7.4) at 37ºC in a total incubation volume of 0.2mL. Enzyme activity was initiated by the addition of NADPH generating system (1mM $NADP^+$, 10mM glucose-6-phosphate, 2IU glucose-6-phosphate dehydrogenase, 5mM $MgCl_2$). The formation of metabolites from different drug substrates required varying incubation conditions and will therefore be described in each relevant chapter. Where appropriate, substrate stock solutions were prepared in organic solvents such that the final concentration of solvent in incubations was <1%. Dilutions of all stock solutions were confirmed by HPLC to ensure substrate linearity. Drug-enzyme reactions were terminated by precipitation of all proteins present in incubations, and each metabolite assayed from the soluble fraction. The

method of protein precipitation varied depending on the incubation conditions and will therefore be described in each relevant chapter.

2.2.8 HPLC conditions

The separation and detection of Res employed a Hewlett Packard Series 1100 HPLC system (Hewlett Packard, Victoria, Australia). The system 1100 consisted of a gradient solvent delivery system (quaternary pump), mobile phase degasser, auto sampler, thermostated column compartment, and fluorescence detector.

The separation and detection of AIC required an Agilent Series 1100 HPLC system (Agilent Technologies, Victoria, Australia) comprising of a gradient solvent delivery system (quaternary pump), mobile phase degasser, auto sampler, thermostated column compartment, and variable wavelength UV-Vis detector.

CHAPTER 3
COMPARATIVE HOMOLOGY MODELING OF HUMAN CYP1A1

3.1 Introduction

Differences in P450 amino acid sequence give rise to the distinct substrate selectivities of the members of this enzyme family. Structure-function analyses and directed-evolution techniques have traditionally been employed to identify residues involved in substrate selectivity. More recently, these techniques have been complemented by *in silico* approaches based on the X-ray crystal structures of mammalian and bacterial P450 enzymes. X-ray crystal structures are currently available for a limited number of human P450s (section 1.5), and these 'static' structures provide the necessary structural templates for homology modeling. Moreover, analysis of these structures (in addition to the bacterial and rabbit P450 crystal structures) has revealed a universal folding pattern derived from the numerous conserved regions (de Graaf, Vermeulen & Feenstra 2005; Otyepka et al. 2007).

The aim of homology modeling is to build a 3-dimensional model for a protein of interest (referred to here as the 'target' protein) based on one or more proteins of known structure. In order to achieve a structurally valid and useful model, it is necessary that reasonable sequence similarity (usually >30%) exists between the target and the template. By partitioning both target and template sequences into conserved core regions, the target proteins structure can be deduced from that of the template (Greer 1981). In the case where more than one homologous template is

used, the atomic coordinates of each template are averaged to generate a 'static' template of conserved regions. In the absence of a CYP1A1 crystal structure, the generation of a chemically valid homology model is an important factor for characterizing structure-function relationships. Although, CYP1A1 homology models based on several crystallographic templates, including $P450_{TERP}$, $P450_{BM3}$, $P450_{CAM}$, and rabbit CYP2C5, have been reported (Iori et al. 2005; Lewis, Lake & Dickins 2004; Szklarz & Paulsen 2002; Testa 2004), none utilize human crystallographic X-ray data.

The ability to obtain a valid target structure is not solely dependant on utilizing a homologous template (Lewis 2002a). Moreover, it is important to estimate the accuracy of the modeled protein. Errors in structural models emerge from a variety of sources but initially arise from the incorrect assignment of homologous regions between template and target via the amino acid sequence alignment. In this study, rigorous optimization was achieved with all sequence alignments. One way to ensure the removal of bias from the amino acid alignment is to score all homologs (relative to the query sequence) based on a formal probabilistic scoring method.

In the present study a profile hidden Markov statistical model (HMM) was employed to aid generation of each CYP1A1 model. HMM are better known for their application in temporal pattern recognition such as speech, handwriting, and gesture (Eddy 1998). For the purpose of generating a protein structure based on closely related homologs, HMM can be used to generate a statistical model of multiple sequence alignments by capturing the position-specific information about how conserved each column of an alignment is, and which residues are more likely to occur at a particular position. This property of HMM therefore resolves important information about the degree of conservation at specific positions in the multiple

alignment, and the varying degree to which gaps and insertions are allowed. In contrast, traditional pair-wise alignment software such as BLAST and FASTA use position-independent scoring parameters.

HMM theory was utilized here to describe the probability distribution of CYP1A1 amino acids over those sequences deposited in the UniProt consortium database. This approach ensured the identification of human P450s that were closely related to CYP1A1. In total 33 CYP1A1 homology models were generated throughout this study, although only three will be described due to the optimization of alignment, modeling, and refinement methods. Two CYP1A1 homology models were generated based on single homologs using either the rabbit CYP2C5 [CYP1A1-(2C5)] or the human CYP1A2 crystal coordinates alone [CYP1A1-(1A2)]. A third model was additionally generated utilizing a homologous basic-set that consisted of the human CYP2C8 and CYP2C9, and the rabbit CYP2C5 crystal coordinates [CYP1A1-(HMM)]. All models were generated for comparative purposes and their structures and stereochemistry's evaluated.

In humans, CYP1A1 preferentially metabolizes PAHs (section 1.3.5.1). However, 7-ethoxyresorufin (Eres; Figure 3.1) is employed most widely as the prototypic CYP1A1 substrate (Lewis, Lake & Dickins 2004). CYP1A1 catalyses the *O*-deethylation of Eres; the site of oxidation is the α-carbon. Given the widespread use of Eres as a model CYP1A1 substrate, this compound was utilized in the automated *in silico* docking performed with the most valid CYP1A1 model.

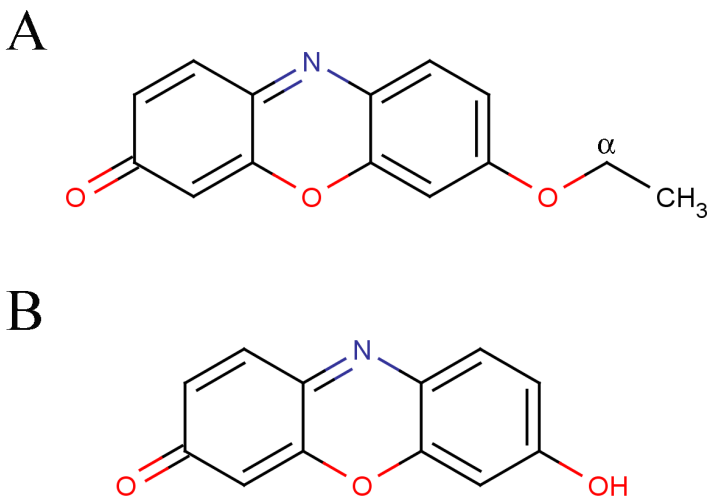

Figure 3.1 The chemical structures of 7-ethoxyresorufin (Eres) and its metabolite resorufin (Res). (a) Eres is *O*-deethylated by CYP1A1, with the site of oxidation located at the carbon atom α to the ethoxy oxygen. (b) *O*-deethylation by CYP1A1 forms the more soluble fluorescent metabolite, Res.

The general aim of this chapter was to generate a chemically and energetically valid structure of human CYP1A1.

Specific aims were to:

1. Identify and score those mammalian P450s that are closely related to human CYP1A1.
2. Optimize the alignment of homologous crystal templates by both amino acid residue type and secondary structure to reveal the "seed residues" required for modeling in addition to conserved regions of tertiary structure.
3. Generate 3-dimensional homology models of human CYP1A1.
4. Computationally refine each model to create a chemically and energetically realistic structure.

5. Conduct *in silico* docking experiments using the prototypical CYP1A1 substrate Eres to resolve those potentially important amino acid residues involved in the binding and orientation of substrates within the CYP1A1 active-site.

3.2 Materials and methods

3.2.1 Profile hidden Markov models

The computational program *hmmsearch* was employed to search the UniProt database for statistical descriptors of CYP1A1 and to score homologs relative to the CYP1A1 seed consensus (HMMER-2.3.2) (Eddy 1998). Data are represented by two scoring criteria: the HMMER raw score and an E-value. The best E-value is calculated from the bit score, which is a log-odds score (equation 3.1).

$$S = \log_2 \left(\frac{P\left(seq \mid HMM\right)}{P\left(seq \mid null\right)} \right) \qquad \text{(eq 3.1)}$$

where P(seq|HMM) is the probability of the target sequence according to the HMM and P(seq|null) is the probability of the target sequence given a “null hypothesis” model of the statistics of random sequence.

E-values denote the expected number of false positives with scores at least as high as the query sequence. The E-value is dependant on the size of the database which is searched.

3.2.2 Sequence alignment and optimization

Homolog alignments were optimized by both amino acid residue type and secondary structure using ClustalX-1.8 and Cn3D respectively, with alignment data characterized by the computational software INFOALIGN (EMBOSS). INFOALIGN measures sequence length, the number of gaps, and numbers of identical, similar and different residues or bases in this sequence when compared to a reference sequence, in addition to the percent change between the reference sequence and the query sequence.

3.2.3 Homology modeling

Three homology models of CYP1A1 were generated for comparative purposes: (a) CYP1A1-(2C5) was generated using the rabbit CYP2C5 crystal coordinates (1N6B, 1NR6); (b) CYP1A1-(HMM); a composite model generated using the combined crystal coordinates of human CYP2C8 (1PQ2) and CYP2C9 (1OG5, 1R9O), along with the coordinates of rabbit CYP2C5 (1N6B, 1NR6), and (c) CYP1A1-(1A2); which utilized the coordinates of CYP1A2 (2HI4) published during the course of this thesis.

The CYP1A1-(2C5), CYP1A1-(HMM), and CYP1A1-(1A2) models were constructed with COMPOSER (SYBYL7.3, Tripos™) by means of the p-mutation homology matrix (Dayhoff, Schwartz & Orcutt 1979; Greer 1981). Data and crystal structures for those homologs identified by the profile HMM were obtained from the Brookhaven Protein Data Bank (PDB). The minimum identity required for selection of homologous sequences was 0.28 (28%). The highest acceptable inter-Cα distance between equivalent residues within a sequence conserved region (SCR) was 1.5Å,

with a RMS difference of 0.00001Å considered significant. Loops positioned between SCRs foreign to homologs within the basic set were found by loop threading all crystal structures of the PDB. Loops with the most stringent fit to the anchor regions of SCRs were built with the anchor coordinates of the model left intact. Phi (ϕ) Psi (ψ) torsional angles of the database loops were adjusted to match those of the flanking anchor regions of CYP1A1. The heme prosthetic group was modeled as a separate heteroatom based on its coordination to the sulfur atom of the conserved cysteine at residue 457.

3.2.4 Computational refinement of homology models

Refinement of all models was achieved by scanning main-chain and side-chain torsions to relieve unacceptable van der Waals contacts, starting with those torsions furthest from the main-chain. The backbone of each model was defined and held as an aggregate while the remainder of the model was minimized by the Powell method (Powell 1977) (conjugate-gradient minimizer) using the Tripos™ Force Field (TRIPOS 5.2). The aggregate was then removed and each protein minimized as a whole. An initial simplex optimization was achieved with a threshold value of 1000 kcal.mol^{-1}. The number of iterations performed during each minimization step was 10,000 with a termination gradient of <0.05 kcal.mol^{-1}.Å.

3.2.5 Structure analysis of homology models

Protein structure analysis involved examination of the data obtained by PROCHECK v3.5.4 (Laskowski et al. 1993) and ProSa2003 v.4.0 (Sippl 1993). The program

PocketPicker (Weisel, Proschak & Schnider 2007) was employed to confirm the presence of the proposed substrate access and egress channels in the CYP1A1 homology models.

3.2.6 Automated substrate docking

Automated docking of Eres into the active-site of CYP1A1 was achieved using FlexX (SYBYL7.3, Tripos™). The ligand was reconstructed in the active-site using an algorithm based on pattern recognition pose clustering (Olson 1994). Placement of the ligand was consensus scored (CScore) based on its interactions with the protein. Key residues involved in stabilizing and orientating Eres in the active-site of the most chemically valid CYP1A1 model were identified.

3.3 Results

3.3.1 Identification of closely related P450 homologs

The profile HMM returned position- and residue-specific information about the degree of residue conservation at various positions of CYP1A1 against those sequence parsed domains of the UniProt database (~80,000 sequences). Protein sequences showing the lowest E-values relative to the CYP1A1 query were, in rank order, CYP1A1 <1A2 <2C8 <1B1 <2C5 <2C9 <2C19 <2C18 <2J2 <3A7 <3A5 <3A4 <2D6 <2A6 with all sequences being of human origin except for rabbit CYP2C5 (Table 3.1). In the absence of CYP1A2 crystallographic data, CYP2C8 was the best crystallized homolog for generation of a CYP1A1 homology model, followed by CYP2C5.

Table 3.1 *hmmsearch* of the UniProt sequence database with a profile HMM. CYP1A1 query is highlighted in red with human P450 homologs in blue.

Sequence	Description	Score	E-value
P04798|CP11_HUMAN	Cytochrome P450 1A1	1066.5	0
P00184|CP11_MOUSE	Cytochrome P450 1A1	1048.9	0
P00185|CP11_RAT	Cytochrome P450 1A1	1038.8	0
P79761|CP15_CHICK	Cytochrome P450 1A5	1036.1	0
P56591|CP11_SHEEP	Cytochrome P450 1A1	1022.4	0
P00187|CP12_RABBIT	Cytochrome P450 1A2	998.3	5.10E-295
P05176|CP11_RABBIT	Cytochrome P450 1A1	997.1	1.20E-294
P00186|CP12_MOUSE	Cytochrome P450 1A2	990	1.60E-292
P04799|CP12_RAT	Cytochrome P450 1A2	967.3	1.10E-285
*P05177|CP12_HUMAN	Cytochrome P450 1A2	955.9	2.90E-282
P79760|CP14_CHICK	Cytochrome P450 1A4	942.7	2.80E-278
Q64429|CP1B_MOUSE	Cytochrome P450 1B1	848.9	4.80E-250
Q64678|CP1B_RAT	Cytochrome P450 1B1	818.9	5.20E-241
*P10632|CPC8_HUMAN	Cytochrome P450 2C8	790.8	1.50E-232
Q16678|CP1B_HUMAN	Cytochrome P450 1B1	787.4	1.60E-231
P15123|CPCG_RABBIT	Cytochrome P450 2C16	784	1.60E-230
P11371|CPC4_RABBIT	Cytochrome P450 2C4	778.3	8.30E-229
*P00179|CPC5_RABBIT	Cytochrome P450 2C5	776.4	3.10E-228
P12394|CPT7_CHICK	Cytochrome P450 17A1	776.2	3.70E-228
P00181|CPC2_RABBIT	Cytochrome P450 2C2	770.4	2.10E-226
Q29510|CPCU_RABBIT	Cytochrome P450 2C30	758.2	9.30E-223
P17666|CPCE_RABBIT	Cytochrome P450 2C14	756.4	3.30E-222
*P11712|CPC9_HUMAN	Cytochrome P450 2C9	743	3.70E-218
P00180|CPC1_RABBIT	Cytochrome P450 2C1	741.4	1.10E-217
P33261|CPCJ_HUMAN	Cytochrome P450 2C19	738.5	8.00E-217
P33260|CPCI_HUMAN	Cytochrome P450 2C18	737.1	2.10E-216
P51589|CPJ2_HUMAN	Cytochrome P450 2J2	735.8	5.10E-216
P56656|CPZ4_MOUSE	Cytochrome P450 2C39	731.9	8.20E-215
P08683|CPCB_RAT	Cytochrome P450 2C11	727.1	2.30E-213
P00182|CPC3_RABBIT	Cytochrome P450 2C3	718.7	7.60E-211

Sequence	Description	Score	E-value
Q64458|CPCT_MOUSE	Cytochrome P450 2C29	712.4	6.10E-209
P56655|CPZ3_MOUSE	Cytochrome P450 2C38	705.4	7.40E-207
P05178|CPC6_RAT	Cytochrome P450 2C6	692.5	5.60E-203
P05179|CPC7_RAT	Cytochrome P450 2C7	691.3	1.30E-202
P56654|CPZ2_MOUSE	Cytochrome P450 2C37	687.3	2.10E-201
O54750|CPJ6_MOUSE	Cytochrome P450 2J6	676.5	3.70E-198
P24470|CPCN_RAT	Cytochrome P450 2C23	670.8	1.90E-196
P24462|CP37_HUMAN	Cytochrome P450 3A7	668.1	1.30E-195
P20815|CP35_HUMAN	Cytochrome P450 3A5	663.2	3.90E-194
P20814|CPCD_RAT	Cytochrome P450 2C13	663.1	4.10E-194
P20678|CPH2_CHICK	Cytochrome P450 2H2	662.4	6.50E-194
O54749|CPJ5_MOUSE	Cytochrome P450 2J5	658	1.40E-192
P19225|CPCM_RAT	Cytochrome P450 2C22	647.5	2.00E-189
P51590|CPJ3_RAT	Cytochrome P450 2J3	644.4	1.70E-188
P05180|CPH1_CHICK	Cytochrome P450 2H1	644.1	2.20E-188
P52786|CPJ1_RABBIT	Cytochrome P450 2J1	642.8	5.10E-188
*P08684|CP34_HUMAN	Cytochrome P450 3A4	637.7	1.80E-186
P56657|CPZ5_MOUSE	Cytochrome P450 2C40	628.3	1.20E-183

[a]Scores were obtained for complete sequences including all protein domains. *Denotes mammalian P450s where crystal data is available.

Note that X-ray crystal structures are not available for all sequences related to the CYP1A1 HMM. Moreover, some crystallized homologs give a greatly reduced score relative to the CYP1A1 query, indicating that sequence homology is not ideal for modeling. Homologs identified by the HMM used in modeling are shown in Table 3.2. The sequence identities represented in Table 3.2 (ClustalW algorithm) clearly shows that in the absence of CYP1A2 crystal data the closest homolog to CYP1A1

should be that of CYP2C9. This identifies degeneracy among the traditional pair-wise alignment software which use position-independent scoring parameters, and that of HMMER which assigns statistical scoring to both residue type and residue position.

3.3.2 Amino-terminal truncation of the CYP1A1 query sequence

Increasing the solubility of eukaryotic P450s by removing the hydrophobic NH_2-terminus is critical for successful crystallization and subsequent structure determination (section 1.5.2). Consistent with the experimental approach, the NH_2-terminus of CYP1A1 was modified prior to modeling. Use of the TMHMM Server (v.2.0) revealed a transmembrane helix comprising residues 12 through 29 in the full length CYP1A1 sequence (accession P04798) (Figure 3.2). Residues 1 through 11 were predicted to be on the luminal side of the ER, and residues 30 to 512 largely cytosolic. Numerous hydrophobic domains are scattered throughout the CYP1A1 cytoplasmic domain which may potentially associate with the ER membrane. On the basis of these observations, the first 32 NH_2-terminal residues from the CYP1A1 protein sequence were removed. Removal of these residues ensures deletion of the transmembrane helical domain in addition to part of a membrane associating region which spans the first 100 amino acid residues (Figure 3.2).

Table 3.2 *Hmmsearch* results showing the crystallized P450s used in generating each respective homology model. Alignment data were generated using the ClustalW algorithm.

Protein	Crystal Templates (PDB)	Identity (%)	Similarity (%)
CYP1A1	-	100	100
CYP1A2	2HI4	72	80.1
CYP2C8	1PQ2	27.7	42
CYP2C5	1DT6, 1NR6, 1N6B	28.2	43.4
CYP2C9	1OG2, 1OG5, 1R90	28.7	43.5

3.3.3 Optimization of P450 sequence alignments

The alignment of all crystallized P450s reveals conservation in the secondary structure motifs among 2B, 2C, and 3A P450 families (Figure 3.3). The structural overlay (Figures 3.4a and 3.4b) of the alignment seen in Figure 3.3 additionally reveals an analogous tertiary fold. Although the alignment and conserved secondary structure motifs display a strong correlation for all crystallized isoforms, the alignment data for CYP2B4 (1PO5) and CYP3A4 (1W0G, 1TQN) were omitted to avoid bias from protein structures with low sequence homology to CYP1A1. In addition, data from the CYP2C5 protein structure (specifically 1DT6) was removed since the extended region between P211 through L223 was not present in the crystal data. Results from the subsequent alignment were initially used to guide the homology modeling process for each of the three models generated [CYP1A1-(1A2), CYP1A1-(2C5), and CYP1A1-(HMM)].

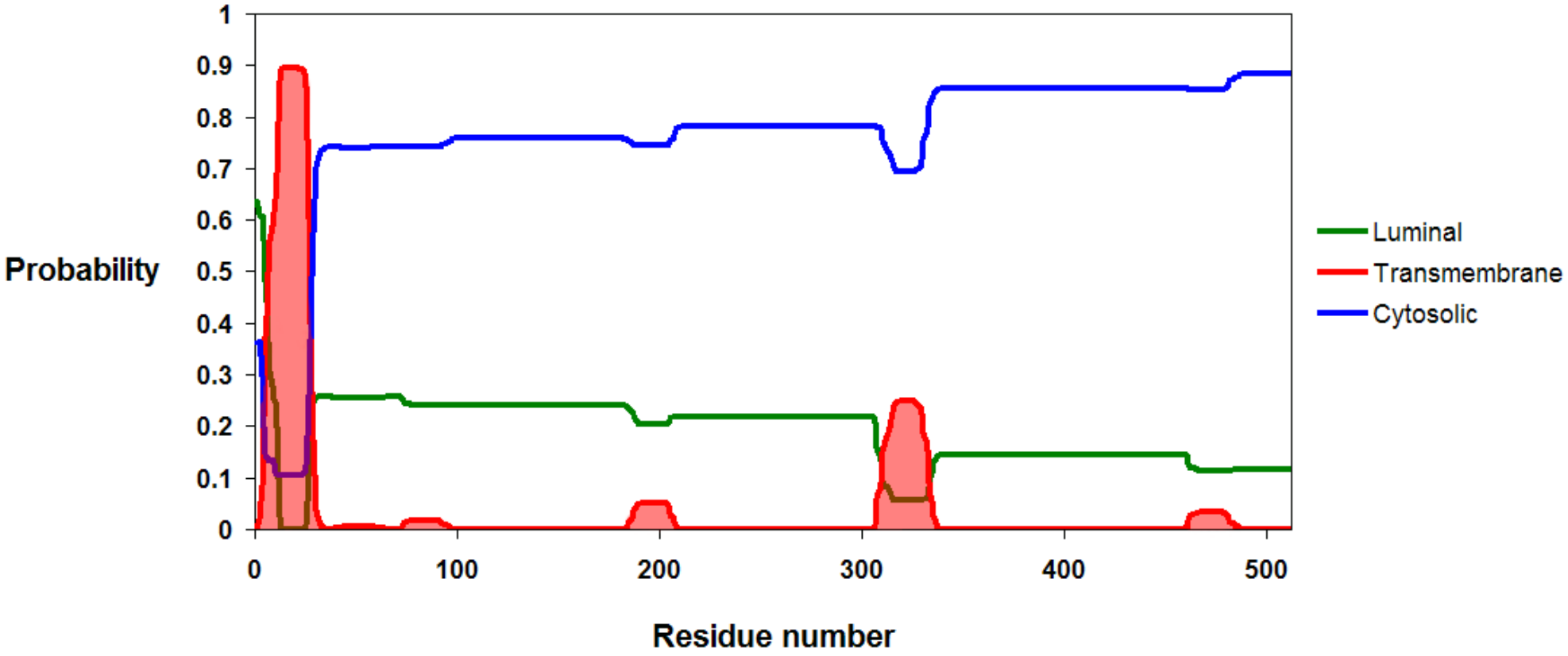

Figure 3.2 Transmembrane helical plot showing the probabilities of luminal, cytosolic, and transmenbrane helical domains of CYP1A1. The prediction gives the most probable location and orientation of transmembrane helices in the sequence.

```
                10        20        30        40        50        60
           ....*....|....*....|....*....|....*....|....*....|....*....|
1PQ2_A   1 MA~KKTSSk~GKl~~~PPGPTPLPIIGNMLQIDVKDICKSFTNFSKVYGPVFTVYFGMNP 55
1DT6_A   1 MA~KKTSSk~GKl~~~PPGPTPFPIIGNILQIDAKDISKSLTKFSECYGPVFTVYLGMKP 55
1NR6_A   1 MA~KKTSSk~GKl~~~PPGPTPFPIIGNILQIDAKDISKSLTKFSECYGPVFTVYLGMKP 55
1N6B_A   1 MA~KKTSSk~GKl~~~PPGPTPFPIIGNILQIDAKDISKSLTKFSECYGPVFTVYLGMKP 55
1OG2_B   1 MA~KKTSSk~GR~~~~PPGPTPLPVIGNILQIGIKDISKSLTNLSKVYGPVFTLYFGLKP 54
1OG5_A   1 MA~KKTSSk~GR~~~~PPGPTPLPVIGNILQIGIKDISKSLTNLSKVYGPVFTLYFGLKP 54
1R9O_A   1 MA~KKTSSgrGKl~~~PPGPTPLPVIGNILQIGIKDISKSLTNLSKVYGPVFTLYFGLKP 56
1PO5_A   1 MA~KKTSSk~GKl~~~PPGPSPLPVLGNLLQMDRKGLLRSFLRLREKYGDVFTVYLGSRP 55
1W0G_A   1 MA~YGTHSh~GLfkklGIPGPTPLPFLGNILSYHKGFCMFDMECHKKYGKVWGFYDGQQP 58
1TQN_A   1 MAlYGTHSh~GLfkklGIPGPTPLPFLGNILSYHKGFCMFDMECHKKYGKVWGFYDGQQP 59

                70        80        90       100       110       120
           ....*....|....*....|....*....|....*....|....*....|....*....|
1PQ2_A  56 IVVFHGYEAVKEALIDNGEEFSGRGNSPISQRITKGLGIISSNGKRWKEIRRFSLTTLRN 115
1DT6_A  56 TVVLHGYEAVKEALVDLGEEFAGRGSVPILEKVSKGLGIAFSNAKTWKEMRRFSLMTLRN 115
1NR6_A  56 TVVLHGYEAVKEALVDLGEEFAGRGSVPILEKVSKGLGIAFSNAKTWKEMRRFSLMTLRN 115
1N6B_A  56 TVVLHGYEAVKEALVDLGEEFAGRGSVPILEKVSKGLGIAFSNAKTWKEMRRFSLMTLRN 115
1OG2_B  55 IVVLHGYEAVKEALIDLGEEFSGRGIFPLAERANRGFGIVFSNGKKWKEIRRFSLMTLRN 114
1OG5_A  55 IVVLHGYEAVKEALIDLGEEFSGRGIFPLAERANRGFGIVFSNGKKWKEIRRFSLMTLRN 114
1R9O_A  57 IVVLHGYEAVKEALIDLGEEFSGRGIFPLAERANRGFGIVFSNGKKWKEIRRFSLMTLRN 116
1PO5_A  56 VVVLCGTDAIREALVDQAEAFSGRGKIAVVDPIFQGYGVIFANGERWRALRRFSLATMRD 115
1W0G_A  59 VLAITDPDMIKTVLVKECYSVFTNRRPFGPVGFMKSAISIAEDEEWKRLRSLLSPTFTSG 118
1TQN_A  60 VLAITDPDMIKTVLVKECYSVFTNRRPFGPVGFMKSAISIAEDEEWKRLRSLLSPTFTSG 119

                130       140       150       160       170       180
           ....*....|....*....|....*....|....*....|....*....|....*....|
1PQ2_A 116 FGMGKRSIEDRVQEEAHCLVEELRKTKASPCDPTFILGCAPCNVICSVVFQKRFDYKDQN 175
1DT6_A 116 FGMGKRSIEDRIQEEARCLVEELRKTNASPCDPTFILGCAPCNVICSVIFHNRFDYKDEE 175
1NR6_A 116 FGMGKRSIEDRIQEEARCLVEELRKTNASPCDPTFILGCAPCNVICSVIFHNRFDYKDEE 175
1N6B_A 116 FGMGKRSIEDRIQEEARCLVEELRKTNASPCDPTFILGCAPCNVICSVIFHNRFDYKDEE 175
1OG2_B 115 FGMGKRSIEDRVQEEARCLVEELRKTKASPCDPTFILGCAPCNVICSIIFHKRFDYKDQQ 174
1OG5_A 115 FGMGKRSIEDRVQEEARCLVEELRKTKASPCDPTFILGCAPCNVICSIIFHKRFDYKDQQ 174
1R9O_A 117 FGMGKRSIEDRVQEEARCLVEELRKTKASPCDPTFILGCAPCNVICSIIFHKRFDYKDQQ 176
1PO5_A 116 FGMGKRSVEERIQEEARCLVEELRKSKGALLDNTLLFHSITSNIICSIVFGKRFDYKDPV 175
1W0G_A 119 KLKEMVPIIAQYGDVLVRNLRREAETGKPVTLKDVFGAYSMDVITSTSFGVNIDSLNNPQ 178
1TQN_A 120 KLKEMVPIIAQYGDVLVRNLRREAETGKPVTLKDVFGAYSMDVITSTSFGVNIDSLNNPQ 179

                190       200       210       220       230       240
           ....*....|....*....|....*....|....*....|....*....|....*....|
1PQ2_A 176 FLTLMKRFNENFRILNSPWIQVCNNFPLLIDCFPGTHNKVLKNVALTRSYIREKVKEHQA 235
1DT6_A 176 FLKLMESLHENVELLGTPWLQVYNNFPALLDYFPGIHKTLLKNADYIKNFIMEKVKEHQK 235
1NR6_A 176 FLKLMESLHENVELLGTPWLQVYNNFPALLDYFPGIHKTLLKNADYIKNFIMEKVKEHQK 235
1N6B_A 176 FLKLMESLHENVELLGTPWLQVYNNFPALLDYFPGIHKTLLKNADYIKNFIMEKVKEHQK 235
1OG2_B 175 FLNLMEKLNENIEILSSPWIQVYNNFPALLDYFPGTHNKLLKNVAFMKSYILEKVKEHQE 234
1OG5_A 175 FLNLMEKLNENIEILSSPWIQVYNNFPALLDYFPGTHNKLLKNVAFMKSYILEKVKEHQE 234
1R9O_A 177 FLNLMEKLNENIKILSSPWIQICNNFSPIIDYFPGTHNKLLKNVAFMKSYILEKVKEHQE 236
1PO5_A 176 FLRLLDLFFQSFSLISSFSSQVFELFSGFLKHFPGTHRQIYRNLQEINTFIGQSVEKHRA 235
1W0G_A 179 DPFVENTKKLLRFDFLDPFFLSITVFPFLIPILEVLNICVFPREVTNFLRKSVKRMKESR 238
1TQN_A 180 DPFVENTKKLLRFDFLDPFFLSITVFPFLIPILEVLNICVFPREVTNFLRKSVKRMKESR 239

                250       260       270       280       290       300
           ....*....|....*....|....*....|....*....|....*....|....*....|
1PQ2_A 236 SLDVNNPRDFIDCFLIKMEQEkdnqkSEFNIENLVGTVADLFVAGTETTSTTLRYGLLLL 295
1DT6_A 236 LLDVNNPRDFIDCFLIKMEQEn~~~nLEFTLESLVIAVSDLFGAGTETTSTTLRYSLLLL 292
1NR6_A 236 LLDVNNPRDFIDCFLIKMEQEn~~~nLEFTLESLVIAVSDLFGAGTETTSTTLRYSLLLL 292
1N6B_A 236 LLDVNNPRDFIDCFLIKMEQEn~~~nLEFTLESLVIAVSDLFGAGTETTSTTLRYSLLLL 292
1OG2_B 235 SMDMNNPQDFIDCFLMKMEKEkhnqpSEFTIESLENTAVDLFGAGTETTSTTLRYALLLL 294
1OG5_A 235 SMDMNNPQDFIDCFLMKMEKEkhnqpSEFTIESLENTAVDLFGAGTETTSTTLRYALLLL 294
1R9O_A 237 SMDMNNPQDFIDCFLMKMEKEkhnqpSEFTIESLENTAVDLFGAGTETTSTTLRYALLLL 296
1PO5_A 236 TLDPSNPRDFIDVYLLRMEKDksdpsSEFHHQNLILTVLSLFFAGTETTSTTLRYGFLLM 295
1W0G_A 239 LEDTQKHRVDFLQLMIDSQNSketesHKALSDLELVAQSIIFIFAGYETTSSVLSFIMYE 298
1TQN_A 240 LEDTQKHRVDFLQLMIDSQNSketesHKALSDLELVAQSIIFIFAGYETTSSVLSFIMYE 299
```

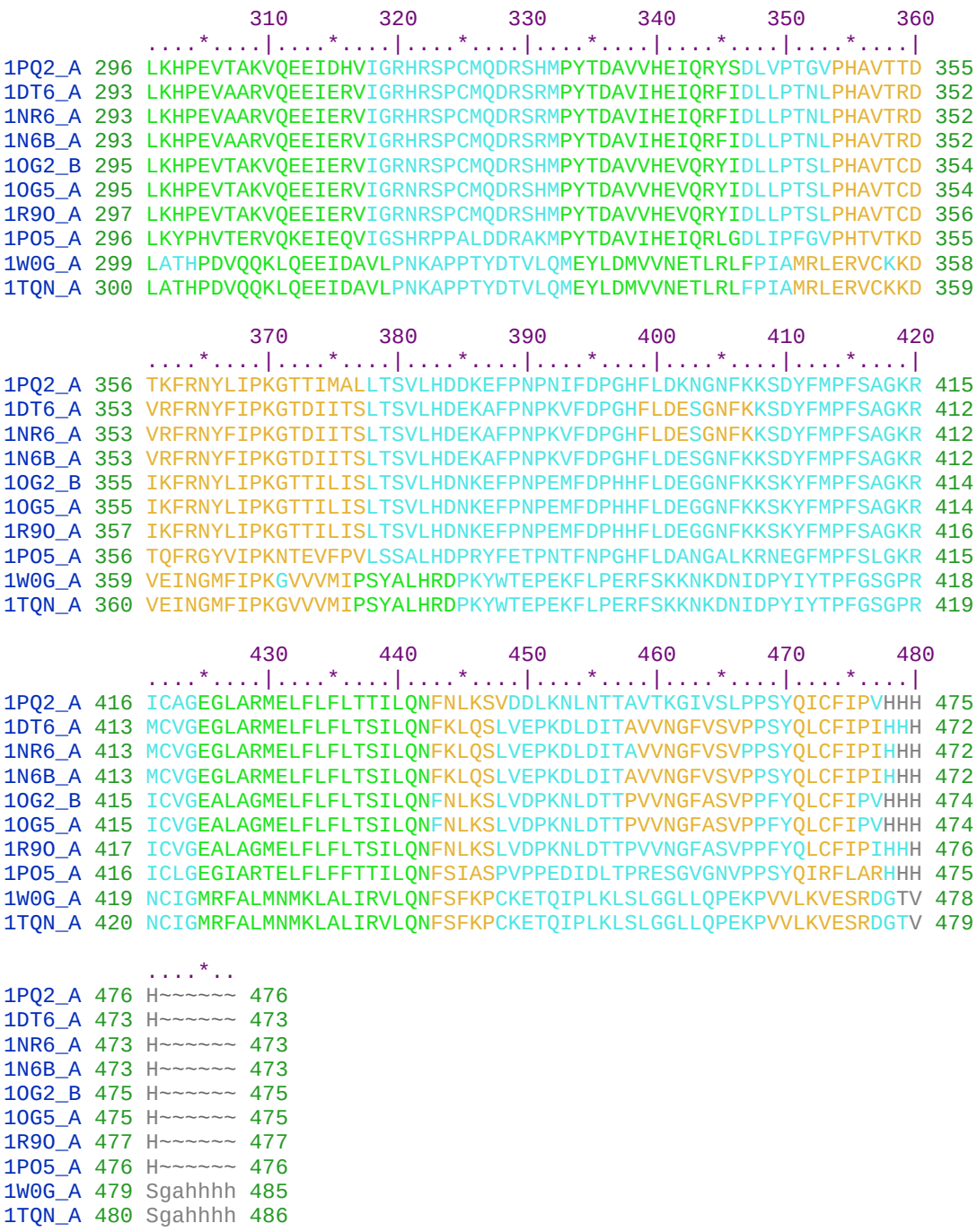

Figure 3.3 Structural alignment of crystallized cytochromes P450 based on secondary structure. Helices are shown in green, sheets in yellow, loops in blue, with black denoting no secondary structure assignment.

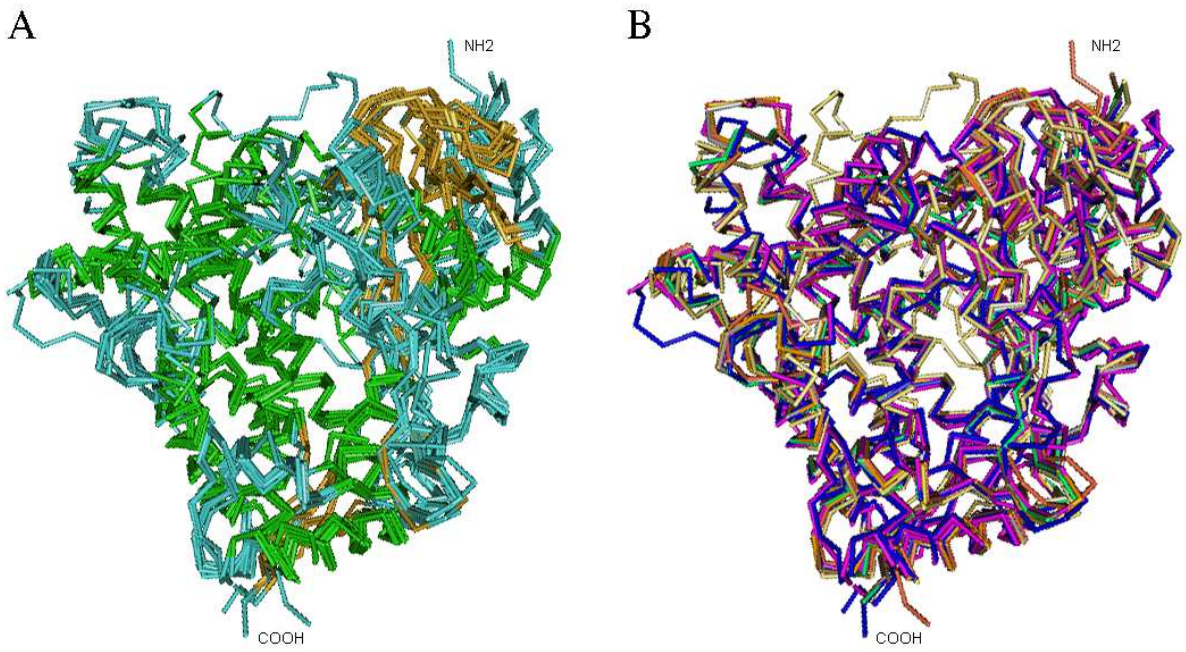

Figure 3.4 The 3-dimensional alignment of all crystallized human P450 structures. (a) Overlay of tertiary structures based on secondary structure alignment show little deviation in the Cα-carbon backbone; helices green, sheets yellow, loops blue. (b) Individual crystallized P450s in the overlay are identified; 1DT6 (CYP2C5) dark blue, 1N6B (CYP2C5) green, 1NR6 (CYP2C9) brown, 1OG2 (CYP2C9) yellow, 1OG5 (CYP2C9) grey, 1R90 (CYP2C9) orange, 1PQ2 (CYP2C8) magenta, 1PO5 (CYP2B4) tan, 1TQN (CYP3A4) blue, 1W0G (CYP3A4) purple.

Two versions of the primary sequence alignment were generated. The first was generated by the modeling software, SYBYL 7.3, whereby only position-independent scoring parameters were utilized to generate a model template with the highest possible number of seed residues (i.e. residues whose Cα coordinates are definitively used in the model). The second was initially generated by the *hmmalign* alignment with each sequence to the HMM, thus generating a statistical model of multiple sequence alignments, which captures both residue- and position-specific information. Each *hmmalign* alignment was optimized using ClustalX alignment software where regions of decreased sequence similarity or gaps were manipulated to

fall within loop regions of the crystal template(s). Both sets of alignment data for each homology model were scored using the INFOALIGN software.

Of the three alignments conducted, two gave markedly improved results after optimization with ClustalX compared to the alignments generated by SYBYL (Table 3.3). Optimization of the CYP1A1-CYP2C5 (1N6B/1NR6) alignment resulted in a decrease in both the number of gaps and gap length in the CYP1A1 sequence (Table 3.3). The CYP2C5 residues scored as either 'identical' or 'similar' increased from 120 to 148 and from 75 to 79, respectively. Conversely, alignment optimization decreased the number of 'different' residues from 285 to 254. The zero 'percent change' obtained for CYP1A1 identifies that all manipulations were conducted within the CYP2C5 template. Moreover, a reduction in 'percent change' for CYP2C5 was observed, from 75% to 69%, indicating greater complementarity to CYP1A1. Data obtained for the CYP1A1-CYP2C5-CYP2C8-CYP2C9 (1N6B/1NR6, 1PQ2, 1OG2/1OG5, 1R90) alignment is more complex due to the increased number of templates used. However, the results are similar (Table 3.3). Once again, the number of gaps in CYP1A1 is reduced from 11 in the SYBYL alignment to 6 in the ClustalX alignment. Reorganization of all sequences generated a significant increase in the number of 'identical' residues in CYP1A1; from 119 to 148, a 5% increase over the entire template. This is reflected by the reduction in the 'percent change' value, from 75.5% to 69.2%. Not surprisingly, the CYP2C8 (1PQ2) template exhibited the least change relative to CYP1A1, confirming its relatedness to CYP1A1 based on the *hmmalign* data (Table 3.1). Not surprisingly, no difference was observed in the alignment of CYP1A1 and CYP1A2 (2HI4) due to the high homology and relatedness of the two templates.

Table 3.3 Optimization data for the multiple sequence alignment of the CYP1A1 query to the homologous template(s) used for modeling.

Sequence	Alignment	Sequence Length	Aligned Length	Gaps	Gap length	Difference	Identity	Similarity	Change (%)
CYP1A1	Sybyl	482	489	5	7	0	482	0	0
1N6B/1NR6		480	489	4	18	285	120	75	75
CYP1A1	ClustalX	481	487	4	6	0	481	0	0
1N6B/1NR6		481	500	6	19	254	148	79	69.23
CYP1A1	Sybyl	486	497	6	11	286	119	81	75.51
1N6B/1NR6		480	498	4	18	76	370	34	22.91
1PQ2		479	495	4	16	99	353	27	26.30
1OG2/1OG5		475	489	3	14	63	396	14	16.63
1R90		481	500	4	17	74	390	17	18.92
CYP1A1	ClustalX	481	487	4	6	245	148	88	69.23
1N6B/1NR6		481	500	7	19	76	371	34	22.86
1PQ2		479	495	6	16	101	351	27	26.72
1OG2/1OG5		478	493	6	16	66	393	18	17.61
1R90		483	504	7	21	76	391	16	19.04
CYP1A1	Sybyl	476	477	1	1	74	402	0	15.54
2HI4		497	499	1	2	95	347	55	30.18
CYP1A1	ClustalX	476	477	1	1	74	402	0	15.54
2HI4		497	499	1	2	95	347	55	30.18

3.3.4 Molecular modeling of human CYP1A1

The CYP1A1-(2C5), CYP1A1-(HMM), and CYP1A1-(1A2) models were constructed with COMPOSER (SYBYL7.3, Tripos™) using the optimized *hmmalign* template alignments (Table 3.3). As expected, the quality of tertiary and secondary structure of the initial models was variable and depended greatly on both the quality of the sequence alignment (specific to a localized area), and the initial resolution of each crystal template.

Initial energy data obtained for all models identified poor side-chain rotamer probabilities, poor solvation energies, poor Cα temperature factors (B-factors; positional variability), and poor fractional surface area for side-chains (data not shown). Energy calculations encompassing bond stretching, torsional strain, and van der Waals forces (vdW) are given in Table 3.4. Not surprisingly, all energy data for the CYP1A1-(1A2) homology model, other than the vdW term, is the most favored energetically. Conversely, the vdW term was most favored with the CYP1A1-(HMM) homology model. All other energies for CYP1A1-(HMM) are distinctly better compared to the CYP1A1-(2C5) homology model. This may imply that better energetics are obtained in a structure generated with increased structural degeneracy (i.e. from many reasonable crystal templates) compared to a structure based on a single poor crystal homolog as in the case of the CYP1A1-(2C5) homology model.

Table 3.4 Energy data for the unrefined CYP1A1 homology models.

Energy (kcals/mol)	CYP1A1-(2C5)	CYP1A1-(HMM)	CYP1A1-(1A2)
Bond stretch	9090	8148	4380
Angle bend	4045	3556	2480
Torsional energy	1548	1562	1445
Out of plane bend	596	552	316
vdW	$1.3x10^{12}$	$6.7x10^{11}$	$8.5x10^{11}$
Total energy	$1.34x10^{12}$	$6.71x10^{11}$	$8.51\ x10^{11}$
Solvent accessible surface area ($Å^3$)	23542	23801	22632

3-Dimensional plots of each raw CYP1A1 model were undertaken to identify the regions with high energies. Residue energies between -4.75 and 30kcal.mol^{-1} are represented in Figure 3.5 by tube diameter and color. Although there is no distinct trend with the locations of high energies in each model, it is obvious that numerous unfavorable energies result in an increase in the solvent accessible surface area of each model (Figure 3.5; Table 3.4). Residue fold complementarity and packing ability is clearly related to the homology between target and template proteins.

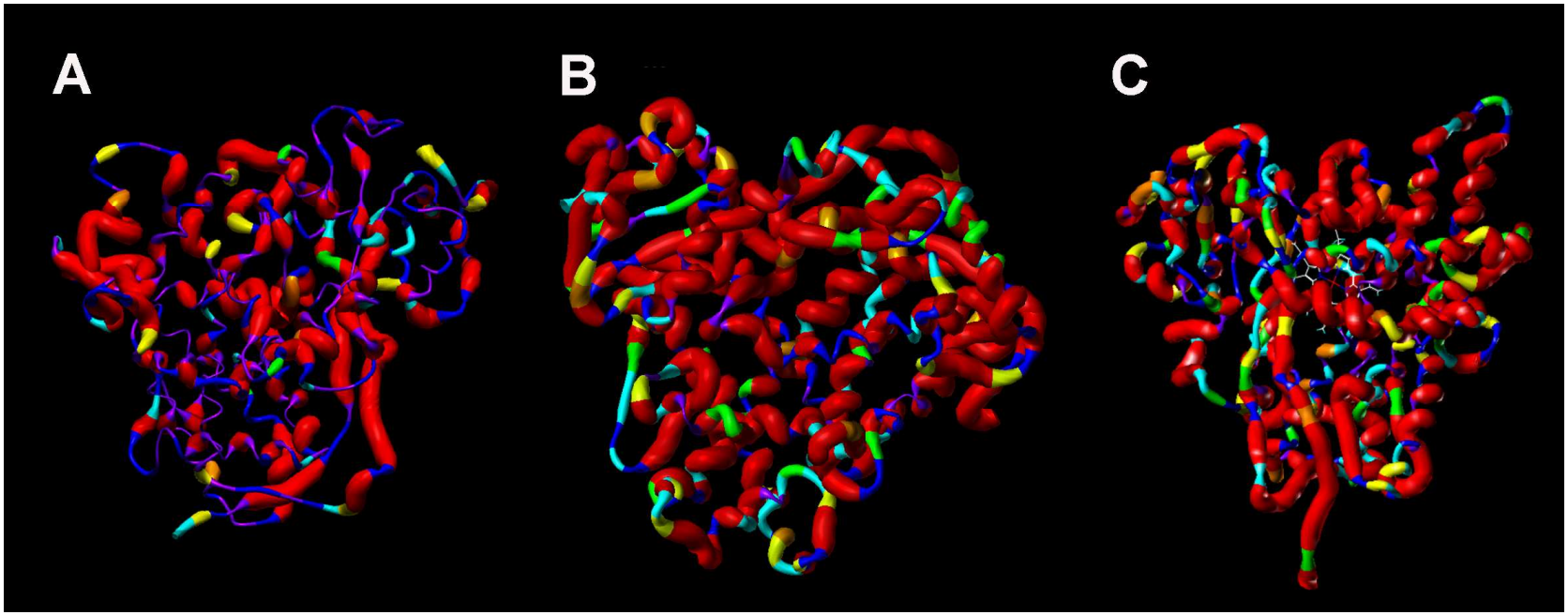

Figure 3.5 Unrefined CYP1A1 homology models ploted with tube diameter relative to residue energy. (a) CYP1A1-(2C5), (b) CYP1A1-(HMM), and (c) CYP1A1-(1A2). Colors represent the following energy range (kcal.mol^{-1}): <0.6 purple, 0.6-5 blue, 5-10 cyan, 10-15 green, 15-20 yellow, 20-25 orange, and >25 red.

3.3.5 Homology model refinement

Compared to the unrefined models (section 3.3.4), successive minimizations gave rise to greatly improved energetics along with a decrease in the solvent accessible surface area (Figure 3.6). The 3-dimensional energy plots displayed in Figure 3.6a show each model after the first minimization, which comprised 10,000 iterations. However, the majority of residues still exhibited energies >10 kcal.mol^{-1}. As shown in Figure 3.6b, a marked decrease (<5 kcal.mol^{-1}) in the total energy for each residue in all CYP1A1 models occurred after a further 10,000 iterations (or termination at <0.05 kcal.mol^{-1}).

The fully minimized CYP1A1-(2C5), CYP1A1-(HMM), and CYP1A1-(1A2) homology models all display the highly conserved secondary structure motifs analogous to all crystallized P450s (Figure 3.7). Additionally, each model returned RMSD values between 0.98Å and 2.5Å relative to each homolog in the basic set (Table 3.5).

Based on the final energy of models as a whole, CYP1A1-(1A2) obtained a total energy value of 406.85 kcal.mol^{-1}, which is in close approximation to the mean total energy calculated for all P450 crystal structures (417.92 kcal.mol^{-1}; Table 3.5). Moreover, CYP1A1-(1A2) presented a greatly reduced bond stretching energy of 211.67 kcal.mol^{-1} compared to the CYP1A1-(2C5) (592.35 kcal.mol^{-1}) and CYP1A1-(HMM) (1240.7 kcal.mol^{-1}) models, indicating less bond extension or compression and hence less electron density overlap between atoms. Although energetically favorable, the decreased bond stretching energy for CYP1A1-(1A2) is lower than those obtained for all crystal structures (Table 3.5), and is potentially an artifact intrinsic to either the query sequence and homolog template combination, or the

static nature of protein crystallization. Evidence of the 'query sequence and homolog template combination artifact' exists in the bond stretching energy of CYP1A1-(HMM), where greater degeneracy in bond stretching is introduced due to the increased number of homologs in the basic set. Angle bending energies of all models are in good agreement with those of the crystal structures. However, the energy required to overcome torsional strain is approximately 2.5-times that of the torsional energies of the crystal structures (Table 3.5). Individual analysis of omega and zeta torsional angles in the main-chain of each model identified deviations in the peptide bond planarity and the presence of Cα tetrahedral distortions in CYP1A1-(2C5) and CYP1A1-(HMM), but not in CYP1A1-(1A2). Similarly, no such distortions exist in the crystal structures. Interestingly, the torsional strains seen in CYP1A1-(2C5) and CYP1A1-(HMM) are prevalent in SRS1 through SRS6 which may impact on substrate docking experiments. In addition, calculated vdW forces indicate that the three-dimensional folding of CYP1A1-(2C5) may contain errors (Table 3.5), implying a less stable structure for human CYP1A1. This may be due to unfavorable amino acid packing density or an effect generated by inappropriately minimized hydrogen atoms. In contrast, CYP1A1-(1A2) and CYP1A1-(HMM) display strong negative vdW forces demonstrating complementarity in most residue interactions. The large differences between the vdW forces of CYP1A1-(1A2), CYP1A1-(2C5), and CYP1A1-(HMM) vdW forces (viz. -3275.55, -163.79, and -3201.38 $kcal.mol^{-1}$, respectively) is due in part to the steep distance dependence of the energy term. Differences between the vdW forces of the crystal structures and those of CYP1A1-(1A2) and CYP1A1-(HMM) may be attributed to by the absence of hydrogen's in the crystallographic data.

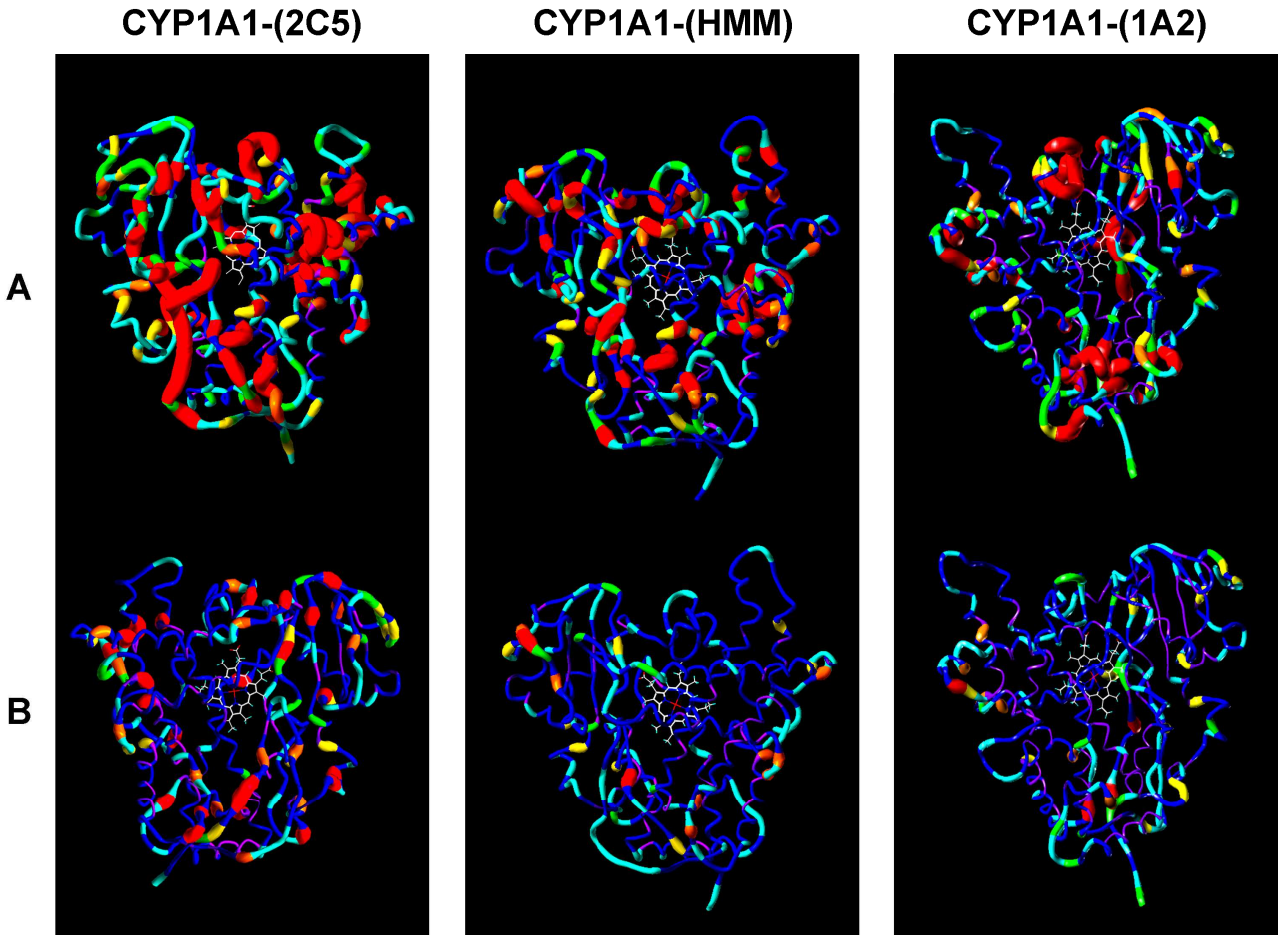

Figure 3.6 Energy minimized CYP1A1 homology models plotted as tube diameter relative to residue energy. (a) Displays each model after the initial 10,000 minimization iterations on the side-chains, and (b) shows each model after the second 10,000 minimization iterations on the entire protein. Colors represent the following energy ranges (kcal.mol^{-1}): <0.6 purple, 0.6-5 blue, 5-10 cyan, 10-15 green, 15-20 yellow, 20-25 orange, and >25 red.

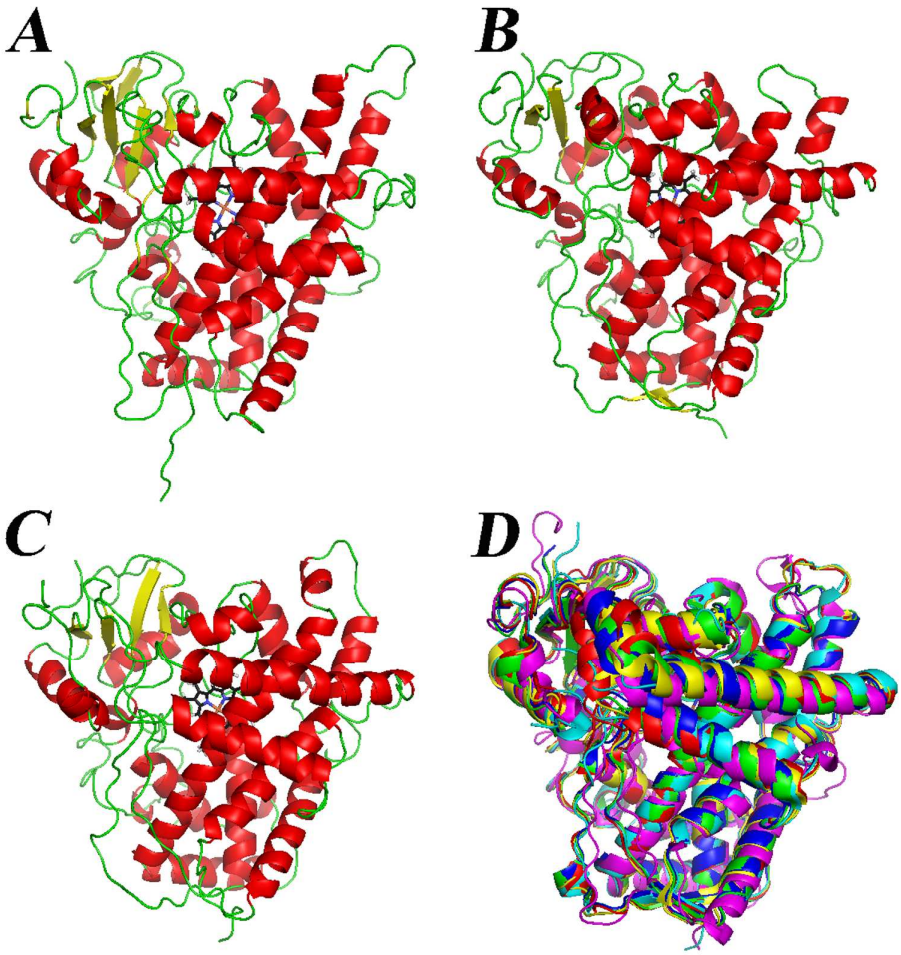

Figure 3.7 CYP1A1 homology models. (a) CYP1A1-(1A2), (b) CYP1A1-(2C5), and (c) CYP1A1-(HMM). The models show structural resemblance to that of the crystallized P450s. Helices are shown as red ribbons, β-sheets are in yellow, and loops colored green. The structural overlay (d) displays all crystallized homologs of the basic set (1NR6; blue, 1N6B; green, 1OG5; red, 1PQ2; yellow, 1R9O; cyan, and 2HI4; magenta). See Table 3.5 for RMSD data calculated between homologs.

Table 3.5 Comparative minimization data for CYP1A1 homology models and the crystallized homologs of the basic-set. [a]

Model/Crystal	Solvent Accessible Surface Area (Å^2)	Homolog RMSD[b]						Bond Stretching Energy[c]	Angle Bending Energy[c]	Torsional Energy[c]	van der Waals Forces[c]	Total Energy[c]
		2HI4	1NR6	1N6B	1PQ2	1OG5	1R90					
CYP1A1-(2C5)	22053.5	-	1.04	0.98	-	-	-	592.35	1639.74	1189.99	-163.79	3889.08
CYP1A1-(HMM)	22579.59	-	1.76	1.71	2	1.95	2.5	1240.7	1265.38	1155.73	-3201.38	1072.18
CYP1A1-(1A2)	22191.83	1.14	-	-	-	-	-	211.67	1445.36	1253.68	-3275.55	406.85
CYP1A2 (2HI4)	21281.85	0						1237.74	1159.08	465.44	-1989.26	780.4
CYP2C5 (1NR6)	20566.95	2.68	0					651.64	981.66	424.51	-2048.59	-135.64
CYP2C5 (1N6B)	21248.57	2.66	0.655	0				747.85	1048.43	457.15	-1847.57	270.61
CYP2C8 (1PQ2)	21292.09	2.37	1.073	1.053	0			719.78	1064.78	463.06	-1774.86	354.74
CYP2C9 (1OG5)	21039.68	2.65	1.451	1.327	0.995	0		927.7	1202.14	469.05	-1826.72	676.83
CYP2C9 (1R9O)	20944.57	3.61	1.883	1.923	1.924	1.946	0	1073.85	1032.37	452.7	-1916.06	560.6

[a] Data are specific to the energy calculations generated by the Tripos™ Force Field. [b] Root Mean Squared Deviation (RMSD) is calculated from the Cα backbone.

[c] Energy units in kcal.mol^{-1}.

3.3.6 CYP1A1 protein structure quality

Evaluation of the models for protein structure quality identified various anomalies in the stereochemistry of CYP1A1-(2C5) with phi (ϕ) and psi (ψ) torsional angles (dihedral angle between ϕ: C'-N-C^{α}-C' and ψ: N-C^{α}-C'-N) from 26 residues (6.2%) residing on the high energy plateau of the Ramachandran [ϕ,ψ] plot and a further 75 residues (18%) in 'additionally allowed' regions (Figure 3.8a). The composite model, CYP1A1-(HMM), showed improved stereochemistry with only 14 residues (3.3%) in unfavored regions and 84 residues (20.2%) in 'additionally allowed' regions (Figure 3.8b). These data suggest that a homology model generated with a composite of distally related homologs may bias the protein fold to a lesser extent than a single poor homolog such as rabbit CYP2C5. As expected, the closest homolog to CYP1A1, CYP1A2, gave near ideal stereochemical quality for the CYP1A1-(1A2) homology model, with only three residues in generously allowed/disallowed regions. Moreover, 87.7% of all residues were positioned in the most favored valleys of the Ramachandran Plot (Figure 3.8c). The stereochemical data obtained for CYP1A1-(1A2) resembles the stereochemical qualities of crystallized human P450s (Figure 3.8d). Thus, the structural and physicochemical data collectively identified the CYP1A1-(1A2) homology model as the most chemically valid model to use in automated molecular docking experiments.

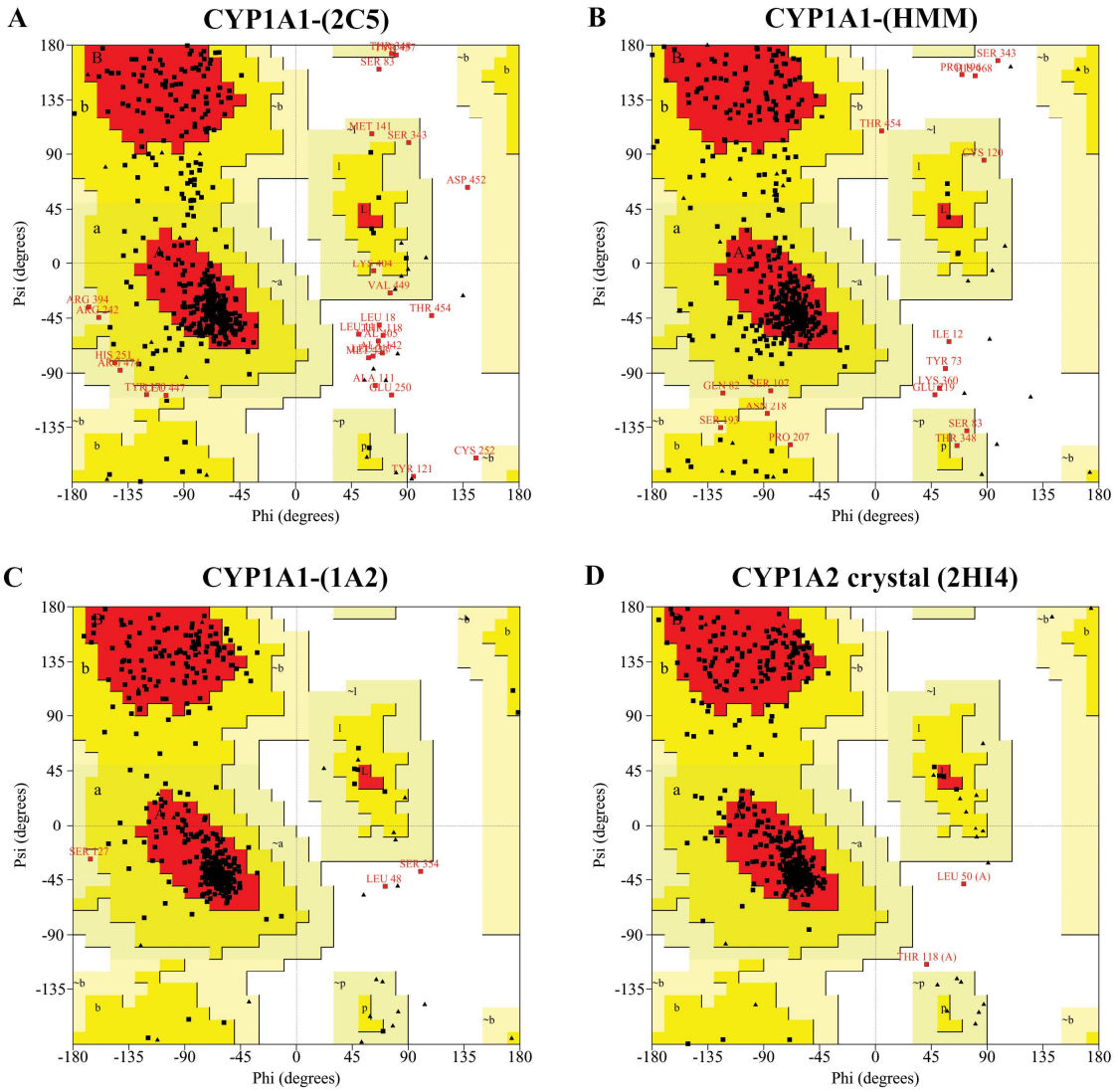

Figure 3.8 Ramachandran Plots for all CYP1A1 homology models and the CYP1A2 crystal structure. (*a*) CYP1A1-(2C5), (*b*) CYP1A1-(HMM), and (*c*) CYP1A1-(1A2) homology models. (*d*) A Ramachandran Plot of crystallized CYP1A2 (2HI4). Phi (ϕ) and psi (ψ) torsional angles for all residues are displayed. Red troughs correspond to the most favored stereochemistries with α-helicies $\phi = \psi = -60^{o}$, β-sheets $\phi = -135^{o}$ and $\psi = 135^{o}$, and left-handed helicies $\phi = 60^{o}$ and $\psi = 45^{o}$. Glycine residues are not subject to steric constraints and are shown as triangles. The ring constraints of proline results in $\phi = -65^{o}$. Residues highlighted in red text identify those positioned in either 'generously allowed' or 'disallowed' regions.

3.3.7 The tertiary organization of human CYP1A1

Detailed investigation of the CYP1A1-(1A2) homology model revealed twelve α-helices and five β-sheets, designated A-L and 1-5, respectively. Two additional helices, B´ and K´, are also present. Figure 3.9 shows a schematic representation of the CYP1A1 tertiary organization based on the CYP1A1-(1A2) homology model. The tertiary structure of CYP1A1-(1A2) shows close resemblance to crystallized CYP1A2, with a RMSD of 1.14Å (Table 3.5). The volume of the active-site cavity of CYP1A1-(1A2) was calculated as 339Å^3 (1.0Å grid resolution; SiteID™), slightly less than that of the CYP1A2 crystal structure (363Å^3). Like CYP1A2, the CYP1A1-(1A2) homology model is devoid of the F´ and G´ α-helices that usually disrupt the F-G loop in many mammalian P450s. Compared to CYP1A2, the CYP1A1 structure varies in arrangement of β-sheets at the C-terminus. The E-F loop is tighter and more uniform in the CYP1A1 model leading into the F-helix. The F-helix itself remains intact at the anterior (unlike CYP1A2) and curves inward to form, in part, the ceiling of the active-site cavity. The G-helix extends an additional thirteen residues in CYP1A2, implying greater flexibility in the G-H loop of CYP1A1 based on the CYP1A1 structure. The H-I loop of CYP1A1 protrudes more equatorially compared to the axial (constricted) H-I loop of CYP1A2. Moreover, the additional β-3 sheet observed in the H-I loop of CYP1A2 is not apparent in the CYP1A1 structure.

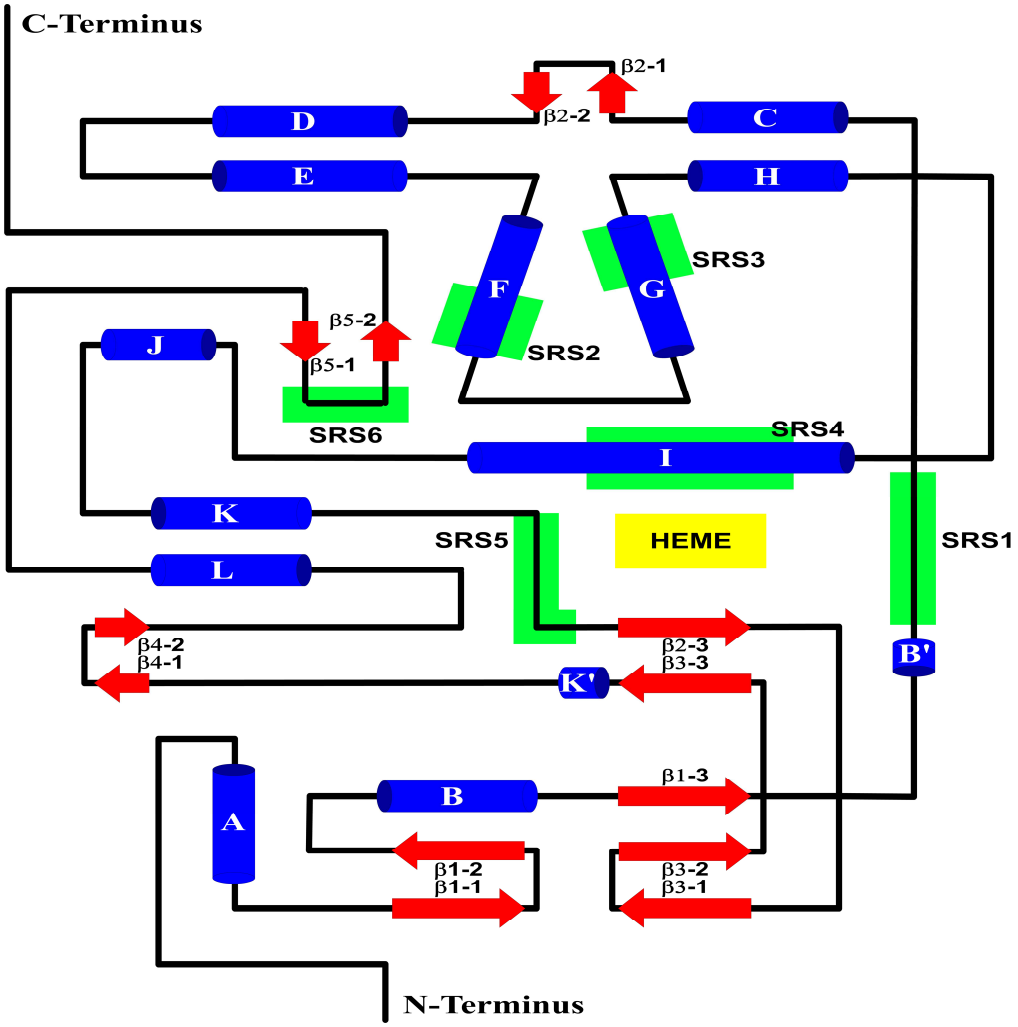

Figure 3.9 Schematic representation of the secondary and tertiary organization of CYP1A1-(1A2). α-Helices are displayed in blue, β-sheets in red, the main-chain in black, substrate recognition regions in green, and the heme in yellow. Residues defining each SRS are presented in Table 3.6.

Table 3.6 Substrate recognition site residues that form the active-site cavity of human CYP1A1.

Residue	Type[a]	Secondary Structure Motif[b]	SRS[c]
I115	Nonpolar, aliphatic	B'-C loop	1
M121	Polar, uncharged	B'-C loop	1
S122	Polar, uncharged	B'-C loop	1
F123	Aromatic	B'-C loop	1
F224	Aromatic	F-Helix	2
G225	Nonpolar, aliphatic	F-Helix	2
F258	Aromatic	G-Helix	3
Y259	Aromatic	G-Helix	3
D313	Negatively charged	I-helix	4
G316	Nonpolar, aliphatic	I-helix	4
A317	Nonpolar, aliphatic	I-helix	4
D320	Negatively charged	I-helix	4
T321	Polar, uncharged	I-helix	4
F381	Aromatic	K-Helix/β2-3 loop	5
V382	Nonpolar, aliphatic	K-Helix/β2-3 loop	5
I386	Nonpolar, aliphatic	K-Helix/β2-3 loop	5
L496	Nonpolar, aliphatic	β5-1/β5-2 loop	6
T497	Polar, uncharged	β5-1/β5-2 loop	6

[a] Amino acid types are characterized by charge state at pH 7.0. [b]See Figure 3.9 for schematic representation of the secondary and tertiary structure organization. [c] Substrate recognition regions adapted from those reported by Gotoh (1992).

3.3.8 Automated docking of 7-ethoxyresofufin (Eres)

Using the CYP1A1-(1A2) homology model, Eres was docked into the protein active-site using the automated docking software, FlexX (SYBYL7.3, Tripos™). The binding mode of Eres was assisted by the inclusion of virtual water molecules that bridged interactions between the ligand and the core pocket targeted for docking. Key residues involved in formation of the CYP1A1 active-site pocket are presented in Table 3.6. The best-pose orientation places the α-carbon adjacent to the ether oxygen of Eres at 4.4Å from the heme iron at an angle of 106.4º perpendicular to the heme plane from the pyrrole nitrogen (Figure 3.10a). These measurements are similar to the geometries calculated for the Fe^{2+}-O-O-R intermediate using covalent atomic radii and are comparable to the experimental data reported by Meunier, de Visser and Shaik (2004), Ogliaro, de Visser and Shaik (2002), and Shaik et al. (2005). Binding and orientation of Eres within the active-site involves residues S120, S122, F123, F224, F258, Y259, D313, T321, V382, and I386, with all residues positioned within a 3Å radius from the substrate (Figure 3.10b). The hydroxyl oxygen of S120 resides 3.4Å from the carbonyl group distal to the catalytic site of Eres. Although this distance is too great to hydrogen bond directly to the substrate, it is likely a water bridge is utilized to stabilize the substrate. Hydrogen bonding is, however, observed from S122 to the oxazine ring oxygen of Eres. An edge-to-face aromatic interaction occurs between the central oxazine ring of Eres and F123, in addition to the parallel displaced aromatic interactions with F224, F258, and Y259 (Figure 3.10b). Each phenyl ring of this triad is positioned at a mean distance of 4.60Å from one another and would be expected to contribute to the binding of polycyclic aromatic compounds in the CYP1A1 active-site. T321 and V382 are positioned at the front of the active-site, stabilizing the ethoxy group of Eres (Figure

3.10b). The β-branching of T321 and V382 restricts flexibility of these residues to that of the main-chain conformation. Thus, T321 and V382 act as a 'steric boundary' for the substrate. Additionally, T321 has the ability to form H-bonds with a variety of polar substrates and may also interact with water molecules in the active-site. Being charged and polar, D313 is in close proximity to the partially positively charged C4 carbon of Eres positioned between the oxygen of the oxazine ring and the carbonyl group distal to the catalytic site of Eres (Figure 3.10b). This interaction may affect the orientation of the substrate in the active-site. The β-branched residue I386 additionally lies within 3Å of Eres. Due to its rigid conformation, I386 may be involved in both the recognition of hydrophobic ligands and, more importantly, in reducing flexibility at the substrate access/active-site boundary (Figure 3.10b). Closer inspection of the residues in the vicinity of I386 reveals a potential substrate access channel primarily consisting of nonpolar, aliphatic amino acids (Table 3.7). The surface opening of the access channel is defined by residues V228, N232, L240, and N245 (Figure 3.11). The polar uncharged nature of N232 may aid the orientation of substrates for entry into the access channel. The channel itself is arranged primarily by residues which make up the F-G loop, with contributions from residues located in the B´-helix and the K-helix/β2-3 loop. In contrast to the substrate access channel, a proposed product egress channel almost exclusively exists of polar, uncharged residues, signifying this is not an alternative access channel for highly aromatic CYP1A1 substrates (Table 3.7). The egress channel extends from the active-site beneath the G-helix, running parallel to the terminal end of the I-helix and is enclosed by the B´-helix/C-loop (Figure 3.11). In contrast to lipophilic substrates entering the access channel via the membrane attachment surface of CYP1A1, the egress channel would allow more polar metabolites to readily exit the active site into

the cytoplasm. The surface opening of the egress channel is defined by residues of the B´-helix/C-loop clamping against the G- and I-helices. R134 and R135 of the C-helix flank M121 of the B´-helix/C-loop and may be involved in a mechanism used for gating or reducing elasticity of the product egress channel at such times when the protein exists in a closed conformation.

For comparative purposes, automated docking of Eres was also performed with the human CYP1A2 crystal structure. The active-site residues of CYP1A1 (Table 3.6) and CYP1A2 share 72.2% sequence identity, with differences occurring at M121 (L123 in CYP1A2), S122 (T124), G225 (V227), Y259 (L261), and V382 (L382). As with M121 of CYP1A1, L123 of CYP1A2 contributes minimally to the binding of Eres (Wade et al. 2004). However, like S122 of CYP1A1, T124 in CYP1A2 forms an H-bond with the oxazine ring oxygen of Eres. G225 of CYP1A1, corresponding to V227 in CYP1A2, resides at the distal end of the F-helix, the region of least homology between the two enzymes. The F-helix in CYP1A1 is terminated by the tight turn generated by G225, whereas this helix is extended by a further residue in CYP1A2. Replacement of Y259 in CYP1A1 with L261 in CYP1A2 marginally increases the size of the active-site cavity around the I/G-helix junction in the latter enzyme. Compared to V382 in CYP1A1, L382 of CYP1A2 protrudes deeper into the active-site toward the ethoxy substituent of bound Eres. The V382L mutation in CYP1A1 has been shown to dramatically decrease EROD activity by disrupting alignment of the ethoxy substituent (Wade et al. 2004).

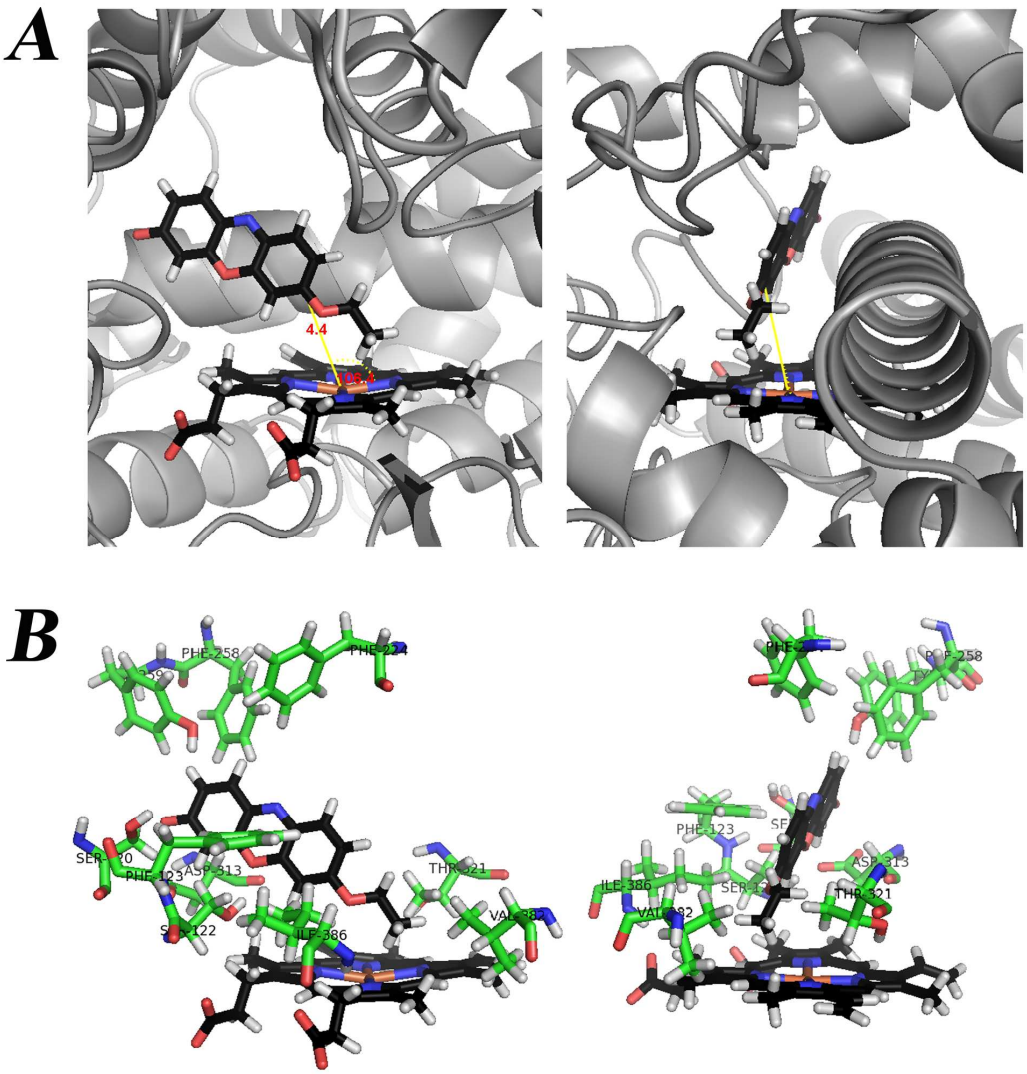

Figure 3.10 Orthogonal imaging of the key residues involved in formation of the active-site pocket of CYP1A1 with the α-carbon of the ethoxy substituent positioned in the desired orientation for O-deethylation. (a) substrate orientation along the I-helix, (b) binding and orientation of Eres within the active-site showing the involvement of S120, S122, F123, F224, F258, Y259, D313, T321, V382, and I386, with all residues positioned within a 3Å radius from the substrate.

Table 3.7 Residues proposed to form the substrate access and egress channels in CYP1A1.

Access Channel	Type[a]	Secondary Structure Motif[b]	Egress Channel	Type[a]	Secondary Structure Motif[b]
L109	Nonpolar, aliphatic	β1-3/B'-Helix	S116	Polar, uncharged	B'-Helix/C-loop
T111	Polar, uncharged	B'-Helix	N117	Polar, uncharged	B'-Helix/C-loop
F113	Aromatic	B'-Helix	Q119	Polar, uncharged	B'-Helix/C-loop
E226	Negatively charged	F-G loop	S120	Polar, uncharged	B'-Helix/C-loop
V227	Nonpolar, aliphatic	F-G loop	Q263	Polar, uncharged	G-Helix
V228	Nonpolar, aliphatic	F-G loop	N309	Polar, uncharged	I-Helix
G229	Nonpolar, aliphatic	F-G loop	L312	Nonpolar, aliphatic	I-Helix
S230	Polar, uncharged	F-G loop			
G231	Nonpolar, aliphatic	F-G loop			
N232	Polar, uncharged	F-G loop			
P233	Nonpolar, aliphatic	F-G loop			
A234	Nonpolar, aliphatic	F-G loop			
D235	Negatively charged	F-G loop			
L240	Nonpolar, aliphatic	F-G loop			
N245	Polar,	F-G loop			

Access Channel	Type[a]	Secondary Structure Motif[b]	Egress Channel	Type[a]	Secondary Structure Motif[b]
	uncharged				
F251	Aromatic	G-Helix			
I386	Nonpolar, aliphatic	K-Helix/β2-3 loop			
P387	Nonpolar, aliphatic	K-Helix/β2-3 loop			

[a] Amino acid types are characterized as they would occur at pH 7.0. [b] See Figure 3.9 for schematic representation of the secondary and tertiary structure organization.

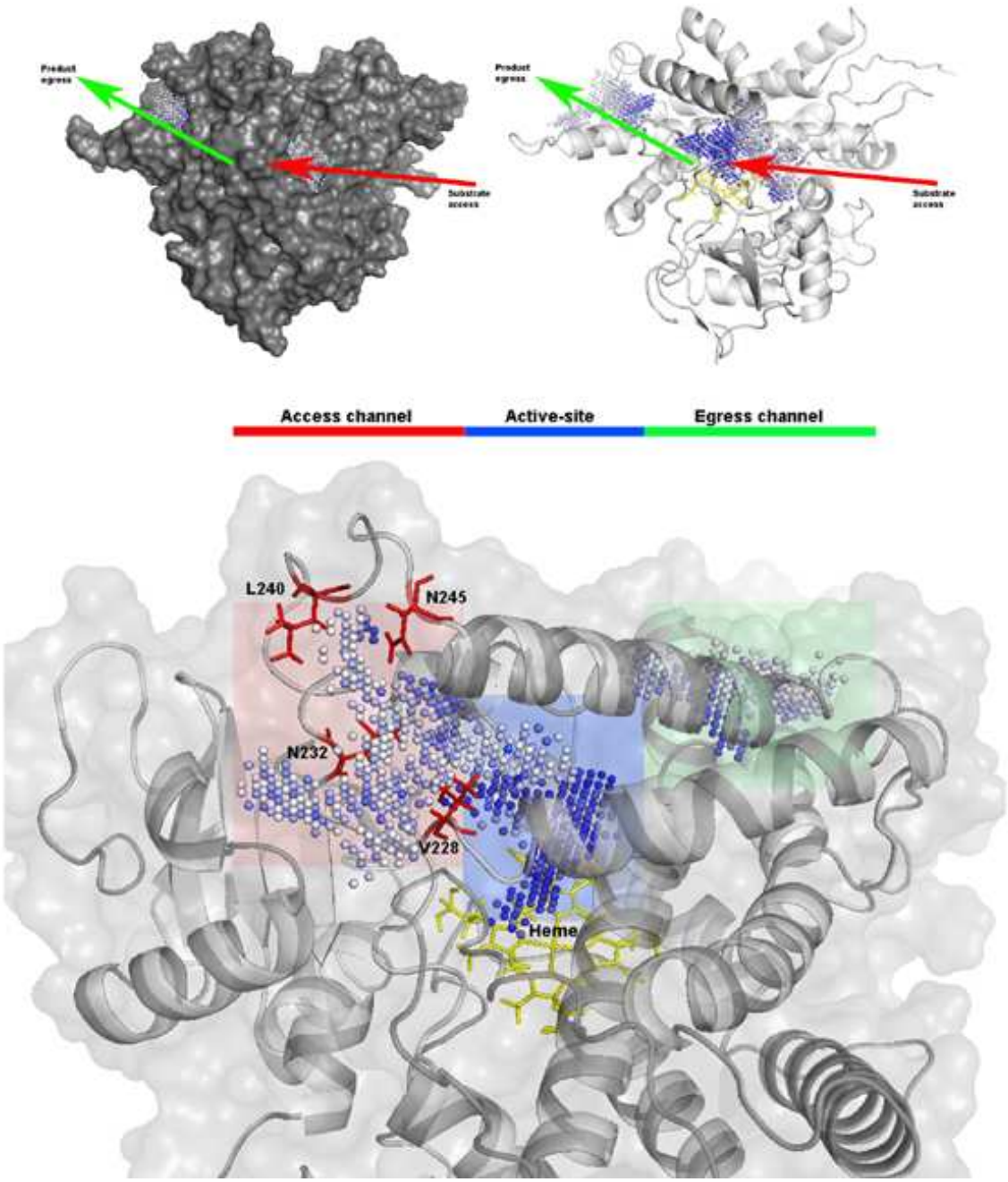

Figure 3.11 Surface toplogy and secondary structure views of the proposed substrate access channel and product egress channel. Water molecules (blue spheres) flood the protein cavity occupying the substrate access channel (red), active-site (blue), and product egress channel (green). Hydrophillic substrates enter the CYP1A1 active-site via the membrane attachment region of the protein (NH_2-terminal domain) with the more polar metabolites released into the cytoplasm via the product egress channel.

3.4 Discussion

Previously published homology models of CYP1A1 show the desired secondary structure motifs characteristic of human P450s (Lewis, Ioannides & Parke 1994b; Lewis, Lake & Dickins 2004; Szklarz & Paulsen 2002). However, since most models reflect the bacterial or rabbit homologs with which they were modeled (<28% homology), variance in the backbone and loop regions gives rise to structural distortions. Changes in secondary and tertiary organization directly affect the active-site architecture and may distort enzyme-substrate interactions. Of the published human CYP1A1 homology models, only two were generated using mammalian homologs, namely rabbit CYP2C5 (Lewis, Ioannides & Parke 1994a; Szklarz & Paulsen 2002). Generation of a chemically valid CYP1A1 homology model using human P450 templates is required for predicting desirable side-chain stereochemistry and in-turn, better *in silico* predictions of substrate binding and orientation. This thesis is the first to report a human CYP1A1 homology model based on human data at >80% sequence similarity.

The comparative modeling data presented here demonstrates that the CYP1A1 homology model based on a composite of homologs, namely CYP2C5, CYP2C8, and CYP2C9, resulted in a structurally and energetically superior CYP1A1 homology model (Figure 3.7; Table 3.5) compared to that based on rabbit CYP2C5 alone. Thus, in the absence of crystallographic data for a highly homologous protein, the generation of a homology model using a composite of distally related proteins appears more valid. Use of a profile HMM identified CYP1A2 and CYP2C8 as the closest crystallized homologs to CYP1A1 based on position- and residue-specific distributions. However, generation of a CYP1A1 model based on CYP2C8 (1PQ2) alone (data not shown), the closest CYP1A1 homolog (27.4% identity, 41.8%

similarity) in the absence of the CYP1A2 crystallographic data, confirmed the proposed 'composite homology model theory'. Analysis of CYP1A1-(2C8) revealed a reasonable model based on energetic considerations, but one that was disfavored structurally based on stereochemistry, indeed more so than the CYP1A1-(2C5) homology model. The CYP1A1-(2C5) and CYP1A1-(HMM) homology models also displayed structural inaccuracies, particularly deviations in peptide bond planarity, poor residue packing densities, and distortions in Cα tetrahedral angles. Although these deviations occurred from SRS1 through SRS6, they were not evident in the crystallized homologs of the basic-set nor in the CYP1A1-(1A2) homology model. Stereochemical analysis of the crystal structures of the basic-set and all homology models identified additional anomalies in the CYP1A1-(2C5) and CYP1A1-(HMM) structures (Figures 3.8a and 3.8b).

The CYP1A1-(1A2) homology model displayed 87.7% of all residues with optimal ϕ and ψ torsional angles and therefore showed close to ideal secondary structure organization (Figure 3.8c). This result is comparable to the features of crystallized P450s, for example: CYP1A2 (2HI4); 90.4% Ramachandran, CYP2C9 (1R9O); 86.5%, CYP2C8 (1PQ2); 85.5%, and CYP2C5 (1NR6); 86.9%. Based on structural and energy data, CYP1A1-(1A2) is clearly the most valid model to use in automated substrate docking experiments. It should be noted, however, that the molecular mechanics employed to predict the energies associated with the conformation of each model was based on a data-set of discretely crystallized proteins. Importantly, the absolute numerical value of each calculated energy has no physical meaning however, differences in energies between each model within this study are physically meaningful, as are the comparisons of relative energies between the different crystal structures.

Detailed investigation of the CYP1A1 homology model revealed a number of key residues that were involved in the active-site pocket and the substrate access and egress channels (Tables 3.6 and 3.7). The largely non-polar substrate access channel consists of residues that make up the F-G loop and meanders inward toward the active-site incorporating residues from the B´-helix and the K-helix/β2-3 loop (Figure 3.11). Such regions are highly variable in sequence among all P450s and highly variable in structure among the crystallized proteins. Despite variability in the F-G loop regions of the different homology models generated (Figure 3.7), structural similarities also exist between the CYP1A1-(1A2) and CYP1A1-(HMM) models. Not surprisingly, perturbations within the F-G loop region would clearly have effects on substrate access. Based on *in silico* predictions, the loop composition of the CYP1A1-(1A2) model is ideal with respect to both side-chain stereochemistry and secondary structure (Figure 3.8). The polar substrate egress channel is proposed to extend from the active-site beneath the G-helix, running parallel with the I-helix, enclosed by the B´-helix/C-loop (Figure 3.11). The proposed substrate access and egress channels of CYP1A1 show close resemblance to the pw2a and pw2c pathways identified by Sudarko, Williams, and Wade in numerous bacterial and mammalian crystal structures (Schleinkofer et al. 2005; Wade et al. 2004; Williams et al. 2000a). Not surprisingly, the presence of such channels were inconclusively determined if proteins adopted a closed conformation.

Automated *in silico* docking was used as a tool to identify key residues involved in the orientation and stabilization of Eres within the CYP1A1 active-site cavity (Figure 3.10). The most energetically favorable pose placed the catalytic α-carbon adjacent to the ether oxygen of Eres at 4.4Å from the heme iron, at an angle of 106.4º perpendicular to the planar heme (Figure 3.10). S120, S122, F123, F224, F258,

Y259, D313, T321, V382, and I386 were all positioned within 3Å of the best posed substrate molecule.

In summary, numerous computational techniques were employed to generate the chemically valid human CYP1A1 homology model presented here. Such techniques are dependant on the quality of the structural data obtained from X-ray crystallography and nuclear magnetic resonance spectroscopy. A structure-based approach (section 1.5.3.1) was then employed to identify the residues involved in the binding and orientation of Eres in the CYP1A1 active-site.

CHAPTER 4
EXPERIMENTAL VALIDATION OF THE CYP1A1 HOMOLOGY MODEL

4.1 Introduction

An understanding of the structural organization and chemical interactions between P450 enzymes and their respective substrates is pivotal for characterizing structure-activity relationships. The two major methods used to predict the interactions between enzymes and their substrates are: (i) data modeling, which utilizes statistical correlations between molecular and structural descriptors, and (ii) molecular modeling approaches, which combine the *in silico* analysis of substrate binding (via docking) with protein modeling (Yu et al. 2006). In the vast majority of cases, the latter is used to predict the key residues involved in substrate binding and orientation in the enzyme active-site. Despite the availability of site-directed mutagenesis as a tool to investigate structure-activity relationships of enzymes, not all molecular modeling studies experimentally validate computational models. Chapter 3 of this thesis described the energetically favorable binding of Eres in the CYP1A1 active-site using molecular docking. Moreover, those residues involved in binding and orientation of Eres were identified. However, the *in silico* docking of Eres does not give rise to an estimate of binding affinity or enzyme function, nor an estimate of enzyme conformational change during binding of the substrate.

To date, the analysis of mammalian structure-activity relationships has primarily focused on the CYP2B, CYP2C, CYP2D, and CYP3A sub-families (Domanski & Halpert 2001). Mutagenesis is usually targeted at predicted active-site residues

whereby substitutions are made to the corresponding amino acid of a closely related enzyme or homolog. Substitution of amino acids in this way usually results in alterations in substrate selectivity and/or catalytic efficiency. Negishi *et al.* (1996) addressed the functional flexibility of mammalian P450s by introducing certain neutral amino acid substitutions and suggested that the size of the side-chain is the most important descriptor of substrate selectivity, thereby outweighing other factors such as polarity or charge (Negishi et al. 1996).

However, other factors often play a major part in determining the role of a side-chain. For example, π-stacking and electrostatic interactions are also critical. Haining *et al.* (1999) investigated the π-stacking interactions of a substrate with specific amino acids in the CYP2C9 active-site. A CYP2C9 homology model identified F110 and F114 as potential hydrophobic, aromatic active-site residues which may π-stack with the phenyl ring of warfarin (Haining et al. 1999). To test this hypothesis Haining *et al.* (1999) generated F110L, F110Y, and F114L mutants. The F110Y mutant did not express. However, F110L and F114L mutant proteins were tested with numerous substrates. The F110L mutant consistently displayed modest changes in kinetic parameters, independent of substrate. Interestingly, the F114L mutant exhibited significant changes in the metabolite ratios for each warfarin enantiomer. These data supported the hypothesis that π-stacking at F114 occurs with particular aromatic substrates.

In structure-activity studies utilizing CYP3A4, the L210A mutant was shown to exhibit marginally higher testosterone hydroxylase activity compared to the wild-type (Harlow & Halpert 1997). In comparison, a L210F mutant displayed a 2-fold increase in testosterone hydroxylase activity (Harlow & Halpert 1998). Additionally, studies conducted with CYP2B1 by He *et al.* (1992) revealed that substitutions to

amino acids containing larger side-chains at the polymorphic Gly478 residue affected the total androstenedione and testosterone hydroxylase activities (He et al. 1992). Surprisingly, however, testosterone metabolite formation dramatically decreased with substitution to alanine, providing evidence that minor spatial reorganization of the void volume in the P450 active-site can dramatically affect productive substrate orientation and potentially substrate recognition.

Based on the above considerations, it appears that the structural role each amino acid plays in forming the substrate active-site is essential for the productive orientation and catalysis of P450 substrates. Changes in either residue position, the complementary and energetically favored fit to an adjacent amino acid, or in residue type, can alter substrate selectivity or enzyme dynamics.

Superposition of the CYP1A1 homology model against the crystallized human CYP1A2 structure reveals that all but five putative active-site residues are highly conserved (Figure 4.1). Table 4.1 lists the alternate residues found at identical locations within the CYP1A1 and CYP1A2 active-sites (see Table 3.6 for a full list of CYP1A1 active-site residues; section 3.3.7). Although the number of different active-site residues between CYP1A1 and CYP1A2 is low, as noted above, changes in amino acid type and the relaxation of adjacent/neighboring structures must also be taken into consideration. This is evident from the work of Liu *et al.* (2004) that generated the five reciprocal mutants between CYP1A1 and CYP1A2 (section 1.3.4). Typically, residue substitutions dramatically reduced methoxyresorufin *O*-deethylation (MROD) and EROD in both CYP1A1 and CYP1A2 (Liu et al. 2004). Interestingly, the authors did not identify which residues confer substrate selectivity, or which chemical interactions are critical for the productive alignment of alkoxyresorufins in the CYP1A active-site.

Inspection of the superimposed CYP1A1 and CYP1A2 structures reveals a number of homologous residues that neighbor the five alternate CYP1A2 residues discussed above. Consideration of the spatial assembly of residues between CYP1A1 and CYP1A2 shows that homologous amino acids adopt different spatial coordinates. Therefore, homologous amino acids located in identical primary sequence position may be functionally dissimilar between proteins. Directed mutagenesis experiments carried out in this chapter utilized mutants which introduce residues with side-chains of sizes and charges both similar and markedly different from those of the wild-type and, importantly, not corresponding to an alternate P450. Substitutions of this type should more accurately verify the roles of amino acids involved in CYP1A1 substrate orientation, selectivity, and catalysis. Thus, the studies reported in this chapter focused on confirming the predictivity of the 'static' CYP1A1 homology model generated in Chapter 3, and were additionally aimed to define the critical physicochemical properties responsible for the productive alignment and orientation of substrates in the CYP1A1 active-site.

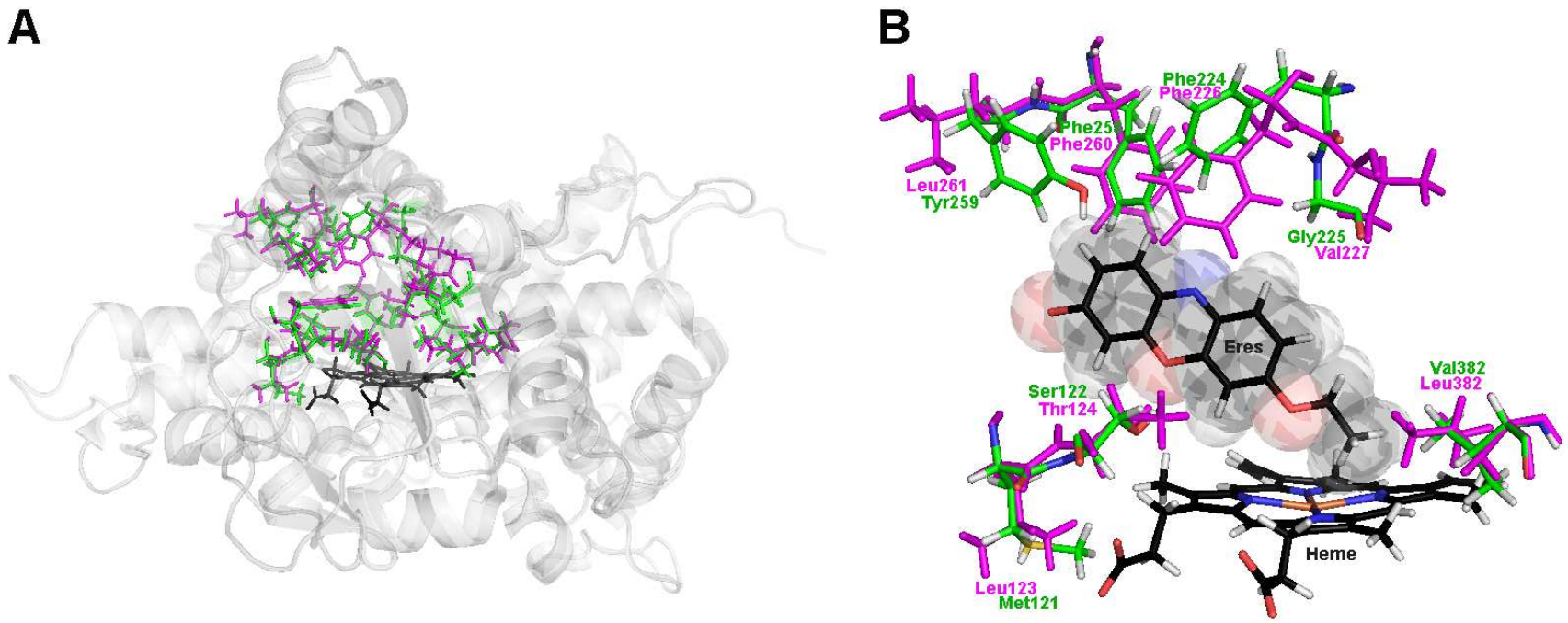

Figure 4.1 Conserved putative active-site residues of CYP1A1 and CYP1A2. (a) Structural overlay of the CYP1A1 homology model (green) with the crystallized human CYP1A2 crystal structure (2HI4; magenta) identifies the highly conserved residues of the putative active-site. RMSD Cα backbone 1.14Å. (b) Differences in active-site residues between CYP1A1 and CYP1A2.

Table 4.1 Differing active-site residues of CYP1A1 and CYP1A2. All remaining residues from SRS1 through SRS6 are conserved.

CYP1A1	CYP1A2
Met121	Leu123
Ser122	Thr124
Gly225	Val227
Tyr259	Leu261
Val382	Leu382

The substrate chosen for structural validation of the CYP1A1 homology model was 7-ethoxyresorufin (Eres), the same compound used for *in silico* docking experiments (section 3.3.8). Eres is routinely used for determining the contribution of CYP1A enzymes during drug metabolism experiments in the presence of multiple P450 enzymes (Chang & Waxman; Hakkola et al. 1996; Nakajima et al. 2002; Shimada et al. 2002). Furthermore, Eres is frequently employed as a 'model' CYP1A1 substrate due to its relative selectivity for CYP1A1 over CYP1A2. This was the basis for the use of Eres in molecular docking experiments, and for the characterization of CYP1A1 structure-activity relationships. The reported apparent K_m values for EROD catalyzed by cDNA-expressed human CYP1A1 range from 0.5-0.9μM (Chang & Waxman; Chun et al. 1997; Guo et al. 1994; Liu et al. 2003). However, few studies have published kinetic plots of EROD by human CYP1A1, and the Michaelis-Menten equation has typically been uncritically employed for kinetic modeling.

The general aim of this chapter is to confirm the predictivity of the CYP1A1 computational model generated in Chapter 3.

Specific aims were to:

1. Heterologously co-express active CYP1A1 and OxR in *E. coli*.
2. Use directed mutagenesis to confirm the active-site residues involved in the binding and orientation of substrates within the CYP1A1 active-site.
3. Define the critical physicochemical properties of residues responsible for the productive alignment and orientation of Eres in the CYP1A1 active-site.
4. Confirm the kinetic constants for 7-ethoxyresorufin *O*-deethylation by CYP1A1.

4.2 Materials and methods

4.2.1 Targeted mutagenesis

4.2.1.1 Identification of 7-ethoxyresorufin-binding residues for mutagenesis

A number of active-site mutations were required to confirm the predictivity of the CYP1A1 computational model generated in Chapter 3. Sites for mutagenesis were determined based on their proximity to the docked structure of Eres generated *in silico*. This was achieved by identifying all residues within a 3Å radius of the docked structure (section 3.3.8; Figure 3.10b) and consideration of the nature of the side-chain/substrate interaction. Of particular interest were the edge-to-face and parallel-displaced aromatic interactions arising from aromatic amino acids, and the hydrogen bonding interactions from polar amino acids. Residues potentially involved in the activation of oxygen at the sixth coordination position of the heme were also targeted. All substitutions were guided by consideration of the importance of the original side-chains functional group(s) and how they contribute to substrate alignment, orientation, and enzyme activity.

4.2.1.2 Generation of active-site mutants

The wild-type 17α-CYP1A1 cDNA in pBluescript-II-SK(+) was used as the template for mutagenesis using the one-step site-directed and site-saturation mutagenesis protocol described by Zheng, Baumann and Reymond (2004) (section 2.2.3). Primers employed for mutagenesis are shown in Table 4.2. Mutagenesis PCR conditions and cycling parameters are described in sections 2.2.3.3 and 2.2.3.4, respectively. All mutations were confirmed by DNA sequencing on both strands (ABI 3130-XL DNA sequencer, Applied Biosystems, Victoria, Australia).

4.2.2 Protein expression and immunochemical detection

4.2.2.1 Co-expression of CYP1A1 with OxR

The pBS-CYP1A1 wild-type, S122A, F123A, F224A, A317Y, T321G, and I386G constructs generated by mutagenesis were ligated into the pCW ori(+) bacterial expression plasmid using *NdeI* and *XbaI* restriction sites (section 2.2.2.2). Individual pCW constructs were transformed into DH5α *E. coli* cells that were stably transformed with the pACYC OmpA-rOxR construct. Ampicillin/chloramphenicol selected colonies were screened for the correct plasmids by restriction enzyme analysis. Cells were cultured and membrane fractions separated as described in sections 2.2.4.2 and 2.2.4.3, respectively. The total protein of membrane fractions was determined by the method of Lowry *et al.* (1951) (section 2.2.4.4) and expressed holo-enzyme was quantified by cytochrome P450 reduced difference spectroscopy (Omura & Sato 1964a; Omura & Sato 1964b) (section 2.2.4.5). OxR activity was

determined using cytochrome *c* as an alternative electron acceptor using the method outlined in section 2.2.4.6 (Yasukochi & Masters 1976).

4.2.2.2 Immunochemical detection of CYP1A1 wild-type and mutants

Equal amounts of total membrane protein (25µg) were subjected separately to SDS PAGE (section 2.2.6.1). Separated proteins were rectilinearly transferred onto nitrocellulose (section 2.2.6.2) and probed with anti-human CYP1A1 primary antiserum (1:3000 dilution) and anti-rabbit IgG (1:4000 dilution; H+L-HRP) as the secondary antibody (Pierce Biotechnology, Inc., Rockford, IL, USA), using microsomes (25µg) prepared from the liver of a non-smoker as a negative control. Membrane-bound peptides conjugated with HRP were detected by BM Chemiluminescence (Roche Diagnostics, Mannheim, Germany) and subsequently exposed to Omat auto-radiographic film (Kodak, Australia).

Table 4.2 Primers used for site-directed mutagenesis [a,b]

CYP1A1 Mutant	Primer Overlap (5' forward to 5' reverse)	ΔG^o of Heterodimerization (kcal/mol)
S122A	5'CAGAGCATG**G**CCTTCAGCCCAGACTCTGG 3'	-36.3
	3'GTCATTACCAGTCTCGTAC**C**GGAAGTCG 5'	
F123A	5'GCATGTCC**GC**CAGCCCAGACTCTGGACC 3'	-40.7
	3'CATTACCAGTCTCGTACAGG**CG**GTCGGGTC 5'	
F224A	5'GAATAATAAT**GC**CGGGGAGGTGGTTGGCTC 3'	-40.9
	3'GGATCAGTTGGACTTATTATTA**CG**GCCCCTCC 5'	
A317Y	5'CTCTTTGGA**TA**TGGGTTTGACACAGTCAC 3'	-34.4
	3'GCAGAACCTGGAGAAACCT**AT**ACCCAAAC 5'	
T321G	5'GGTTTGAC**GG**AGTCACAACTGCTATCTCC 3'	-34.4
	3'GGAGAAACCTCGACCCAAACTG**CC**TCAGTGTTG 5'	
I386G	5'CCTTCACC**GG**CCCCCACAGCACAACAAGAG 3'	-41.9
	3'GAAGGAAGCAGGGGAAGTGG**CC**GGGGGTGT 5'	

[a] Mutagenic nucleotides are highlighted in red. [b] Wild-type CYP1A1 (Accession NM_000499) was used as the parent template to generate all mutants.

4.2.3 Enzyme kinetics and the derivation of kinetic parameters

4.2.3.1 Measurement of 7-ethoxyresorufin O-deethylase activity

EROD activity was determined in opaque glass tubes at 37ºC in a total incubation volume of 0.2mL. Incubation mixtures contained co-expressed CYP1A1 (0.1pmol) and OxR (0.7 ± 0.1pmol), NADPH generating system (1mM $NADP^+$, 10mM glucose-6-phosphate, 2IU glucose-6-phosphate dehydrogenase, 5mM $MgCl_2$) and Eres (0.05-3.0μM) in phosphate buffer (0.1M, pH 7.4). Eres stock solutions were prepared in methanol such that the final concentration of solvent in incubations was <1%. Dilutions of the Eres stock solutions were confirmed by HPLC to ensure linearity; r^2 values were typically >0.999. Following a 5 min pre-incubation at 37ºC in a shaking water bath, reactions were initiated by the addition of NADPH generating system. Incubations were terminated after 10min by the addition of 0.2mL of methanol (4ºC) containing the internal standard, 4-methylumbelliferone (4-MU; 12mM; freshly prepared). Reaction mixtures were vortex mixed, cooled on ice for 10 min, centrifuged (5000x *g* for 10min at 4ºC), and an aliquot of the supernatant fraction (15μL) injected onto the HPLC column.

4.2.3.2 Measurement of resorufin formation

Res was separated on an Ultrasphere C18 column (250 x 4.6mm, 5μm; Beckman Coulter, Fullerton, CA, USA) which was eluted with 20mM phosphate buffer (pH 6.8)/methanol/acetonitrile (AcN) (50:40:10) containing 0.02% triethylamine (TEA) at a flow rate of 1.5mL/min. Res and 4-MU were monitored by fluorescence detection at excitation and emission wavelengths of 530 and 584nm, respectively. The respective retention times of Res and 4-MU were 1.9min and 2.9min. Unknown

concentrations of Res were determined by reference to a calibration curve constructed over the concentration range 0.01 to 0.2μM.

4.2.3.3 Measurement of 7-ethoxyresorufin binding by equilibrium dialysis

To identify the possibility of non-specific binding of Eres to protein in incubation mixtures, the binding of Eres to *E. coli* membranes was measured by equilibrium dialysis according to the method described by McLure, Miners and Birkett (2000). Equilibrium dialysis was performed in Teflon™ dialysis cells (Dianorm G. Maierhofer GmbH, München, Germany) divided into two compartments (A and B) with a 12.4 kDa cut-off dialysis cellulose membrane (Sigma Aldrich; cat. # D9652). One side of the dialysis cell was loaded with a solution of Eres (0.05-3μM) in phosphate buffer (1mL, 0.1M; pH 7.4) and dialyzed against co-expressed CYP1A1 (0.1pmol) with OxR (0.7 ± 0.1pmol) suspended in phosphate buffer (1mL, 0.1M; pH 7.4). The dialysis cell assembly was incubated at 37ºC in a rotating water bath (12 rpm) for 3hr. Each dialysis experiment had controls consisting of $Eres^{A}$/$buffer^{B}$ and Eres + $protein^{A}$/$buffer^{B}$ at the highest Eres concentration (3μM) to ensure equilibrium was attained. A 0.2mL aliquot was removed from both sides of the dialysis cell and the protein precipitated by the addition of 0.2mL of methanol (4ºC) (section 4.2.3.1). Dialysis samples were then vortex mixed, cooled on ice for 10min, centrifuged (5000x *g* for 10min at 4ºC), and an aliquot of the supernatant fraction (15μL) injected onto the HPLC column.

4.2.3.4 Estimation of kinetic parameters for 7-ethoxyresorufin metabolism

The rate of Res formation over a range of substrate concentrations (0.05-3.0μM) was measured under the initial rate conditions given in section 4.2.3.1. Kinetic constants (K_m, V_{max}, and K_{si}) for Res formation were derived from fitting either the Michaelis-Menten (MM) equation (eq 4.1) or the substrate inhibition (SI) equation (eq 4.2) to the experimental data. Goodness of fit was assessed from the F-statistic, 95% confidence intervals, r^2 value, and standard error of the parameter fit.

MM equation:

$$v = \frac{V_{max}[S]}{K_m + [S]} \tag{4.1}$$

where v is the rate of reaction (rate of metabolite formation), V_{max} is the maximal velocity, $[S]$ is the substrate concentration, and K_m is the Michaelis constant.

SI equation:

$$v = \frac{V_{max}}{1 + \left(\frac{K_m}{[S]}\right) + \left(\frac{[S]}{K_{si}}\right)} \tag{4.2}$$

where v is the rate of reaction (rate of metabolite formation), V_{max} is the maximal velocity, $[S]$ is the substrate concentration, and K_{si} is the constant describing the substrate inhibition interaction.

Statistical analysis (multivariate general linear model; Tukey *post hoc*) was undertaken using SPSS version 12.0.1 (SPSS Inc. Chicargo, USA). Values of $P<0.05$ were considered significant.

4.3 Results

4.3.1 Directed mutagenesis of the putative active-site residues

In order to validate the homology model of CYP1A1, a series of mutants were constructed with single amino acid substitutions at S122, F123, F224, A317, T321, and I386. S122, F123, and F224 were all substituted for alanine to truncate each corresponding side-chain beyond the C-β atom. A317 was substituted for tyrosine to sterically hinder the productive access of substrate to the CYP1A1 catalytic site, and T321 and I386 were substituted with glycine in order to remove the structural rigidity associated with C-β branching, thereby introducing flexibility in the main-chain around each residue. It should also be noted that the S122A and T321G substitutions resulted in decreased polarity at these positions, while the F123A and F224A mutations resulted in loss of aromaticity.

4.3.2 Heterologous expression of CYP1A1 wild-type and mutants

The CYP1A1 wild-type, and mutants S122A, F123A, F224A, A317Y, T321G and I386G, were individually co-expressed with OxR. The expression of holo-enzyme achieved in *E. coli* (≥4 experiments), estimated from the carbon monoxide difference spectrum, varied between wild-type CYP1A1 and each mutant. Mean expression of the wild-type CYP1A1 construct containing the 17α-leader sequence was 44.2pmol

P450/mg protein. Except for a 2-fold increase in holo-enzyme for F224A (81.8pmol P450/mg protein), expression of all mutants were similar to, or lower than, that obtained for the wild-type. The mean yield of F123A was 40pmol P450/mg protein, while yields of S122A, T321G, and I386G were 20.0, 10.2, and 17.0pmol P450/mg protein, respectively. No functional holo-enzyme was detected for the A317Y mutant. Levels of co-expressed OxR displayed relatively little variation between wild-type and mutant enzyme expressions, with a mean yield of 201 (±50)pmol reductase/mg protein (>20 experiments).

Despite differences in functional protein expression, western blotting showed that total P450 expression (holo- and apo-enzyme) was consistent (Figure 4.2). Interestingly, the CYP1A1 immuno-reactive band for the A317Y mutant was similar to that of the wild-type. This result confirms both the orientation and positional organization of the I-helix relative to the heme predicted by the CYP1A1 homology model. Residue 317 protrudes into the active-site above the parallel plane of the heme. The unfavored A317Y substitution results in loss of a productive substrate binding mode due to steric hindrance (Figure 4.3). Similarly, steric interactions between the A317Y mutant and the heme iron will impede competitive binding of lone pair electron donors (O_2 or CO), resulting in the absence of reduced holo-enzyme in the Fe^{2+}•CO vs Fe^{3+} difference spectra. Fe^{3+} product was detected at 417nm, indicating that heme was present yet potentially mis-incorporated in the nascent active-site.

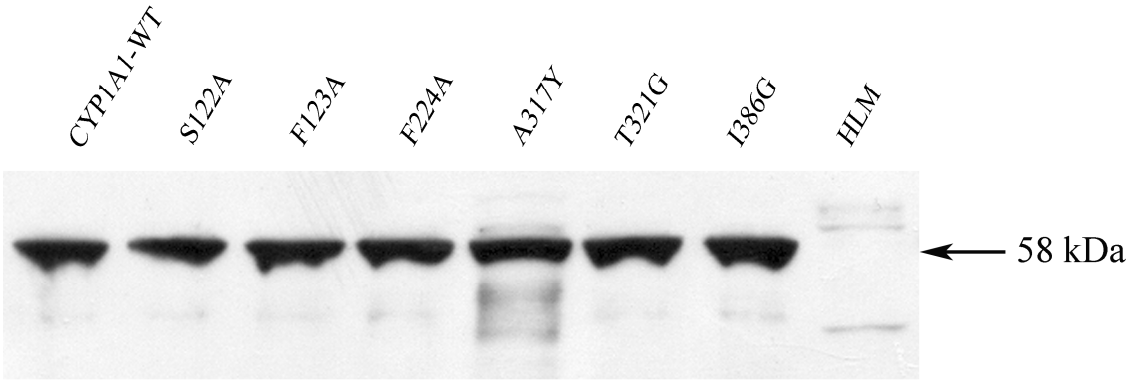

Figure 4.2 Immunoblot of wild-type and mutant CYP1A1 proteins showing relative total (holo + apo) expression. 25µg of the indicated membrane preparations were resolved by SDS-PAGE, blotted to nitrocellulose, and probed with anti-CYP1A1 antiserum. CYP1A1-WT (*lane 1*), CYP1A1-S122A (*lane 2*), CYP1A1-F123A (*lane 3*), CYP1A1-F224A (*lane 4*), CYP1A1-A317Y (*lane 5*), CYP1A1-T321G (*lane 6*), CYP1A1-I386G (*lane 7*), and human liver microsomes; negative control *(lane 8*). Immuno-reactive bands are present at 58kDa.

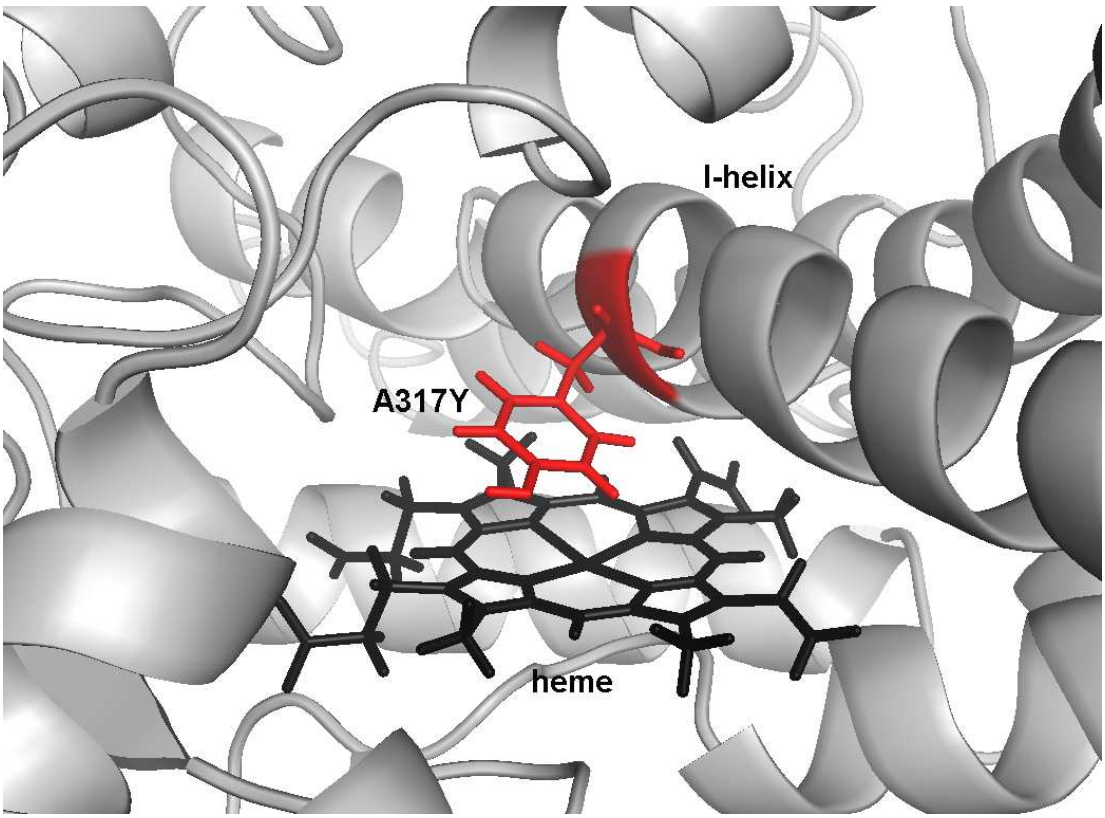

Figure 4.3 Steric hindrance arising from the A317Y mutation. The A317Y residue (red) blocks productive access of the substrate to the catalytic heme centre.

4.3.3 Assay optimization and reproducibility

Linearity of Res formation, with respect to incubation time and P450 protein concentration, was assessed using the wild-type CYP1A1 protein. Holo-enzyme concentration, determined by difference spectroscopy (section 2.2.4.5), and incubation time varied from 0.1-0.75pmol CYP1A1 and 5-40min, respectively. The linearity of Res formation was investigated at two substrate concentrations, 0.05 and 3.0μM. Res formation was linear to 0.75pmol CYP1A1 when the incubation time was held constant at 20min (Figure 4.4a). Similarly, EROD activity was linear for incubation times to 20min when CYP1A1 concentration was held constant (Figure 4.4b). Thus, the CYP1A1 concentration (0.1pmol) and incubation time (10min) utilized in incubations (section 4.2.3.1) ensured initial rate conditions, with substrate utilization < 20%.

Overall within day assay reproducibility was assessed by measuring Res formation in eight separate incubations of the same batch of expressed CYP1A1. Coefficients of variation were 6.1% and 3.8% for Eres concentrations of 0.05 and 3μM, respectively.

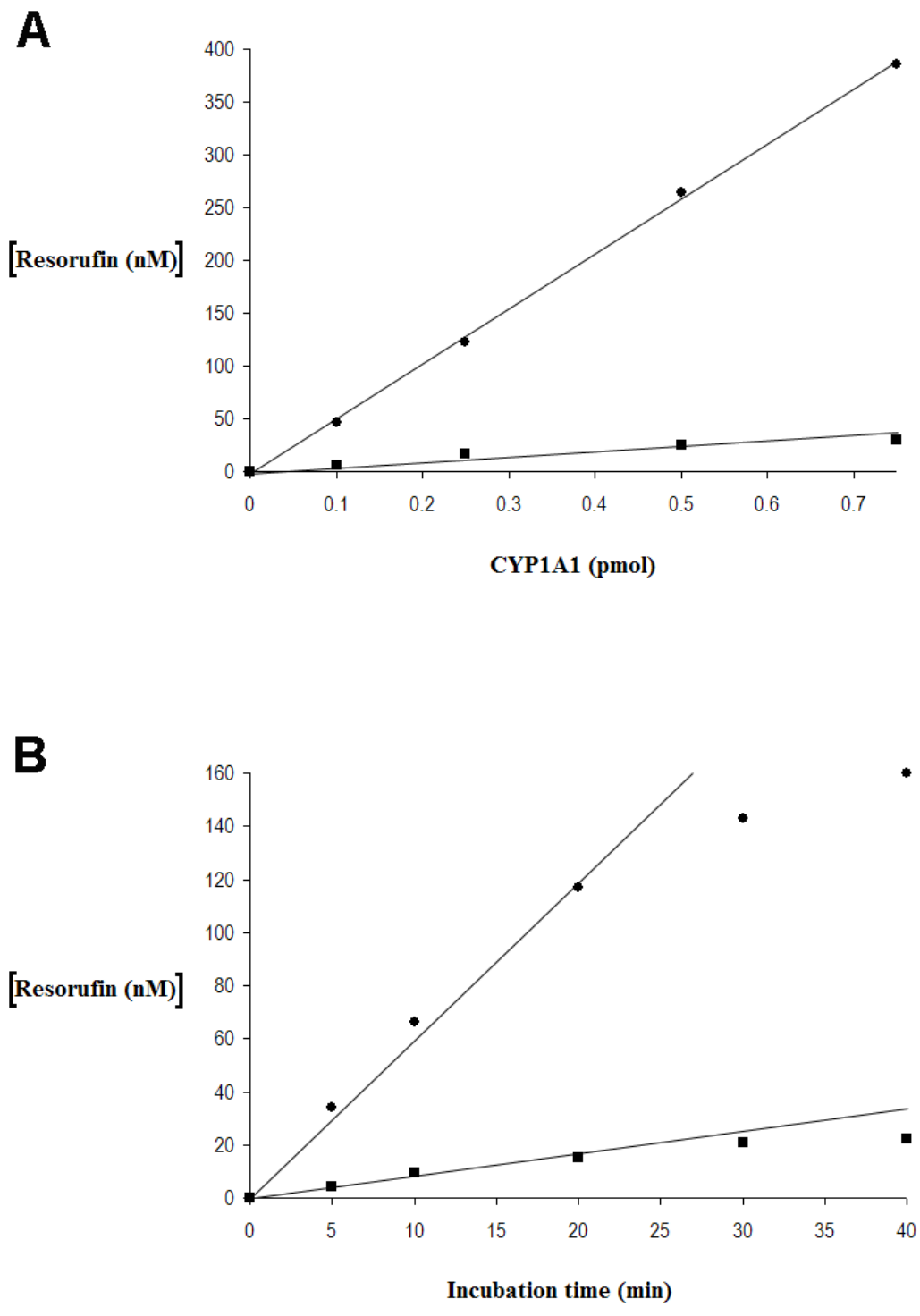

Figure 4.4 Time and protein linearity of EROD activity. Linearity with respect to (a) holo CYP1A1 content and (b) incubation time at substrate concentrations of 0.05µM (■) and 3µM (●).

4.3.4 Nonspecific binding of 7-ethoxyresorufin to *E. coli* membranes

The non-specific binding of Eres to *E. coli* membrane proteins was negligible at concentrations of 0.05μM (3.2%), 0.6μM (3.0%), and 3.0μM (0.65%). Correction of kinetic data for non-specific binding was not therefore required.

4.3.5 Effects of active-site mutations on CYP1A1 7-ethoxyresorufin O-deethylase activity

4.3.5.1 7-ethoxyresorufin O-deethylase in vitro kinetic parameters

The importance of selected residues for the activity of CYP1A1 was analyzed by deriving the kinetic parameters of both wild-type and mutant CYP1A1 proteins. The kinetic parameters obtained for EROD with wild-type and mutant CYP1A1 proteins are summarized in Table 4.3. Wild-type CYP1A1 and the S122A, F224A, and T321G mutants all catalyzed Eres *O*-deethylation. In contrast, the F123A, A317Y, and I386G mutants lacked activity. With the exception of T321G (Michaelis-Menten kinetics), the active mutants all exhibited kinetics characteristic of substrate inhibition and data were well modeled by the substrate inhibition equation (Figure 4.5). The kinetic parameters for Eres *O*-deethylation by wild-type CYP1A1 (V_{max} 28.6 ± 3.8pmol/min/pmol P450, K_m 0.51 ± 0.1μM) are in good agreement with literature reports, although previous studies have generally not acknowledged substrate inhibition (Chun et al. 1997; Guo et al. 1994; Liu et al. 2003). The S122A substitution produced a 2-fold increase in V_{max} (58 ± 11pmol/min/pmol P450) and a 74% increase in K_m (0.9 ± 0.2μM), resulting in no significant change in V_{max}/K_m ($P>0.05$). The F224A and T321G mutations both decreased V_{max} by an order of magnitude (2.5 ± 0.7; 3.0 ± 0.4pmol/min/pmol P450, respectively) compared to wild-

type CYP1A1, but differed in terms of effect on K_m; the F224A mutation decreased K_m by 75% (0.13 ± 0.01μM) whereas the T321G mutation had no significant effect on this parameter (K_m 0.67 ± 0.06μM; P = 0.458).

Table 4.3 Kinetic Parameters for EROD activity by wild-type and mutant CYP1A1[a].

Enzyme	V_{max}[a] (pmol/min/pmol P450)	Apparent K_m[a] (μM)	K_{si}	V_{max}/K_m (μl/min/pmol P450)
wild-type[b]	28.6 ± 3.8	0.51 ± 0.10	2.6 ± 0.5	56
S122A[b]	58 ± 11*	0.89 ± 0.22*	1.6 ± 0.2	65.1
F123A	na[d]	na	na	na
F224A[b]	2.5 ± 0.7*	0.13 ± 0.01*	3.8 ± 1.2	18.4*
A317Y	na	na	na	na
T321G[c]	3.0 ± 0.4*	0.67 ± 0.06	-	4.5*
I386G	na	na	na	na

[a]Apparent K_m, V_{max}, and K_{si} values are given as mean ± SD of four experiments. [b]Rate data for EROD activities were best fitted by the substrate inhibition model. [c]T321G was best fitted to the Michaelis-Menten equation. [d]Implies no detectable activity. *P<0.05 compared to the corresponding parameter for the wild-type CYP1A1.

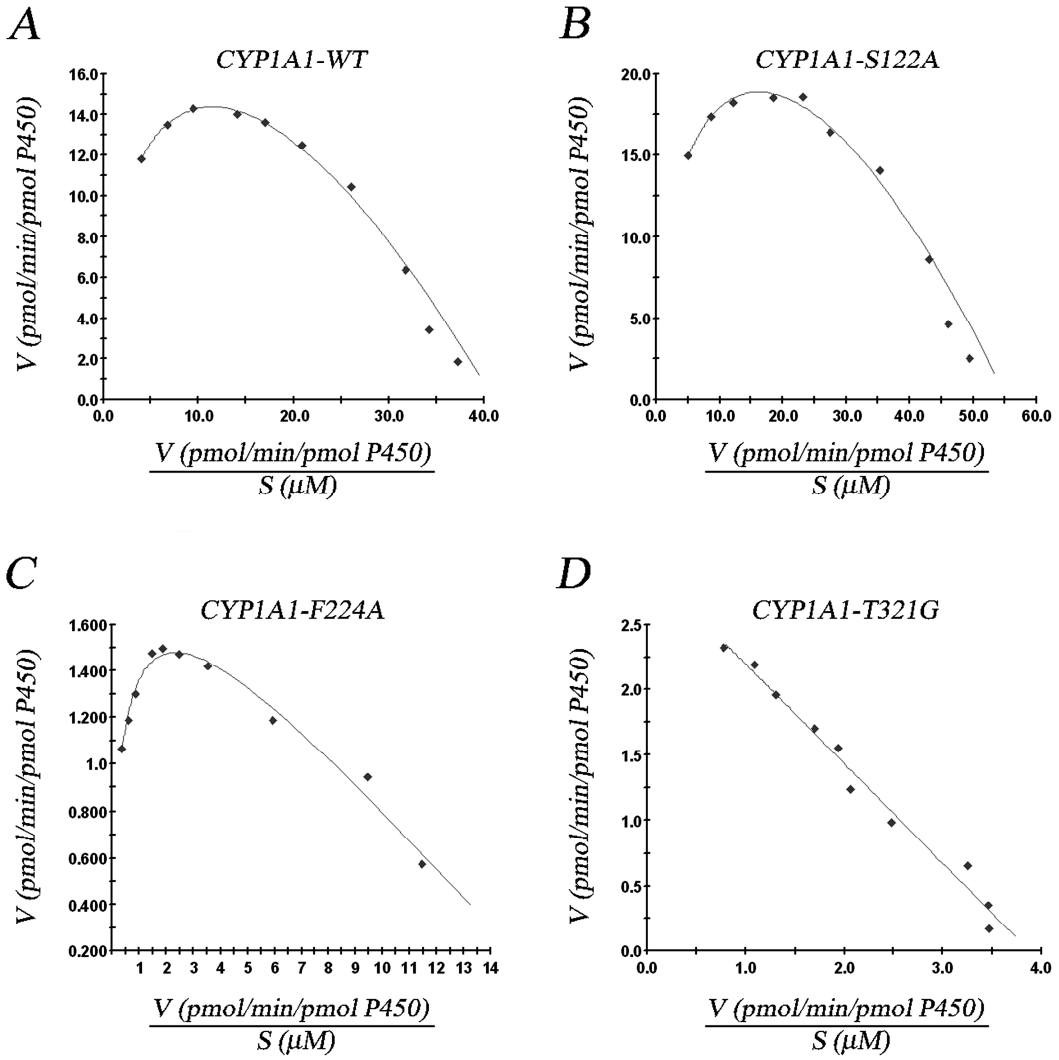

Figure 4.5 Eadie-Hofstee plots for EROD by (a) wild-type CYP1A1, (b) CYP1A1-S122A mutant, (c) CYP1A1-F224A mutant, and (d) CYP1A1-T321G mutant. Data points are the average of duplicate measurements. The solid lines represent data model-fitted using the non-linear curve fitting program EnzFitter (Biosoft, Cambridge, UK). Plots are representative of four separate experiments.

4.3.5.2 In silico enzyme-substrate interactions

Although substitution of S122 to an aliphatic alanine (S122A) eliminates the H-bonding interaction between CYP1A1 and Eres within the active-site (Figure 4.6b) loss of the polar interaction at S122 appears to invoke H-bonding of the phenoxazine carbonyl of Eres to Y259. Docking with the S122A mutant shows formation of an enhanced productive binding mode where the α-carbon adjacent to the ether oxygen of Eres resides at 3.9Å from the heme iron at an angle of 133.4º perpendicular to the planar heme. Structurally, the S122A mutation widens the CYP1A1 active-site cavity at SRS1, thereby marginally increasing the active-site volume compared to the wild-type (Figures 4.6a and b). In the F224A mutant, the SRS2 region of the active-site is substantially enlarged with H-bonding again seen from S122 to the oxazine ring oxygen of Eres (Figure 4.6c). The distance of the α-carbon adjacent to the ether oxygen of Eres was measured at 4.2Å from the heme iron at an angle of 117.3º perpendicular to the planar heme. Substitution of polar T321 to an aliphatic, non-polar glycine (T321G) removed the restricted secondary structure generated by β-branching of the threonine. The glycine introduced conformational flexibility in the I-helix, implementing a tighter turn at residue 321, therefore increasing the active-site volume at SRS4 (Figure 4.6d). Docking experiments conducted with the T321G mutant shows orientation of the productive binding mode with H-bonding at S122 to the oxazine ring oxygen of Eres (Figure 4.6d). The α-carbon adjacent to the ether oxygen of Eres was positioned 3.6Å from the heme iron at an angle of 117.8º perpendicular to the pyrrole nitrogen of the planar heme.

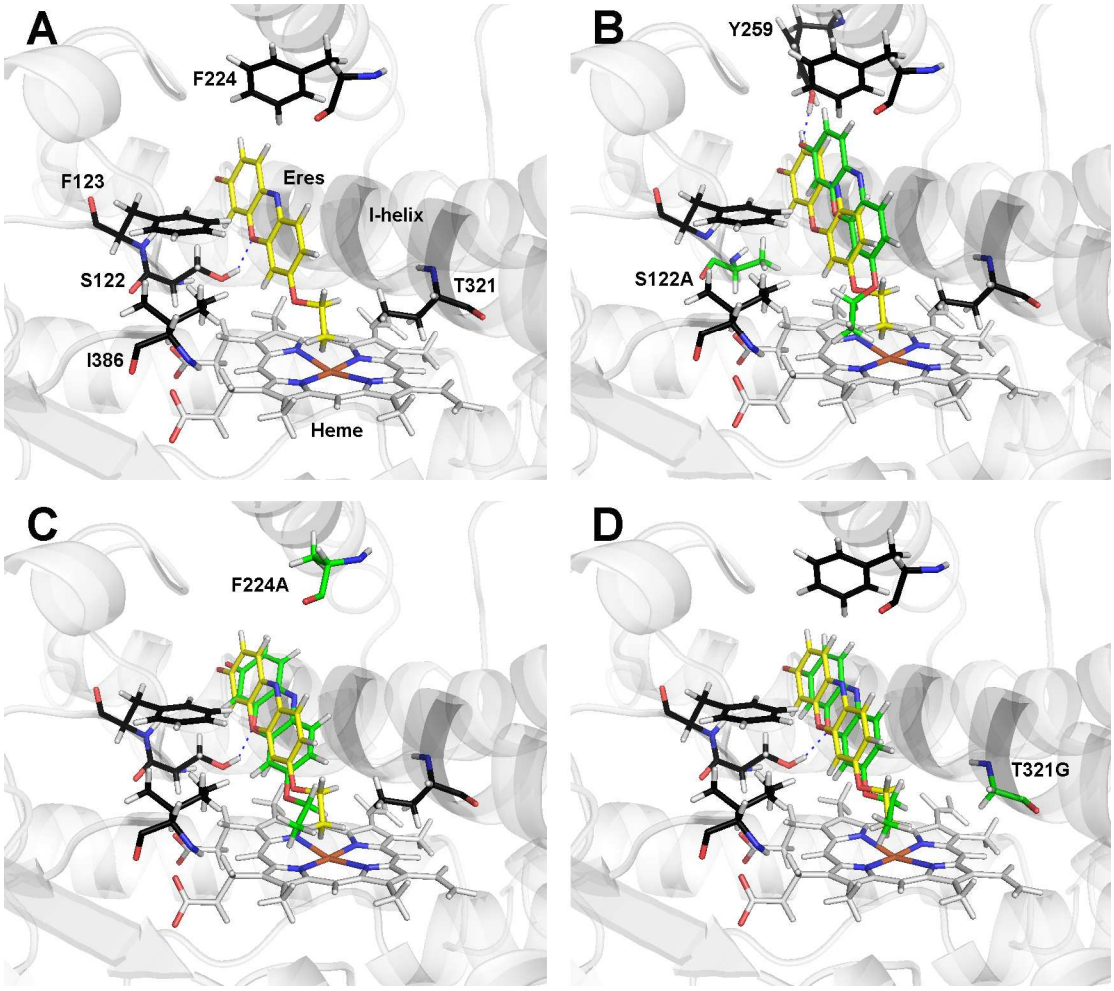

Figure 4.6 Enzyme-substrate interactions in wild-type and mutated CYP1A1 enzymes with EROD activity. (a) CYP1A1-WT, (b) CYP1A1-S122A, (c) CYP1A1-F224A, and (d) CYP1A1-T321G. Wild-type Eres pose (yellow); mutant residues and Eres pose (green).

4.3.6 Kinetic and structural analysis of 7-ethoxyresorufin *O*-deethylase activity

Kinetic data for Res formation by the wild-type, S122A, and F224A were best described by the substrate inhibition equation, whereas kinetic data for the T321G mutant were best fit by the Michaelis-Menten equation (Figure 4.5). The observed substrate inhibition is uncompetitive in form, since inhibition occurs at high substrate concentrations in the absence of a 'true inhibitor'.

Due to the small, longitudinal shape of the CYP1A1 active-site cavity, in conjunction with the electronically rich nature of Eres, it is unlikely inhibition occurs by simultaneous binding of two (or more) substrate molecules at different sub-sites (Figure 4.7). Indeed, attempted docking of a second substrate molecule within the CYP1A1 active-site proved unsuccessful. Thus, it would appear that substrate inhibition arises from the binding of a second substrate molecule outside of the active-site. Docking experiments showed that polar interactions within the substrate access channel, from T111, S230, and N232, provide potential binding sites for a second substrate molecule. Interestingly, *in silico* data revealed that unproductive binding of Eres in the CYP1A1 active-site may arise from substrate molecules adopting a 'reverse' binding orientation. The near symmetrical nature of Eres, along with product Res, allows 'reverse' binding to be energetically favorable. 'Reverse' binding is established by H-bonding of the ethoxy oxygen of Eres to the Y259 residue (Figure 4.8).

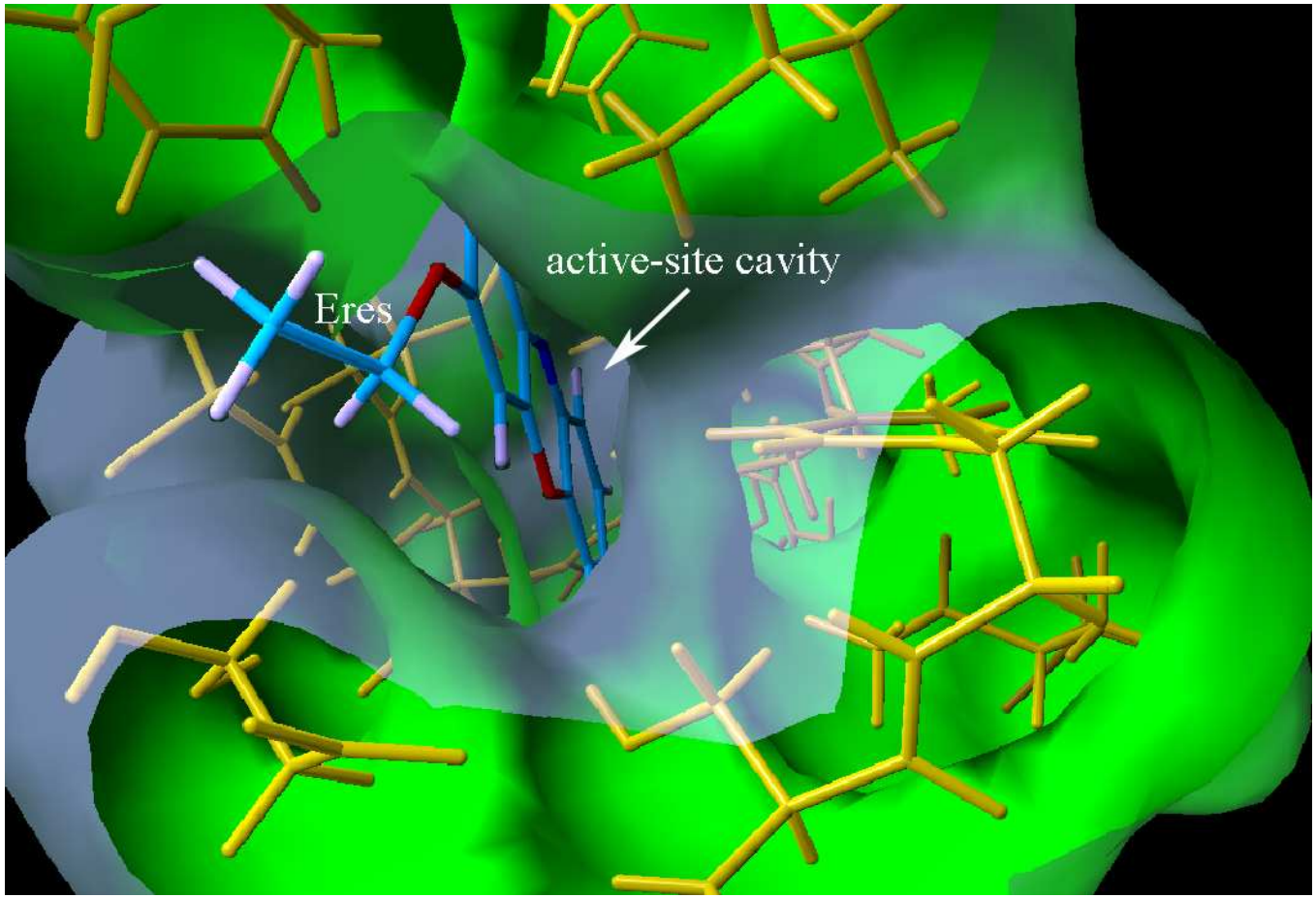

Figure 4.7 Space filling image of the CYP1A1 active-site cavity with docked Eres. The narrow shape of the active-site can only accommodate one substrate molecule.

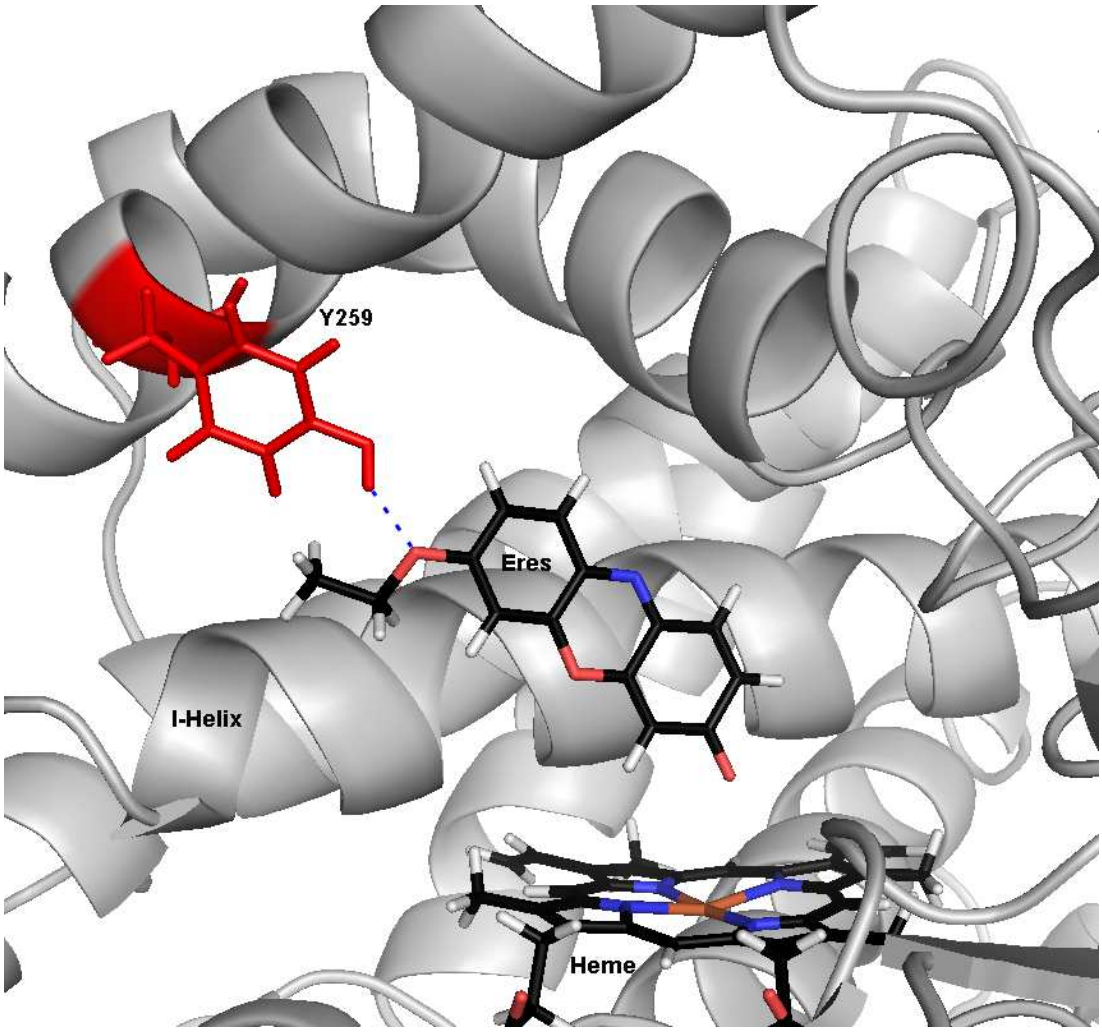

Figure 4.8 'Reverse' binding of Eres in the CYP1A1 active-site. The symmetrical nature of Eres, allows 'reverse' binding to be energetically favorable whereby H-bonding (blue dash) of the ethoxy oxygen occurs with Y259 (red).

A shift from substrate inhibition to Michaelis-Menten kinetics was observed for the T321G mutant (Table 4.3). Of the total number of docking poses returned for each enzyme, the T321G mutant exhibited <5% of substrate molecules in the 'reverse' orientation. Enzymes which exhibited substrate inhibition identified on average 38.8% of substrate molecules in the 'reverse' orientation with the wild-type, S122A,

and F224A enzymes highly ranking the reversely bound Eres molecule (i.e. within the top three poses). The mechanistic implications of these observations are unclear.

4.4 Discussion

Automated *in silico* docking identified S122, F123, F224, A317, T321, and I386 as key residues involved in the orientation and stabilization of Eres within the CYP1A1 active-site cavity. These residues are representative of SRS 1, 2, 4, and 5 (Table 3.6; section 3.3.7) and were targeted for structure-activity analyses. In conjunction with the *in silico* data, each residue within the subset was substituted with different amino acids in an attempt to identify the structural and physicochemical properties responsible for EROD activity. The altered EROD activity of each mutant was then compared to that of wild-type CYP1A1 in an attempt to identify structure-activity relationships.

The F123A, A317Y, and I386G mutants exhibited a complete lack of EROD activity (Table 4.3) despite displaying expression levels of apo- and holo-enzyme comparable to that of the wild-type (Figure 4.2). This result was expected with the A317Y mutant due to the steric bulkiness of the tyrosine residue protruding into the active-site cavity (Figure 4.3), therefore hindering productive access of Eres to the heme iron. Likewise, the lack of EROD activity with the I386G mutant was expected as a result of increasing conformational flexibility of the K-helix/β2-3 loop in addition to altering the electrostatic environment about the heme prosthetic group. Moreover, solvent effects and perturbation of the substrate access-channel may affect the activity of this mutant. However, the complete loss of activity observed with the F123A mutant was unexpected. On closer inspection, the geometrically preferred

interactions between Eres and aromatic residues within the CYP1A1 active-site identified π-σ orbital attractions between the edge-face orientation of F123 and the oxazine ring of Eres. The π-σ attraction was clearly favored over the marginally less energetically favorable repulsion of π-π face stacking electronic interactions (Hunter & Sanders 1990), which could quite easily arise in the highly aromatic CYP1A1 active-site.

The phenylalanine positioned at residue 224 is influenced by parallel displaced π-σ attractive forces and is part of a closely packed triad of aromatic residues (F224, F258, and Y259) forming, in part, the ceiling of the CYP1A1 active-site (Figure 4.1b). These aromatic groups clearly aid the alignment of planar aromatic substrates via electrostatic and orbital interactions. Loss of the aromaticity associated with the F224A mutant was not sufficient to completely abolish EROD activity and highlights the contributions of other aromatic interactions provided from F258 and Y259. Substitution of F224 to alanine not only removed the aromaticity but additionally introduced a greater spatial void for Eres to orientate for productive catalysis. Thus, despite an almost 4-fold increase in the apparent binding affinity for the F224A mutant (reflected by K_m), a significant reduction in EROD activity (V_{max}) resulted due to less than optimal substrate alignment over the heme catalytic site (Table 4.3).

Based on docking experiments, the significant loss in EROD activity observed with the T321G mutant was not caused by misalignment of the substrate (Figure 4.6d) and is reflected in the binding affinity (measured as K_m) being comparable to that of the wild-type enzyme (Table 4.3). The decrease in V_{max}/K_m by the T321G mutant arises from the almost 10-fold decrease in V_{max} and is most likely due to the disruption of either the axial water, positioned above the heme, or the water bound in the I-helix at the so-called ‘proton transfer groove’. The water molecules in question are well

documented throughout the crystallographic literature (Chun et al. 1997; Ogliaro, de Visser & Shaik 2002; Williams et al. 2003) and are known to mediate proton transport during catalysis via interactions at the highly conserved threonine positioned at T321 in CYP1A1 (Haines et al. 2001; Manna & Mazumdar 2006; Meunier, de Visser & Shaik 2004; Otyepka et al. 2007; Shaik et al. 2005; Williams et al. 2000a). The axial water molecule, which usually acts as the sixth coordination site of the octahedral heme Fe and is positioned between the substrate and iron, is potentially displaced in the T321G mutant. Moreover, disruption to the I-helix architecture in the CYP1A1 model suggests that the water bound in the proton transfer groove is the main cause of decreased EROD activity by the T321G mutant. The T321G mutation further indicates that solvent interactions occur in the CYP1A1 active-site and are important in productive EROD activity.

Most surprising was the doubling of the V_{max} (relative to wild-type) observed with the S122A mutant (Table 4.3). Since numerous variables are responsible for conferring catalytic activity (e.g. substrate access, substrate orientation, enzyme-substrate affinity, etc.), it is usually easier to disrupt substrate turnover via mutagenesis than it is to enhance it. Removal of the well documented S122 polar interaction (Otyepka et al. 2007; Schleinkofer et al. 2005; Szklarz & Paulsen 2002) with the S122A mutant was initially undertaken in an attempt to introduce 'sloppiness' in the CYP1A1 active-site, with increased K_m and decreased substrate turnover due to a less favored substrate orientation. In actual fact, the *in vitro* data disprove the notion that the interaction with S122 is essential for binding and aligning Eres for optimal catalytic turnover. The loss of H-bonding of the oxazine ring oxygen of Eres in the S122A mutant (Figure 4.6b) invoked a more productive binding orientation with H-bonding of the phenoxazine carbonyl of Eres to the Y259

residue occurs. Docking data obtained with the S122A mutant revealed the angle of the catalytic α-carbon had increased to 133.4º compared to that of the wild-type (106.4º). Reorientation of the substrate in this manner may facilitate product egress without perturbing the productive catalytic position of the ethoxy substituent.

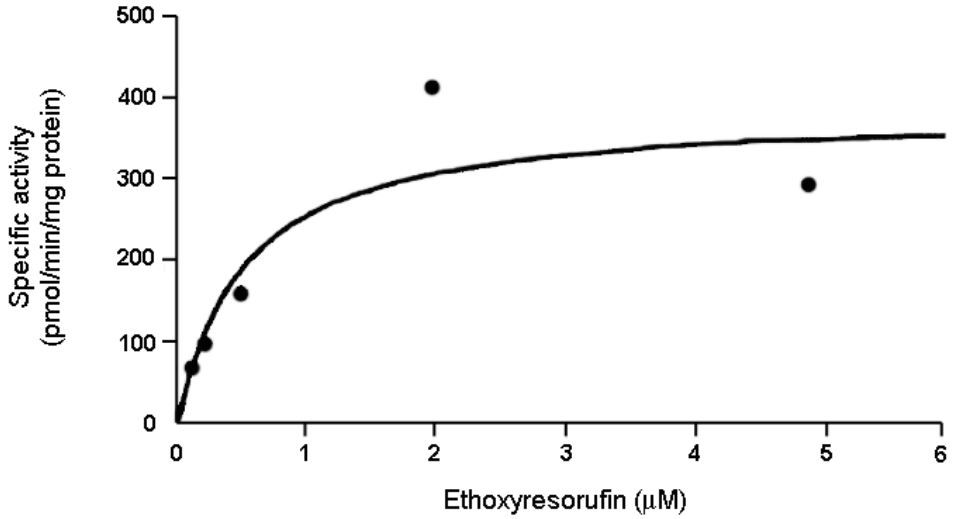

Figure 4.9 Typical Michaelis-Menten plot published for the metabolism of Eres by recombinant CYP1A1. Taken from (Chun et al. 1997).

Most P450 catalyzed reactions are adequately described by the Michaelis-Menten equation, as were data obtained for the T321G mutant (Figure 4.5d). However, kinetic analysis of EROD activity undertaken on the wild-type, S122A, and F224A CYP1A1 proteins clearly identified substrate inhibition as the preferred kinetic model (Figures 4.5a, b, and c). All previous reports of Res formation by CYP1A1 indicate Michaelis-Menten kinetics. However, inspections of published kinetic plots clearly display characteristics *suggestive* of substrate inhibition (Figure 4.9) (Chun et al. 1997). It should be noted that the occurrence of hyperbolic curves forced through

non Michaelis-Menten kinetic data is not uncommon in the literature. In other cases the paucity of data points precludes any meaningful selection of an alternative model (Houston & Kenworthy 2000). The substrate inhibition data observed with CYP1A1 draws parallels with data published by Lin et al. (2001) for Eres *O*-deethylation by CYP1A2. The authors propose that substrate inhibition in most cases behaves as partial inhibition, since inhibition does not approach zero even at very high substrate concentrations. The kinetic model for substrate inhibition (Figure 4.10) shows formation of an unproductive SES inhibitory complex due to the binding of a second substrate molecule to a second binding site. However, not all proteins allow multiple ligands to bind in a single active-site that promotes direct hydrophobic interactions, electrostatic effects, or H-bonding between each ligand (Atkins 2005). In an attempt to identify a second substrate binding site in CYP1A1, experiments were conducted where an Eres molecule was docked in the active-site cavity of CYP1A1 (in the productive binding orientation) and docking of a second Eres molecule was attempted. The simultaneous binding of two Eres molecules was not possible, which is not surprising considering the narrow, longitudinal shape of the CYP1A1 active-site cavity (Figure 4.7). However, polar interactions within the substrate access channel from T111, S230, and N232 were identified as potential Eres binding sites which may be invoked in the reduction of substrate turnover at high concentrations. Based on further *in silico* data, the energetically favorable 'reverse' orientation of Eres (Figure 4.8) warrants comment. In this case, formation of the unproductive substrate binding orientation appears plausible due to the symmetrical nature of Eres. The concept of symmetrical substrates binding in a 'reverse' orientation is not novel with shifts in regioselectivity observed in the glucuronidation of many hydroxysteroids (Bowalgaha et al. 2007; Jin, Mackenzie & Miners 1997).

Additionally, the more highly symmetrical product generated by CYP1A1 mediated *O*-deethylation of Eres, Res, may behave as a reversible inhibitor when present in the reaction mixture, thus further complicating the elucidation of a single mechanism for the observed substrate inhibition.

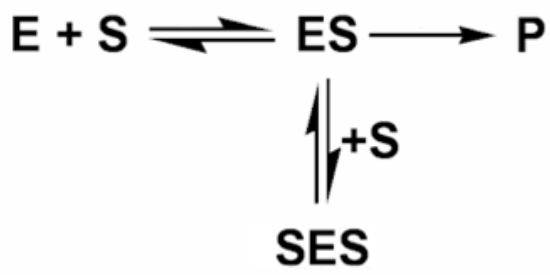

Figure 4.10 Mechanism that produces substrate inhibition. Binding of a second substrate molecule to the enzyme-substrate (ES) complex forms the unproductive SES inhibitory complex. Modified from (Cornish-Bowden 2004).

In summary, the predictivity of the CYP1A1 computational model generated in Chapter 3 was confirmed using directed mutagenesis to identify the active-site residues responsible for the orientation and stabilization of Eres during productive catalysis. The validation of the structural organization of CYP1A1 has contributed to the understanding of Eres structure-activity relationships. The complete loss of EROD activity observed with the F123A mutant highlights the importance of aromatic interactions over hydrogen bonding from Ser122. Additionally, many P450 catalyzed reactions are adequately described by single enzyme Michaelis-Menten kinetics. However, kinetic analysis of the EROD activity of the wild-type, S122A, and F224A CYP1A1 proteins clearly identified substrate inhibition as the preferred kinetic model.

CHAPTER 5
ENHANCED ACTIVATION OF THE CHEMOTHERAPEUTIC AGENT DACARBAZINE

5.1 Introduction

Dacarbazine (5-(3,3-dimethyltriazen-1-yl)-1-imidazole-4-carboxamide; DTIC; NSC-45388) is a triazene derivative of 5-diazoimidazole-4-carboxamide (NSC-22420), an intermediate compound made during the transformation of 5-amino-1-imidazole-4-carboxamide hydrochloride (AIC; NSC-113496) into 8-azahypoxanthine (NSC-22709) (Figure 5.1) (Luce et al. 1970). DTIC was first synthesized by (Shealy et al. 1961) and was investigated as a possible antitumor agent due to its increased stability in solution compared to the lead antitumor agent 5-diazoimidazole-4-carboxamide (Carter & Friedman 1972), which had shown activity against numerous carcinomas.

During initial toxicological studies in dogs and monkeys, DTIC produced myelosuppression, lymphoid depletion, and hepatic and renal toxicity. As in dogs and monkeys, the major adverse effect of DTIC in humans is myelosuppression. Anemia also occurs in almost all patients but can be mild. Leukopenia and thrombocytopenia occurs in 65-80% of all patients, and bone marrow biopsies show a decrease in cellularity in patients with cytopenia. No change in DTIC tolerance is observed throughout treatment.

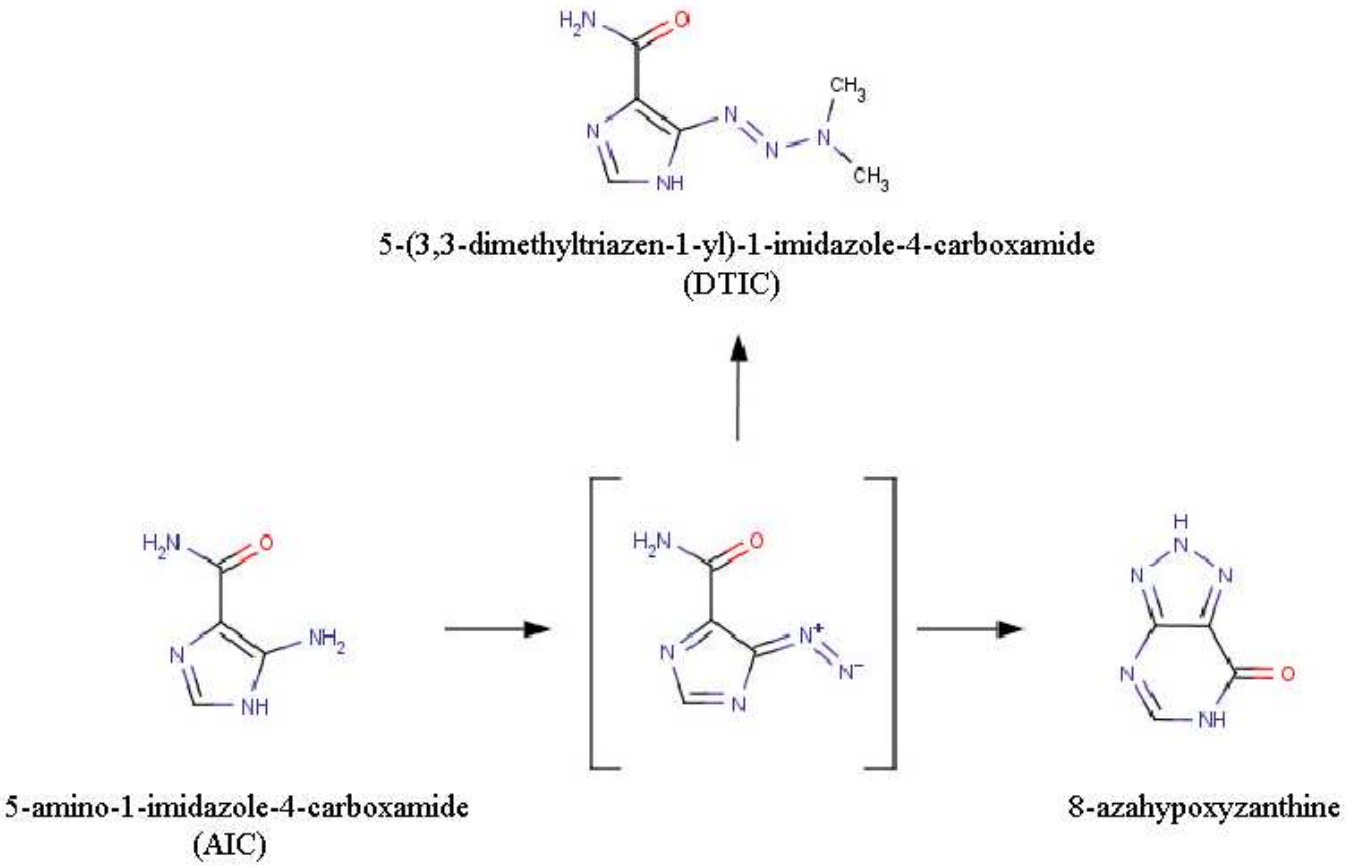

Figure 5.1 The chemical synthesis of DTIC. DTIC is a derivative of the intermediate product generated in the transformation of 5-amino-1-imidazole-4-carboxamide (AIC) to 8-azahypoxyzanthine.

DTIC produces a considerable response in both solid tumors and leukemias in rodent models. However, DTIC activity in humans is modest primarily due to the lower activity of P450 enzymes responsible for its activation compared to that observed in rodents (Reid et al. 1999). Thus, in humans, DTIC is essentially restricted to intracranial carcinoma, malignant melanoma, neuroblastoma, soft tissue sarcoma, Hodgkin's disease, and neuroendocrine tumors (Baxter 2004). DTIC is typically used in a curative regimen with other chemotherapeutic agents for the majority of malignancies, however it is the most effective single agent for the treatment of malignant melanoma. DTIC produces a reasonable antitumor response in patients with melanoma (~19%) (Luce et al. 1970), but mortality is significantly higher in male patients over the age of 65 years (Linos et al. 2009). Treatment of Stage-I melanoma has a good prognosis, although five year survival rates in patients with stage-IV disease remains poor at only 5-10%, with biotherapies and chemotherapies resulting in response rates of ~10%. During the past twenty years, all phase-III clinical trials in metastatic melanoma including biotherapy and chemotherapy, immunotherapy, and innovative drugs, have failed to show improved responses compared to DTIC (Erdmann 2010).

DTIC requires metabolic activation in order to become cytotoxic. When converted to its active metabolite, DTIC induces apoptosis and mutagenicity via the formation of *O*-alkylguanine-DNA adducts (Figure 5.2). The main metabolic pathway involves α-hydroxylation of one of the *N*-methyl residues by P450 enzymes to form the reactive *N*-demethylated species, 5-(3-hydroxy-methyl-3-methyl-triazen-1-yl)-imidazole-4-carboxamide (HMMTIC). This metabolite is chemically unstable, losing formaldehyde to generate 5-(3-methyl-triazen-1-yl)-imidazole-4-carboxamide (MTIC) (Rooseboom, Commandeur & Vermeulen 2004; Sanada et al. 2004). Rapid

decomposition of MTIC yields the major plasma and urine metabolite 5-aminoimidazole-4-carboxamide (AIC) and the reactive species methane diazohydroxide, which produces molecular nitrogen and a methyl cation believed to be the DNA-alkylating species (Meer et al. 1986).

N-Demethylation of DTIC is monitored by the formation of AIC, the decomposition product of the initial oxidative metabolite HMMTIC (Figure 5.2). P450-dependant *N*-demethylation of DTIC, giving rise to the formation of AIC, is confirmed by observations *in vitro*: (i) AIC formation is dependant on the presence of the P450 generating system and (ii) AIC formation does not occur in incubation mixtures excluding P450 enzyme.

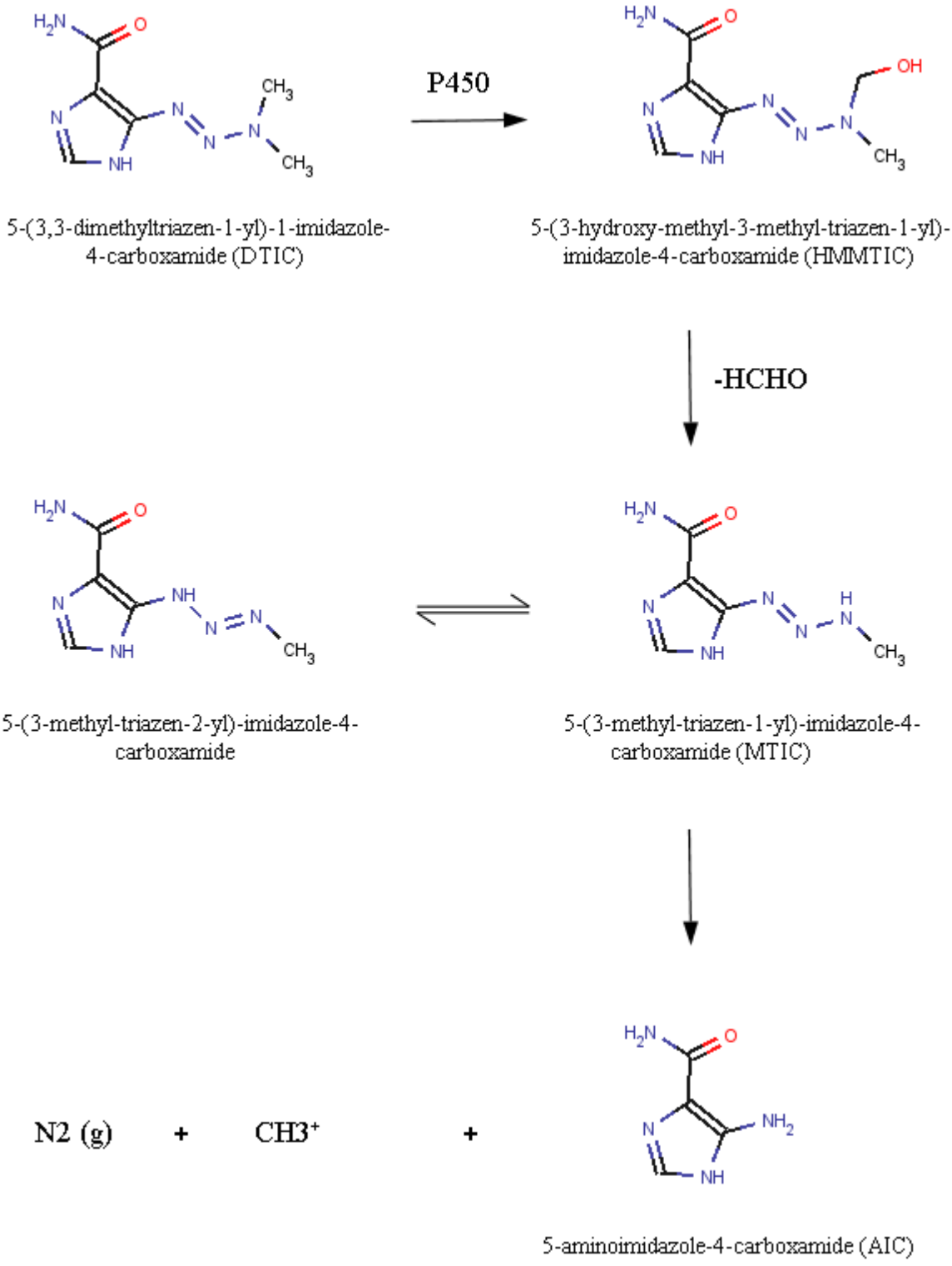

Figure 5.2 Pathways of dacarbazine (DTIC) metabolism. Taken from Reid *et al.* (1999).

The only study to specifically investigate the role of CYP1A1 in DTIC activation was conducted by Reid et al. (1999). The authors report that the DTIC *N*-demethylation pathway leading to MTIC formation was primarily catalyzed by CYP1A1, CYP1A2, and CYP2E1. The most potent inhibitors of the *N*-demethylation of DITC were α-naphthoflavone (CYP1A1 and CYP1A2), chlorzoxazone (CYP2E1 and possibly other P450's), and disulfiram (predominantly CYP2E1). Concentration-dependant inhibition by chlorzoxazone and disulfiram was observed over the range of 20-200μM, whereas inhibition by α-naphthoflavone was essentially complete (>85%) at concentrations above 0.2μM, indicating a predominant role for the CYP1A enzymes. Consistent with the predominant role of CYP1A enzymes, DTIC *N*-demethylation activity correlated significantly with phenacetin *O*-deethylase and caffeine *N*3-demethylase activity in microsomes from a panel of human livers. In contrast, the correlation between DTIC *N*-demethylation and the CYP2E1 marker, chlorzoxazone 7-hydroxylation, was not significant. DTIC metabolism (200-2000μM) by recombinant human CYP1A1 and CYP1A2 gave respective K_m (V_{max}) values of 595μM (0.684nmol/min/mg protein) and 659μM (1.74nmol/min/mg protein). Analysis of the CYP2E1 kinetic data over the same concentration range suggested a K_m value greater than 2.8mM. Higher concentrations of DTIC were not examined by Reid *et al* (1999) due to the limited aqueous solubility of DTIC. Human CYP2C9, CYP2C19, CYP2D6, and CYP3A4 did not demethylate DTIC (Reid et al. 1999).

Efforts to improve DTIC activation have focused on the development of chemical analogues that improve the delivery of the methylating metabolites responsible for DNA alkylation. For example, the recent clinical development of temozolomide (Figure 5.3), an analogue of DTIC, was based on the assumption that greater

exposure to MTIC could be achieved by the chemical hydrolysis of temozolomide at physiological pH, rather than by the hepatic/extra-hepatic metabolism associated with DTIC (Stevens et al. 1987). The disadvantage of such a mechanism is highlighted by the non-specific activation of temozolomide. The activated metabolite requires transfer to the tumor site via the circulatory system, resulting in systemic exposure to the cytotoxic metabolites. Containment of the cytotoxic metabolites in the tumor environment would clearly reduce the adverse effects experienced during conventional chemotherapy with DTIC.

Figure 5.3 Structure of temozolomide.

The gene directed enzyme prodrug therapy (GDEPT) approach, introduced in section 1.4.2, is currently being utilized in two clinical trials for the treatment of cancer. Oxford BioMedica are developing an approach using a direct Moloney murine leukaemia virus (MLV)-based vector for gene delivery of human CYP2B6, termed MetXia, in combination with orally administered cyclophosphamide for the treatment of solid tumors (Kan et al. 2001). In addition, the Bavarian Nordic Research Institute in Germany is currently conducting clinical trials using encapsulated allogenic cells expressing rat CYP2B1 in cellulose sulfate capsules

followed by treatment with ifosfamide in patients with inoperable (stage III-IV) pancreatic adenocarcinomas (Lohr et al. 2001). Although the results from preclinical trials are encouraging with respect to the vectors and promoters utilized for gene expression, improvements in the efficiency of the therapeutic enzymes are required. Only a handful of P450-based GDEPT strategies using human enzymes have been published (Table 5.1). Interestingly, none of these studies utilize therapeutic P450's with improved or enhanced prodrug activation. Furthermore, only a handful of studies have incorporated the co-expression of the P450 redox partner, cytochrome P450 oxidoreductase. There are, however, a number of publications which have increased the catalytic efficiency of certain P450 enzymes with the aim to improve the performance of P450-based GDEPT (Chen et al. 2004; Jounaidi et al. 2006; Kumar et al. 2005; Nguyen et al. 2008). Notably, no studies with CYP1A1 or DTIC have been performed.

Table 5.1 P450-based GDEPT strategies using human therapeutic enzymes.

Human P450	Prodrug	Reference
CYP1A2	Paracetamol	Thatcher et al. (2000)
CYP2B6	Cyclophosphamide/ ifosphamide	Jounaidi & Waxman (2000, 2001); Kan et al. (2001); Schwartz & Waxman (2001)
CYP2C8	Cyclophosphamide/ ifosphamide	Jounaidi, Hecht & Waxman (1998)
CYP2C9	Cyclophosphamide/ ifosphamide	Jounaidi, Hecht & Waxman (1998); Zhou et al. (2000)
CYP2C18	Cyclophosphamide/ ifosphamide	Jounaidi, Hecht & Waxman (1998)
CYP2C19	Cyclophosphamide/ ifosphamide	Jounaidi, Hecht & Waxman (1998)
CYP3A4	Cyclophosphamide/ ifosphamide	Jounaidi, Hecht & Waxman (1998)

GDEPT potentially provides a clinically effective approach to cancer therapy using P450's for prodrug activation (El-Aneed 2004; Johannes et al. 2006; Kan, Kingsman & Naylor 2002; McFadyen, Melvin & Murray 2004; Scripture, Sparreboom & Figg 2005). However, since this approach requires the systemic administration of the prodrug, P450-based GDEPT would appear most effective when catalytic efficiency is high. Therefore, the general aim of this chapter was to structurally modify the human CYP1A1 enzyme to increase its catalytic efficiency (V_{max}/K_m) for *N*-demethylation and subsequent activation of DTIC.

Specific aims were to:

1. Conduct *in silico* docking experiments to identify the critical amino acid residues involved in the binding and orientation of DTIC within the CYP1A1 active-site.
2. Use directed mutagenesis to confirm the active-site residues involved in the binding and orientation of DTIC within the CYP1A1 active-site.
3. Use the data obtained in (2) to generate mutants with altered DTIC intrinsic clearance.
4. Heterologously co-express high yields of mutant CYP1A1 proteins with OxR in *E. coli*.
5. Characterize the kinetic parameters for DTIC *N*-demethylation by wild-type and mutant CYP1A1 proteins, and CYP1A2.
6. Identify the structure-function relationships responsible for the enhanced activation of DTIC by mutant CYP1A1 enzymes.

5.2 Materials and methods

5.2.1 Model generation

Homology models containing mutations were built using the wild-type CYP1A1 homology model generated in Chapter 3 as the template (section 3.3.4). Targeted residues were mutated *in silico,* incorporating the desired amino acid. Each substituted residue was energy minimized as a subset of the entire protein molecule using the Powell conjugate gradient method with an energy cutoff set to 0.05kcal/mol.Å. A 'hot region' of 6Å surrounding the substituted residue was

established where the side-chains of all residues were allowed to be minimized. A further 'intermediate region' of 12Å was generated to set the minimization environment without side-chain movement. Minimization by this method allows changes in the energetic forces felt by residues that either adjoin or neighbor the substituted amino acid.

5.2.2 Automated substrate docking

Automated docking of DTIC utilized the wild-type CYP1A1 homology model generated in Chapter 3 along with all mutant protein models (section 5.2.1). Docking was achieved using the FlexX docking suite (SYBYL7.3, Tripos™; section 3.2.6). Docking of the ligand was consensus scored (CScore) based on its interactions with the protein and the key residues involved in binding and orientation of DTIC in the protein active-site.

5.2.3 Targeted mutagenesis

5.2.3.1 Identification of DTIC-binding residues for mutagenesis

Active-site residues involved in the binding and orientation of DTIC were targeted based on their proximity to the docked DTIC molecule generated *in silico*. Residues within a 3Å radius whose side-chain chemistry interacted with the docked substrate were considered for mutagenesis. In addition, residues thought to affect the electrostatic environment surrounding the heme, the reductase binding domain, sites of genetic polymorphism, and residues potentially involved in the metabolism of heterocyclic amines in rat CYP1A1, were targeted. All substitutions were guided by

consideration of the importance of the side-chain functional group(s) and how they contribute to substrate alignment, orientation, and enzyme function.

5.2.3.2 Generation of CYP1A1 mutants

The wild-type 17α-CYP1A1 cDNA in pBluescript-II-SK(+) was used as the template for mutagenesis, as described in section 4.2.1.2. Primers employed for generating 29 CYP1A1 mutants are shown in Table 5.2, while mutagenesis PCR conditions and cycling parameters are described in sections 2.2.3.3 and 2.2.3.4, respectively. All mutations were confirmed by DNA sequencing on both strands (ABI 3130-XL DNA sequencer, Applied Biosystems, Victoria, Australia).

5.2.3.3 Construction of the CYP1A2 expression plasmid

Analogous to CYP1A1, the N-terminal membrane anchor of wild-type CYP1A2 cDNA (accession NM_000761) was replaced with a modified sequence derived from bovine CYP17A. Generation of the 17α-hydroxylase leader sequence in CYP1A2 followed the method described by (Polasek et al. 2006). Briefly, polymerase chain reaction (PCR)-directed mutagenesis was used to delete codons 3-10 using the following primers: Sense, 5 TA**CATATG**GCTCTGTTATTAGCAGTTTTT CTGTTCTGCCTGGTATTCTGGGTGC-3; antisense, 5 AT**AAGCTT**TCAATT GATGGAGAAGCGCCGC-3. To facilitate directional ligation into the pCW ori(+) expression plasmid, *NdeI* and *HindIII* restriction sites (bold text) were incorporated into the sense and antisense CYP1A2 oligonucleotides, respectively. The 1515-bp 17α-CYP1A2 PCR products were digested with *NdeI* and *HindIII* prior to ligation. The pCW 17α-CYP1A2 construct was transformed into DH5α *E. coli* cells (section

2.2.2.3) and colonies screened for the desired insert by restriction enzyme analysis (sections 2.2.2.5 and 2.2.2.6). The 17α-CYP1A2 DNA sequence was confirmed on both strands (ABI 3130-XL DNA sequencer; Applied Biosystems, Victoria, Australia).

Table 5.2 Primers used for site-directed mutagenesis [a,b,c].

CYP1A1 Mutant	Primer Overlap (5' forward to 5' reverse)	ΔG^{o} of Heterodimerization (kcal/mol)
S116A	5'CCCTCATC**GC**TAATGGTCAGAGCATGTCC 3'	-34.98
	3'GTGGAAGTGGGAGTAG**CG**ATTACCAG 5'	
S122T	5'CAGAGCATG**A**CCTTCAGCCCAGACTCTGG 3'	-33.04
	3'GTCATTACCAGTCTCGTAC**T**GGAAGTCG 5'	
E161K	5'CCTCAACCTCCTGCTACCTGGAA**A**AGCATGTGAGCAAGGAGG 3'	-83.02
	3'GGAGTTGGAGGACGATGGACCTT**T**TCGTACACTCGTTCCTCC 5'	
E166Q	5'GGAAGAGCATGTGAGCAAG**C**AGGCTGAGGTCCTGATAAGC 3'	-77.91
	3'CCTTCTCGTACACTCGTTC**G**TCCGACTCCAGGACTATTCG 5'	
V191M	5'CTTTAACCCCTACAGGTATGTG**A**TGGTATCAGTGACCAATG 3'	-72.08
	3'GAAATTGGGGATGTCCATACAC**T**ACCATAGTCACTGGTTAC 5'	
N223E	5'CCTGAATAAT**G**A**G**TTCGGGGAGGTGGTTGGC 3'	-38.8
	3'CGGATCAGTTGGACTTATTA**C**T**C**AAGCCCC 5'	
V228T	5'GGGAGGTG**AC**TGGCTCTGGAAACCCAGC 3'	-35.08
	3'CTTATTATTAAAGCCCCTCCAC**TG**ACCGAGAC 5'	
E256K	5'ACCTGAAT**A**AGAAGTTCTACAGCTTC 3'	-27.44
	3'CGGAAGTTCCTGGACTTA**T**TCTTCAAG 5'	
Y259F	5'GAAGTTCT**T**CAGCTTCATGCAGAAGATG 3'	-26.91
	3'GGACTTACTCTTCAAGA**A**GTCGAAG 5'	

CYP1A1 Mutant	Primer Overlap (5' forward to 5' reverse)	ΔG^{o} of Heterodimerization (kcal/mol)
N309T	5'GATCATTACCATCGTCTTGGACCTCTTTGG 3' 3'CAGTCTACTCTTCTAGTAATGGTAGCAGA 5'	-28.5
L312F	5'CATCGTCTTTGACCTCTTTGGAGCTGGG 3' 3'CTAGTAATTGTAGCAGAAACTGGAGAA 5'	-31.68
D313A	5'CGTCTTGGCCCTCTTTGGAGCTGGGTTTGAC 3' 3'CTCTTCTAGTAATTGTAGCAGAACCGGGAGAAACC 5'	-38.06
D313N	5'GAAGATCATTAACATCGTCTTGAACCTCTTTGGAGCTGGG 3' 3'CTTCTAGTAATTGTAGCAGAACTTGGAGAAACCTCGACCC 5'	-74.01
G316V	5'CCTCTTTGTAGCTGGGTTTGACACAG 3' 3'GCAGAACCTGGAGAAACATCGACCC 5'	-30.42
A317G	5'CTTTGGAGGTGGGTTTGACACAGTC 3' 3'GCAGAACCTGGAGAAACCTCCACCCAAAC 5'	-33.37
D320A	5'CTGGGTTTGCCACAGTCACAACTGCTATCTC 3' 3'CTGGAGAAACCTCGACCCAAACGGTGTCAGTG 5'	-36.15
T321P	5'CTGGGTTTGACCCAGTCACAACTGCTATCTCC 3' 3'CTGGAGAAACCTCGACCCAAACTGGGTCAGTG 5'	-35.7
T321S	5'GGTTTGACTCAGTCACAACTGCTATCTCC 3' 3'GGAGAAACCTCGACCCAAACTGAGTCAGTG 5'	-26.11
V322A	5'GACACAGCCACAACTGCTATCTCC 3' 3'CTCGACCCAAACTGTGTCGGTGTTGAC 5'	-28.06

CYP1A1 Mutant	Primer Overlap (5' forward to 5' reverse)	ΔG^{o} of Heterodimerization (kcal/mol)
I386V	5'CCTTCACCGTCCCCCACAGCACAACAAG 3' 3'GGAAGCAGGGGAAGTGGCAGGGGGTG 5'	-36.65
I458P	5'GCATGGGCAAGCGGAAGTGTCCCGGTGAGACCATTGCCCG 3' 3'CGTACCCGTTCGCCTTCACAGGGCCACTCTGGTAACGGGC 5'	-89.94
I458V	5'GCATGGGCAAGCGGAAGTGTGTCGGTGAGACCATTGCCCGC 3' 3'CGTACCCGTTCGCCTTCACACAGCCACTCTGGTAACGGGCG 5'	-90.23
T461N (*4)	5'CGGAAGTGTATCGGTGAGAACATTGCCCGCTGGGAGGTC 3' 3'GCCTTCACATAGCCACTCTTGTAACGGGCGACCCTCCAG 5'	-80.66
I462V (*2)	5'CGGAAGTGTATCGGTGAGACCGTTGCCCGCTGGGAGGTC 3' 3'GCCTTCACATAGCCACTCTGGCAACGGGCGACCCTCCAG 5'	-83.31
T497S	5'GGGCTATCCATGAAGCATGCCTGC 3' 3'GGGGGTAGATACCCGATAGGTACTTC 5'	-28.46

[a] Mutagenic nucleotides are highlighted in red. [b] Wild-type CYP1A1 (Accession NM_000499) was used as the parent template to generate all mutants. [c] Oligonucleotides used to generate S122A, F123A, F224A, A317Y, T321G, and I386G mutants can be seen in Table 4.2 (section 4.2.1.2).

5.2.4 Protein preparation and quantification

5.2.4.1 Optimization of CYP1A1 and OxR co-expression

The pCW 17α-CYP1A1 wild-type cDNA's, all CYP1A1 mutants (Table 5.2), and the pCW 17α-CYP1A2 wild-type were individually transformed into DH5α *E. coli* cells that were stably transformed with the pACYC OmpA-rOxR construct. Ampicillin/Chloramphenicol selected colonies were screened for the correct plasmids by restriction enzyme analysis (sections 2.2.2.5 and 2.2.2.6). Cells were cultured using a modification of the method described in section 2.2.4.2. Briefly, overnight cultures (5mL) grown in LB broth with ampicillin (100μg/mL) and chloramphenicol (10μg/mL) at 37ºC were used to inoculate 100mL cultures of Terrific broth containing 100μg/mL ampicillin, 10μg/mL chloramphenicol, and rare elements solution (25μM $FeCl_3.6H_2O$, 2μM $ZnCl_3.4H_2O$, 2.5μM $CaCl_2.6H_20$, 2.5μM Na_2MoO_4, 1.7μM $CaCl_2.2H_2O$, 1.85μM $CuCl_2$, 2μM H_3BO_3, 30μM HCl). Cultures were grown at 37ºC with shaking (160 rpm) for 4h, or until reaching an optical density of 0.7 to 0.9 AU at 600nm. After cooling to 26ºC, cultures were induced with isopropyl-1-thio-β-D-galactopyranoside (IPTG; 1mM) and δ-aminolevulinic acid (δ-ALA; 1.0mM) and then grown at 26ºC with shaking (160 rpm) for an additional 64h in <1% dissolved oxygen. Membrane fractions were separated as described in section 2.2.4.3.

5.2.4.2 Quantification of holo-CYP1A1 and OxR proteins

The total protein content of wild-type and mutant membrane fractions was determined by the method of Lowry *et al.* (1951) (section 2.2.4.4). Expressed holo-enzyme was quantified by cytochrome P450 reduced difference spectroscopy

(section 2.2.4.5). OxR activity was measured using cytochrome *c* as the alternate electron acceptor by the method outlined in section 2.2.4.6.

5.2.5 Enzyme kinetics and the derivation of kinetic parameters

5.2.5.1 Measurement of DTIC N-demethylation activity

AIC formation was determined in opaque glass tubes at 37ºC in a total incubation volume of 0.2mL. Incubation mixtures contained co-expressed CYP1A1 (5.0pmol) and OxR (10 ± 0.5pmol), NADPH generating system (1mM $NADP^+$, 10mM glucose-6-phosphate, 2IU glucose-6-phosphate dehydrogenase, 5mM $MgCl_2$) and DTIC (100-6000μM) in phosphate buffer (0.1M, pH 7.4). Following a 5min pre-incubation at 37ºC in a shaking water bath, reactions were initiated by the addition of NADPH generating system. Incubations were terminated after 60min by the addition of 2.0μL of ice cold 70% perchloric acid. Reaction mixtures were vortex mixed, cooled on ice for 10 min, centrifuged (5000x*g* for 10min at 4ºC), and an aliquot of the supernatant fraction (20μL) injected onto the HPLC column.

5.2.5.2 Estimation of kinetic parameters for DTIC metabolism

The rate of AIC formation over the range of substrate concentrations (100-6000μM) was measured under the initial rate conditions given in section 5.2.5.1. The kinetic constants (K_m, V_{max}, n, and S_{50}) for AIC formation were derived from fitting either the Michaelis-Menten (MM) equation (eq 4.1; section 4.2.3.4) or the Hill equation (eq 5.1) to experimental data. Goodness of fit was assessed from the F-statistic, 95% confidence intervals, r^2 value, and standard error of the parameter fit.

Hill equation:

$$v = \frac{V_{max}[S]^n}{S_{50}^{\ n} + [S]^n} \quad (5.1)$$

where v is the rate of reaction (rate of metabolite formation), V_{max} is the maximal velocity, S is the substrate concentration, S_{50} is the substrate concentration at ½V_{max}, and n is the Hill coefficient.

Statistical analysis (multivariate general linear model; Tukey *post hoc*) was undertaken using PASW Statistics version 18.0 (SPSS Inc. Chicargo, USA). Data are given as the mean ± SD of four separate experiments with values of $P<0.05$ considered significant.

5.2.6 Assay for DTIC *N*-demethylation

5.2.6.1 Measurement of amino-imidazole-carboxamide formation

AIC was separated using a Waters Nova-Pak® C18 column (150 x 3.9mm, 4µm; Waters Corporation, MA, USA) consisting of mobile phase (A) 10mM heptane sulfonic acid, 5% (v/v) acetonitrile (AcN), and 0.1% (v/v) TEA, adjusted to pH 3.0 with 85% orthophosphoric acid (filter sterilized; 0.45µ) and mobile phase (B) AcN (100%). The following mobile phase gradient was used to elute AIC: 100% A held for 5.1min, then changed to 70% A/30% B over 0.7min, and held for 0.1min, followed by returning to 100% A over 0.1min and held for 5.1min. AIC was monitored by UV detection at 267nm. The retention time of AIC was 5.2min using a mobile phase flow rate of 1.0mL/min. Unknown concentrations of AIC were

determined by comparison of the peak area to a calibration curve constructed in the concentration range 2.5 to 100μM.

DTIC stock solutions were prepared as a 1:1 molar ratio of HCl in water. Dilutions of the DTIC stock solutions were confirmed by HPLC to ensure linearity; r^2 values were >0.991. Samples were prepared by diluting 1:100 with mobile phase and an aliquot (4μL) injected onto the HPLC column. The following isocratic mobile phase was used to elute DTIC: 80% A and 20% B held over 4min. Elution was monitored by UV detection at 267nm. The retention time of DTIC was 1.4min using a mobile phase flow rate of 1.0mL/min.

5.3 Results

5.3.1 Automated docking of DTIC

5.3.1.1 Wild-type CYP1A1

Using the CYP1A1 homology model generated in Chapter 3, DTIC was docked into the protein active-site following the procedure outlined in section 3.2.6. The energetically favored pose of DTIC places the α-carbon of the side-chain *N*-methyl at 5.6Å from the heme iron at an angle of 105.3º perpendicular to the heme plane from the pyrrole nitrogen (Figure 5.4a). This measurement is dependant on free rotation about the *N*-dimethyl side-chain of the triazene. Interestingly, the angle of DTIC in the CYP1A1 active-site is not dissimilar to that of Eres (106.4º), but the distance from the α-carbon of the catalytic methyl to the heme Fe is about 20% greater than for Eres (4.4Å). Figure 5.5 shows a space-filling view of docked DTIC overlaid with Eres. The overlay identifies that the catalytic carbon targeted for hydroxylation in DTIC resides further from the heme catalytic Fe, compared to Eres.

Binding and orientation of DTIC within the active-site involves I115, S120, S122, F123, F224, F258, Y259, D313, G316, A317, I386, and L496, with all twelve residues positioned within a 3Å radius from DTIC (Figure 5.4b). The van der Waals surface of the substrate identifies strong interactions with S122, F123, D313, A317, I386, Y259, and L496. In contrast to the docked Eres structure, there are no interactions with T321 or V382. H-bonding can occur between the hydroxy oxygen of S122 and the triazene N6 nitrogen of DTIC. However, based on the speciation of DTIC at pH7.4, H-bonding at this location is unlikely unless the active-site pH drops below 4.0 during substrate binding or catalysis. Further H-bonding is observed between the hydroxy hydrogen of Y259 and the N2 aromatic nitrogen of the imidazole ring. H-bonding at this location is likely to occur in all substrate molecules at physiological pH (Figure 5.6). Parallel displaced aromatic interactions are again predominant with F224, F258, and Y259 (Figure 5.4b). The free rotation of the *N*-dimethyl substituent of DTIC appears to be dependant on the size of residues located at positions 317 (I-helix; SRS 4) and 386 (K-helix/β2-3 loop; SRS5). Intriguingly, residue 317 is the small nonpolar aliphatic alanine and residue 386 is the Cβ-branched nonpolar aliphatic isoleucine. These two residues constrain the width of the catalytic region of the active-site to 5.4Å.

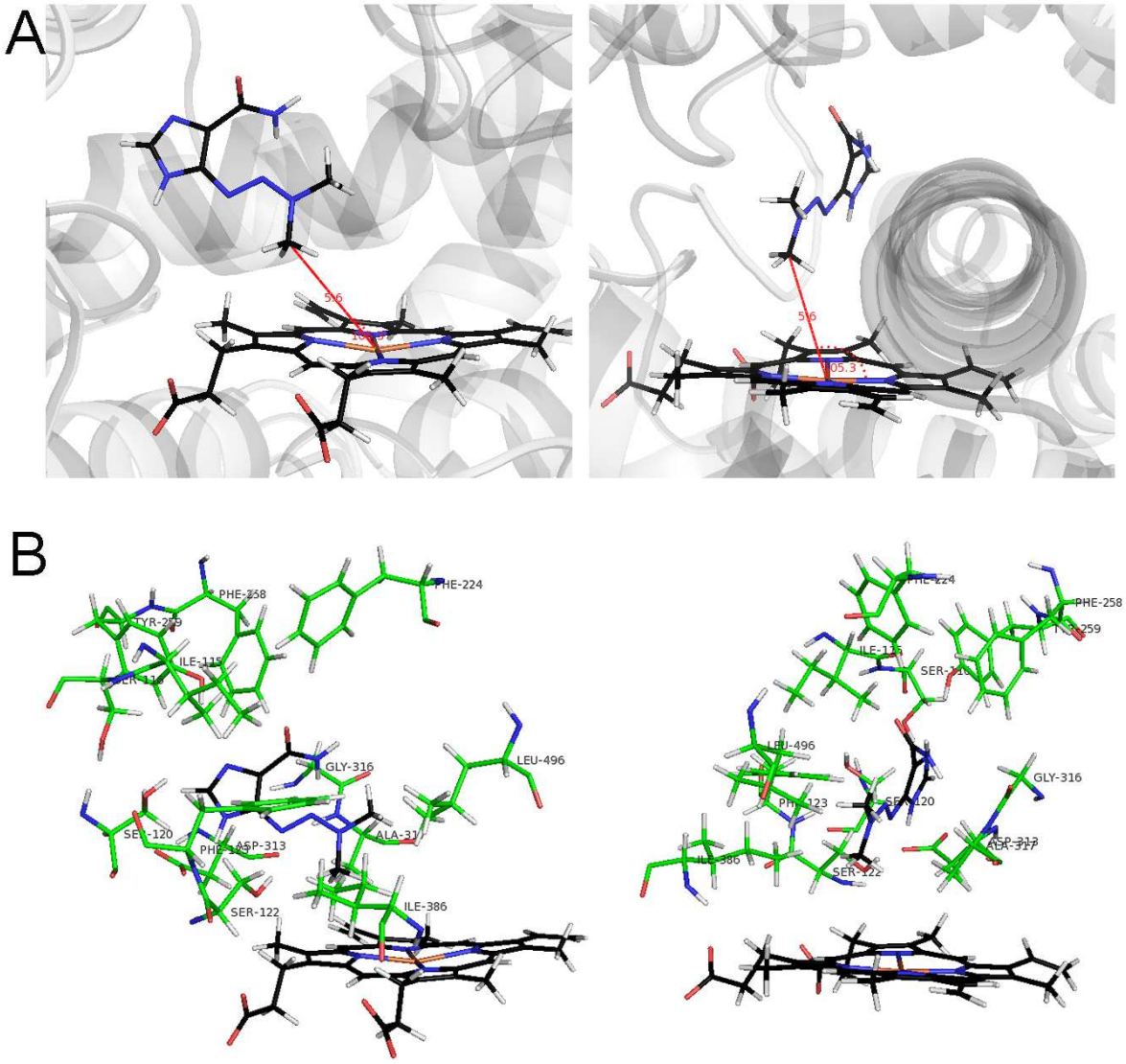

Figure 5.4 Orientation of DTIC in the CYP1A1 active-site. Orthogonal image of (a) the α-carbon of the *N*-dimethyl substituent positioned in the energetically favored orientation for *N*-demethylation, and (b) the key amino acids involved in binding and orientation of DTIC.

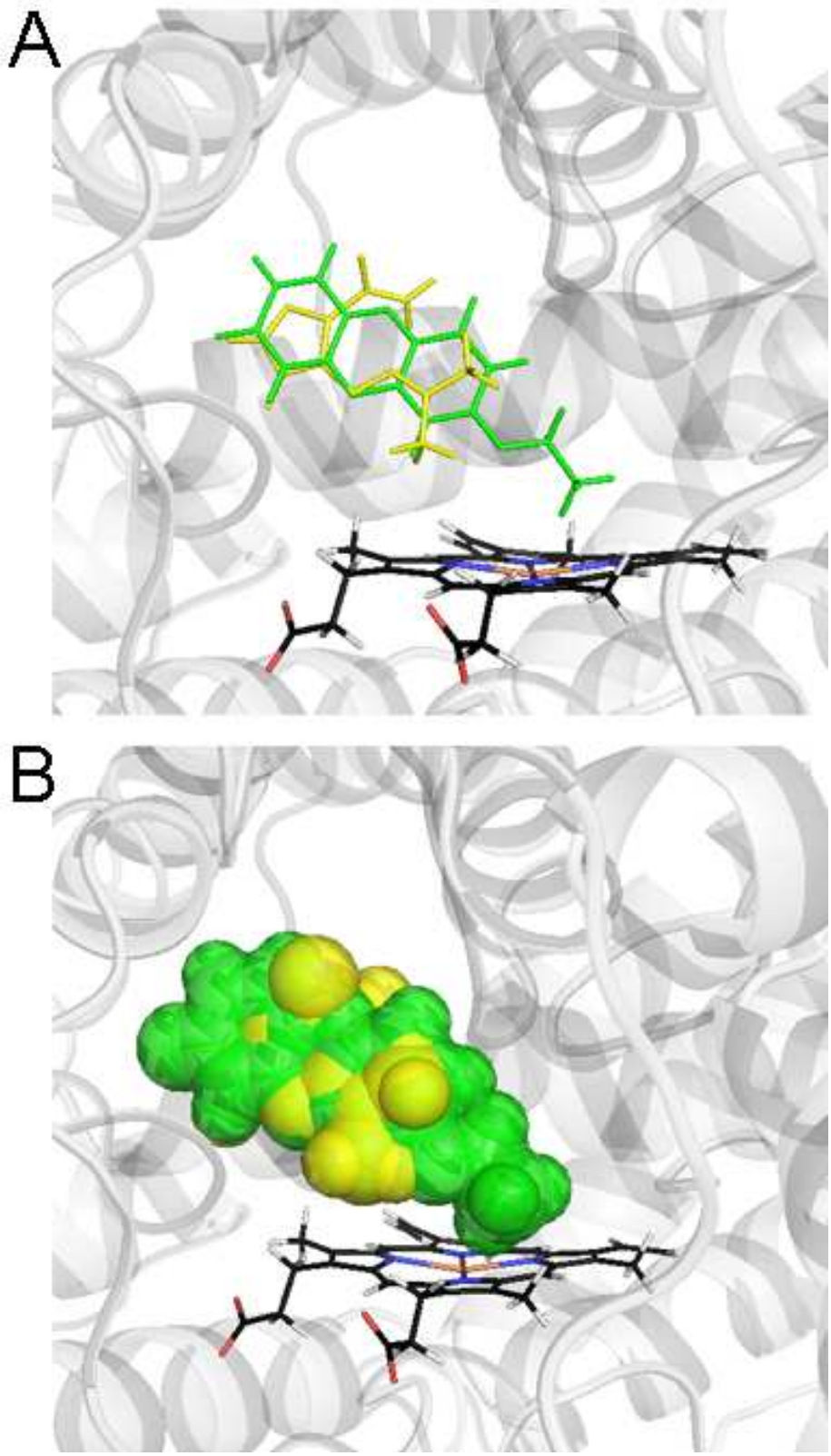

Figure 5.5 Overlay of docked DTIC and Eres. (a) DTIC (yellow) superimposed with Eres (green) in the CYP1A1 active-site. (b) Space-filling view of docked Eres and DTIC in the CYP1A1 active-site.

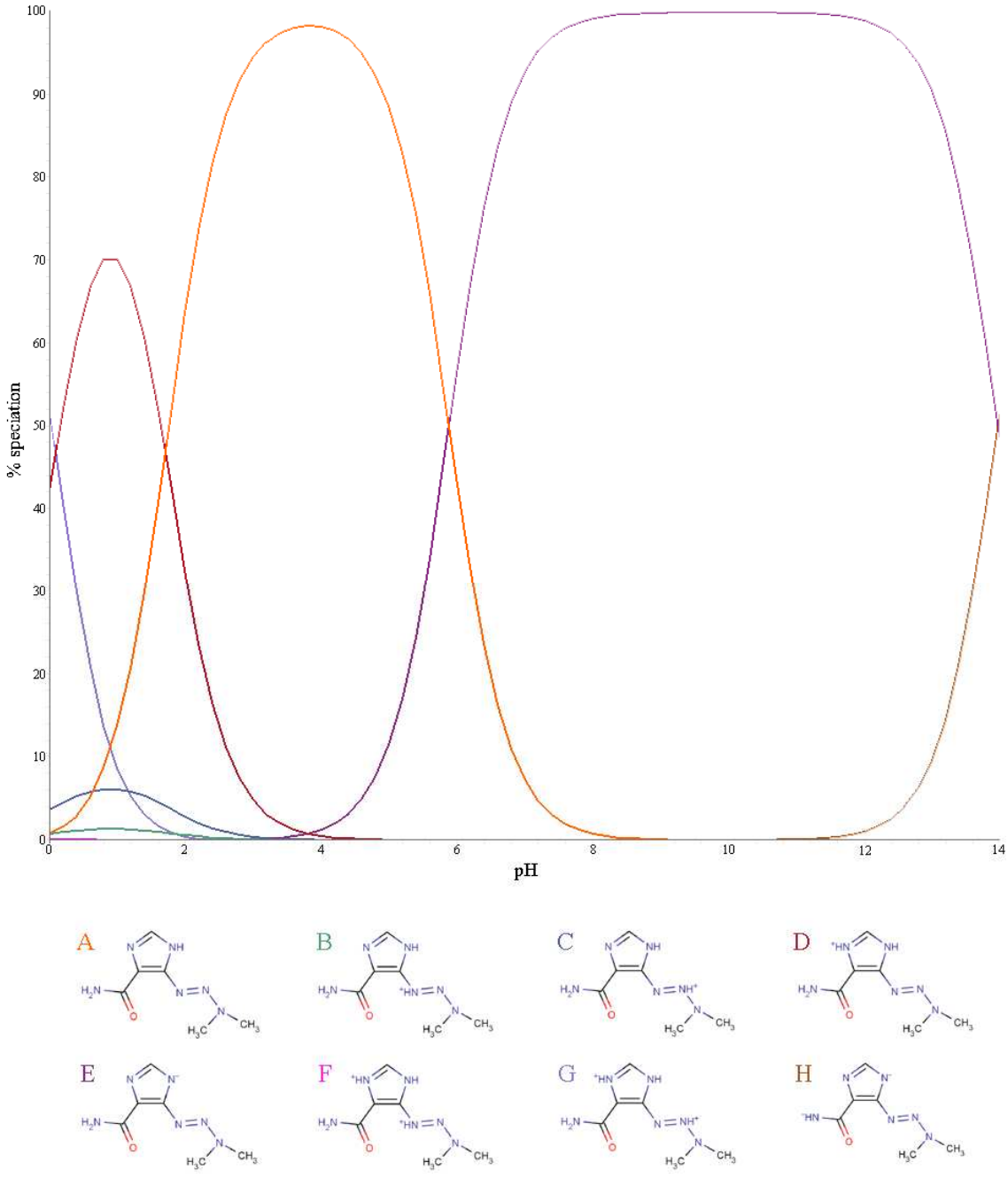

Figure 5.6 Percent protonated DTIC species distribution with varying pH.

D313 is in close proximity to the aromatic nitrogen closest to the triazene substituent. At pH7.4 this nitrogen is negatively charged in 97% of DTIC molecules (Figure 5.6). Thus, strong charge interactions contributed by D313 may affect the orientation of DTIC in the CYP1A1 active-site.

5.3.1.2 Mutant CYP1A1 enzymes

Structural models were built to assist interpretation of the differences observed in catalytic efficiency. The CYP1A1 mutants listed in Table 5.3 were generated based on the criteria described in section 5.2.3.1. The rationale for each mutation is summarized in Table 5.3 with reference to the image showing the docked DTIC molecule relative to the wild-type docking pose.

Table 5.3 CYP1A1 mutants generated to determine which residues affect DTIC catalytic efficiency.

Mutant	RMSD[a]	Rationale	DTIC Orientation[b]	Image Reference
S116A	0.1307	S116 forms part of the product egress channel and is in close proximity to Y259 (2.5Å). Substitution to Ala will abolish the polarity at this position and enlarge the product egress channel. S116 H-bonds to Q119 (also in the egress-channel) which may additionally affect product egress.	95.2º; 6.2Å	5.7i
S122A	0.0287	Removing the potential H-bonding interaction at residue 122 may allow DTIC to move more freely in the active-site.	99.7º; 5.5Å	5.7ii
S122T	0.0408	If H-bonding to DTIC is maintained the larger Thr may force DTIC deeper into the active-site, closer to the heme Fe. Thr is the alternate residue found in CYP1A2.	115.2º; 4.3Å	5.7iii
F123A	0.0739	This substitution affected catalytic efficiency of EROD via a π-σ orbital interaction.	114.6º; 4.8Å	5.7iv
E161K	0.0718	This mutation is known to affect reductase binding in CYP1A2. A triple mutant of E163K/V191M/K170Q in CYP1A2 caused a 5-fold increase in k_{cat} compared to the wild-type with 7-methoxyresorufin as substrate.	126.3º; 4.3Å	5.7v
E166Q	0.0512	As for E161K.	105.3º; 5.0Å	5.7vi
V191M	0.058	As for E161K.	106.8º; 4.9Å	5.7vii
F224A	0.1327	This substitution reduced catalytic efficiency of EROD 3-fold due to its π-π interaction with the highly aromatic substrate.	106.0º; 4.7Å	5.7viii
V228T	0.0978	Heterocyclic aromatic amine metabolism by rat CYP1A1 is more efficient than with human CYP1A1. This substitution is based on the rat sequence and may affect substrate access to the active-site via polar interactions.	108.2º; 5.8Å	5.7ix
E256K	0.0680	As for V228T, except this mutation may affect aromatic interactions involving F258 and Y259.	95.4º; 6.8Å	5.7x

Mutant	RMSD[a]	Rationale	DTIC Orientation[b]	Image Reference
Y259F	0.1174	This substitution removes the H-bonding ability of Tyr but retains the aromaticity of this residue.	120.4º; 4.0Å	5.7xi
N309T	0.0631	As for V228T except this mutation may affect product egress due to enhanced polar interactions.	102.8º; 5.7Å	5.7xii
L312F	0.0652	A change to Phe may alter the orientation of F258 and Y259 and subsequently affect aromatic stacking in the active-site.	92.2º; 6.5Å	5.7xiii
D313A	0.0434	A change to Ala will remove the charge state associated with Asp. If D313 H-bonds to DTIC then the D313A mutation should abolish this polar interaction.	101.7º; 4.5Å	5.7xiv
D313N	0.0678	N297 in CYP2A6 is critical for the metabolism of nitrogen-containing compounds. This residue resides at position 313 in CYP1A1. Removal of the charge interaction by substitution with Asn may improve DTIC substrate alignment.	122.6º; 4.1Å	5.7xv
G316V	0.0449	An increase in side-chain volume may constrain DTIC in the CYP1A1 active-site.	132.6º; 2.9Å	5.7xvi
A317G	0.0297	This substitution should increase the volume at the base of the active-site allowing DTIC more space to orientate.	111.7º; 4.5Å	5.7xvii
D320A	0.0693	This charged residue of the I-helix may interact with neighboring residues in the F-helix and the β5-1/β5-2 loop therefore impacting on the orientation of residues in SRS2 and SRS6, respectively.	102.6º; 5.2Å	5.7xviii
T321G	0.0525	This substitution should affect the alignment of water in the active-site cavity above the heme Fe.	124.5º; 3.8Å	5.7xix
T321P	0.0728	Residue 321 is located in the I-helix. A change to Pro should hinder DTIC activation by altering the electrostatic interactions contributed by the I-helix.	113.8º; 4.3Å	5.7xx
T321S	0.0212	This mutation will remove the β-branching of Thr without affecting the alignment of water in the active-site.	110.8º; 5.0Å	5.7xxi
V322A	0.0441	This substitution has been shown to increase the V_{max} for Eres, phenacetin, and MeIQ metabolism by CYP1A2.	119.5º; 4.5Å	5.7xxii

Mutant	RMSD[a]	Rationale	DTIC Orientation[b]	Image Reference
I386G	0.0326	EROD activity was abolished by this mutation possibly due to an increase in flexibility of the K-helix/β2-3 loop thus altering the environment about the heme.	115.5º; 4.9Å	5.7xxiii
I386V	0.0359	This substitution should allow greater freedom of rotation for the side-chain *N*-dimethyl group of DTIC yet maintain the β-branching and rigidity of the K-helix/β2-3 loop main-chain.	127.1º; 3.9Å	5.7xxiv
I458P	0.0362	This residue is located in the β4-2/L-helix loop and neighbors the conserved Cys responsible for heme incorporation at position 457. Substitution to proline will maintain β-branching yet incorporate a turn into this loop. This may cause a shift in heme orientation thus affecting substrate turnover.	112.2º; 4.5Å	5.7xxv
I458V	0.0505	As for I458P, except substitution with Val should maintain the main-chain conformation but alter the electrostatic environment about the heme.	106.4º; 4.8Å	5.7xxvi
T461N	0.0343	This mutation is a SNP present in 5.7% of Caucasians and is termed CYP1A1*4. The affect of this mutation on DTIC activation has not been reported.	105.3º; 5.0Å	5.7xxvii
I462V	0.0439	This mutation is a SNP present in 8.9% of Caucasians, 20% Japanese, and 22% of African Americans. The allelic variant is termed CYP1A1*2B. The affect of this mutation on DTIC activation has not been reported.	120.4º; 4.4Å	5.7xxviii
T497S	0.1016	A change to Ser at residue 497 should increase the active-site volume but retain the H-bonding necessary for stabilization of the surrounding secondary structures.	123.4º; 4.7Å	5.7xxix

[a] Root mean squared deviation (RMSD) is calculated from the Cα backbone compared to that of the wild-type CYP1A1 template. [b] DTIC orientation is based on the distance of the α-carbon targeted for *N*-dealkylation from the heme Fe and its angle relative to the planar heme.

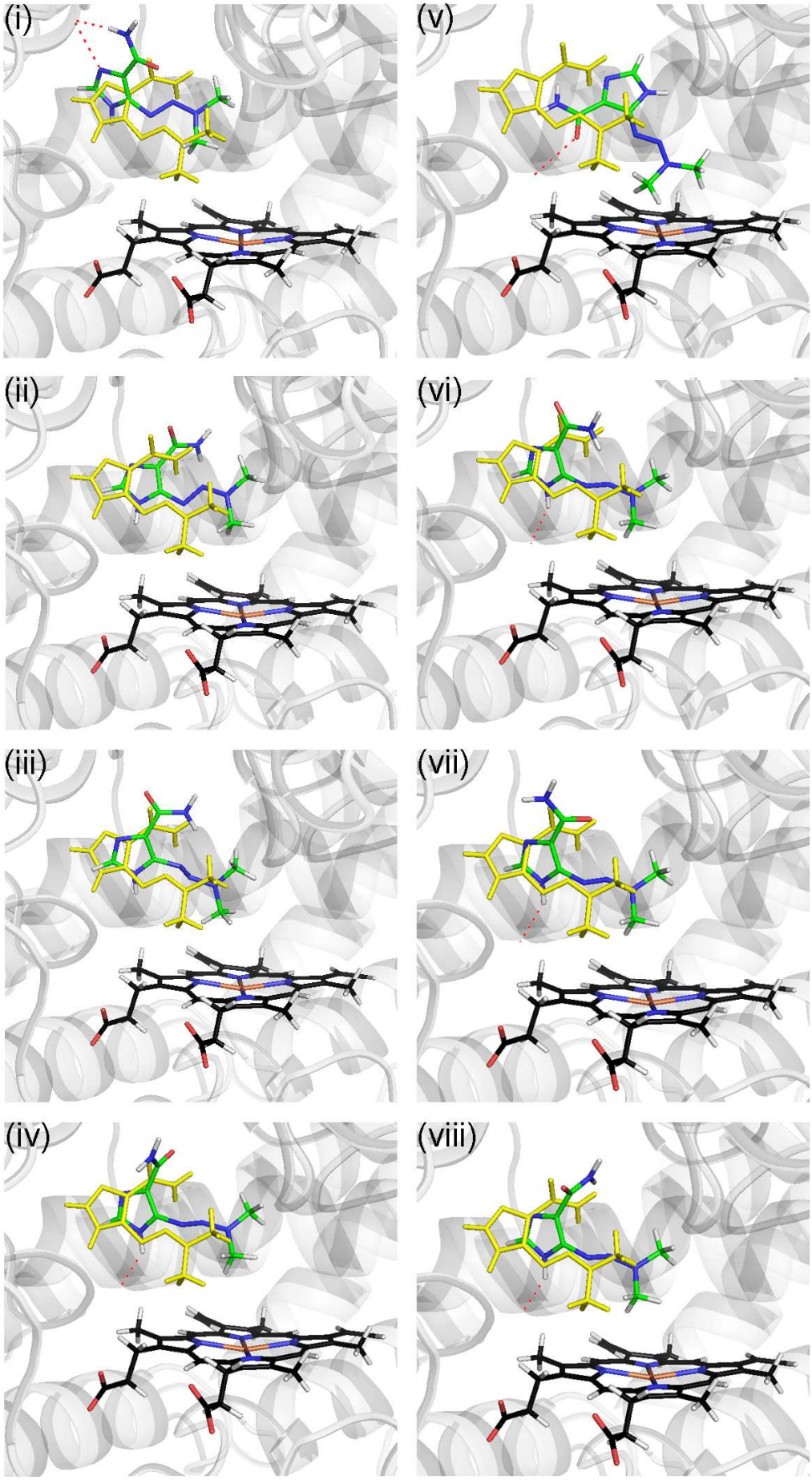
(i)
(v)
(ii)
(vi)
(iii)
(vii)
(iv)
(viii)

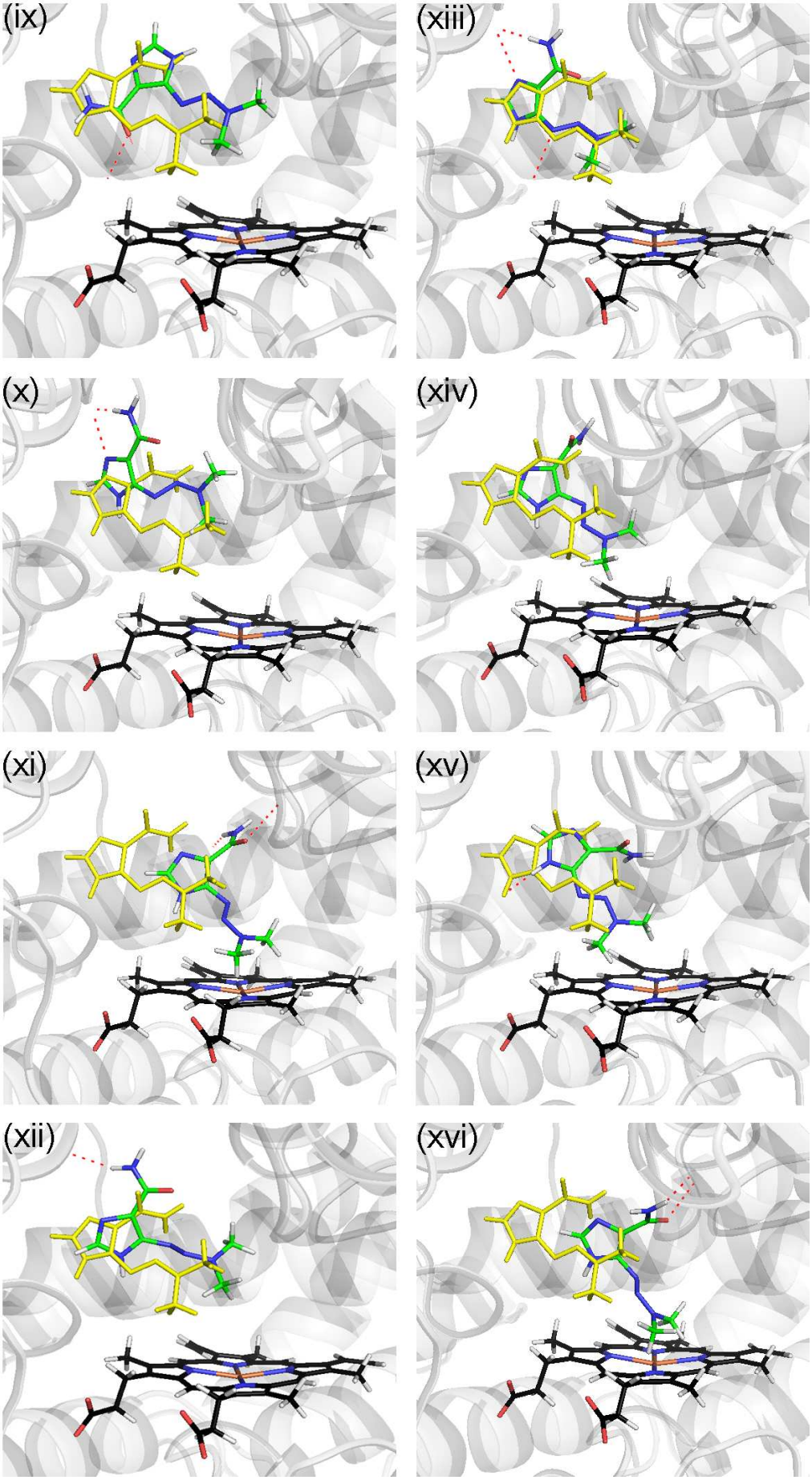
(ix)
(xiii)
(x)
(xiv)
(xi)
(xv)
(xii)
(xvi)

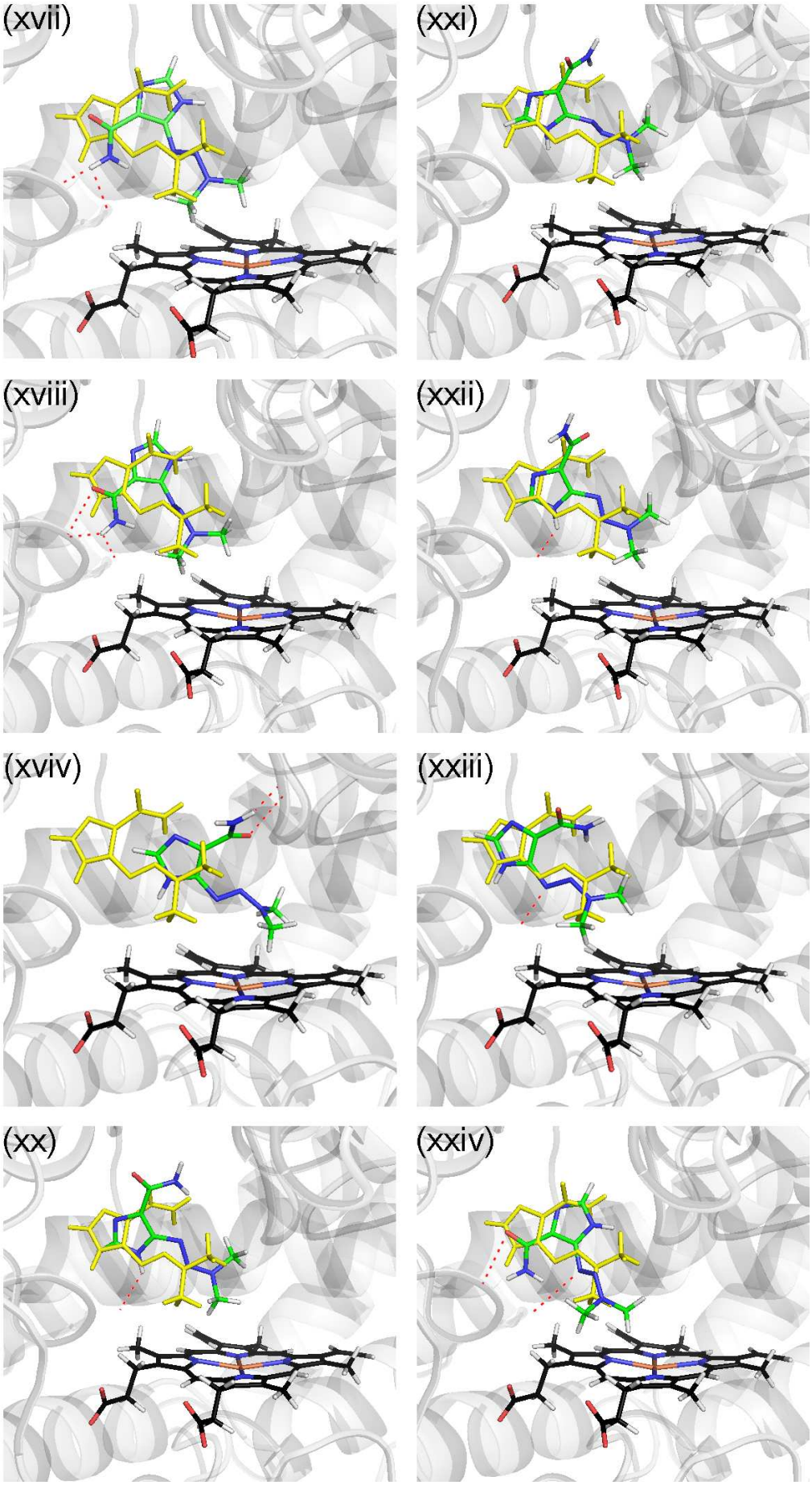
(xvii)
(xxi)
(xviii)
(xxii)
(xviv)
(xxiii)
(xx)
(xxiv)

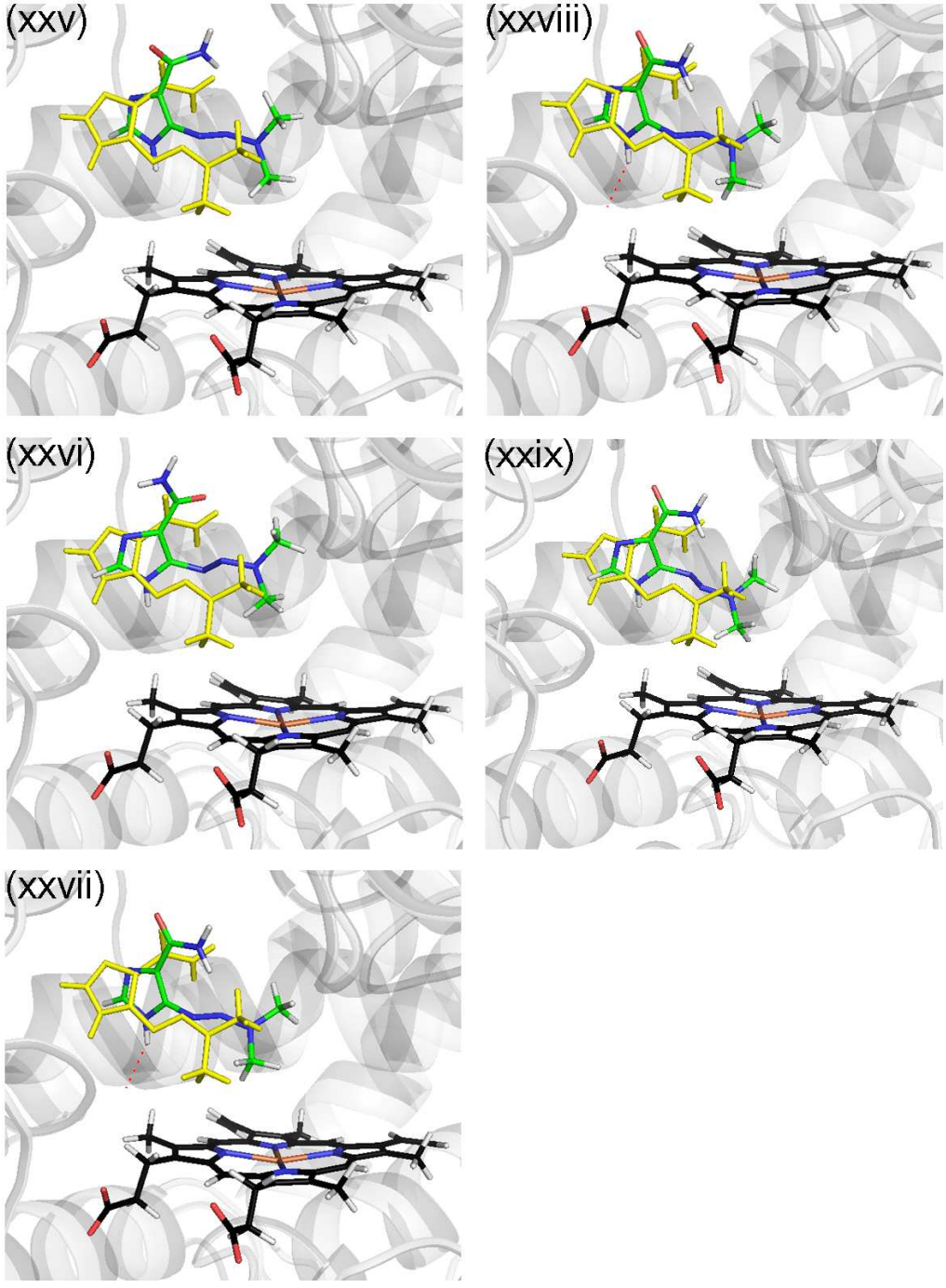

Figure 5.7 Enzyme-substrate interactions generated with DTIC and each *in silico* CYP1A1 mutant. Wild-type DTIC pose (yellow); mutant residues and DTIC pose (green). See Table 5.3 for the corresponding image reference.

5.3.2 Heterologous expression of CYP1A1, CYP1A1 mutants, and CYP1A2

Wild-type CYP1A1 and CYP1A2 and mutant CYP1A1 enzymes (listed in Table 5.3) were individually co-expressed with OxR. The expression of holo-enzyme achieved in *E. coli* (≥3 experiments), estimated from the carbon monoxide difference spectrum, varied between each enzyme. Mean expression data is given in Table 5.4. Interestingly, expression of the wild-type CYP1A1 construct yielded, on average, 141 (±8)pmol P450/mg protein using the optimized method described in section 5.2.4.1. Thus, this method results in approximately 3.5-fold higher expression of holo-CYP1A1 compared to the method described in section 4.2.2.1 and was therefore utilized to express the P450 proteins generated in this Chapter. Both the V191M and D320A CYP1A1 mutants yielded greater than 220pmol P450/mg protein with ~45% of all mutants yielding ≥100pmol P450/mg protein. Approximately 20% of all mutants yielded ≤50pmol P450/mg protein. Apart from E166Q, those mutants that expressed less than 50pmol P450/mg protein affect direct access to the heme prosthetic group. This result may indicate that the 'rare elements solution' utilized in the expression of P450 proteins (section 5.2.4.1) may enhance expression yields by stabilizing the heme during incorporation and folding in *E. coli*. Levels of co-expressed OxR varied to a lesser extent, with a mean yield of 292 (±64)pmol reductase/mg protein (>60 experiments).

Table 5.4 Holo-P450 yields for enzymes expressed in *E. coli*.

Enzyme	pmol P450/mg Protein[a]	Standard Deviation
CYP1A2	128	2
CYP1A1	141	8
S116A	103	7
S122A	56	2
S122T	61	0.5
F123A	9	3
E161K	94	9
E166Q	33	7
V191M	225	9
F224A	54	12
V228T	95	11
E256K	115	36
Y259F	115	5
N309T	132	2
L312F	115	4
D313A	57	3
D313N	35	3
G316V	165	13
A317G	101	5
D320A	223	9
T321G	59	2
T321P	59	12
T321S	57	2
V322A	27	9
I386G	22	7
I386V	42	32
I458P	134	26
I458V	89	6
T461N	41	1
I462V	109	4
T497S	84	5

[a]Expression yields are given as the mean ± SD of ≥3 experiments.

5.3.3 Assay optimization and reproducibility

Linearity of AIC formation with respect to incubation time and P450 protein concentration was assessed using the wild-type CYP1A1 and CYP1A2 proteins. Holo-enzyme concentration, determined by difference spectroscopy (section 2.2.4.5), and incubation time were varied from 10-60pmol of CYP1A1 and 30-120min, respectively, and from 10-30pmol of CYP1A2 and 15-120min, respectively. The linearity of AIC formation was investigated at two substrate concentrations; 300μM and 3000μM for CYP1A1 and 100μM and 3000μM for CYP1A2. AIC formation was linear to 40pmol CYP1A1 when the incubation time was held constant at 60min (Figure 5.8a). Similarly, DTIC *N*-demethylase activity was linear for incubation times to 60min when the CYP1A1 content was held constant at 20pmol (Figure 5.8b). AIC formation was linear to 30pmol CYP1A2 when the incubation time was held constant at 60min (Figure 5.8c), and linear DTIC *N*-demethylase activity for incubation times to 60min when the CYP1A2 concentration was held constant at 10pmol (Figure 5.8d). Thus, the CYP1A1 and CYP1A2 concentration (5pmol) and incubation time (60min) utilized in incubations (section 5.2.5.1) ensured initial rate conditions, with substrate utilization <10%.

Overall within day assay reproducibility was assessed by measuring AIC formation in eight separate incubations of the same batch of expressed CYP1A1 and CYP1A2. Coefficients of variation for CYP1A1 were 3.6% and 2.4% for DTIC concentrations of 250 and 3000μM, respectively. Coefficients of variation for CYP1A2 were 3.9% and 1.5% for DTIC concentrations of 250 and 3000μM, respectively.

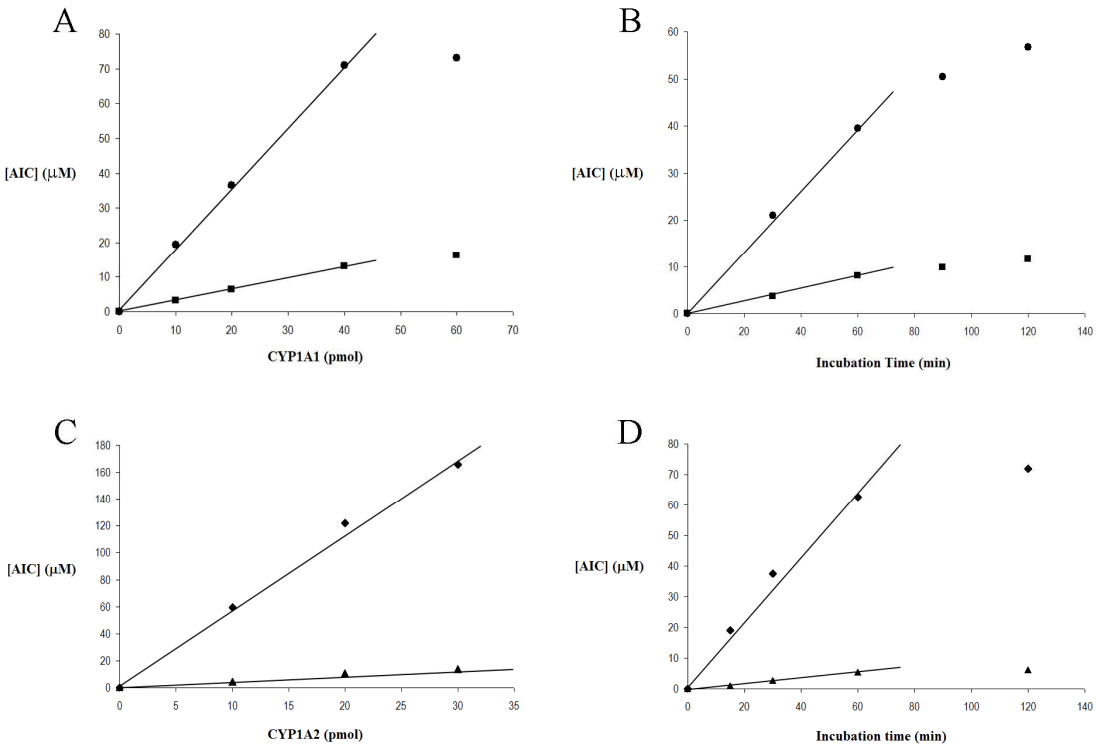

Figure 5.8 Time and protein linearity of CYP1A1 and CYP1A2 DTIC *N*-demethylase activity. Linearity with respect to (a) holo-CYP1A1 content, (b) CYP1A1 incubation time at substrate concentrations of 300μM (■) and 3000μM (●), (c) holo-CYP1A2 content, and (d) CYP1A2 incubation time at substrate concentrations of 100μM (▲) and 3000μM (◆).

5.3.4 Effects of CYP1A1 mutations on DTIC activation

All wild-type CYP1A1 and CYP1A2, and mutant CYP1A1 enzymes were characterized for DTIC *N*-demethylase activity to generate kinetic parameters. Derived kinetic parameters are summarized in Table 5.5. With the exception of the CYP1A1 I386G mutant, all enzymes catalyzed DTIC *N*-demethylation. The wild-type CYP1A2 and mutant CYP1A1 enzymes S122A, S122T, E166Q, D313A, D313N, T321G, T321P, T321S, and T497S all displayed negative cooperative kinetics and data were modeled using the Hill equation. Wild-type CYP1A1 and all

remaining CYP1A1 mutants displayed hyperbolic V/[S] plots characteristic of single-enzyme Michaelis-Menten kinetics and data were well described by the Michaelis-Menten equation. Although full kinetic plots were generated for all enzymes, only those that exhibited a significant variation in catalytic efficiency compared to the wild-type CYP1A1 enzyme will be discussed. Noteworthy, the enhanced catalytic efficiency of DTIC *N*-demethylation obtained by the CYP1A1 E161K, E256K, and I458V mutants was of great importance to this study.

Figure 5.9 shows representative Eadie-Hofstee plots for DTIC *N*-demethylation by wild-type CYP1A1 and CYP1A2, and mutant CYP1A1 enzymes E161K, V228T, E256K, I386V, I458V, T461N, and I462V. The kinetic parameters for DTIC *N*-demethylation by wild-type CYP1A1 (V_{max} 28 ± 4pmol/min/pmol P450, K_m 408 ± 43 μM) are in good agreement with the only other CYP1A1 data available with this substrate (CYP1A1 V_{max} 10.2 ± 2.1pmol/min/pmol P450; K_m 595 ± 111 μM) (Reid et al. 1999).

Table 5.5 Derived kinetic parameters for DTIC *N*-demethylase activity by wild-type CYP1A1 and CYP1A2, and mutant CYP1A1 enzymes.

Enzyme	V_{max} (pmol/min/pmol P450)	K_m or S_{50} (μM)	V_{max}/K_m (μL/min/pmol P450)	Hill Coefficient
CYP1A2 [b]	38 ± 0.5	1502 ± 30*	-	0.70
CYP1A1[a]	**28 ± 4**	**408 ± 43**	**0.069**	**-**
S116A	26.7	412	0.065	-
S122A [b]	81.6	328233	-	0.44
S122T [b]	23.3	1132	-	0.70
F123A[d]	23.5	18363	0.001	-
E161K[a]	**30 ± 5**	**249 ± 22***	**0.120***	**-**
E166Q [b]	34.8	1492	-	0.80
V191M	23	501	0.046	-
F224A	31.4	468	0.067	-
V228T[a]	**32.4 ± 1.5**	**386 ± 22**	**0.090**	**-**
E256K[a]	**29 ± 3**	**238 ± 32***	**0.121***	**-**
Y259F	25.9	1082	0.024	-
N309T	33.9	533	0.064	-
L312F	32.7	773	0.042	-
D313A [b]	40.4	10953	-	0.80
D313N [b]	26.5	22849	-	0.75

Enzyme	V_{max} (pmol/min/pmol P450)	K_m or S_{50} (μM)	V_{max}/K_m (μL/min/pmol P450)	Hill Coefficient
G316V	19.7	6963	0.003	-
A317G[d]	21.1	12207	0.001	-
D320A	18.3	1091	0.017	-
T321G [b]	8.7	1117	-	0.70
T321P [b]	23.1	2543	-	0.75
T321S [b]	56.9	3119	-	0.60
V322A	32.2	680	0.047	-
I386G	nd[c]	nd	nd	nd
I386V	**44.2 ± 4***	**765 ± 30***	**0.058**	-
I458P	33.1	587	0.056	-
I458V[a]	**22 ± 4**	**183 ± 61***	**0.118***	**-**
T461N[a]	**35 ± 3**	**694 ± 154***	**0.050**	-
I462V[a]	**24 ± 5**	**502 ± 52**	**0.048**	-
T497S [d]	126.4	112571	0.000	-

[a]K_m and V_{max} values are given as the mean ± SD of four experiments. [b]Data from fitting with the Hill equation. [c]No detectable activity. [d]The kinetic model for these mutants could not be characterized. *P<0.05 compared to the corresponding parameter for the wild-type.

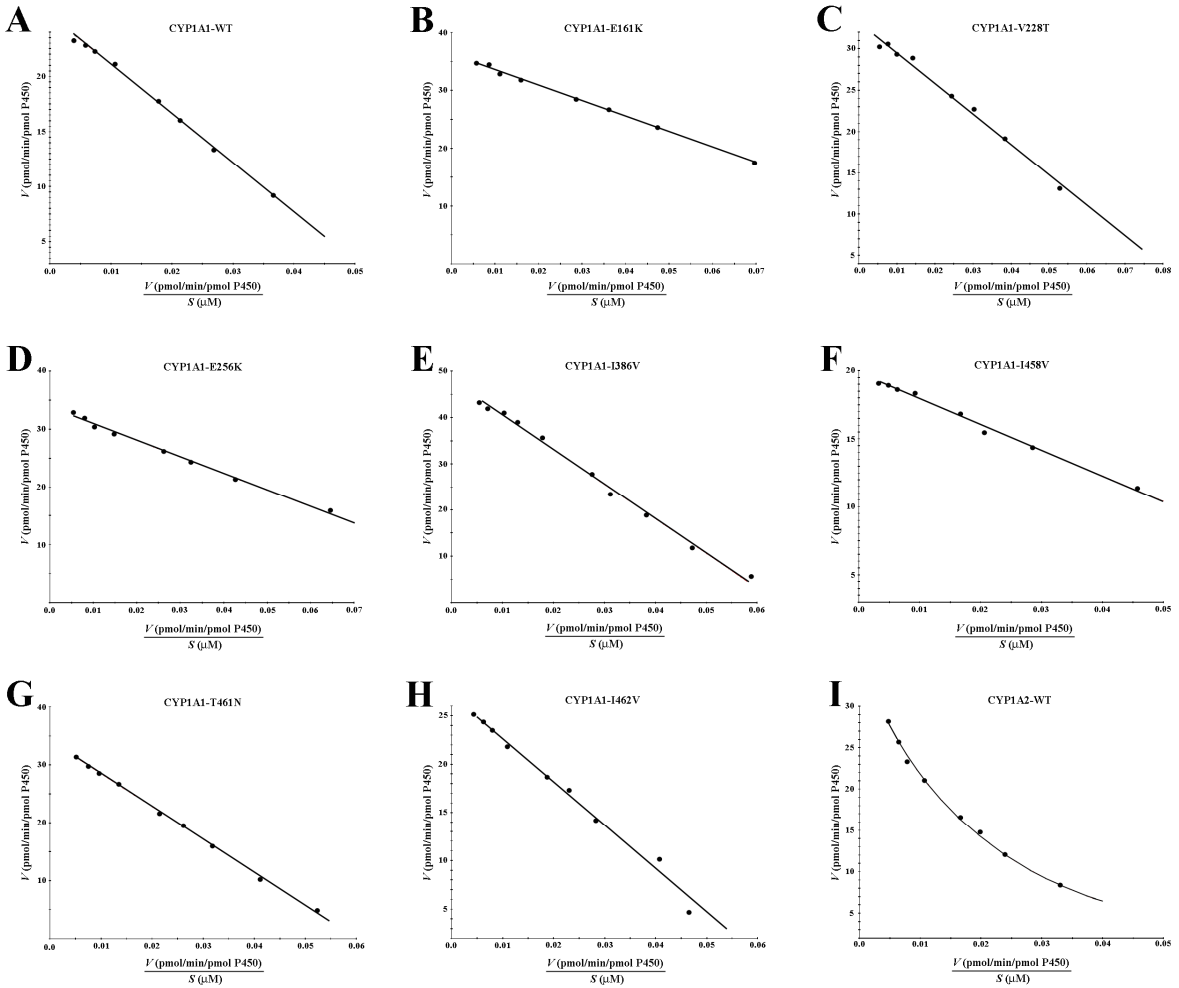

Figure 5.9 Representative Eadie-Hofste plots for DTIC *N*-demethylation. (a) wild-type CYP1A1, (b) CYP1A1-E161K, (c) CYP1A1-V228T, (d) CYP1A1-E256K, (e) CYP1A1-I386V, (f) CYP1A1-I458V, (g) CYP1A1-T461N, (h) CYP1A1-I462V, and (i) wild-type CYP1A2.

The kinetic parameters for DTIC *N*-demethylation by wild-type CYP1A2 (V_{max} 38 ± 0.5pmol/min/pmol P450, S_{50} 1502 ± 30μM, n = 0.70) differed from those published by Reid *et al.* (1999) (V_{max} 13.8 ± 2.4pmol/min/pmol P450; K_m 659 ± 88μM). However, Reid *et al.* (1999) did not present kinetic plots for DTIC *N*-demethylation by CYP1A1 or CYP1A2, and hence the validity of fitting their data to the Michaelis-Menten equation cannot be assessed.

The majority of CYP1A1 mutant proteins exhibited substantial decreases in catalytic efficiency (CL_{int}) (Table 5.5). However, the E161K, E256K, and I458V substitutions all produced an approximate two-fold increase in binding affinity (i.e. decrease in K_m) with no change in V_{max}, thereby doubling CL_{int} ($P<0.05$). The V228T mutant exhibited an elevated V_{max} generating a 23% increase in CL_{int} for this mutant. There were significant increases in both V_{max} and K_m of the I386V mutant ($P<0.05$), resulting in no overall change in CL_{int} ($P=0.872$). Interestingly, the most common polymorphic CYP1A1 variants T461N (CYP1A1*4) and I462V (CYP1A1*2) exhibited a decrease in CL_{int} of almost 30%, arising from an increase in V_{max} and K_m for T461N and an increase in K_m for the I462V mutant.

From the results obtained with the different CYP1A1 mutants, five double mutants were constructed in an attempt to further enhance the catalytic efficiency of DTIC *N*-demethylation by CYP1A1. As shown in Table 5.6, no significant increase in CL_{int} was obtained with the CYP1A1 double mutants E256K/E161K, E256K/V228T, E256K/V322A, E256K/I386V, or E256K/I458V, compared to the wild-type CYP1A1 enzyme.

Table 5.6 Kinetic parameters of DTIC *N*-demethylation by CYP1A1 double mutants.

Enzyme	V_{max} (pmol/min/pmol P450)	K_m (μM)	V_{max}/K_m (μL/min/pmol P450)
CYP1A1	28 ± 4	408 ± 43	0.069
E256K/E161K[a]	19.3	343	0.056
E256K/V228T[a]	23.0	426	0.054
E256K/V322A[a]	30.4	652	0.047
E256K/I386V[a]	45.1	767	0.059
E256K/I458V[a]	26.1	383	0.068

[a]K_m and V_{max} values for double mutants were obtained in duplicate. Rate data for DTIC *N*-demethylase activities were model fitted using the Michaelis-Menten equation.

The molar ratio of P450:OxR in the microsomal membranes of vertebrate liver can be as high as 20:1 (Estabrook et al. 1971). As noted in section 5.2.5.1, the P450:OxR ratio for the wild-type CYP1A1 was approximately 1:2.1. The P450:OxR ratio for wild-type CYP1A2 and all CYP1A1 mutants was in the range of 1:1.9 to 1:3.1 and as such these ratios are unlikely to contribute to the differences seen in DTIC *N*-demethylation activities.

5.3.5 Kinetic and structural analysis of DTIC activation

Kinetic data for DTIC activation by the wild-type CYP1A1 were best described by the Michaelis-Menten equation, while data for wild-type CYP1A2 were best described by the Hill equation (Figure 5.9). The negative cooperative kinetics observed with the wild-type CYP1A2 enzyme is likewise seen with the CYP1A1-S122T mutant, a mutant that was generated to be "CYP1A2-like" (Table 5.5).

Differences in the active-site residues between CYP1A1 and CYP1A2 are displayed in Table 4.1 (section 4.1). The kinetic parameters for DTIC *N*-demethylation by the CYP1A1-S122T mutant (V_{max} 23.3pmol/min/pmol P450, S_{50} 1132μM, n = 0.70) are reasonably similar to those documented for wild-type CYP1A2 (V_{max} 38pmol/min/pmol P450, S_{50} 1502 μM, n = 0.70). Relative to CYP1A2, the decrease in V_{max} observed for the CYP1A1-S122T mutant is most likely due to the mis-alignment of DTIC in the CYP1A1 active-site generated by aromatic contributions from Y259, which is substituted for leucine in CYP1A2. Confirmation of this interaction is additionally seen in the CYP1A1-S122A mutant, also well modeled by the Hill equation (r^2 = 0.996). Thus, the CYP1A1 residue located at position 122 (corresponding to residue 124 in CYP1A2) contributes to the negative cooperativity observed for DTIC *N*-demethylation by CYP1A2. The enzyme-substrate interaction that leads to negative cooperativity is thus not dependant on polarity but appears to rely on the terminal side-chain methyl which is absent in serine (see Appendix II). The kinetic parameters displayed in Table 5.5 identify that, relative to wild-type CYP1A1, it is primarily the binding characteristics (S_{50}) of DTIC that are altered in enzymes modeled by the Hill equation. Allosterism therefore creates a decrease in the hyperbolic nature of the V/[S] plots in this case causing negative homotropic cooperativity of substrate binding (n<1). In the CYP1A1-S122T mutant, the introduction of the methyl side-chain of threonine is sufficient to alter the active-site chemistry. Usually it is a 'modifier molecule' that changes the binding characteristics of the enzyme for the substrate (Palmer 1981). However, in this case, it is the altered chemistry of the active-site which has changed the binding characteristics of the enzyme for the substrate in the absence of a true modifier.

A switch to negative cooperative kinetics is also seen in the E166Q, D313A, D313N, T321G, T321P, and T321S mutants. Residues 166 and 321 are both in locations involved in electron transfer to the heme catalytic centre. The E166Q substitution is located in the D-helix on the outer surface of CYP1A1 and may influence protein-protein interactions between CYP1A1 and OxR (Figure 5.10a). Residue 321 is located in the I-helix and aids the alignment of water in the 'proton transfer groove' (Figure 5.10b). In addition to the structural influences that affect efficient electron transfer, it is likely a switch to negative cooperative kinetics occurs due to a substrate dependant change in the redox potential of the heme. It should be noted that, the T321G mutant displayed shift to Michaelis-Menten kinetics with Eres (section 4.3.5.1). Not surprisingly, the reactivity of DTIC *N*-demethylation is dependant on the charge state of the residue at 166 and also dependant on the polarity of the residue at position 321 (Table 5.5). Relative to all other enzymes displaying negative cooperative kinetics, the D313A and D313N substitutions showed considerable increases in S_{50}. Replacement of one of the terminally charged oxygen's of aspartate to an amino group had no effect on enzyme reactivity (Figure 5.10c). However, the tightness of substrate binding was greatly reduced primarily due to the charge states of both DTIC and N313 at pH 7.4. Less of an effect on S_{50} is seen with the alanine mutant, which removes the strong charge interaction between aspartate and DTIC.

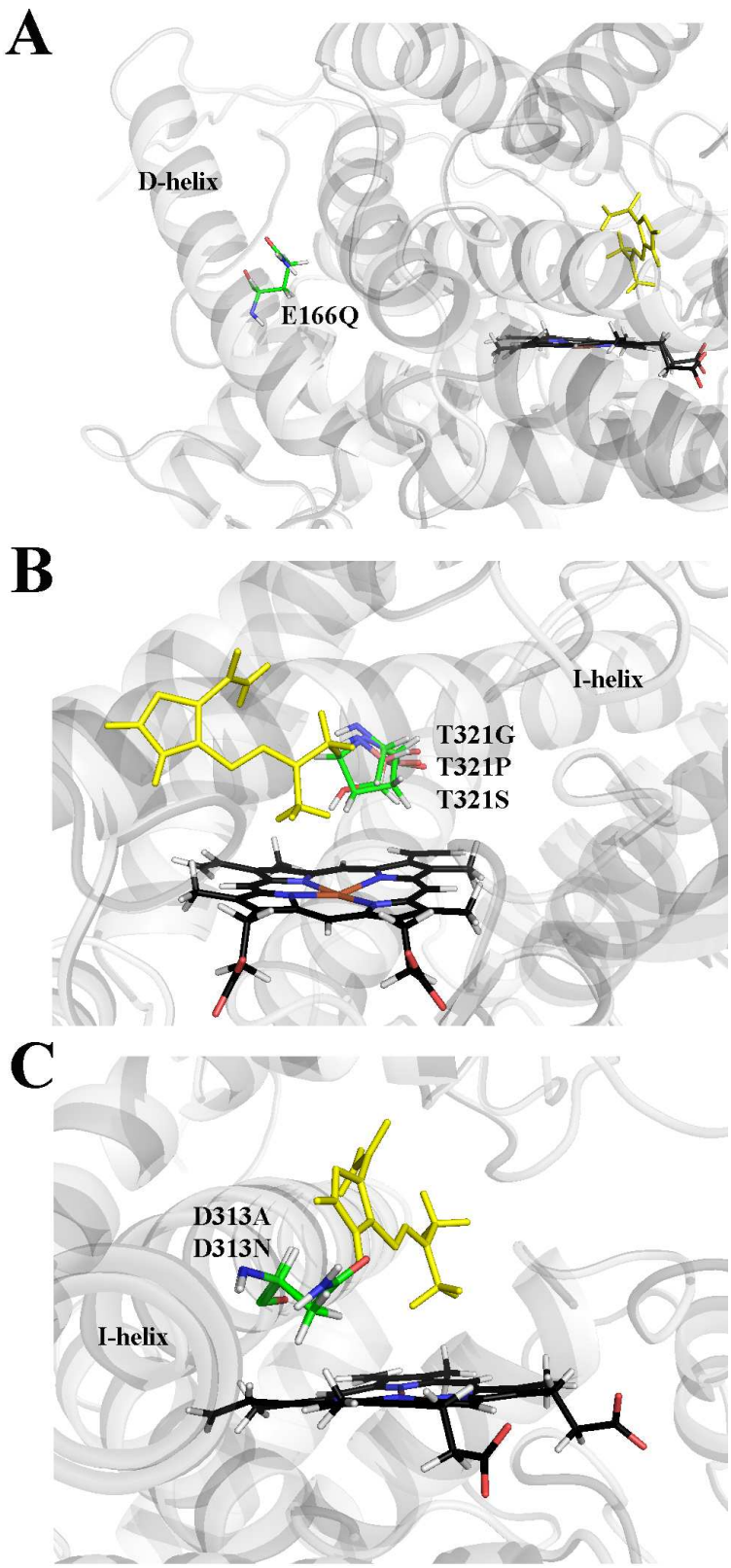

Figure 5.10 Mutations that affect electron transfer to the heme Fe. (a) CYP1A1-E166Q, (b) CYP1A1-T321G/T321P/T321S, and (c) CYP1A1-D313A/D313N. Mutant residues (green) are displayed relative to the wild-type CYP1A1 docked DTIC molecule (yellow).

5.4 Discussion

As a chemotherapeutic agent, DTIC has relatively poor clinical activity in human malignancies and results in numerous deleterious adverse effects. However, since its approval by the FDA in May 1975, DTIC is still the most effective single agent used when treating metastatic malignant melanoma and various sarcomas (Erdmann 2010). The pharmacology and pharmacokinetics of DTIC are well understood, but only a single study has investigated the metabolism of this compound by cytochromes P450 (Reid et al. 1999). Given that DTIC requires metabolic activation by P450's to become cytotoxic, an ideal opportunity exists to enhance the activation of DTIC using gene-based therapy. If the activation of DTIC can be localized to a specific tissue type, organ, or tumor environment, then in the presence of CYP1A specific inhibitors, higher concentrations of the inert prodrug may be systemically administered thereby alleviating prodrug activation in the liver and possible hepatic toxicity. GDEPT appears to be a valid approach to cancer therapy using the P450's for prodrug activation (El-Aneed 2004; Johannes et al. 2006; Kan, Kingsman & Naylor 2002; McFadyen, Melvin & Murray 2004; Scripture, Sparreboom & Figg 2005). However, this strategy only appears valid if the affinity between the prodrug and the drug-activating enzyme is high (low K_m). The present study was therefore undertaken to alter the catalytic efficiency of CYP1A1 for the activation of DTIC by utilizing the CYP1A1 homology model generated in Chapter 3.

The expression of CYP1A1 in *E. coli* is problematic due to low yields, normally 20-25nmol P450/mg protein (Guo et al. 1994), compared to most other P450's (usually 200-700nmol P450/mg protein) (Gonzalez & Korzekwa 1995; Jana & Deb 2005; Johnson et al. 2005a; Polasek et al. 2004; Polasek et al. 2006). As the vast majority of mutations were generated in residues that make up the CYP1A1 active-site, it was

important to optimize the expression system to ensure enough holo-enzyme was produced for each kinetic study. Expression of the wild-type CYP1A1 construct yielded on average 141pmol P450/mg protein (Table 5.4), which represents an approximate 3.5-fold greater amount of holo-CYP1A1 compared to the expressions undertaken in Chapter 4 (44pmol P450/mg protein). In turn, this was almost double that reported previously. All mutants expressed holo-enzyme in the range of 22-225pmol P450/mg protein, with V191M and D320A CYP1A1 mutants yielding ~220pmol P450/mg protein. Mutants that previously expressed poorly or displayed no holo-enzyme were found to express levels greater than 50pmol P450/mg protein using the method outlined in section 5.2.4.1. Interestingly, the expression of CYP1A2 (128pmol P450/mg protein) was roughly half that obtained using the method outlined by Polasek et al. (2006), suggesting that expression conditions were optimized primarily for CYP1A1 protein folding. The levels of OxR obtained using the optimized expression method shows no significant difference in yield compared to the method outlined in 4.2.2.1. Thus, the effect of the 'rare elements solution' is clearly P450 specific and potentially related to stabilization of the heme prosthetic group during incorporation and protein folding. Furthermore, increased levels of holo-enzyme obtained in expressions using low concentrations of chloramphenicol (used for clonal selection) identified that folding of nascent CYP1A1 may be inhibited by this antibiotic (Halpert, Miller & Gorsky 1985; Harnastai, Gilep & Usanov 2006).

The narrow, elongated shape of the CYP1A1 active-site (closed conformation) allows DTIC to orientate in close proximity to S122, F123, D313, A317, I386, Y259, and L496 residues. *In silico* docking experiments identified that alternate amino acid substitutions clearly affect the binding and orientation of DTIC in the CYP1A1

active-site (section 5.3.1.2). In the wild-type enzyme, DTIC places the α-carbon of the catalytic methyl at 5.6Å from the heme iron at an angle of 105.3º perpendicular to the heme plane with H-bonding predominantly seen from Y259 to the N2 aromatic nitrogen of the imidazole ring. Variations in the orientation and intermolecular bonding of DTIC are seen in all mutants (Table 5.3; Figure 5.7). In addition to Y259, H-bonding interactions of mutant enzymes utilized residues at positions 122, 313, and 316, and were clearly dependant on residue type. Interestingly, the energy favored orientation of DTIC in the E256K mutant revealed H-bonding not only from the N2 nitrogen of the imidazole but also from the H9 of the carboxamide to Y259. The observed stronger intermolecular interaction may be associated with the increase in affinity (i.e. decreased K_m; Table 5.5).

All enzymes catalyzed DTIC *N*-demethylation except for the I386G mutant, despite the presence of holo-P450. The lack of both DTIC *N*-demethylation and Eres *O*-deethylation (section 4.3.5.1) confirms earlier suspicions of introduced flexibility in the K-helix/β2-3 loop that impacts on the substrate access channel/active-site boundary. The CYP1A1 computational model identifies that F123 relaxes into a void in the CYP1A1 substrate access channel generated by the I386G mutant. The aromatic side-chain of F123 pivots inwards toward the heme prosthetic group by 25.4º. Although the distance between F123 and I396 in the wild-type (3.1Å) is the same as that between F123 and G386 in the mutant, it is the decrease in side-chain size (-2.2 Å) which results in constriction at the CYP1A1 substrate access channel/active-site boundary. Proline 387 is similarly affected by the glycine substitution in the I386G mutant. Interestingly, proline behaves like a Cβ-branched residue because its side-chain is connected to the protein backbone. In this sense, the proline at residue 387 can be considered chemically opposite to that of glycine

(substituted at residue 386), thus disrupting the substrate-access channels main-chain architecture. However, this disruption is clearly not sufficient to hinder heme incorporation during protein folding or the access of $CO_{(g)}$.

The kinetic parameters for DTIC *N*-demethylation by wild-type CYP1A1 (V_{max} 28pmol/min/pmol P450; K_m 408μM) and CYP1A2 (V_{max} 38pmol/min/pmol P450, S_{50} 1502μM, n = 0.70) were well described by the Michaelis-Menten and Hill equations, respectively. In contrast to this thesis, the DTIC *N*-demethylation data reported by Reid *et al.* (1999) were not critically model-fitted. The data obtained for CYP1A2 in this study were additionally fit using the Michaelis-Menten equation giving V_{max} = 27.85 ± 0.5pmol/min/pmol P450 and K_m = 655 ± 43μM. Interestingly, the K_m is in close agreement to that described by Reid *et al.* (1999) (V_{max} 13.8 ± 2.4pmol/min/pmol P450; K_m 659 ± 88μM). However, in this study, the Hill equation was distinguished from the Michaelis-Menten equation by use of the F-statistic, 95% confidence interval, r^2, and standard error of the parameter fit values. Furthermore, the concentration range of DTIC used in experiments performed by Reid *et al.* (1999) was limited to 200-2000μM due to the solubility of DTIC. However, this problem was overcome in the current study, and hence a wider concentration range (up to 6000μM) was investigated.

DTIC *N*-demethylation by the CYP1A1 E161K, E256K, and I458V mutants exhibited Michaelis-Menten kinetics (Figure 5.9), with decreases in K_m that doubled the catalytic efficiency (Table 5.5). By contrast, V_{max} values of the E161K, E256K, and I458V mutants were not significantly different to that of the wild-type CYP1A1 enzyme (P = 0.998, 1.000, and 0.348, respectively; Table 5.5). The mechanism(s) associated with the substrate binding affinity is different for each of these 'high-

active' mutants. The substitution of glutamate for lysine generates a swap in charge-state of the substituted amino acid (negative to positive), with a change in protonation at physiological pH (glutamate de-protonated, lysine protonated). It is difficult to interpret the structure-activity relationships in the E161K mutant from the static CYP1A1 model due to the possible involvement of cytochrome P450 OxR. However, it is well known that glutamate is frequently involved in the formation of salt-bridges, where it pairs with a positively charged amino acid to create a stabilizing hydrogen bond. Conversely, substitution to lysine disfavors the formation of salt-bridges with positively charged residues, although lysines may pair with a negatively charged amino acid (e.g. aspartate). Thus, the localized charge effects seen with the E161K mutant may aid a more complementary alignment of OxR via intermolecular interactions between the two proteins. The CYP1A1 homology model revealed that localized charge effects seen with the E256K substitution aids the formation of H-bonding to D253, giving rise to altered conformation of the main-chain of the G-helix. Most evident is the modification in side-chain orientation for F258 and Y259, which clearly impacts on substrate alignment in the CYP1A1 active-site (Figure 5.11). Amino acid substitution in the I458V CYP1A1 mutant distinctly affects the alignment of the heme prosthetic group (Figure 5.12). Importantly, Cβ-branching is preserved thus maintaining the rigid conformation of the β4-2/L-helix loop.

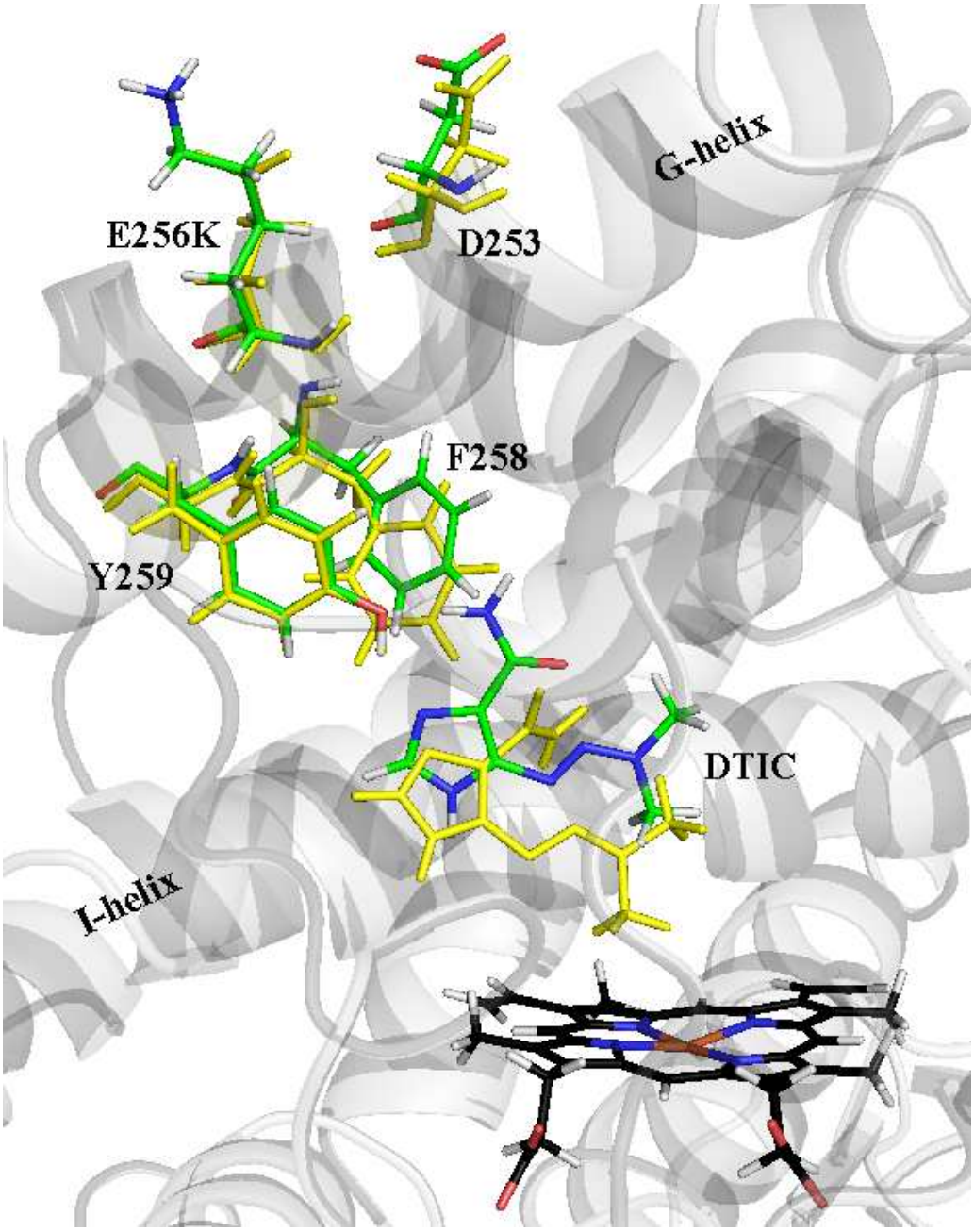

Figure 5.11 Effects on side-chain orientation for F258 and Y259 in the E256K CYP1A1 mutant. The E256K substitution modifies the side-chain orientation of F258 and Y259 (green) which alters DTIC alignment compared to the wild-type CYP1A1 enzyme (yellow).

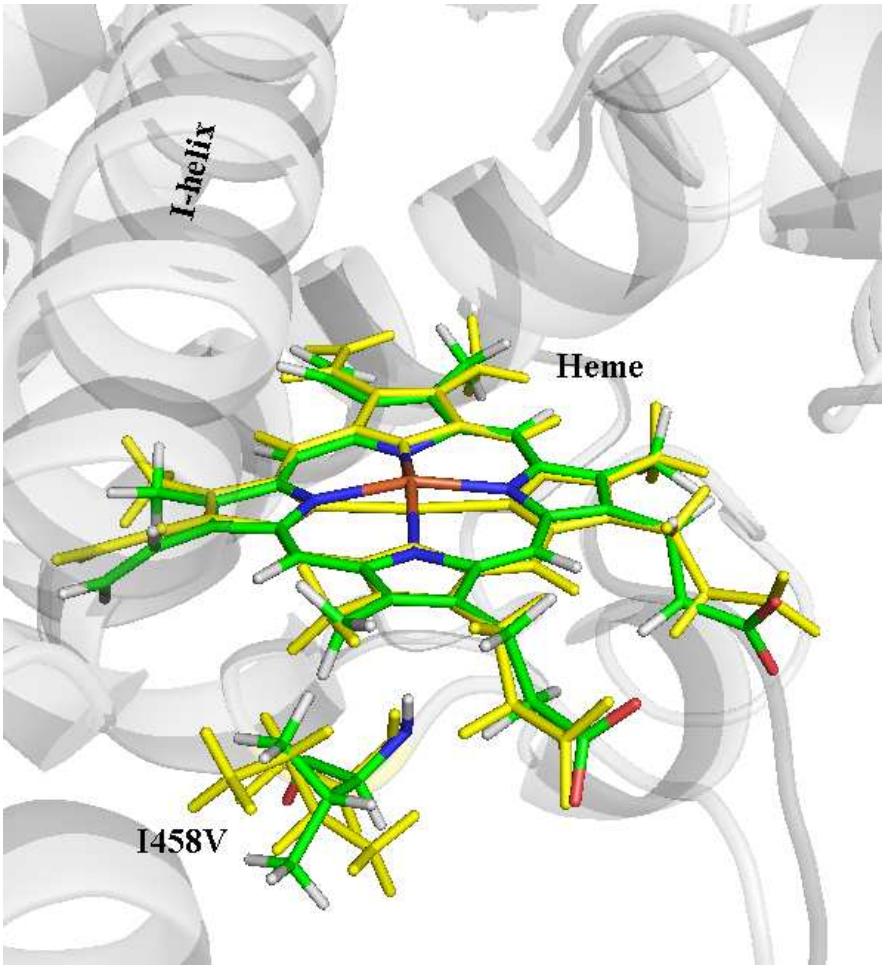

Figure 5.12 Effects on heme electrostatics in the I458V CYP1A1 mutant. Substitution to valine in the I458V CYP1A1 mutant (green) maintains the main-chain conformation yet alters the electrostatic environment about the heme prosthetic group relative to the wild-type (yellow).

Of the numerous genetic polymorphisms associated with CYP1A1 (section 1.3.5.2) three show moderate frequencies in the general population: CYP1A1*2A (*m*1) generated by the nucleotide change T3698C in the 3' flanking region; CYP1A1*2C (*m*2) generated by the nucleotide change A2455G in the CDS forming I462V; and CYP1A1*4 (*m*4) generated by the nucleotide change C2453A in the CDS forming T461N (Table 1.2). Interestingly, the *m*1 genotype correlates with lung cancer (Kawajiri et al. 1990). Furthermore, studies in Japanese populations revealed 97% linkage of the *m*4 polymorphism to the *m*2 genotype (pVal; *m*2 = 0.972; assuming Hardy-Weinberg equilibrium), suggesting an increased susceptibility to lung cancer for carriers of the I462V mutation (Hayashi et al. 1991). However, studies in other ethnic groups do not support the Japanese findings (Cascorbi, Brockmoller & Roots 1996; Nebert, McKinnon & Puga 1996). Interestingly, *in vitro* studies investigating CYP1A1 dependant EROD activity and the 3-hydroxylation of benzo(a)pyrene showed no differences in kinetics between the I462V and wild-type enzymes (Persson, Johansson & IngelmanSundberg 1997), although differential metabolic activation of 17β-estradiol and estrone was shown to be dependant on CYP1A1 genotype (Kisselev et al. 2005). Thus, the influence of CYP1A1 polymorphism on drug metabolism is substrate dependant. In Caucasians, the I462V and T461N polymorphic variants are present in 2.67% and 2.95% of the population, respectively (Cascorbi, Brockmoller & Roots 1996).

To my knowledge, this is the first study to characterize the kinetics of DTIC *N*-demethylation by the CYP1A1*2C (*m*2; I462V) and CYP1A1*4 (*m*4; T461N) polymorphic variants. A decrease of approximately 30% in catalytic efficiency was observed for both mutants, most likely arising from altered electrostatics around the heme prosthetic group. Furthermore, a statistically significant increase in K_m was

observed with the T461N mutant ($P<0.05$). Thus, patients with malignancies who carry either polymorphism may not respond as well to DTIC treatment compared to those expressing the wild-type enzyme.

In summary, this work has demonstrated that E161K, E256K, and I458V substitutions in human CYP1A1 can enhance activation of the chemotherapeutic agent DTIC via the *N*-demethylation pathway. Kinetic analysis of DTIC *N*-demethylation by CYP1A1 and CYP1A2 revealed Michaelis-Menten and negative cooperative Hill kinetics, respectively. Combination of the kinetic analyses with the *in silico* docking data has permitted interpretation of the structure-activity relationships of this enzyme-substrate pair.

CHAPTER 6
CHEMOSENSITIVITY OF MAMMALIAN CELLS TO DTIC ACTIVATION

6.1 Introduction

Metabolism by P450 enzymes modulates the activity of numerous chemotherapeutic agents (Table 6.1). The objective of current cancer therapy is to eliminate both primary tumors and metastases. However, in doing so, treatment is additionally associated with numerous toxicities due to systemic exposure to the active moiety.

Despite the availability of temozolomide, nitrosoureas, platinum analogs, and the microtubular toxins, DTIC continues to be the standard of care for most patients with metastatic melanoma (Bhatia, Tykodi & Thompson 2009; Chapman et al. 1999; Eggermont 2005). The recommended dosage and administration of DTIC treatment is 150-200mg/m^2/day i.v. for 5 days, or an alternate bolus i.v. dose of 800-1000mg/m^2 with doses repeated every 3-4 weeks (Baxter 2004). The adverse effects associated with DTIC treatment begin 0.5-1h after administration, indicating that toxic metabolites have readily entered the systemic circulation by this time.

Interestingly, few studies report the distribution of DTIC in humans (Alberts & Chen 1980; Breithaupt, Dammann & Aigner 1982; Loo et al. 1968; Luce et al. 1970). During isolated extremity perfusion experiments for the treatment of malignant melanoma of the extremities, concentrations of DTIC have been recorded from 150-500μg/mL perfusate. However, no evidence of AIC formation was observed. Yet, in isolated canine liver perfusion experiments, the metabolic conversion of DTIC to AIC was well demonstrated (Breithaupt, Dammann & Aigner 1982), as it is in *in*

vitro experiments with human liver microsomes (Long & Dolan 2001; Reid et al. 1999). Thus, the problem associated with prodrug activation in humans is the high level of P450's found in the liver (Code et al. 1997). The microsomal *N*-demethylation of DTIC in the liver is prominent since ~13% of total liver P450's is comprised of CYP1A2 (section 1.3.3). Low levels of CYP1A1 mRNA have been detected in human liver following induction by PAH's, however functional CYP1A1 protein has not been detected (section 1.3.5.1). Thus, involvement of extra-hepatic CYP1A1 in the activation of DTIC is far more desirable for increasing the concentration of AIC in peripheral tissues. One way to increase the concentration of AIC in peripheral tissues during treatment would be to enhance activation of DTIC in these regions and, at the same time, inhibit activation within the liver.

The E161K, E256K, and I458V mutant CYP1A1 enzymes described in Chapter 5 display enhanced catalytic efficiency for DTIC *N*-demethylation in isolated *in vitro* incubations using bacterially expressed enzyme. As such, these enzymes are potential candidates for use in GDEPT for the treatment of malignancies. However, further validation of their effectiveness in mammalian *in vitro* systems is required.

In order to validate the cytotoxic effect of each mutant, bioactivation needs to be exhibited in a mammalian cell line lacking endogenous CYP1A1. In this Chapter, the African Green Monkey kidney fibroblast cell line, COS-7, and the human skin malignant melanoma cell line, SK-MEL-28, were employed to determine the cytotoxicity and the kinetic parameters of DTIC *N*-demethylation by wild-type CYP1A1 and the E161K, E256K, and I458V mutants.

Table 6.1 Anticancer agents that are known substrates of the cytochromes P450.

Anticancer Agents	P450 Enzyme
bexarotene	2C9, 3A4
busulfan	3A4
cisplatin	2E1, 3A4
cyclophosphamide	2B6, 2C9, 3A4
cytarabine	3A4
dacarbazine	1A1, 1A2, 2E1
docetaxel	1B1, 3A4, 3A5
doxorubicin	2D6, 3A4
erlotinib	1A1, 1A2, 3A4
etoposide	1A2, 2E1, 3A4, 3A5
exemestane	3A4
fluvestrant	3A4
gefitinib	3A4
idarubicin	2D6, 2C9
ifosfamide	2A6, 2B1, 2B6, 2C9, 2C18, 2C19, 3A4, 3A5
imatinib	1A2, 2C9, 2C19, 2D6, 3A4
irinotecan	3A4, 3A5
letrozole	2A6, 3A4
paclitaxel	2C8, 3A4, 3A5
procarbazine	1A, 2B
tamoxifen	1A1, 1A2, 1B1, 2B6, 2C9, 2C19, 2D6, 2E1, 3A4, 3A5
teniposide	3A4, 3A5
thiotepa	2B1, 2C11
topotecan	3A4
toremifene	1A2, 3A4
tretinoin	2C8, 2C9, 2E, 3A4
vinblastine	3A4
vincristine	3A4
vinorelbine	3A4

Previous work conducted in this laboratory demonstrated the absence of endogenous CYP1A1 in COS-7 cells (Tassaneeyakul et al. 1992). The absence of CYP1A1 in SK-MEL-28 cells was similarly demonstrated by Matias *et al.* (2001), who characterized the P450 enzyme expression patterns of all 60 NCI human tumor cell lines. In addition to SK-MEL-28 cells, these authors tested the human malignant melanoma cell lines LOX-IMVI, M14, MALME-3M, SK-MEL-2, SK-MEL-5, UACC-62, and UACC-257. It was found that SK-MEL-28 cells have low 7-ethoxycoumarin *O*-deethylase (7-ECOD) (~1pmol 7-HC/min.mg) and coumarin 7-hydroxylase (~0.4pmol 7-HC/min.mg) activities, substantial 7-benzyloxyresorufin *O*-deethylase (7-BROD) activity (~40pmol resorufin/min.mg), and undetectable 7-EROD activity. These data indicate that SK-MEL-28 cells lack CYP1 enzymes. Interestingly, all melanoma cell lines displayed significant EROD activity apart from SK-MEL-28. Moreover, marginal OxR activity was observed in SK-MEL-28 cells (~0.003nmol OxR/mg protein) (Matias et al. 2001). The absence of endogenous CYP1A1 in both COS-7 and SK-MEL-28 cells implies these cell lines are ideal for use in cell sensitization assays using DTIC with cotransfected CYP1A1 and OxR.

One of the major concerns with gene therapy approaches utilizing P450's is the need to cotransfect OxR. The addition of exogenous OxR has been shown to further enhance the rate of intratumoral drug activation (Johannes et al. 2006), and has been demonstrated in cell culture along with numerous animal tumor models (Jounaidi & Waxman 2000). However, the cotransfection approach is limited as transfected tumor cells cannot be placed under selection (*in vivo*) to ensure the presence of both constructs as they are *in vitro* or in transplanted cell animal models. In mammalian systems, this problem has been circumvented through use of internal ribosomal entry site (IRES) sequences to enable bicistronic expression of multiple

transgenes. However, the success of IRES-based gene expression in gene therapy is limited, primarily due to the excessive size of the polycistronic vectors and their notorious nonstoichiometric translation of the desired proteins (de Felipe et al. 2004; Provost, Rhee & Leach 2007).

An alternative approach uses the replication mechanism of positive-stranded RNA viruses such as the picornaviruses; poliovirus and foot-and-mouth disease virus. Picornaviruses encode all of their proteins within a single ORF. In the case of the foot-and-mouth disease virus, an 18 amino acid '2A' peptide directs peptide separation for each self-processing polyprotein. Thus, one way to generate stoichiometric amounts of heteromultimeric proteins is to separate each gene in the vector with a viral 2A or 2A-like peptide. 2A-like sequences are not proteolytic elements or substrates for cellular proteinases. The mechanism of 2A cleavage occurs during translation where the 2A peptide adversely interacts with the exit tunnel of the ribosome therefore 'skipping' synthesis of a glycine-proline peptide bond at the C-terminus of the 2A sequence (de Felipe et al. 2006; de Felipe et al., 2004). The nascent protein is released from the ribosome which can then resume translation of the downstream sequences. Table 6.2 lists the major viral 2A and 2A-like sequences.

The level of uncleaved 2A products during translation is documented as ~10% (de Felipe et al. 2006). Data reported by Holst *et al.* (2006) showed that addition of a glycine-serine-glycine (GSG) linker to the N-terminus of the 2A sequence reduced the level of uncleaved 2A products during translation to ~1% (Holst et al. 2006).

Table 6.2 Viral 2A and 2A-like sequences used for 'skipping' peptide bond formation at the C-terminus of the 2A peptide.

Virus	Virus Family	Host	2A or 2A-like Sequence
foot-and-mouth	*Picornavirida*	mammals	-PVKQLLNFDLLKLAGDVESNPG*P…
equine rhinitis A	*Picornavirida*	mammals	----QCTNYALLKLAGDVESNPG*P…
porcine teschovirus-1	*Picornavirida*	mammals	-----ATNFSLLKQAGDVEENPG*P…
thosea asigna virus	*Tetraviridae*	insects	------EGRGSLLTCGDVEENPG*P…

*Site of peptide bond skip. Taken from (de Felipe et al. 2006).

Lengler *et al.* (2005) were the first to employ the 2A sequence with P450's, where the 2A cleavage of CYP2B1 and different fluorescent tags were used to track expression levels in HEK293 cells (Lengler et al. 2005). Moreover, 2A skipping has been shown in retrovirus and adeno-associated virus gene therapy strategies for the expression of reporter proteins in transient or stable cell lines and in animals (Szymczak et al. 2004; Wargo et al. 2009; Yang et al. 2008). However, it has not been used in GDEPT to express a P450 with its redox partner. The use of expression vectors containing the CYP1A1-2A-OxR ORF would enable the transfection of a single small construct into COS-7 and SK-MEL-28 cells whereby a 1:1 stoichiometric amount of each protein is translated. In addition, use of the 2A-peptide would alleviate the transfection constraints placed on gene therapy strategies which require the independent co-expression of multiple viral vectors.

The general aim of this Chapter is to undertake kinetic and cell sensitization assays using DTIC in COS-7 and SK-MEL-28 cell lines. The 'high active' CYP1A1 enzymes described in Chapter 5 will be individually transfected into each cell line as a single CYP1A1-2A-OxR ORF. Experiments will be undertaken to determine if the observed kinetic parameters of AIC formation correlates with cell survival.

Specific aims of this Chapter were to:

1. Measure the rate of multiplication and growth of COS-7 and SK-MEL-28 cells.
2. Generate the desired mutant expression constructs containing the CYP1A1-2A-OxR motif and prepare stable cell lines in COS-7 and SK-MEL-28 cells.
3. Determine the CYP1A1:OxR expression ratio.
4. Characterize the kinetic parameters for DTIC *N*-demethylation by wild-type and mutant CYP1A1 proteins stably expressed in COS-7 and SK-MEL-28 cells.
5. Use the sulphorhodamine B (SRB) assay to detect the cytotoxicity of SK-MEL-28 cells transfected with wild-type CYP1A1 and CYP1A1 mutants with enhanced catalytic efficiency.
6. Determine if the cytotoxic effect seen in (5) is cytostatic or cytocidal.

6.2 Materials and methods

6.2.1 Cloning of viral-2A fusion constructs

Generation of the CYP1A1-2A-OxR ORF utilized cDNA encoding the full length CYP1A1 gene (GenBank Accession No. NM_000499) and the full length OxR gene (GenBank Accession No. NM_031576).

6.2.1.1 CYP1A1-2A-OxR primer design

The pEF-IRES(5) expression plasmid containing the *porcine teschovirus*-1 viral-2A cleavage sequence (2A) and the OxR CDS was achieved by nested PCR. The pCW ori(+) 17α-CYP1A1 (wild-type and mutants) and pACYC OmpA-rOXR DNA templates were used in conjunction with the oligonucleotides listed in Table 6.3. All oligonucleotides were synthesized by Sigma-Genosys (Sigma-Aldrich; Sydney, Australia) and purified by PAGE gel electrophoresis.

6.2.1.2 Nested PCR conditions

All PCR reactions were carried out using the reaction components outlined in section 2.2.3.3.

6.2.1.3 Nested PCR cycling parameters

All reactions were carried out for a total of 35 cycles using a Robocycler® Gradient 96 PCR machine (Stratagene, CA, USA) thermal cycler. During the first cycle, *Pfu* HS Ultra II Polymerase (Stratagene, CA, USA) was activated by incubation at 95ºC for 2min. All subsequent cycles consisted of denaturation of the template at 95ºC for

1min, primer annealing across a temperature gradient of 56-67ºC for 45sec, polymerization and extension at 72ºC for 2min, and in the final cycle, a conclusive strand extension at 68ºC for 5min. The products obtained from all annealing temperatures were pooled.

6.2.1.4 Nested template construction

Generation of the linear CYP1A1-2A-OxR construct (Figure 6.1) was achieved in three stages. Stage 1 utilized the primer pairs For_1A1-2A/Rev_1A1-2A and For_OxR-2A/Rev_OxR-2A with 17α-CYP1A1 (wild-type and mutants) and pACYC OmpA-rOXR DNA templates, respectively. Products generated from CYP1A1 templates (1589bp) were digested with *XhoI* and *BamHI* restriction enzymes and subsequently gel purified using the method outlined in section 2.2.2.7. Stage 2 utilized the primer pair For_OxR-2A_2/Rev_OxR-2A with the gel purified OxR product generated in stage 1 (2082bp). Finally, stage 3 utilized the primer pair For_OxR-2A_3/Rev_OxR-2A with the gel purified OxR product generated in stage 2 (2105pb) producing the linear 2A-OxR fragment (2130bp). The 2A-OxR fragment and the pEF-IRES(5) expression plasmid were digested with *BamHI* and *EcoRV* restriction sites (Figure 6.1), the fragment gel purified, and subsequently ligated using the method outlined in section 2.2.2.8. Following transformation and plasmid amplification (sections 2.2.2.3, 2.2.2.4, and 2.2.2.5), the purified and digested cDNA's encoding the CYP1A1 wild-type and E161K, E256K, I386V, T461N, I462V, and I458V CYP1A1 mutants were shuttled into the pEF-IRES 2A-OxR construct utilizing *XhoI* and *BamHI* restriction sites, thus generating the pEF-IRES CYP1A1-2A-OxR expression plasmids (Figure 6.2a). In addition, the full-length CYP1A1-2A-OxR inserts (wild-type and mutants) from the pEF-IRES CYP1A1-2A-

OxR constructs were digested with *XhoI* and *EcoRV* (blunt), ligated into the pCI-neo mammalian expression plasmid digested with *XhoI* and *SmaI* (blunt), forming the pCI-neo CYP1A1-2A-OxR expression plasmids (Figure 6.2b). All constructs were confirmed by DNA sequencing on both strands (ABI 3130-XL DNA sequencer, Applied Biosystems, Victoria, Australia).

6.2.2 Tissue culture

6.2.2.1 Cell lines

COS-7 and SK-MEL-28 cell lines were used for the stable expression of CYP1A1-2A-OxR wild-type and mutant proteins. The COS-7 cell line (Figure 6.3a) originates from the CV-1 cell line from the kidney of an African green monkey (*Cercopithecus aethiops*) and was developed via transformation with an origin defective mutant of SV40 that codes for the wild-type virus T-antigen (ATCC cat. no. CRL-1651). COS-7 cells display adherent fibroblast morphology. The human malignant skin melanoma cell line SK-MEL-28 (Figure 6.3b) is a monoclonal continuous culture obtained from a 51 year old male human (ATCC cat. no. HTB-72). SK-MEL-28 cells display polygonal morphology and are tumorigenic in nude mice.

Table 6.3 Primers used for generating the CYP1A1-OxR viral-2A constructs by nested PCR.

Primer Name	Oligonucleotide sequence (5' to 3')
For_1A1-2A	AACCGCTCGAGCGGACCGGTGCCGCCACCATGCTTTTCCCAATCTCCATG
Rev_1A1-2A	GCTAAAGTTGGTCGCGCCGGATCCAGAGCGCAGCTGCATTTGGAAGTGC
Rev_1A1-2A-OXR	GGTTTTCTTCCACATCGCCCGCCTGTTTCAGCAGGCTAAAGTTGGTCGCG
For_OXR-2A	ATGTGGAAGAAAACCCGGGCCCGATGGGGGACTCTCACGAAGACACCAG
For_OXR-2A_2	TAGCCTGCTGAAACAGGCGGGCGATGTGGAAGAAAACC
For_OXR-2A_3	GCTCTGGATCCGGCGCGACCAACTTTAGCCTGCTGAAACA
Rev_OXR-2A	TTAGCGATATCGCACTAGTCTACTAGCTCCACACATCTAGTGAGTAGCGG

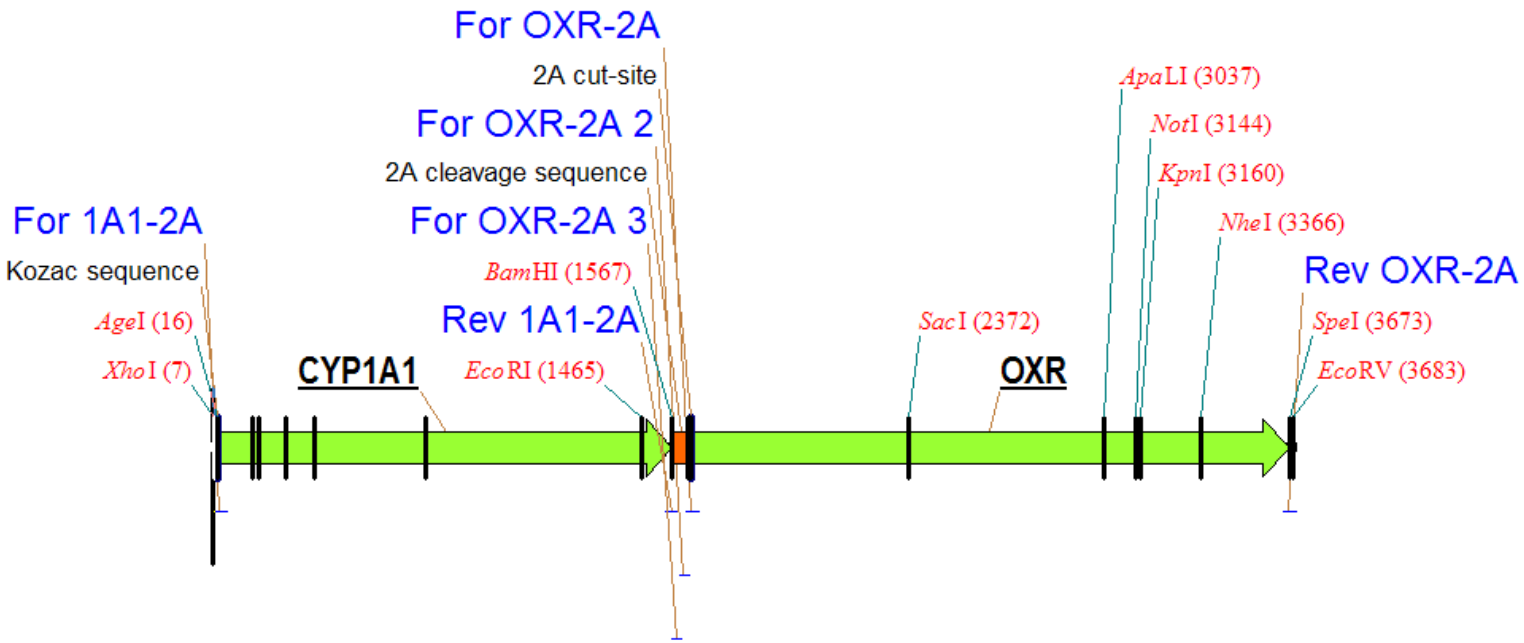

Figure 6.1 Linear CYP1A1-2A-OxR ORF constructed using nested PCR. Oligonucleotides used in nested PCR (blue), CYP1A1 and OxR CDS (green arrows), viral-2A cleavage sequence (orange), and unique restriction enzyme sites (red).

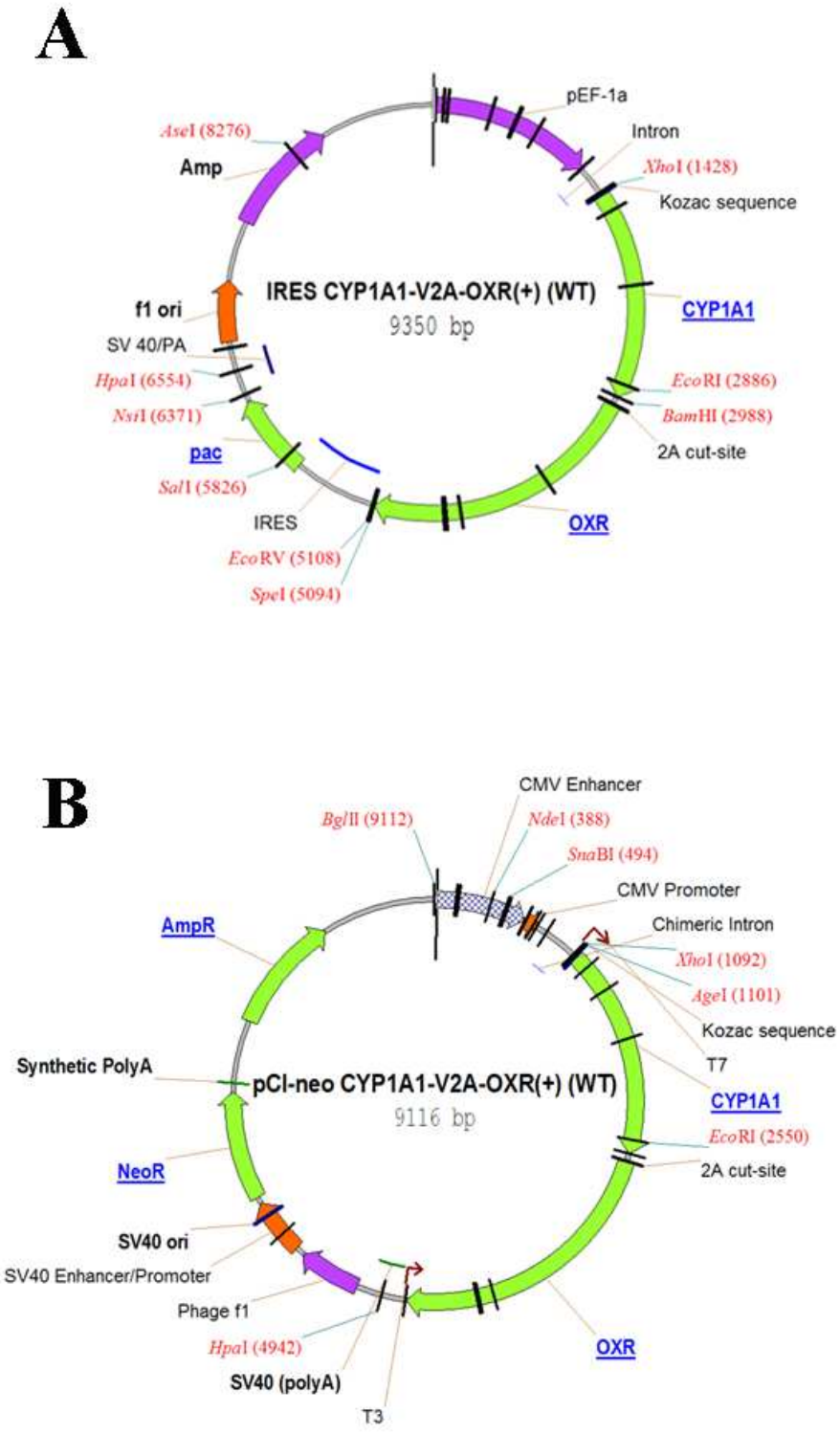

Figure 6.2 Mammalian expression constructs containing the CYP1A1-2A-OxR ORF. (a) The pEF-IRES CYP1A1-2A-OxR expression construct utilizing puromycin resistance (pac) and (b) the pCI-neo CYP1A1-2A-OxR expression construct requires selection with G418 (geneticin; NeoR).

6.2.2.2 Conditioned media

All cells were cultured in sterile tissue culture flasks (non-pyrogenic) in Dulbecco's Modified Eagle Medium (DMEM) (high glucose/L-glutamine/pyroxidine hydrochloride; Invitrogen®), penicillin/streptomycin solution (GIBCO®, penicillin G +5000 Units/mL, streptomycin sulphate +5000µg/mL), 1% (v/v) MEM non-essential amino acids (100x solution, Invitrogen®), and 1% (v/v) MEM sodium pyruvate (100x solution, Invitrogen®) containing 10% (v/v) foetal bovine serum (FBS; TRACE® MultiSer™ sterile). Stable cell lines transfected with the pEF-IRES and pCI-neo mammalian expression plasmids utilized 'complete' DMEM containing 0.5µg/mL puromycin (Sigma-Aldrich, NSW, Australia) and 1000µg/mL G418 (Geneticin; Invitrogen, VIC, Australia), respectively.

6.2.2.3 Culture conditions

All cells were grown to 90-95% of their dividing capacity (confluence) in 175cm^2 sterile Nunclon™ Δ surface tissue culture flasks by incubation at 37ºC in a controlled humidified atmosphere of 10% CO_2 and 90% air (IR Sensor; Sanyo Electrical Biomedical Co. Ltd., Japan). To subculture or 'split' cells, the conditioned medium was decanted and the cultured cells rinsed with PBS (8mL; pre-warmed to 37ºC) then covered with pre-warmed (37ºC) 1x trypsin solution (3mL; Invitrogen®). Excess trypsin was decanted and the cells incubated for 5min at 37ºC, after which prostatic cells were dislodged from the base of the tissue culture flask. Fresh 'complete' medium (20mL; pre-warmed to 37ºC) was added to the cells. Four mL of the media/cell suspension was removed and transferred to a 175cm^2 sterile tissue culture flask containing 16mL of 'complete medium' (1:5 dilution) for further culturing. The new passage was incubated at 37ºC until confluency again reached 90-95%.

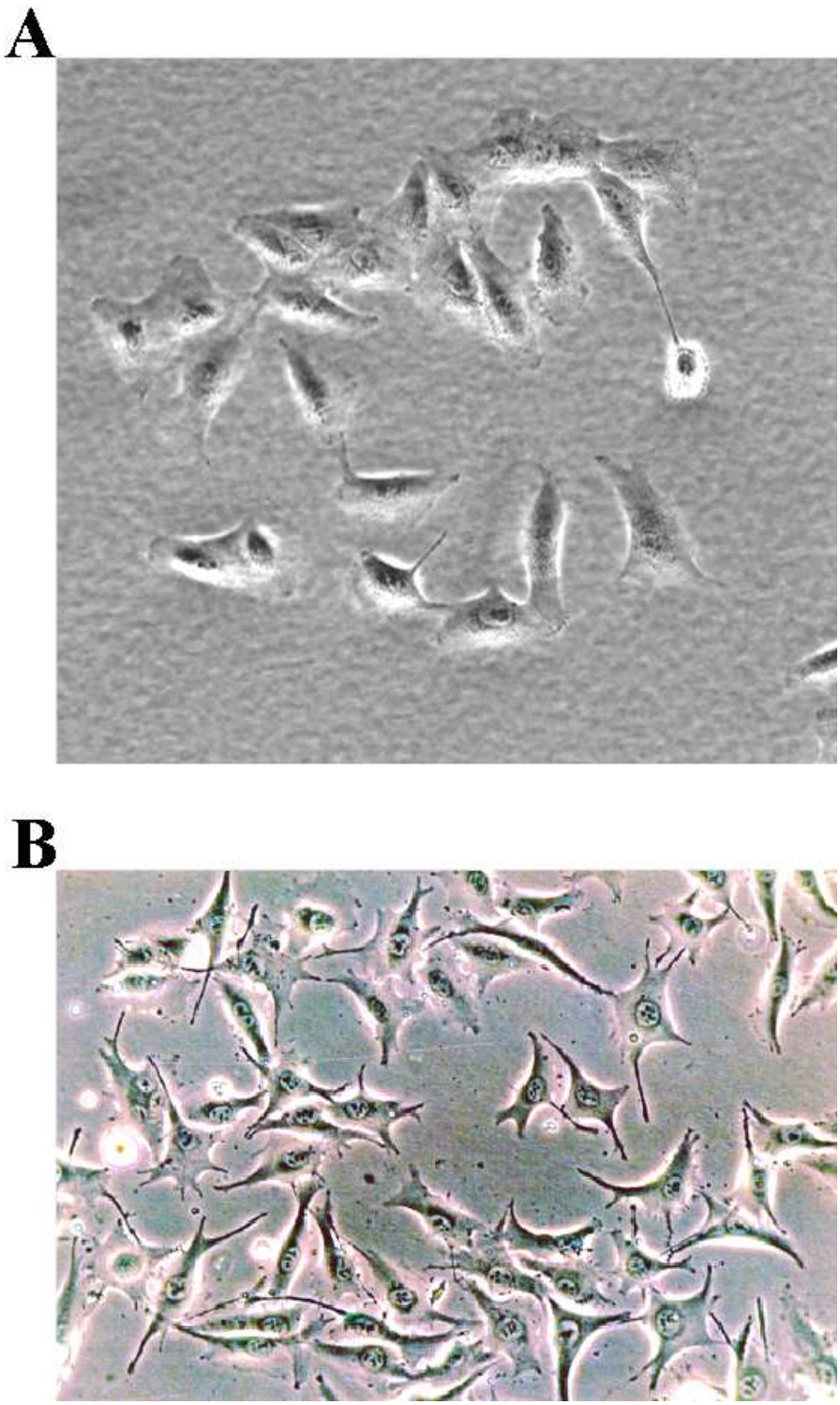

Figure 6.3 Mammalian COS-7 and SK-MEL-28 cells. (a) The COS-7 kidney cell line from an African green monkey and (b) the human malignant skin melanoma cell line SK-MEL-28.

6.2.2.4 Generation of transient cell lines

Transient cell lines coexpressing CYP1A1 (wild-type and mutant) and OxR proteins were generated in the absence of the selectable antibiotic. Cells were incubated for 48h post transfection (section 6.2.3.1) prior to harvesting (section 6.2.2.6).

6.2.2.5 Generation of stable cell lines

Stable cell lines constitutively expressing the CYP1A1 wild-type and mutant proteins were prepared by diluting cells (1:10) in the desired antibiotic 48h post transfection. G418 (1000μg/mL) was used as the selective agent for cells that contained the pCI-neo vector. G418 is toxic to prokaryotic and eukaryotic cells and blocks polypeptide synthesis by inhibiting elongation. Resistance to G418 is conferred by the neo gene encoding an aminoglycoside 3'-phosphotransferase derived from the *Micromonospora rhodorangea* bacterium.

6.2.2.6 Cell harvesting

The cell-conditioned growth medium was decanted and cells rinsed with PBS (8mL; pre-warmed to 37ºC) then covered with pre-warmed (37ºC) 1x trypsin solution (section 6.2.2.3). To inactivate trypsin, transfected cells were resuspended in 10mL of 'complete' DMEM containing the desired selectable antibiotic. The cultured cells were subsequently centrifuged at 1,912x *g* (3,000 rpm; Sigma laboratory 4K15) for 10min at 4ºC. The supernatant fraction was decanted and the cell pellet resuspended in pre-chilled PBS, followed by a further spin at 1,912x *g* (3,000 rpm) for 10min at 4ºC. The PBS washing process was repeated twice. PBS was finally decanted and the cultured cells of each 175cm^2 flask resuspended in harvest buffer (500μL; 100mM

phosphate buffer, K_2HPO_4/KH_2PO_4; pH 7.4). Harvested cells were frozen at -80ºC until further use.

Harvested cells were allowed to thaw on ice, supplemented with protease inhibitors (20µL of 30mg/mL stock per 500µL suspension), then lysed by sonicating (1sec bursts separated by 60sec cooling) 6 times on a salted ice-bath, with the sonicator set to 'continuous' with 40% duty cycle. Lysed cells were centrifuged at 15,000x *g* (13000 rpm; Beckman 18 centrifuge) for 1min at 4ºC. The resulting supernatant fraction was carefully decanted and stored at -80ºC until further use.

Cell Freezer stocks were prepared by aspirating the DMEM and rinsing in PBS (8mL; pre-warmed to 37ºC). The cells were then covered with 1x trypsin solution (pre-warmed; 37ºC) and incubated at 37ºC for 5min (section 6.2.2.3). To inactivate trypsin, cells were resuspended (by gentle pipetting) in 10mL of 'complete' DMEM containing the desired selection antibiotic. The cultured cells were then centrifuged at 212x *g* (1,000 rpm; Sigma laboratory 4K15) for 5min at room temperature. The supernatant fraction was decanted and the cell pellet from each 175cm^2 culture flask resuspended in 5mL FBS/10% DMSO solution. Cell suspensions were subsequently aliquoted into 1.0mL cryotubes (NUNC™) and stored at -80ºC overnight and then transferred to long term storage under liquid N_2.

6.2.3 Protein expression and immunochemical detection

6.2.3.1 Transfection of plasmid DNA

Plasmid DNA was transfected into cells in a 6-well format. Cells were plated at a density of 1.0x 10^5 cells per well in 2.0mL of complete DMEM (without antibiotic) two days prior to transfection so that cells were between 50-80% confluent on the

day of transfection. The growth medium was replaced with 2.0mL of fresh DMEM post-transfection. Plasmid DNA for transfection (10μg) was diluted into 500μL of Opti-MEM® I Reduced Serum Media (Invitrogen®) without serum, to which PLUS™ Reagent (10μL; Invitrogen®) was added. The DNA/Opti-MEM®/PLUS™ solution was gently mixed and subsequently incubated for 10min at room temperature. Lipofectamine LTX™ Reagent (25μL; Invitrogen, Victoria, Australia) was added to each DNA/Opti-MEM®/PLUS™ solution and the mixture incubated for 30min at room temperature to form the DNA-Lipofectamine LTX™ complexes. After incubation, the DNA-Lipofectamine LTX™ complexes were delivered directly to each well where transfection occurred. Plates were incubated at 37ºC in a CO_2 (10%) incubator for 24h, after which time the growth medium was replaced with 2.0mL of fresh pre-warmed DMEM (without antibiotic). Twenty-four hours post-transfection, cells were dislodged from each well by trypsinization (200μL), resuspended in 10mL of fresh pre-warmed DMEM and subsequently transferred into a T75 tissue culture flask (75cm^2). Cells were incubated overnight prior to replacing the growth medium with DMEM containing G418 (1000μg/mL) or puromycin (0.5μg/mL), which allowed for the selection of stable transfectants. Cells were maintained at 37ºC in a CO_2 (10%) incubator and the growth medium (containing the selectable antibiotic) replaced every 3-4 days until the cells were harvested from T175 flasks (175cm^2) at 90-95% confluency (section 6.2.2.6).

6.2.3.2 Quantification of holo-CYP1A1 and OxR proteins

The total protein contained in mammalian cell lysates was determined by the method of Lowry *et al.* (1951) (section 2.2.4.4) with OxR activity calculated with cytochrome *c* as an alternative electron acceptor using 0.5mg/mL protein (amended

from section 2.2.4.6). The holo-P450 content was not determined using cytochrome P450 reduced difference spectroscopy (2.2.4.5) due to the presence of endogenous P450s other than CYP1A1 (section 6.1). Therefore, enzyme concentrations from mammalian cell lysates were estimated based on the peak area of AIC formation relative to that of the analogous bacterial enzyme (17α-CYP1A1 wild-type and mutants). The use of mammalian cells transfected with a 2A-OxR control (i.e. no CYP1A1 CDS) ensured AIC formation was specific to holo-CYP1A1. AIC formation was determined using the method outlined in section 6.2.3.3, except incubation mixtures contained 400μg (2mg/mL) of mammalian cell lysate and 6000μM DTIC. AIC formation was measured using the method described in section 5.2.6.1. The concentration of holo-CYP1A1 in mammalian cell lysates was estimated using the derivation in equation 6.1.

(a) $$\mathrm{PAR} = \frac{\mathrm{PA}_{[S_j]}\ \text{known}}{\mathrm{PA}_{[S_j]}\ \text{unknown}}$$

(b) $$\mu\text{g to give known}_{[\mathrm{CYP}]} = \mathrm{PAR} \times [\mathrm{lysate}_{\mathrm{inc}}] \qquad \text{(eq. 6.1)}$$

(c) $$\text{pmol CYP/}m\text{g lysate} = \left(\frac{1000}{\mu\text{g to give known}_{[\mathrm{CYP}]}} \right) \times [\mathrm{known}_{\mathrm{CYP}}]$$

where PAR is the peak area ratio of AIC peak areas (PA) obtained using known and unknown holo-CYP1A1 concentrations at substrate concentration [S_j]; [$\mathrm{lysate}_{\mathrm{inc}}$] is the protein concentration (μg) of lysate in incubations with unknown CYP1A1

concentrations; and [known$_{CYP}$] is the known concentration of holo-CYP1A1 (pmol P450).

6.2.3.3 Detection of AIC formation by CYP1A1-2A-OxR

The measurement of DTIC *N*-demethylation activity was conducted using the method described in section 5.2.5.1, except incubation mixtures contained 2mg/mL of expressed CYP1A1-2A-OxR.

6.2.3.4 Immunochemical detection of CYP1A1 wild-type and mutants

Equal amounts of total protein from each cell lysate (50µg) were subjected separately to SDS PAGE (section 2.2.6.1). Separated proteins were rectilinearly transferred onto nitrocellulose (section 2.2.6.2) and probed with anti-human CYP1A1 primary antiserum (1:3000 dilution) and anti-rabbit IgG (1:2000 dilution; H+L-HRP, 50% glycerol) as the secondary antibody (Pierce Biotechnology, Inc., Rockford, IL, USA), using bacterially expressed wild-type 17α-CYP1A1 (25µg) as a positive control. Membrane-bound peptides conjugated with HRP were detected by BM Chemiluminescence (Roche Diagnostics, Mannheim, Germany) and subsequently detected using the FUJIFILM LAS-400 image reader (version 2.0; FUJIFILM Life Science Corporation; Tokyo, Japan) (section 2.2.6.3).

6.2.4 Cytotoxicity assays

6.2.4.1 Determination of cell cycle time

The MultiTox-Fluor Multiplex Cytotoxicity Assay kit (Promega, NSW, Australia) was utilized to measure the total cell cycle time of SK-MEL-28 and COS-7 cells.

This was achieved by measuring the protease activity restricted to intact viable cells and was measured using a fluorogenic, cell-permeable, peptide substrate (glycyl-phenylalanyl-amino-fluorocoumarin; GF-AFC). The substrate enters the intact cells where it is cleaved by a live-cell protease to generate amino-fluorocoumarin (AFC). The fluorescent signal emitted by AFC is proportional to the number of living cells. The live cell protease becomes inactive upon loss of cell membrane integrity.

Cells were plated at densities of $2x10^3$, $4x10^3$, and $6x10^3$ cells/well (96-well format; n=3) and incubated at 37ºC in a CO_2 (10%) incubator for 12-120h, after which time the GF-AFC substrate (100µL) was added to the growth medium, mixed, and incubated a further 30min at 37ºC protected from light. The number of live cells was measured by fluorescence detection at excitation and emission wavelengths of 360 and 500nm, respectively (DTX 880 Multimode Detector; Beckman Coulter, NSW, Australia). The total number of live cells was calculated by comparison to a calibration curve prepared with SK-MEL-28 and COS-7 cells in the range of $1x10^3$ to $1.5x10^4$ cells/well.

6.3 Results

6.3.1 Determination of total cell cycle time

Determination of the cell cycle time is important to ensure the seeding density of cells for cytotocity experiments does not exceed the capacity of the 96-well plate over the incubation period. At higher densities, contact inhibition of cell growth occurs and nutrients from the medium can be exhausted too quickly, thereby affecting the experimental outcome. Figure 6.4 shows growth curves generated for each cell line. Table 6.4 lists the cell cycle times for cells at differing cell densities.

Not surprisingly, the log phase of each cell line was different with cell cycle times calculated between 36-60h for SK-MEL-28 cells and between 72-96h for COS-7 cells. The prolonged log phase evident in COS-7 cells accounts for the approximate doubling in cell number over all incubation periods compared to SK-MEL-28 cells. Interestingly, the doubling time at low cell density (2000 cell/well) in COS-7 cells (14h) is roughly three times faster than that observed for SK-MEL-28 cells (38h). Thus, cell interactions with neighboring cells regulate proliferation in both COS-7 and SK-MEL-28 cells, yet in opposite ways (Table 6.4). At low cell densities, SK-MEL-28 cells have a prolonged quiescent G_0 state, whereas COS-7 cells have a transient nonproliferative state.

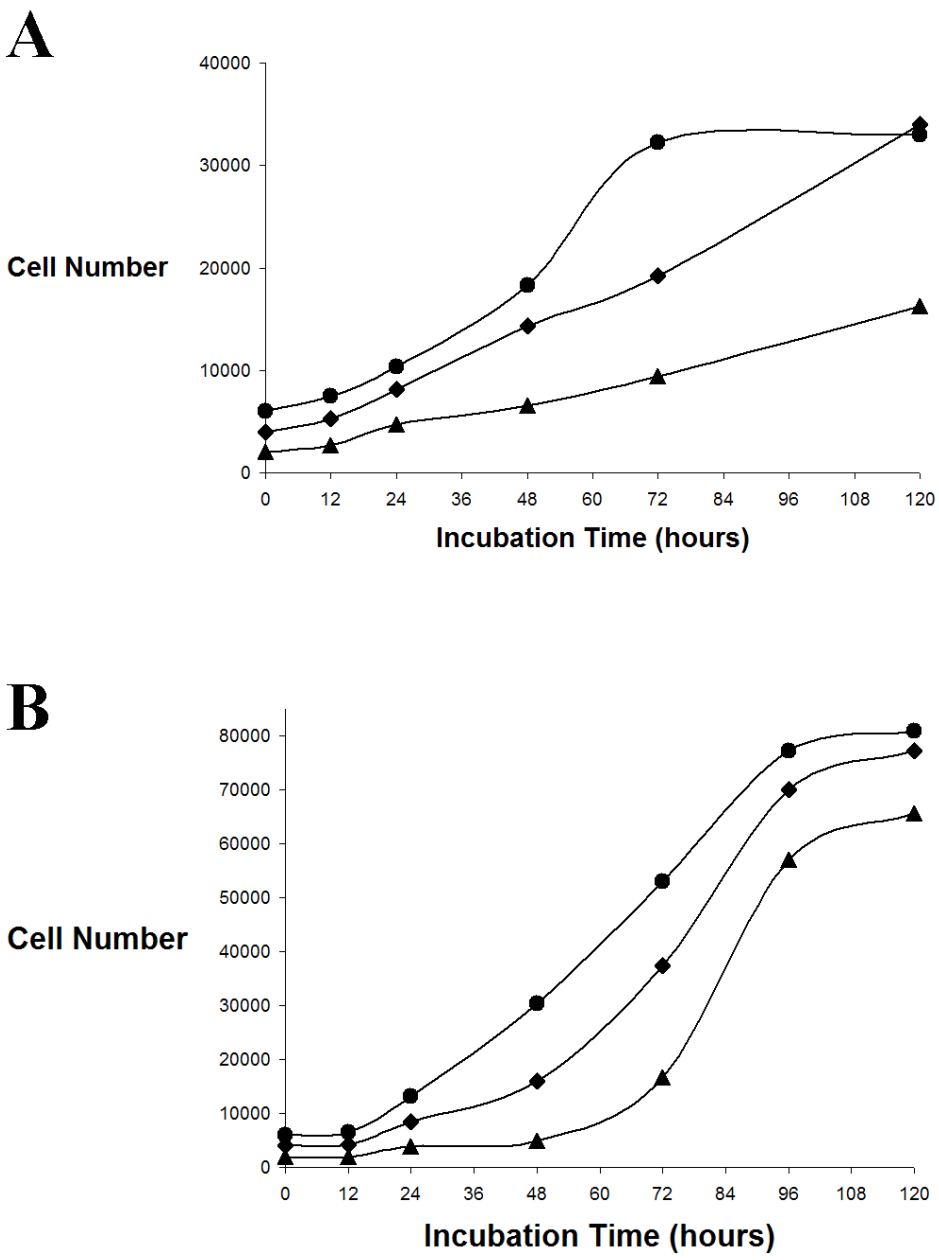

Figure 6.4 Cell cycle growth curves for (A) SK-MEL-28 and (B) COS-7 cells. Cells were incubated at densities of 2000(▲), 4000(◆), and 6000(●) cells/well and incubated from 12-120h.

Table 6.4 Cell cycle times for SK-MEL-28 and COS-7 cells.

Cell line	Cell doubling time (h)		
	2000 (cell/well)	4000 (cell/well)	6000 (cell/well)
SK-MEL-28	38	29	29
COS-7	14	26	33

6.3.2 Heterologous expression of CYP1A1 in COS-7 and SK-MEL-28 cells

The CYP1A1 wild-type, and mutants E161K, E256K, and I458V were transiently co-expressed with OxR using the CYP1A1-2A-OxR ORF in the pCI-neo mammalian expression plasmid (section 6.2.3.1). The expression of holo-enzyme achieved in each mammalian cell line was estimated from the formation of AIC via the *N*-demethylation of DTIC (section 6.2.3.2). The mean expression of all CYP1A1 constructs containing the CYP1A1-2A-OxR ORF was 6.3 (±0.5)pmol P450/mg protein with little variation observed between wild-type and mutant yields. Likewise, the level of co-expressed OxR displayed relatively little variation between wild-type and mutant enzyme expressions, with mean yields of 48 (±3.8)pmol reductase/mg protein. Thus, the molar P450:OxR ratio for all CYP1A1 expressions was approximately 1:7. In addition, a 2A-OxR control construct devoid of the CYP1A1 CDS confirmed the presence of expressed OxR (54pmol reductase/mg protein) but, as expected, displayed no holo-CYP1A1 in either cell line. Attempts to stably express CYP1A1 or OxR in the COS-7 or SK-MEL-28 cell lines were not successful. Immunoreactive CYP1A1 was detected in the CYP1A1-2A-OxR transiently transfected COS-7 and SK-MEL-28 cell lines (Figure 6.5a). However,

immunoreactivity was not observed in lysates prepared from stably expressed CYP1A1-2A-OxR (Figure 6.5b). A bacterially expressed recombinant CYP1A1 positive control indicated that experimental conditions and reagents were capable of detecting CYP1A1.

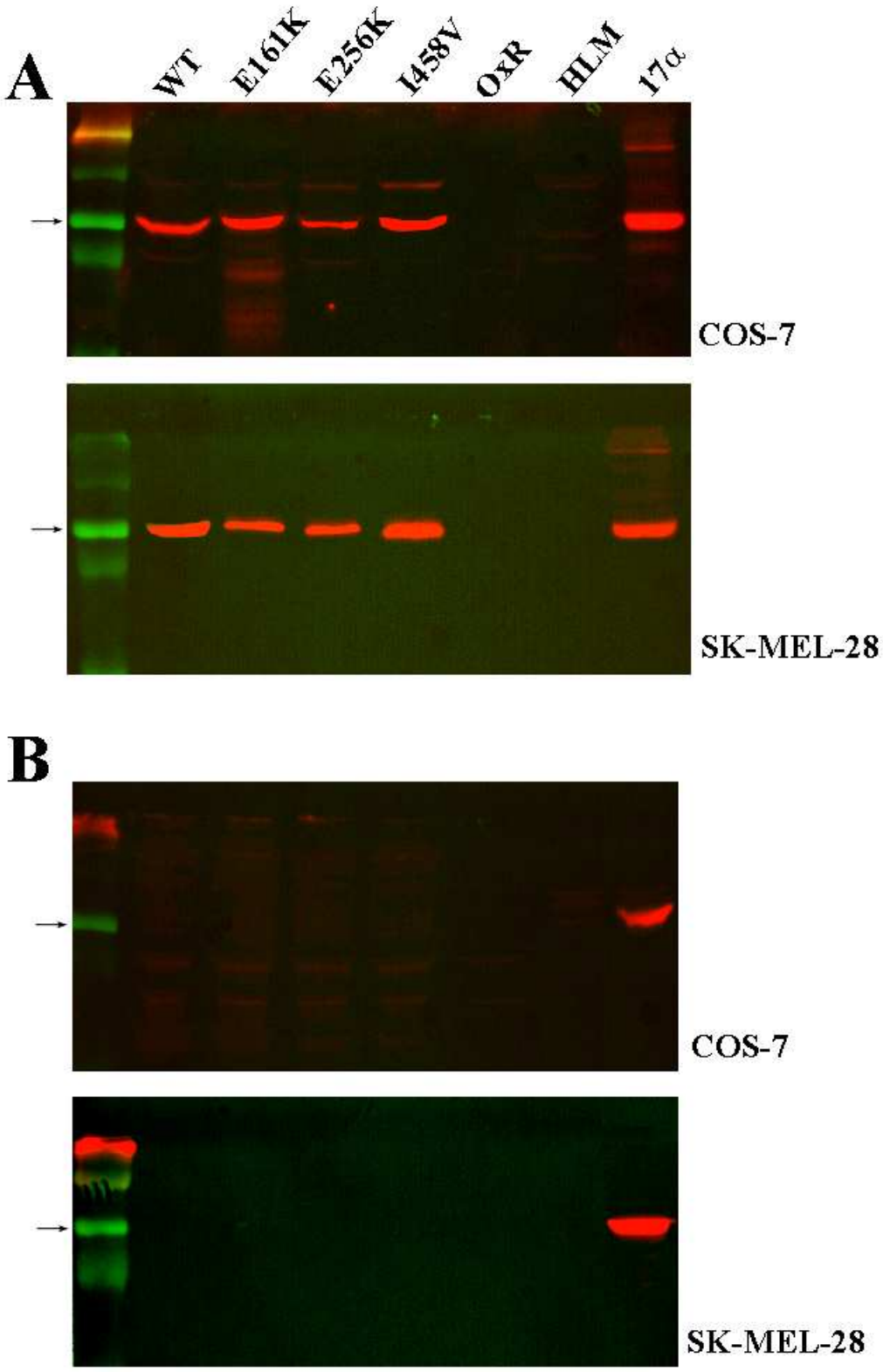

Figure 6.5 Immunoblot of (a) transiently expressed and (b) stably expressed wild-type and mutant CYP1A1 proteins in COS-7 and SK-MEL-28 cells. 100µg of the indicated cell lysates were resolved by SDS-PAGE, blotted to nitrocellulose, and probed with anti-CYP1A1 antiserum. Human liver microsomes (HLM) was used as a negative control and bacterially expressed 17α-CYP1A1(WT) acted as a positive control. Immuno-reactive bands are present at 58kDa (arrow).

6.4 Discussion

COS-7 and SK-MEL-28 cells were transfected with the mammalian expression plasmid, pCI-neo, encoding the CYP1A1-2A-OxR ORF comprising either the wild-type, E161K, E256K, or I458V coding regions. The transient expression of CYP1A1 and OxR was achieved in both COS-7 and SK-MEL-28 cells, albeit at markedly reduced levels compared to bacterially expressed protein (section 5.3.2). The picornavirus 2A cleavage peptide was emplyed to ensure 1:1 translation of CYP1A1 and its redox partner, OxR. Interestingly, the observed molar ratio of holo-CYP1A1 to OxR was 1:7, suggesting heme incorporation and protein folding may be unproductive under heterologous expression conditions in these cell lines compared to bacterial heterologous expression systems.

The generation of stable cell lines co-expressing wild-type, E161K, E256K, and I458V CYP1A1 with OxR was required to characterize the kinetic parameters for DTIC *N*-demethylation in COS-7 and SK-MEL-28 cells. Ideally, the kinetics of DTIC *N*-demethylation obtained with bacterially expressed wild-type and mutant CYP1A1 enzymes should be similar in COS-7 and SK-MEL-28 cells. However, differences in enzyme sources are known to affect kinetic parameters. For example, single-enzyme Michaelis-Menten kinetics have been reported for phenacetin *O*-deethylation by CYP1A2 in transiently transfected COS-7 cells (Tassaneeyakul et al. 1993), yet in studies utilizing *E. coli* expressed CYP1A2, data were best described by the negative-cooperative Hill equation (Polasek, Elliot & Miners 2006). Likewise, Michaelis-Menten data reported for heterologously expressed CYP2C9 in Supersomes, Baculosomes, reconstituted, and purified enzyme systems exhibited differences in product formation rates (Kumar et al. 2006). Unfortunately, the generation of stable cell lines was not accomplished. This not only hindered the

derivation of kinetic parameters but also meant that constitutive expression of CYP1A1 proteins could not be achieved in cell line sensitization assays. The constitutive expression of CYP1A1 was an important aspect in elucidating a valid and reproducible dose response to DTIC.

The stable expression of proteins is influenced by three factors; the transfection method, the vector containing the transgene(s), and the chromosomal incorporation of the transgene(s). In this study the use of four transfection methods (Lipofectamine2000, Lipofectamine LTX PLUS, DOTAP, and electroporation) in conjunction with a fluorescently tagged plasmid control (eYFP; data not shown) and the presence of transiently expressed protein identified that the plasmids harboring the CYP1A1-2A-OxR ORF were indeed transported into the nucleus. In addition, the use of two separate mammalian expression plasmids, pEF-IRES(5) and pCI-neo, containing different selectable markers, puromycin-*N*-acetyltransferase and neomycin phosphtransferase, respectively, did not aid the generation of stable cell lines.

The linearization of plasmid DNA was employed to improve the chromosomal incorporation of the CYP1A1-2A-OxR ORF, on the basis that linearized plasmid DNA taken up into cells in a DNase-resistant state allows unchanged incorporation of the linear fragment into a chromosome (Biswas, Burnstein & Sparling 1986; von Groll et al. 2006). Incorporation of the DNA in this way ensures the CDS of each transgene is uninterrupted. In contrast to linear DNA, circular supercoiled plasmid DNA demonstrates higher transfection efficiencies, although the CDS of the desired transgene can be interrupted upon non-specific digestion and incorporation of the plasmid into the host chromosome. However, in this study the transfection of linearized plasmids did not aid the generation of COS-7 and SK-MEL-28 stable cell

lines. Interestingly, the incubation of cells in the desired selectable antibiotic (48h post-transfection) for 3-5 weeks appeared to select those cells expressing the resistance gene products. On this basis of these findings, and my ability to produce numerous stable cell lines (Kubota et al. 2007; Lewis et al. 2007; Udomuksorn et al. 2007), it appears that the degradation of the CYP1A1-2A-OxR mRNA may have contributed to the absence of functional CYP1A1 and OxR proteins.

In summary, the generation of COS-7 and SK-MEL-28 stable cell lines coexpressing CYP1A1 and OxR requires further investigation. In saying this, the modulation of protein expression in gene therapy strategies is not required to be constitutive *in vivo*. This study has, however, successfully developed a vector capable of self-processing functional CYP1A1 coexpressed with OxR. To my knowledge, this is the first study to utilize the 2A-peptide to express a P450 with its redox partner. The use of the 2A-peptide in a CYP1A1-based gene therapy strategy would alleviate the transfection constraints placed on current gene therapy strategies which require the independent co-expression of multiple viral vectors.

CHAPTER 7
GENERAL DISCUSSION

A major problem associated with the use of most cancer chemotherapeutic agents is the undesirable toxicity to non-tumor cells and organs. Anticancer drugs typically possess a narrow therapeutic index, have relatively poor selectivity for cancerous cells, and multi-drug resistance can result from prolonged treatment. One potential therapeutic strategy is to increase tumor specificity and reduce systemic toxicity by the use of prodrugs that are preferentially activated in the tumor environment. However, a potential disadvantage of the use of prodrugs is the low efficiency of enzymatic bioactivation, which in turn leads to a greater potential for prodrug metabolism by other competing enzymes. Therefore, this strategy would appear most useful when the affinity between the prodrug and the prodrug-activating enzyme is high (low K_m) and/or turnover is high (high V_{max}), that is intrinsic clearance (CL_{int}) is high.

The rationale for this study was based on the relatively poor clinical effectiveness of DTIC in human malignancies and the occurrence of serious adverse effects. Despite this, it should be recognized that since its approval by the FDA in 1975, DTIC remains the most effective single agent used when treating metastatic malignant melanoma and various sarcomas (Erdmann 2010). Given that DTIC requires metabolic activation by CYP1A1 (or CYP1A2) for cytotoxicity (Reid et al. 1999), an opportunity exists to utilize this enzyme-prodrug pair as an approach to gene directed enzyme prodrug therapy. As a first step, this thesis investigated the structure-activity

relationships between human CYP1A1 and DTIC using protein homology modeling, site-directed mutagenesis and kinetic analyses.

As discussed throughout this thesis, the generation of a chemically valid CYP1A1 homology model using human P450 templates was essential for predicting desirable side-chain stereochemistry and, in-turn, better *in silico* predictions of substrate binding and orientation. Previously published CYP1A1 models reflect the bacterial or rabbit homologs with which they were modeled (<28% homology) (Lewis, Ioannides & Parke 1994b; Lewis, Lake & Dickins 2004; Szklarz & Paulsen 2002), potentially resulting in the derivation of suboptimal structure-activity relationships. The comparative modeling data presented here demonstrates that the CYP1A1-(HMM) homology model resulted in an improved CYP1A1 homology model compared to a model based on rabbit CYP2C5 alone. Interestingly, the CYP1A1-(2C5) and CYP1A1-(HMM) homology models displayed energy and structural inaccuracies that were not observed in the CYP1A1-(1A2) homology model. The CYP1A1-(1A2) model is the first human P450 structure based on human data at >80% sequence similarity and displayed optimal stereochemistry comparable to those of the crystallized human P450s. Investigation of the CYP1A1 active-site architecture revealed a number of key residues within the active-site pocket and the putative substrate access and egress channels. The non-polar substrate access channel consists of residues that make up the F-G loop incorporating residues from the B´-helix and the K-helix/β2-3 loop. The polar substrate egress channel extends from the active-site beneath the G-helix and is enclosed by the B´-helix/C-loop.

Validation of the 'static' computational CYP1A1 model was necessary to ensure relatedness to the functional CYP1A1 enzyme. This was achieved by correlating the derived kinetic parameters of site-directed mutants with the structural data obtained

by automated *in silico* docking experiments. Experiments were performed with the prototypical CYP1A1 substrate, Eres. Docking experiments were undertaken with the CYP1A1-(1A2) homology model due to its superior structural and energy profile. Active-site residues involved in orientating and binding Eres were identified. The most energetically favorable pose placed the carbon atom hydroxylated by CYP1A1 4.4Å from the Fe atom of the Heme.

The predictivity of the CYP1A1 computational model was confirmed using the active-site mutants S122A, F123A, F224A, A317Y, T321G, and I386G. These residues were targeted to elucidate the structural and physicochemical properties responsible for productive EROD activity. F123A, A317Y, and I386G mutants lacked EROD activity despite displaying holo-enzyme in $CO_{(g)}$ reduced difference spectroscopy (F123A and I386G) and the presence of apo-enzyme in immuno-blots (A317Y). Unfavorable interactions asserted by these mutations include steric hindrance within the active-site cavity (A317Y), electrostatic disruption to the heme prosthetic group (I386G), and the elimination of aromatic interactions between enzyme and substrate (F123A). Of the mutants that displayed EROD activity, changes in the derived kinetic parameters obtained for Eres *O*-deethylation were initiated by displacing π-σ attractive forces (F224A), disrupting the alignment of axial water for catalysis (T321G), and abolishing H-bonding interactions (S122A). Most surprising was the doubling in V_{max} observed with the S122A mutant, relative to wild-type. The loss of H-bonding of the oxazine ring oxygen of Eres invoked a more productive binding orientation. Interestingly, these *in vitro* data contradict the belief that H-bonding to S122 is critical for aligning alkoxyresorufins for productive catalysis (Otyepka et al. 2007; Schleinkofer et al. 2005; Szklarz & Paulsen 2002).

The kinetic analysis of EROD activity clearly identified substrate inhibition as the preferred kinetic model for wild-type CYP1A1 and the S122A and F224A mutants. However, formation of an unproductive SES complex implies the binding of multiple ligands in a single CYP1A1 active-site. Interestingly, docking studies revealed that the narrow and elongated profile of the CYP1A1 active-site prohibits the simultaneous binding of two Eres molecules, although, polar interactions within the substrate access channel (involving T111, S230, and N232) were identified as potential Eres binding sites. Moreover, the symmetry of Eres may provoke the binding of substrate (or metabolite; Res) in a reversely orientated unproductive orientation. Validation of the structural organization of CYP1A1 contributed to the overall understanding of Eres structure-activity relationships, specifically highlighting the importance of aromatic interactions over hydrogen bonding. The CYP1A1 chemical structure elucidated here is the most accurate available to date (last updated July, 2010). This model was subsequently utilized to better understand the structure-activity relationships of DTIC.

Docking studies with DTIC revealed this substrate orientates in close proximity to S122, F123, D313, A317, I386, Y259, and L496. The energetically favorable pose placed the carbon targeted for hydroxylation 5.6Å from the heme catalytic site, with H-bonding predominantly occurring between Y259 and the aromatic nitrogen of the imidazole ring. Based on the predictivity of the model with docked Eres, DTIC binding and orientation was assessed with mutants generated *in silico*. All mutants were designed to enhance the *N*-demethylation of DTIC by manipulating steric, polar, aromatic, or electrochemical interactions. The automated docking of DTIC into each *in silico* mutant identified variations in the orientation and intermolecular bonding of DTIC.

To determine the affect each mutation asserted on DTIC *N*-demethylation, the coexpression of recombinant CYP1A1 proteins with OxR was achieved using an optimized method that increased yield 7-fold compared to literature reports. The kinetics of DTIC *N*-demethylation by CYP1A1 (V_{max} 28pmol/min/pmol P450; K_m 408μM) and CYP1A2 (V_{max} 38pmol/min/pmol P450, S_{50} 1502 μM, n = 0.70) were well modeled using the Michaelis-Menten and Hill equations, respectively. DTIC *N*-demethylation by the CYP1A1 E161K, E256K, and I458V mutants similarly exhibited Michaelis-Menten kinetics, with lowering in K_m values that resulted in the doubling of catalytic efficiencies. It was difficult to elucidate the structure-activity relationships for the E161K mutant since this residue resides on the surface of the protein. It is believed that residue 161 is involved in OxR binding (Parikh, Josephy & Guengerich 1999). Thus, the localized charge effects seen with the E161K substitution may aid a more complementary alignment of OxR. For the E256K mutant, data revealed that localized charge effects enhance H-bonding to D253. Of particular interest were modifications in the side-chain orientations of F258 and Y259, which clearly impact on DTIC alignment over the heme catalytic site. Interestingly, the decrease in K_m obtained with the I458V mutant is apparently induced by realignment of the heme prosthetic group itself.

Characterization of DTIC *N*-demethylation by the CYP1A1*2C (*m*2; I462V) and CYP1A1*4 (*m*4; T461N) polymorphic variants revealed a decrease of approximately 30% in catalytic efficiency. Surprisingly, the kinetics for these polymorphisms had not previously been characterized with DTIC. Data obtained from the CYP1A1 model identified that the mechanism of reduced DTIC activation arises from unfavorable alterations to the heme prosthetic group via electrostatic effects. These polymorphisms may occur in frequencies up to 5.1% in Caucasians, 15% in

Japanese, 25.5% in Africans, 8.9% in Turkish, and 22% in African-Americans (Aynacioglu et al. 1998; Cascorbi, Brockmoller & Roots 1996; Garte et al. 2001). A 30% reduction in the catalytic efficiency of DTIC activation would presumably decrease the already low 19% response rate to DTIC treatment.

In an attempt to characterize the cytotoxic potential of the E161K, E256K, and I458V 'high-active' CYP1A1 enzymes, these constructs were prepared for constitutive expression in COS-7 and SK-MEL-28 cells. The transient expression of holo-CYP1A1 and OxR was achieved in both cell lines. Unfortunately, however, the generation of stable cell lines was not achieved. Cells expressing constitutive levels of CYP1A1 proteins are critical for establishing reliable and reproducible DTIC concentration-effect relationships. Other studies that have investigated cytotoxicity resulting from prodrug activation have generally employed retroviral vector plasmids as a means to improve transgene expression (Huang & Waxman 2001; Johannes et al. 2006; Jounaidi, Hecht & Waxman 1998; Jounaidi & Waxman 2000; Kan et al. 2001; Kan, Kingsman & Naylor 2002). The use of retroviral vectors was beyond the capacity of this thesis due to time constraints. This study did, however, utilize the picornaviral 2A cleavage peptide to ensure 1:1 molar translation of CYP1A1 and OxR. In a CYP1A1-based gene therapy strategy the CYP1A1-2A-OxR ORF would remove the need for independent co-expression of multiple viral vectors, further increasing the effectiveness of CYP1A1-based GDEPT.

Adoption of a CYP1A1-based GDEPT strategy should minimize problems associated with inter-individual variation in first-pass extraction and adverse effects arising from the wide distribution of P450's within the body, and variable catalytic turnover amongst drug-enzyme combinations. The unique characteristics of CYP1A1, particularly its localization and distribution within the body, inhibitor profile, and

regulatory mechanisms, all identify CYP1A1 as a plausible gene candidate. A CYP1A1-based GDEPT strategy using DTIC appears possible, especially if inhibition of non-specific activation within the liver can be achieved. The modulation of cyclophosphamide-based P450 gene therapy using liver P450 inhibitors has been demonstrated by Huang and Waxman (2001). Results showed that the rate of hepatic cyclophosphamide activation could be decreased substantially by inhibitor treatment. Thus, an attractive therapeutic strategy would be to inhibit the CYP1A2 catalyzed hepatic *N*-demethylation of DTIC using 3,5,7-trihydroxyflavone (Zhai et al. 1998) so that the inactive prodrug could still be administered systemically. Since CYP2E1 exhibits low DTIC *N*-demethylation activity (K_m >2.8mM), concurrent inhibition of this enzyme may not be necessary.

A GDEPT approach to treatment would enable CYP1A1 to be expressed in a specific tissue type or tumor environment at high levels. Treatment in this way has several advantages over conventional cancer therapies (El-Aneed 2004; Jounaidi, Hecht & Waxman 1998; Kan et al. 2001; Kan, Kingsman & Naylor 2002; McFadyen, Melvin & Murray 2004; Queirolo & Acquati 2006; Scripture, Sparreboom & Figg 2005; Tarner, Muller-Ladner & Fathman 2004). Furthermore, it would greatly reduce systemic (and hepatic) exposure to toxic metabolites, thus alleviating the characteristic side-effects triggered by conventional chemotherapy. Ideally, the use of human CYP1A1 would remove the potential risk of stimulating the immune system in a way that reduces the effectiveness of the therapy.

In summary, computational techniques were employed here to generate a chemically valid human CYP1A1 homology model. The predictivity of the model was confirmed using directed mutagenesis to identify the active-site residues responsible for the orientation and stabilization of Eres and DTIC during productive catalysis.

Validation of the structural organization of CYP1A1 has contributed to the understanding of structure-activity relationships of both substrates. The data obtained with Eres highlights the importance of aromatic interactions over polar interactions. The data obtained with DTIC further highlights the importance of electrostatic and charge interactions. This work has demonstrated that E161K, E256K, and I458V substitutions in human CYP1A1 can enhance the catalytic efficiency of DTIC activation via the *N*-demethylation pathway. The combination of kinetic analyses with *in silico* docking has permitted interpretation of the structure-activity relationships of this enzyme-substrate pair. The self-processing CYP1A1-2A-OxR ORF developed would be used in future studies to characterize the cytotoxic potential of CYP1A1 enzymes with catalytically enhanced DTIC activation. Importantly, the improved understanding of DTIC activation by CYP1A1 has provided a potential strategy for CYP1A1-based GDEPT in the treatment of metastatic malignant melanoma.

APPENDIX 1

Substrates, inhibitors, and inducers of human CYP1A1

Table A1.1 Reported substrates, inhibitors, and inducers of human CYP1A1. Data from Kuffel et al. (2002), Loaiza-Perez et al. (2004), and Rendic (2002). (-) indicates that specific information was not available.

Compound	Interaction	Mechanism	Compound Category
1-(1-Propynyl)biphenyl	inhibitor	-	PAH
1-(1-Propynyl)pyrene	inhibitor	-	PAH
1,2,5,6- Dimethylbenzanthracene	substrate	-	PAH
1,4-Benzothiazines	inhibitors	mechanism based	Methylenedioxyphenyl
1,8-Dinitropyrene	substrate	Nitroreduction	Nitroarene
1-2, 1-3, 1-4-Phenylenebis(methylene)selenocyanate	inhibitor	-	Antineoplastic
17β-Estradiol	substrate	C2-, C4-, C6α-, C15α-hydroxylation (Quinol formation)	Estrogen, hormone
2-(4-Amino-3-methyl-6-hydroxyphenyl)benzothiazole	inhibitor	active site	Antineoplastic
2-(4-Amino-3-methylphenyl)benzothiazole (NSC 674495)	substrate, inducer AhR agonist	C6-hydroxylation, *N*-acetylation	Antineoplastic
2,3,7,8-Tetrachlorodibenzop-dioxin (TCDD)	inducer AhR agonist	-	Dioxin, Halogenated aromatic hydrocarbon
2,4,6,4-Tetrahydroxy-3-prenylchalcone	inhibitor	-	Prenylated flavonoid
2-Acetoaminofluorene	substrate	-	Pesticide, carcinogen

Compound	Interaction	Mechanism	Compound Category
2-Amino-1-methyl-6-phenylimidazo[4,5-b]pyridine, PhIP	substrate	*N*-hydroxylation	Heterocyclic, aromatic amine
2-Amino-3,8-dimethylimidazo[4,5-f]quinoxaline, MeIQ	substrate	*N*-hydroxylation	Heterocyclic, aromatic amine
2-Amino-3-methylimidazo[4,5-f]quinoline, (IQ)	substrate	*N*-hydroxylation	Heterocyclic, aromatic amine
2-Aminoanthracene	substrate	Oxidation	Aromatic amine
2-Aminoanthracene	substrate	Oxidation	Aromatic amine
3,3’,4,4’,5,5’-hexachlorobiphenyl	inducer	-	Polychlorinated biphenyl (PCB)
3,3’,4,4’,5-pentachlorobiphenyl	inducer	-	PCB
3,4,3′,4′-Tetrachlorobiphenol	inducer AhR agonist	-	Environmental pollutant
3,4,4’,5-tetrachlorobiphenyl	inducer	-	PCB
3,4’,5-trichlorobiphenyl	inducer	-	PCB
3,4-Methylenedioxyethylamphetamine	substrate	*O*-demethylenation, *N*-deethylation	Hallucinogenic
3,5-Diethoxycarbonyl-1,4-dihydro-2,6-dimethyl-4-ethylpyridine (DDEP)	inhibitor	mechanism based	Porphyrinogenic
3-[2-(2,4,6-Trimethylphenyl)thioethyl]-4-methylsydnone	inhibitor	mechanism based	Porphyrinogenic

Compound	Interaction	Mechanism	Compound Category
(TTMS)			
3’-Methoxy-4’-nitroflavone	inhibitor	-	Flavonoid
3-Amino-1,4-dimethyl-5*H*-pyrido[4,3-*b*]indole	substrate	-	Dietary carcinogen
3-Amino-4-methoxyflavone	inducer	-	Flavonoid,
3-Amino-4-methoxyflavone	inhibitor	-	Flavonoid,
3-Cyano-7-ethoxycoumarin	substrate	*O*-deethylation	Alkyloxycoumarin
3-Methoxy-4-aminoazobenzene	substrate	oxidation	Aromatic amine
3-Methylcholanthrene, 3MC	inducer AhR agonist	-	PAH
4-(Methylnitrosamino)-1-(3-pyridyl)-1-butanone (NNK)	substrate	α-methyl/α-methylene hydroxylation	Tobacco-specific nitrosamine
4-Amino-3-methoxyflavone	inhibitor	-	Flavonoid
4-Aminobiphenyl	substrate	Oxidation	Aromatic amine
4-Aminoflavone	inducer	-	Flavonoid
4-Iodoflavone	inhibitor	-	Flavonoid
4-Methoxy-3-nitroflavone	inducer/inhibitor	-	Flavonoid
5,6-benzoflavone, β-naphthoflavone	inducer	-	Flavonoid

Compound	Interaction	Mechanism	Compound Category
5,6-Dimethylchrysene	inducer AhR agonist	-	PAH
5-Methylchrysene	substrate	-	PAH
6,8-Diprenylnaringenin	inhibitor	-	Prenylated flavonoid
6-Aminochrysene	inducer, AhR agonist	-	Polycyclic aromatic hydrocarbon (PAH)
6-Aminochrysene	substrate	Oxidation	Aromatic amine
6-Aminochrysene	substrate	Oxidation	Aromatic amine
6-Aminochrysene-1,2-diol	substrate	Diolepoxide formation	Aromatic amine
6-Nitrochrysene	substrate	trans-1,2-Dihydro-1,2-dihydroxy formation/inducer	Nitroarene
6-Prenylnaringenin	inhibitor	-	Prenylated flavonoid
7,12-Dimethylbenz[a]anthracene (DMBA)	substrate/inducer AhR agonist	Diol formation and CH_3-hydroxylation	PAH
7,12-Dimethylbenz[a]anthracene-3,4-diol (DMBA-3,4-diol)	substrate	oxidation	PAH
7,8-benzoflavone, α-naphthoflavone	inhibitor/inducer	-	Flavonoid
7,8-Dibenzoenzoflavone	inhibitor	active site	Flavonoid
7,8-Dihydroxybenzo[a]pyrene	substrate	Tetrols and triols formation	PAH

Compound	Interaction	Mechanism	Compound Category
7-Ethoxy-4-trifluoromethylcoumarin	substrate	*O*-deethylation	Alkyloxycoumarin
7-Ethoxycoumarin	substrate	*O*-deethylation	Alkyloxycoumarin
7-Ethoxycoumarin	substrate	*O*-deethylation	Alkyloxycoumarin
7-Ethoxyresorufin	substrate	*O*-deethylation	Alkyloxycoumarin
7-Methoxyresorufin	substrate	*O*-demethylation	Alkyloxycoumarin
7-Methylbenz[c]acridine	substrate	Oxidation	Aza-aromatic
7-Pentoxyresorufin	substrate	*O*-depentylation	Alkyloxycoumarin
7α–hydroxy-Δ-tetrahydrocannabinol (THC)	substrate	Oxidation (7-oxo formation, minor reaction)	Psychoactivator
8,9-Dihydroxydibenzo[a,l]pyrene	substrate	C11,C12-Tetrol, (R,R)-	PAH
8-Prenylnaringenin	inhibitor	-	Prenylated flavonoid
Acetonitrile	inhibitor	-	Organic solvent
Acetylenes	inhibitor	-	PAH
Aflatoxin B1	substrate	Epoxidation	Mycotoxin
Aminoflavone (NSC 686288)	substrate, inducer AhR agonist	ring hydroxylation	Flavonoid
Aminopyrine, amidopyrine, aminophenazone	substrate	*N*-demethylation	NSAID

Compound	Interaction	Mechanism	Compound Category
Amiodarone	substrate	*N*-demethylation	Antiarrhythmic
Androstenedione	substrate	C6-β-hydroxylation	Androgen and anabolic, hormone
Apigenin	inhibitor	-	Flavonoid
Arachidonic acid	inhibitor	-	Fatty acid
Benz[a]anthracene	inducer	-	PAH
Benzo[a]perylene	substrate	Oxidation	PAH
Benzo[a]pyrene	substrate/inducer AhR agonist	C3-, C9-, C7-hydroxylation, 7,8-, C9,C10-, C4,C5-dihydrodiols formation	PAH
Benzo[a]pyrene-7,8-diol	substrate	-	PAH
Benzo[b]fluoranthene	inducer	-	PAH
Benzo[b]fluoranthene-9,10-diol	substrate	Oxidation	PAH
Benzo[b]fluoroanthrene	inducer AhR agonist	-	PAH, fluorene
Benzo[b]perylene	substrate	Oxidation	PAH
Benzo[c]phenanthrene	substrate	-	PAH
Benzo[g,h,i]perylene	inducer	-	PAH

Compound	Interaction	Mechanism	Compound Category
Benzo[g]chrysene	inducer AhR agonist	-	PAH
Benzo[k]fluoranthene	inducer	-	PAH
Benzydamine	substrate	*N*-oxidation	NSAID
C3-, C7-hydroxy Flavone	inhibitor	-	Flavonoid
C3-hydroxy, C5-hydroxy Flavone	inhibitor	-	Flavonoid
C7-hydroxy Flavone	inhibitor	-	Flavonoid
Caffeine	substrate	*N*1- and *N*3-demethylation (less specific)	Xanthine, CNS stimulant
Carvedilol (S)- and (R)-	substrate	hydroxylation	Beta blocker
Chlorzoxazone	substrate	C6-hydroxylation	Muscle relaxant
Chrysene	inducer AhR agonist	-	PAH
Chrysin	inhibitor	-	Flavonoid
Cinnarizine	substrate	*N*-dealkylation	Antihistamine
Curcumin	inducer/inhibitor	-	Coloring agent
Dacarbazine	substrate	*N*-demethylation	Antineoplastic
Debrisoquine	substrate	C4-hydroxylation	Antihypertensive

Compound	Interaction	Mechanism	Compound Category
Deethylamiodarone	inhibitor	-	Antiarrhythmic
Dehydrocycloxanthohumol	inhibitor	-	Prenylated flavonoid
Dehydrocycloxanthohumol hydrate	inhibitor	-	Prenylated flavonoid
Dehydroepiandrosterone	inhibitor	-	Oxysterol, hormone
Dibenz[a,j]acridine	substrate	Oxidation	PAH
Dibenzo[j,l]fluoranthene	substrate	Oxidation	PAH
Dibenzo[a,e]fluoranthene	substrate	Oxidation	PAH
Dibenzo[a,f]fluoranthene	substrate	Oxidation	PAH
Dibenzo[a,h]anthracene	Inducer AhR agonist	-	PAH
Dibenzo[a,h]pyrene	substrate	Oxidation	PAH
Dibenzo[a,i]pyrene	substrate	Oxidation	PAH
Dibenzo[a,l]pyrene	substrate	11,12-Dihydrodiol-13,14-epoxide formation	PAH
Dibenzo[a]pyrene	inducer AhR agonist	-	PAH
Diclofenac,	substrate	C5-hydroxylation	NSAID
Diethyldithiocarbamate (metabolite of disulfiram)	inhibitor	-	Antialcoholic

Compound	Interaction	Mechanism	Compound Category
Diosmetin	inducer/inhibitor	-	Flavonoid
Diosmin	inducer	-	Flavonoid
Eicosapentenoic acid	substrate	epoxidation, C19-, C20-hydroxylation	Fatty acid
Ellipticine	substrate	Oxidation	Antineoplastic
Ellipticine (9-hydroxy metabolite)	inhibitor	-	Antineoplastic
Eriodictyol	substrate	-	Flavonoid
Estradiol 3-methyl ether	substrate	*O*-demethylation	Estrogen, hormone
Estrone	substrate	Quinol formation	Estrogen, hormone
Ethanol	inhibitor	-	Organic solvent, Alcohol
Flausterone	inhibitor	XRE antagonist	Adrenocortical steroid
Flavanone	inhibitor	-	Flavonoid
Flunarizine	substrate	*N*-dealkylation	Antihistamine
Fluoranthrene	inducer AhR agonist	-	PAH, fluorene
Flutamide	substrate	C2-hydroxylation	Antineoplastic
Fluvastatin	substrate	C5-hydroxylation	Lipid regulating

Compound	Interaction	Mechanism	Compound Category
Furafylline	inhibitor	mechanism-based	Methylxanthines, Bronchodilator
Furametpyr	substrate	*N*-demethylation	Fungicide
Galangin	inducer/inhibitor	-	Flavonoid
Galangin	substrate	ring hydroxylation	Flavonoid
Genistein	substrate	C3,C4,C5,C7-tetrahydroxyisoflavone formation	Flavonoid
Genistein	substrate	C6-, C8- hydroxylation	Flavonoid
Hesperetin	inhibitor	-	Flavonoid
Hesperetin	substrate	*O*-demethylation (eriodictyol formation)	Flavonoid
Homoeriodictyol	inhibitor	-	Flavonoid
Indolacetic acid	inducer	-	Indole
Indolo[3,2-b]carbazole	inducer	-	Unclassified
Isosafrole	inducer/inhibitor	-	Benzodioxole
Isoxanthohumol	inhibitor	-	Prenylated flavonoid
Kaempferide	substrate	ring hydroxylation	Flavonoid
Kaempferol	inhibitor	-	Flavonoid

Compound	Interaction	Mechanism	Compound Category
Ketoconazole	inhibitor	-	Antifungal
Lansoprazole	inducer	-	Proton pump inhibitor
Lisuride	substrate	*N*-deethylation	Dopaminergic
Meat, chargrilled	inducer	-	Food
Methanol	inhibitor	-	Organic solvent, Alcohol
Methoxsalen	inhibitor	-	Anti-psoriatic
Morin	inhibitor	-	Flavonoid
N,N-Diethyl-2-[4-(phenylmethyl)phenoxy] ethanolamine (DPPE)	substrate	C4-hydroxylation, *N*-demethylation	Antineoplastic
Naphtho[1,2-b]fluoranthene	substrate	Oxidation	PAH
Naphtho[2,3-a]pyrene	substrate	Oxidation	PAH
Naphtho[2,3-e]pyrene	substrate	Oxidation	PAH
Naringenin	inhibitor	-	Flavonoid
N-Hydroxy-2-amino-1-methyl-6-phenylimidazo[4,5-b]pyridine,N-hydroxy (PhIP)	substrate	Oxidation	Heterocyclic, aromatic amine
Nicardipine	substrate	Oxidation	Calcium-channel blocker

Compound	Interaction	Mechanism	Compound Category
Nicotine	substrate	C5-Oxidation (to cotinine at high concentrations)	Alkaloid
Nifedipine	inhibitor	competitive	Calcium-channel blocker
N-methyldibenzo[c,g]carbazole	substrate	Oxidation	Carbazole
o-Aminoazotoluene	substrate	Oxidation	Azoaromatic amine
Ochratoxin A	substrate	C4-(R)-hydroxylation	Mycotoxin
Oltipraz	inhibitor	-	Antineoplastic
Omeprazole	inducer	-	Proton pump inhibitor
Omperazole	inducer AhR agonist	-	Proton pump inhibitor
Pantoprazole	inducer	-	Proton pump inhibitor
Paraxanthine	inhibitor	-	Xanthine, CNS stimulant
Phenacetin	substrate	*O*-deethylation	Analgesic
Phenanthrene	substrate	C9-,C10-dihydrodiol formation	PAH
Phencyclidine	substrate	PCHP formation (minor reaction)	Hallucinogenic
Pregnenolone	substrate	C7β-, C16α-, C17α-hydroxylation	Steroid, hormone
Primaquine	inducer, substrate	C6-hydroxylation	Antimalarial

Compound	Interaction	Mechanism	Compound Category
Progesterone	substrate	C6β-, C16α-hydroxylation	Progestagen, hormone
Propanolol	inhibitor	competitive	Beta blocker
Propofol	inhibitor	-	General anesthetic
Propranolol (S)-, (R)-	substrate	*N*-deisopropylation	Beta blocker
Quercetin	inhibitor/inducer	-	Flavonoid
Quinidine	inhibitor	-	Antiarrhythmic
Quinine	inhibitor	-	Antimalarial
Quinones	substrate	Oxidation	Quinones
Retinal, 9-cis-	substrate	Retinoic acid, C9-cisformation	Retinoic acid receptor modulator
Retinal, all-trans-	substrate	Retinoic acid, all-transformation	Retinoic acid receptor modulator
Rhapontigenin	inhibitor	-	Haemostatic agent
Riluzole	substrate	*N*-hydroxylation, *O*-dealkylation	Glutamate antagonist
Ropivacaine (S)-	substrate	C3-, C4-hydroxylation, *N*-dealkylation	Local anesthetic
S-methyl N,N,-diethylthiolcarbamate	substrate	Sulfoxidation (minor pathway)	Antialcoholic

Compound	Interaction	Mechanism	Compound Category
(DETC-ME)			
Testosterone	substrate	C6β-hydroxylation	Androgen and anabolic, hormone
Tetrahydroxanthohumol	inhibitor	-	Prenylated flavonoid
Theophylline	inhibitor	-	Bronchodilator
Thiabendazole	inducer	-	Antifungal
Toluene	substrate	CH_3-hydroxylation, para-hydroxylation, (p-cresol formation)	Organic solvent, aromatic
Toremifene	substrate	*N*-demethylation	Antineoplastic
trans-Resveratrol (trans-3,4,5-trihydroxystilbene)	inhibitor	-	Phytoalexin
Trichloroethylene	substrate	Chloral hydrate formation	Organic solvent, halogenated alkene
Triton N-101	substrate	Alkyl-hydroxylation	Nonionic phenolic detergent
Troglitazone	substrate	Quinone formation	Antidiabetic
Tryptamine	inducer	-	Neurotransmitter, indoleamine
Ultraviolet B	inducer	-	Unclassified

Compound	Interaction	Mechanism	Compound Category
Uroporphyrinogen	substrate	Oxidation (urophorphyrin formation)	Porphyrinogen
Warfarin, (R)-	substrate	C6-, C7-, C8-hydroxylation	Anticoagulant
x,5-Diprenvlxanthohumol	inhibitor	-	Prenylated flavonoid
Xanthohumol	inhibitor	-	Prenylated flavonoid
Zotepine	substrate	*N*-demethylation, S-oxidation	Antipsychotic
Zoxazolamine	substrate	C6-hydroxylation	Muscle relaxant
α-naphthoflavone	inhibitor	-	Flavonoid
β-naphthoflavone	inducer AhR agonist	-	Flavonoid

APPENDIX 2

Amino acids and symbols

Alanine
ALA; A
Aliphatic (nonpolar)
MW: 89.09
IE: 6.00
Formula: $C_3H_7NO_2$

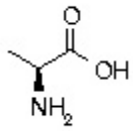

Arginine
ARG; R
Positively charged
MW: 174.20
IE: 11.15
Formula: $C_6H_{14}N_4O_2$

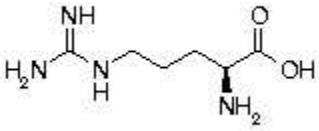

Asparagine
ASN; N
Polar but uncharged
MW: 132.12
IE: 5.41
Formula: $C_4H_8N_2O_3$

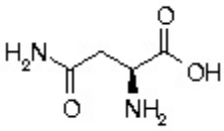

Aspartic Acid
ASP; D
Negatively charged
MW: 133.10
IE: 2.77
Formula: $C_4H_7NO_4$

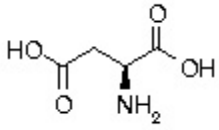

Cysteine
CYS; C
Aliphatic (nonpolar)
MW: 121.16
IE: 5.02
Formula: $C_3H_7NO_2S_1$

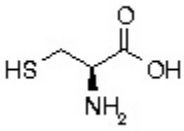

Glutamic Acid
GLU; E
Negatively charged
MW: 147.13
IE: 3.22
Formula: $C_5H_9NO_4$

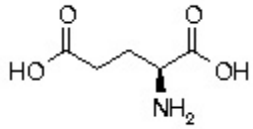

Glutamine
GLN; Q
Polar but not charged
MW: 146.15
IE: 5.65
Formula: $C_5H_{10}N_2O_3$

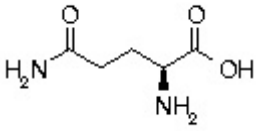

Glycine
GLY; G
Aliphatic (nonpolar)
MW: 75.07
IE: 5.97
Formula: $C_2H_5NO_2$

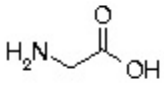

Histidine
HIS; H
Positively charged
MW: 155.16
IE: 7.47
Formula: $C_6H_9N_3O_2$

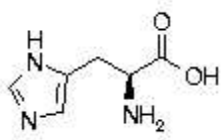

Isoleucine
ILE; I
Aliphatic (nonpolar)
MW: 131.17
IE: 5.94
Formula: $C_6H_{13}NO_2$

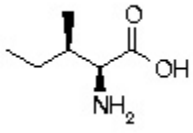

Leucine
LEU; L
Aliphatic (nonpolar)
MW: 131.17
IE: 5.98
Formula: $C_6H_{13}NO_2$

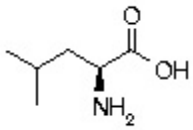

Lysine
LYS; K
Positively charged
MW: 146.19
IE: 9.59
Formula: $C_6H_{14}N_2O_2$

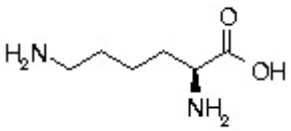

Methionine
MET; M
Aliphatic (nonpolar)
MW: 149.21
IE: 5.74
Formula: $C_5H_{11}NO_2S_1$

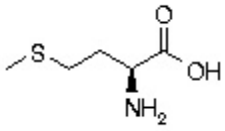

Phenylalanine
PHE; F
Aromatic
MW: 165.19
IE: 5.48
Formula: $C_9H_{11}NO_2$

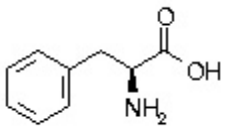

Proline
PRO; P
Aliphatic (nonpolar)
MW: 115.13
IE: 6.30
Formula: $C_5H_9NO_2$

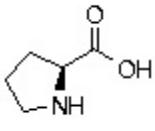

Serine
SER; S
Polar but not charged
MW: 105.09
IE: 5.68
Formula: $C_3H_7NO_3$

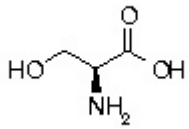

Threonine
THR; T
Polar but not charged
MW: 119.12
IE: 5.64
Formula: $C_4H_9NO_3$

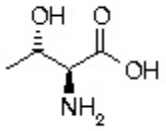

Tryptophan
TRP; W
Aromatic
MW: 204.23
IE: 5.89
Formula: $C_{11}H_{12}N_2O_2$

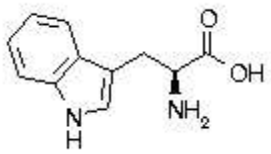

Tyrosine
TYR; Y
Aromatic
MW: 181.19
IE: 5.66
Formula: $C_9H_{11}NO_3$

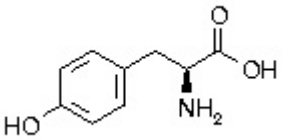

Valine
VAL; V
Aliphatic (nonpolar)
MW: 117.15
IE: 5.96
Formula: $C_5H_{11}NO_2$

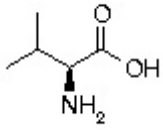

The isoelectric point (IE) is the pH at which a particular molecule carries no net electrical charge.

REFERENCES

Acharya, KR & Lloyd, MD 2005, 'The advantages and limitations of protein crystal structures', *Trends in Pharmacological Sciences,* vol. 26, no. 1, pp. 10-14.

Aghi, M, Hochberg, F & Breakefield, XO 2000, 'Prodrug activation enzymes in cancer gene therapy', *Journal of Gene Medicine,* vol. 2, no. 3, pp. 148-164.

Alberts, DS & Chen, GHS 1980, *Tabular Summary of Pharmacokinetic Parameters Relevant to In Vitro Drug Assay,* Alan R. Liss, Inc., New York.

Atkins, WM 2005, 'Non-Michaelis-Menten kinetics in cytochrome P450-catalyzed reactions', *Annual Review of Pharmacology and Toxicology,* vol. 45, no. pp. 291-310.

Avissar, YJ & Beale, SI 1989, 'Identification of the Enzymatic Basis for Delta-Aminolevulinic-Acid Auxotrophy in a Hema Mutant of Escherichia-Coli', *Journal of Bacteriology,* vol. 171, no. 6, pp. 2919-2924.

Aynacioglu, AS, Cascorbi, I, Mrozikiewicz, PM & Roots, I 1998, 'High frequency of CYP1A1 mutations in a Turkish population', *Archives of Toxicology,* vol. 72, no. 4, pp. 215-218.

Balasubramanian, SP, Cox, A, Brown, NJ & Reed, MW 2004, 'Candidate gene polymorphisms in solid cancers', *European Journal of Surgical Oncology,* vol. 30, no. 6, pp. 593-601.

Baneyx, F & Mujacic, M 2004, 'Recombinant protein folding and misfolding in Escherichia coli', *Nature Biotechnology,* vol. 22, no. 11, pp. 1399-1408.

Barnes, HJ 1996, 'Maximizing expression of eukaryotic cytochrome P450s in Escherichia coli', *Methods in Enzymology,* vol. 272, no. pp. 3-14.

Barnes, HJ, Arlotto, MP & Waterman, MR 1991, 'Expression and enzymatic activity of recombinant cytochrome P450 17 alpha-hydroxylase in Escherichia coli', *Proceedings of the National Academy of Sciences of the United States of America,* vol. 88, no. 13, pp. 5597-5601.

Baxter 2004, *Selected Schedules of Therapy for Malignant Tumours*.

Bayburt, TH & Sligar, SG 2002, 'Single-molecule height measurements on microsomal cytochrome P450 in nanometer-scale phospholipid bilayer disks', *Proc Natl Acad Sci U S A,* vol. 99, no. 10, pp. 6725-6730.

Bhatia, S, Tykodi, SS & Thompson, JA 2009, 'Treatment of metastatic melanoma: an overview.(Report)', *Oncology,* vol. 23, no. 6, pp. 488.

Biswas, GD, Burnstein, KL & Sparling, PF 1986, 'LINEARIZATION OF DONOR DNA DURING PLASMID TRANSFORMATION IN NEISSERIA-GONORRHOEAE', *Journal of Bacteriology,* vol. 168, no. 2, pp. 756-761.

Black, SD 1992, 'Membrane topology of the mammalian P450 cytochromes', *Faseb J,* vol. 6, no. 2, pp. 680-685.

Bowalgaha, K, Elliot, DJ, Mackenzie, PI, Knights, KM & Miners, JO 2007, 'The glucuronidation of Delta(4)-3-keto C19- and C21-hydroxysteroids by human liver

microsomal and recombinant UDP-glucuronosyltransferases (UGTs): 6 alpha- and 21-hydroxyprogesterone are selective substrates for UGT2B7', *Drug Metabolism and Disposition*, vol. 35, no. 3, pp. 363-370.

Bowalgaha, K, Elliot, DJ, Mackenzie, PI, Knights, KM, Swedmark, S & Miners, JO 2005, 'S-Naproxen and desmethylnaproxen glucuronidation by human liver microsomes and recombinant human UDP-glucuronosyltransferases (UGT): role of UGT2B7 in the elimination of naproxen', *British Journal of Clinical Pharmacology*, vol. 60, no. 4, pp. 423-433.

Boye, SL, Kerdpin, O, Elliot, DJ, Miners, JO, Kelly, L, McKinnon, RA, Bhasker, CR, Yoovathahaworn, K & Birkett, DJ 2004, 'Optimizing bacterial expression of catalytically active human cytochromes P450: comparison of CYP2C8 and CYP2C9', *Xenobiotica*, vol. 34, no. 1, pp. 49-60.

Breithaupt, H, Dammann, A & Aigner, K 1982, 'Pharmacokinetics of Dacarbazine (Dtic) and Its Metabolite 5-Aminoimidazole-4-Carboxamide (Aic) Following Different Dose Schedules', *Cancer Chemotherapy and Pharmacology*, vol. 9, no. 2, pp. 103-109.

Burke, MD, Thompson, S, Weaver, RJ, Wolf, CR & Mayer, RT 1994, 'Cytochrome-P450 Specificities of Alkoxyresorufin O-Dealkylation in Human and Rat-Liver', *Biochemical Pharmacology*, vol. 48, no. 5, pp. 923-936.

Carter, SK & Friedman, MA 1972, '5-(3,3-dimethyl-l-triazeno)-imidazole-4-carboxamide (DTIC, DIC, NSC-45388)--a new antitumor agent with activity against malignant melanoma.' *Eur J Cancer.*, vol. 8, no. 1, pp. 85-92.

Cascorbi, I, Brockmoller, J & Roots, I 1996, 'A C4887A polymorphism in exon 7 of human CYP1A1: Population frequency, mutation linkages, and impact on lung cancer susceptibility', *Cancer Research*, vol. 56, no. 21, pp. 4965-4969.

Cass, CE, Young, JD, Baldwin, SA & Baldwin, A 2001, 'Identification of novel enzyme-prodrug combinations for use in cytochrome P450-based gene therapy for cancer', *Molecular Membrane Biology*, vol. 18, no. 1, pp. 53-63.

Chang, CY & Puga, A 1998, 'Constitutive activation of the aromatic hydrocarbon receptor', *Molecular & Cellular Biology*, vol. 18, no. 1, pp. 525-535.

Chang, TKH & Waxman, DJ 2005, *Enzymatic Analysis of cDNA-Expressed Human CYP1A1, CYP1A2, and CYP1B1 With 7-Ethoxyresorufin as Substrate*, Human Press Inc., Totowa, NJ.

Chapman, PB, Einhorn, LH, Meyers, ML, Saxman, S, Destro, AN, Panageas, KS, Begg, CB, Agarwala, SS, Schuchter, LM, Ernstoff, MS, Houghton, AN & Kirkwood, JM 1999, 'Phase III multicenter randomized trial of the dartmouth regimen versus dacarbazine in patients with metastatic melanoma', *Journal of Clinical Oncology*, vol. 17, no. 9, pp. 2745-2751.

Chen, CS, Lin, JT, Goss, KA, He, YA, Halpert, JR & Waxman, DJ 2004, 'Activation of the anticancer prodrugs cyclophosphamide and ifosfamide: Identification of cytochrome P4502B enzymes and site-specific mutants with improved enzyme kinetics', *Molecular Pharmacology*, vol. 65, no. 5, pp. 1278-1285.

Chua, MS, Kashiyama, E, Bradshaw, TD, Stinson, SF, Brantley, E, Sausville, EA & Stevens, MF 2000, 'Role of Cyp1A1 in modulation of antitumor properties of the

novel agent 2-(4-amino-3-methylphenyl)benzothiazole (DF 203, NSC 674495) in human breast cancer cells', *Cancer Research,* vol. 60, no. 18, pp. 5196-5203.

Chun, YJ, Jeong, TC, Roh, JK & Guengerich, FP 1997, 'Characterization of a fusion protein between human cytochrome P450 1A1 and rat NADPH-P450 oxidoreductase in Escherichia coli', *Biochemical and Biophysical Research Communications,* vol. 230, no. 1, pp. 211-214.

Chun, YJ, Kim, MY & Guengerich, FP 1999, 'Resveratrol is a selective human cytochrome P450 1A1 inhibitor', *Biochemical & Biophysical Research Communications,* vol. 262, no. 1, pp. 20-24.

Chun, YJ, Ryu, SY, Jeong, TC & Kim, MY 2001, 'Mechanism-based inhibition of human cytochrome P450 1A1 by rhapontigenin', *Drug Metabolism & Disposition,* vol. 29, no. 4 Pt 1, pp. 389-393.

Chun, YJ, Shimada, T & Guengerich, FP 1996, 'Construction of a human cytochrome P450 1A1: rat NADPH-cytochrome P450 reductase fusion protein cDNA and expression in Escherichia coli, purification, and catalytic properties of the enzyme in bacterial cells and after purification', *Archives of Biochemistry & Biophysics,* vol. 330, no. 1, pp. 48-58.

Ciolino, HP, MacDonald, CJ & Yeh, GC 2002, 'Inhibition of carcinogen-activating enzymes by 16alpha-fluoro-5-androsten-17-one', *Cancer Research,* vol. 62, no. 13, pp. 3685-3690.

Code, EL, Crespi, CL, Penman, BW, Gonzalez, FJ, Chang, TK & Waxman, DJ 1997, 'Human cytochrome P4502B6: interindividual hepatic expression, substrate specificity, and role in procarcinogen activation', *Drug Metabolism & Disposition,* vol. 25, no. 8, pp. 985-993.

Cornish-Bowden, A 2004, *Fundamentals of Enzyme Kinetics,* Protland Press, London.

Cosme, J & Johnson, EF 2000, 'Engineering microsomal cytochrome P4502C5 to be a soluble, monomeric enzyme - Mutations that alter aggregation, phospholipid dependence of catalysis, and membrane binding', *Journal of Biological Chemistry,* vol. 275, no. 4, pp. 2545-2553.

Daly, AK 2003, 'Pharmacogenetics of the major polymorphic metabolizing enzymes', *Fundamental & Clinical Pharmacology,* vol. 17, no. 1, pp. 27-41.

Dayhoff, MO, Schwartz, RM & Orcutt, BC 1979, 'Atlas of protein sequence and structure', vol. 4, no. 3, pp. 345-352.

de Felipe, P, Luke, GA, Hughes, LE, Gani, D, Halpin, C & Ryan, MD 2006, 'E unum pluribus: multiple proteins from a self-processing polyprotein', *Trends in Biotechnology,* vol. 24, no. 2, pp. 68-75.

de Felipe, P, Luke, GA, Koehler, M, Brown, JD & Ryan, MD 'Inhibition of 2A-mediated lsquocleavagersquo of certain artificial polyproteins bearing <I>N</I>-terminal signal sequences', *Biotechnology Journal,* vol. 5, no. 2, pp. 213-223.

de Felipe, P, Luke, GA, Koehler, M, Brown, JD & Ryan, MD 2004, 'Skipping the co-expression problem: the new 2A "CHYSEL" technology', *Genetic Vaccines and Therapy,* vol. 2, no. 1, pp. 13.

de Graaf, C, Vermeulen, NP & Feenstra, KA 2005, 'Cytochrome p450 in silico: an integrative modeling approach', *J Med Chem,* vol. 48, no. 8, pp. 2725-2755.

Deeni, YY, Paine, MJI, Ayrton, AD, Clarke, SE, Chenery, R & Wolf, CR 2001, 'Expression, purification, and biochemical characterization of a human cytochrome P450CYP2D6-NADPH cytochrome P450 reductase fusion protein', *Archives of Biochemistry & Biophysics,* vol. 396, no. 1, pp. 16-24.

Denison, MS & Nagy, SR 2003, 'Activation of the aryl hydrocarbon receptor by structurally diverse exogenous and endogenous chemicals', *Annual Review of Pharmacology & Toxicology,* vol. 43, no. pp. 309-334.

Denny, WA 2002, 'Prodrugs for Gene-Directed Enzyme-Prodrug Therapy (Suicide Gene Therapy)', *Journal of Biomedicine and Biotechnology,* vol. 2003, no. 1, pp. 48-70.

Domanski, TL & Halpert, JR 2001, 'Analysis of Mammalian Cytochrome P450 Structure and Function by Site-Directed Mutagenesis', *Current Drug Metabolism,* vol. 2, no. pp. 117-137.

Dong, J & Porter, TD 1996, 'Coexpression of mammalian cytochrome P450 and reductase in Escherichia coli', *Archives of Biochemistry & Biophysics,* vol. 327, no. 2, pp. 254-259.

Eddy, SR 1998, 'Profile hidden Markov models', *Bioinformatics,* vol. 14, no. 9, pp. 755-763.

Edwards, RJ, Murray, BP, Singleton, AM & Boobis, AR 1991, 'Orientation of cytochromes P450 in the endoplasmic reticulum', *Biochemistry,* vol. 30, no. 1, pp. 71-76.

Eggermont, AMM 2005, 'New and standard management of malignant melanoma', *Ejc Supplements,* vol. 3, no. 3, pp. 454-457.

El-Aneed, A 2004, 'Current strategies in cancer gene therapy', *Eur J Pharmacol,* vol. 498, no. 1-3, pp. 1-8.

Erdmann, MK 2010, 'Immunity unleashed in melanoma', *The Lancet Oncology,* vol. 11, no. 2, pp. 108-109.

Estabrook, RW, Franklin, MR, Cohen, B, Shigamatzu, A & Hildebrandt, AG 1971, 'Influence of hepatic microsomal mixed function oxidation reactions on cellular metabolic control', *Metabolism,* vol. 20, no. 2, pp. 187-199.

Fisher, CW, Shet, MS, Caudle, DL, Martin-Wixtrom, CA & Estabrook, RW 1992, 'High-level expression in Escherichia coli of enzymatically active fusion proteins containing the domains of mammalian cytochromes P450 and NADPH-P450 reductase flavoprotein', *Proceedings of the National Academy of Sciences of the United States of America,* vol. 89, no. 22, pp. 10817-10821.

Fisher, CW, Shet, MS & Estabrook, RW 1996, 'Construction of plasmids and expression in Escherichia coli of enzymatically active fusion proteins containing the heme-domain of a P450 linked to NADPH-P450 reductase', *Methods in Enzymology,* vol. 272, no. pp. 15-25.

Fleming, BD, Tian, Y, Bell, SG, Wong, LL, Urlacher, V & Hill, HA 2003, 'Redox properties of cytochrome p450BM3 measured by direct methods', *European Journal of Biochemistry,* vol. 270, no. 20, pp. 4082-4088.

Fujita, K & Kamataki, T 2002, 'Genetically Engineered Bacterial Cells Co-expressed Human Cytochrome P450 with NADPH-cytochrome P450 Reductase: Prediction of Metabolism and Toxicity of Drugs in Humans', *Drug Metabolism Pharmacokinetics*, vol. 17, no. 1, pp. 1-22.

Galijatovic, A, Beaton, D, Nguyen, N, Chen, S, Bonzo, J, Johnson, R, Maeda, S, Karin, M, Guengerich, FP & Tukey, RH 2004, 'The human CYP1A1 gene is regulated in a developmental and tissue-specific fashion in transgenic mice', *Journal of Biological Chemistry*, vol. 279, no. 23, pp. 23969-23976.

Garte, S, Gaspari, L, Alexandrie, AK, Ambrosone, C, Autrup, H, Autrup, JL, Baranova, H, Bathum, L, Benhamou, S, Boffetta, P, Bouchardy, C, Breskvar, K, Brockmoller, J, Cascorbi, I, Clapper, ML, Coutelle, C, Daly, A, Dell'Omo, M, Dolzan, V, Dresler, CM, Fryer, A, Haugen, A, Hein, DW, Hildesheim, A, Hirvonen, A, Hsieh, LL, Ingelman-Sundberg, M, Kalina, I, Kang, DH, Kihara, M, Kiyohara, C, Kremers, P, Lazarus, P, Le Marchand, L, Lechner, MC, van Lieshout, EMM, London, S, Manni, JJ, Maugard, CM, Morita, S, Nazar-Stewart, V, Noda, K, Oda, Y, Parl, FF, Pastorelli, R, Persson, I, Peters, WHM, Rannug, A, Rebbeck, T, Risch, A, Roelandt, L, Romkes, M, Ryberg, D, Salagovic, J, Schoket, B, Seidegard, J, Shields, PG, Sim, E, Sinnet, D, Strange, RC, Stucker, I, Sugimura, H, To-Figueras, J, Vineis, P, Yu, MC & Taioli, E 2001, 'Metabolic gene polymorphism frequencies in control populations', *Cancer Epidemiology Biomarkers & Prevention*, vol. 10, no. 12, pp. 1239-1248.

Gillam, EM, Wunsch, RM, Ueng, YF, Shimada, T, Reilly, PE, Kamataki, T & Guengerich, FP 1997, 'Expression of cytochrome P450 3A7 in Escherichia coli: effects of 5' modification and catalytic characterization of recombinant enzyme expressed in bicistronic format with NADPH-cytochrome P450 reductase', *Archives of Biochemistry & Biophysics*, vol. 346, no. 1, pp. 81-90.

Gillam, EMJ, Baba, T, Kim, BR, Ohmori, S & Guengerich, FP 1993, 'Expression of Modified Human Cytochrome-P450 3a4 in Escherichia-Coli and Purification and Reconstitution of the Enzyme', *Archives of Biochemistry & Biophysics*, vol. 305, no. 1, pp. 123-131.

Gonzalez, FJ & Korzekwa, KR 1995, 'Cytochromes P450 expression systems', *Annual Review of Pharmacology & Toxicology*, vol. 35, no. pp. 369-390.

Gordon, DB, Marshall, SA & Mayo, SL 1999, 'Energy functions for protein design', *Current Opinion in Structural Biology*, vol. 9, no. 4, pp. 509-513.

Gotoh, O 1992, 'Substrate Recognition Sites in Cytochrome-P450 Family-2 (Cyp2) Proteins Inferred from Comparative Analyses of Amino-Acid and Coding Nucleotide-Sequences', *Journal of Biological Chemistry*, vol. 267, no. 1, pp. 83-90.

Greer, J 1981, 'Comparative Model-building of the Mammalian Serine Protease', *Journal of Molecular Biology*, vol. 153, no. pp. 1027-1042.

Guengerich, FP 2000, 'Metabolism of chemical carcinogens', *Carcinogenesis*, vol. 21, no. 3, pp. 345-351.

Guengerich, FP 2001, 'Common and uncommon cytochrome P450 reactions related to metabolism and chemical toxicity', *Chemical Research in Toxicology*, vol. 14, no. 6, pp. 611-650.

Guengerich, FP, Parikh, A, Yun, CH, Kim, D, Nakamura, K, Notley, LM & Gillam, EMJ 2000, 'What makes P450s work? Searches for answers with known and new P450s [Review]', *Drug Metabolism Reviews*, vol. 32, no. 3-4, pp. 267-281.

Guo, Z, Gillam, EM, Ohmori, S, Tukey, RH & Guengerich, FP 1994, 'Expression of modified human cytochrome P450 1A1 in Escherichia coli: effects of 5' substitution, stabilization, purification, spectral characterization, and catalytic properties', *Archives of Biochemistry & Biophysics*, vol. 312, no. 2, pp. 436-446.

Haines, DC, Tomchick, DR, Machius, M & Peterson, JA 2001, 'Pivotal role of water in the mechanism of P450BM-3', *Biochemistry*, vol. 40, no. 45, pp. 13456-13465.

Haining, RL, Jones, JP, Henne, KR, Fisher, MB, Koop, DR, Trager, WF & Rettie, AE 1999, 'Enzymatic determinants of the substrate specificity of CYP2C9: role of B'-C loop residues in providing the pi-stacking anchor site for warfarin binding', *Biochemistry*, vol. 38, no. 11, pp. 3285-3292.

Hakkola, J, Pasanen, M, Hukkanen, J, Pelkonen, O, Maenpaa, J, Edwards, RJ, Boobis, AR & Raunio, H 1996, 'Expression of xenobiotic-metabolizing cytochrome P450 forms in human full-term placenta', *Biochemical Pharmacology*, vol. 51, no. 4, pp. 403-411.

Halpert, JR, Miller, NE & Gorsky, LD 1985, 'On the mechanism of the inactivation of the major phenobarbital-inducible isozyme of rat liver cytochrome P-450 by chloramphenicol', *Journal of Biological Chemistry*, vol. 260, no. 14, pp. 8397-8403.

Han, W, Pentecost, BT & Spivack, SD 2003, 'Functional evaluation of novel single nucleotide polymorphisms and haplotypes in the promoter regions of CYP1B1 and CYP1A1 genes', *Molecular Carcinogenesis*, vol. 37, no. 3, pp. 158-169.

Hanahan, D 1985, *DNA Cloning: A Practical Approach*, IRL Press, McLean, Virginia, USA.

Hanioka, N, Tatarazako, N, Jinno, H, Arizono, K & Ando, M 2000, 'Determination of cytochrome P450 1A activities in mammalian liver microsomes by high-performance liquid chromatography with fluorescence detection', *Journal of Chromatography B*, vol. 744, no. 2, pp. 399-406.

Harlow, GR & Halpert, JR 1997, 'Alanine-scanning mutagenesis of a putative substrate recognition site in human cytochrome P450 3A4 - Role of residues 210 and 211 in flavonoid activation and substrate specificity', *Journal of Biological Chemistry*, vol. 272, no. 9, pp. 5396-5402.

Harlow, GR & Halpert, JR 1998, 'Analysis of human cytochrome P450 3A4 cooperativity: Construction and characterization of a site-directed mutant that displays hyperbolic steroid hydroxylation kinetics', *Proceedings of the National Academy of Sciences of the United States of America*, vol. 95, no. 12, pp. 6636-6641.

Harnastai, IN, Gilep, AA & Usanov, SA 2006, 'The development of an efficient system for heterologous expression of cytochrome P450s in Escherichia coli using hemA gene co-expression', *Protein Expression and Purification*, vol. 46, no. 1, pp. 47-55.

Hasemann, CA, Kurumbail, RG, Boddupalli, SS, Peterson, JA & Deisenhofer, J 1995, 'Structure and Function of Cytochromes-P450 - a Comparative-Analysis of 3 Crystal-Structures', *Structure*, vol. 3, no. 1, pp. 41-62.

Hayashi, S-i, Watanabe, J, Nakachi, K & Kawajiri, K 1991, 'Genetic Linkage of Lung Cancer-Associated MspI Polymorphisms with Amino Acid Replacement in the Heme Binding Region of the Human Cytochrome P450IA1 Gene', *J Biochem*, vol. 110, no. 3, pp. 407-411.

He, YA, Balfour, CA, Kedzie, KM & Halpert, JR 1992, 'Role of Residue-478 as a Determinant of the Substrate-Specificity of Cytochrome-P450-2b1', *Biochemistry*, vol. 31, no. 38, pp. 9220-9226.

Holst, J, Vignali, KM, Burton, AR & Vignali, DAA 2006, 'Rapid analysis of T-cell selection in vivo using T cell-receptor retrogenic mice', *Nat Meth*, vol. 3, no. 3, pp. 191-197.

Houston, JB & Kenworthy, KE 2000, 'In vitro-in vivo scaling of CYP kinetic data not consistent with the classical Michaelis-Menten model', *Drug Metab Dispos*, vol. 28, no. 3, pp. 246-254.

Huang, Z & Waxman, DJ 2001, 'Modulation of cyclophosphamide-based cytochrome P450 gene therapy using liver P450 inhibitors', *Cancer Gene Ther*, vol. 8, no. 6, pp. 450-458.

Hudecek, J, Hodek, P, Anzenbacherova, E & Anzenbacher, P 2007, 'Structural analysis of cytochromes P450 shows differences in flexibility of heme 2-and 4-vinyls', *Biochimica Et Biophysica Acta-General Subjects*, vol. 1770, no. 3, pp. 413-419.

Hughes, TL, Johnson, T, Razzano, LA, Cassidy, R & Ferguson, MJ 2002, 'The role of pro-drug therapy in the treatment of cancer', *American Journal of Public Health*, vol. 92, no. 7, pp. 1131-1139.

Hunter, CA & Sanders, JKM 1990, 'The Nature of Pi-Pi Interactions', *Journal of the American Chemical Society*, vol. 112, no. 14, pp. 5525-5534.

Ikushiro, S, Sahara, M, Emi, Y, Yabusaki, Y & Iyanagi, T 2004, 'Functional co-expression of xenobiotic metabolizing enzymes, rat cytochrome P450 1A1 and UDP-glucuronosyltransferase 1A6, in yeast microsomes', *Biochimica et Biophysica Acta*, vol. 1672, no. 2, pp. 86-92.

Iori, F, da Fonseca, R, Ramos, MJ & Menziani, MC 2005, 'Theoretical quantitative structure-activity relationships of flavone ligands interacting with cytochrome P450 1A1 and 1A2 isozymes', *Bioorganic & Medicinal Chemistry*, vol. 13, no. 14, pp. 4366-4374.

Iwata, H, Fujita, K, Kushida, H, Suzuki, A, Konno, Y, Nakamura, K, Fujino, A & Kamataki, T 1998, 'High Catalytic Activity of Human Cytochrome P450 Co-Expressed with Human Nadph-Cytochrome P450 Reductase in Escherichia Coli', *Biochemical Pharmacology*, vol. 55, no. 8, pp. 1315-1325.

Jaiswal, AK, Gonzalez, FJ & Nebert, DW 1985, 'Human P1-450 gene sequence and correlation of mRNA with genetic differences in benzo[a]pyrene metabolism.' *Nucleic Acids Res.*, vol. 35, no. 12, pp. 4503-4520.

Jana, S & Deb, JK 2005, 'Strategies for efficient production of heterologous proteins in Escherichia coli', *Applied Microbiology and Biotechnology*, vol. 67, no. 3, pp. 289-298.

Jin, CJ, Mackenzie, PI & Miners, JO 1997, 'The regio- and stereo-selectivity of C19 and C21 hydroxysteroid glucuronidation by UGT2B7 and UGT2B11', *Archives of Biochemistry and Biophysics*, vol. 341, no. 2, pp. 207-211.

Johannes, L, Omann, M, Duvier, D, Holzmuller, H, Gregor, W, Salmons, B, Gunzburg, WH & Renner, M 2006, 'Cytochrome P450 reductase dependent inhibition of cytochrome P4502B1 activity: Implications for gene directed enzyme prodrug therapy', *Biochemical Pharmacology*, vol. 72, no. 7, pp. 893-901.

Johnson, DL, Lewis, BC, Elliot, DJ, Miners, JO & Martin, LL 2005a, 'Electrochemical characterisation of the human cytochrome P450 CYP2C9', *Biochemical Pharmacology*, vol. 69, no. 10, pp. 1533-1541.

Johnson, DL, Lewis, BC, Elliot, DJ, Miners, JO & Martin, LL 2005b, 'Electrochemical characterisation of the human cytochrome P450CYP2C9', *Biochemical Pharmacology*, vol. 69, no. 10, pp. 1533-1541.

Johnson, JA 2003, 'Pharmacogenetics: potential for individualized drug therapy through genetics', *Trends in Genetics*, vol. 19, no. 11, pp. 660-666.

Jounaidi, Y, Chen, CS, Veal, GJ & Waxman, DJ 2006, 'Enhanced antitumor activity of P450 prodrug-based gene therapy using the low K-m cyclophosphamide 4-hydroxylase P4502B11', *Molecular Cancer Therapeutics*, vol. 5, no. 3, pp. 541-555.

Jounaidi, Y, Hecht, JED & Waxman, DJ 1998, 'Retroviral transfer of human cytochrome P450 genes for oxazaphosphorine-based cancer gene therapy', *Cancer Research*, vol. 58, no. 19, pp. 4391-4401.

Jounaidi, Y & Waxman, DJ 2000, 'Combination of the bioreductive drug tirapazamine with the chemotherapeutic prodrug cyclophosphamide for P450/P450-reductase-based cancer gene therapy', *Cancer Research*, vol. 60, no. 14, pp. 3761-3769.

Jounaidi, Y & Waxman, DJ 2001, 'Frequent, moderate-dose cyclophosphamide administration improves the efficacy of cytochrome P-450/cytochrome P-450 reductase-based cancer gene therapy', *Cancer Research*, vol. 61, no. 11, pp. 4437-4444.

Kan, O, Griffiths, L, Baban, D, Iqball, S, Uden, M, Spearman, H, Slingsby, J, Price, T, Esapa, M, Kingsman, S, Kingsman, A, Slade, A & Naylor, S 2001, 'Direct retroviral delivery of human cytochrome P450 2B6 for gene-directed enzyme prodrug therapy of cancer', *Cancer Gene Therapy*, vol. 8, no. 7, pp. 473-482.

Kan, O, Kingsman, S & Naylor, S 2002, 'Cytochrome P450-based cancer gene therapy: current status', *Expert Opinion on Biological Therapy*, vol. 2, no. 8, pp. 857-868.

Kawajiri, K, Nakachi, K, Imai, K, Yoshii, A, Shinoda, N & Watanabe, J 1990, 'Identification of genetically high risk individuals to lung cancer by DNA polymorphisms of the cytochrome P45 0IA1 gene', *Febs Letters*, vol. 263, no. 1, pp. 131-133.

Kawajiri, K, Watanabe, J, Gotoh, O, Tagashira, Y, Sogawa, K & Fujii-Kuriyama, Y 1986, 'Structure and drug inducibility of the human cytochrome P-450c gene.' *Eur J Biochem.*, vol. 159, no. 2, pp. 219-225.

Kerdpin, O, Elliot, DJ, Boye, SL, Birkett, DJ, Yoovathaworn, K & Miners, JO 2004, 'Differential contribution of active site residues in substrate recognition sites 1 and 5 to cytochrome p450 2C8 substrate selectivity and regioselectivity', *Biochemistry,* vol. 43, no. 24, pp. 7834-7842.

Kisselev, P, Schunck, WH, Roots, I & Schwarz, D 2005, 'Association of CYP1A1 polymorphisms with differential metabolic activation of 17 beta-estradiol and estrone', *Cancer Research,* vol. 65, no. 7, pp. 2972-2978.

Krane, DE & Raymer, ML 2003, *Fundamental concepts of bioinformatics.*, Benjamin Cummings, San Francisco, CA.

Kubota, T, Lewis, BC, Elliot, DJ, Mackenzie, PI & Miners, JO 2007, 'Critical roles of residues 36 and 40 in the phenol and tertiary amine aglycone substrate selectivities of UDP-glucuronosyltransferases 1A3 and 1A4', *Molecular Pharmacology,* vol. 72, no. 4, pp. 1054-1062.

Kuffel, MJ, Schroeder, JC, Pobst, LJ, Naylor, S, Reid, JM, Kaufmann, SH & Ames, MM 2002, 'Activation of the antitumor agent aminoflavone (NSC 686288) is mediated by induction of tumor cell cytochrome P450 1A1/1A2', *Molecular Pharmacology,* vol. 62, no. 1, pp. 143-153.

Kumar, S, Chen, CS, Waxman, DJ & Halpert, JR 2005, 'Directed evolution of mammalian cytochrome P4502B1', *Journal of Biological Chemistry*, vol. 280, no. 20, pp. 19569-19575.

Kumar, V, Rock, DA, Warren, CJ, Tracy, TS & Wahlstrom, JL 2006, 'Enzyme source effects on CYP2C9 kinetics and inhibition', *Drug Metabolism and Disposition*, vol. 34, no. 11, pp. 1903-1908.

Laemmli, UK 1970, 'Cleavage of structural proteins during the assembly of the head of bacteriophage T4', *Nature,* vol. 227, no. 259, pp. 680-685.

Laskowski, RA, Macarthur, MW, Moss, DS & Thornton, JM 1993, 'Procheck - a Program to Check the Stereochemical Quality of Protein Structures', *Journal of Applied Crystallography,* vol. 26, no. pp. 283-291.

Lazaridis, T & Karplus, M 2000, 'Effective energy functions for protein structure prediction', *Current Opinion in Structural Biology,* vol. 10, no. 2, pp. 139-145.

Le Ferrec, E, Lagadic-Gossmann, D, Rauch, C, Bardiau, C, Maheo, K, Massiere, F, Le Vee, M, Guillouzo, A & Morel, F 2002, 'Transcriptional induction of CYP1A1 by oltipraz in human Caco-2 cells is aryl hydrocarbon receptor- and calcium-dependent', *Journal of Biological Chemistry,* vol. 277, no. 27, pp. 24780-24787.

Lengler, J, Holzmuller, H, Sahnons, B, Gunzburg, WH & Renner, M 2005, 'FMDV-2A sequence and protein arrangement contribute to functionality of CYP2B1-reporter fusion protein', *Analytical Biochemistry,* vol. 343, no. 1, pp. 116-124.

Lesyng, B & McCammon, JA 1993, 'Molecular Modeling Methods - Basic Techniques and Challenging Problems', *Pharmacology & Therapeutics,* vol. 60, no. 2, pp. 149-&.

Levine-Fridman, A, Chen, L & Elferink, CJ 2004, 'Cytochrome P4501A1 promotes G1 phase cell cycle progression by controlling aryl hydrocarbon receptor activity', *Molecular Pharmacology,* vol. 65, no. 2, pp. 461-469.

Levy, RH, Thummel, K, Trager, WF, Hansten, PD & Eichelbaum, M 2000, *Metabolic Drug Interactions,* Lippincott Williams & Wilkins, New York.

Lewis, BC, Mackenzie, PI, Elliot, DJ, Burchell, B, Bhasker, CR & Miners, JO 2007, 'Amino terminal domains of human UDP-glucuronosyltransferases (UGT) 2B7 and 2B15 associated with substrate selectivity and autoactivation', *Biochemical Pharmacology,* vol. 73, no. 9, pp. 1463-1473.

Lewis, BC, Mackenzie, PI & Miners, JO 2007, 'Comparative homology modeling of human cytochrome P4501A1 (CYP1A1) and confirmation of residues involved in 7-ethoxyresorufin O-deethylation by site-directed mutagenesis and enzyme kinetic analysis', *Archives of Biochemistry and Biophysics,* vol. 468, no. 1, pp. 58-69.

Lewis, DF 2003, 'Essential requirements for substrate binding affinity and selectivity toward human CYP2 family enzymes', *Arch Biochem Biophys,* vol. 409, no. 1, pp. 32-44.

Lewis, DF, Modi, S & Dickins, M 2002, 'Structure-activity relationship for human cytochrome P450 substrates and inhibitors', *Drug Metabolism Reviews,* vol. 34, no. 1-2, pp. 69-82.

Lewis, DFV 2002a, 'Modelling human cytochromes P450 involved in drug metabolism from the CYP2C5 crystallographic template', *Journal of Inorganic Biochemistry,* vol. 91, no. 4, pp. 502-514.

Lewis, DFV 2002b, 'Molecular modeling of human cytochrome P450-substrate interactions', *Drug Metabolism Reviews,* vol. 34, no. 1-2, pp. 55-67.

Lewis, DFV, Ioannides, C & Parke, DV 1994a, 'Molecular Modeling of Cytochrome Cyp1a1 - a Putative Access Channel Explains Differences in Induction Potency between the Isomers Benzo(a)Pyrene and Benzo(E)Pyrene, and 2-Acetylaminofluorene and 4-Acetylaminofluorene', *Toxicology Letters,* vol. 71, no. 3, pp. 235-243.

Lewis, DFV, Ioannides, C & Parke, DV 1994b, 'Molecular modelling of cytochrome CYP1A1: a putative access channel explains differences in induction potency between the isomers benzo(a)pyrene and benzo(e)pyrene, and 2- and 4-acetylaminofluorene', *Toxicology Letters,* vol. 71, no. 3, pp. 235-243.

Lewis, DFV, Ito, Y & Lake, BG 2006, 'Metabolism of coumarin by human P450s: A molecular modelling study', *Toxicology in Vitro,* vol. 20, no. 2, pp. 256-264.

Lewis, DFV & Lake, BG 1996, 'Molecular modelling of CYP1A subfamily members based on an alignment with CYP102: Rationalization of CYP1A substrate specificity in terms of active site amino acid residues', *Xenobiotica,* vol. 26, no. 7, pp. 723-753.

Lewis, DFV, Lake, BG & Dickins, M 2004, 'Quantitative structure-activity relationships within a homologous series of 7-alkoxyresorufins exhibiting activity towards CYP1A and CYP2B enzymes: molecular modelling studies on key members of the resorufin series with CYP2C5-derived models of human CYP1A1, CYP1A2, CYP2B6 and CYP3A4', *Xenobiotica,* vol. 34, no. 6, pp. 501-513.

Lewis, DFV, Lake, BG, George, SG, Dickins, M, Eddershaw, PJ, Tarbit, MH, Beresford, AP, Goldfarb, PS & Guengerich, FP 1999, 'Molecular modelling of CYP1 family enzymes CYP1A1, CYP1A2, CYP1A6 and CYP1B1 based on sequence homology with CYP102', *Toxicology,* vol. 139, no. 1-2, pp. 53-79.

Li, DN, Pritchard, MP, Hanlon, SP, Burchell, B, Wolf, CR & Friedberg, T 1999, 'Competition between cytochrome P-450 isozymes for NADPH-cytochrome P-450 oxidoreductase affects drug metabolism', *Journal of Pharmacology and Experimental Therapeutics*, vol. 289, no. 2, pp. 661-667.

Lin, Y, Lu, P, Tang, C, Mei, Q, Sandig, G, Rodrigues, AD, Rushmore, TH & Shou, M 2001, 'Substrate inhibition kinetics for cytochrome P450-catalyzed reactions', *Drug Metabolism and Disposition*, vol. 29, no. 4, pp. 368-374.

Linge, JP, Williams, MA, Spronk, C, Bonvin, A & Nilges, M 2003, 'Refinement of protein structures in explicit solvent', *Proteins-Structure Function and Genetics*, vol. 50, no. 3, pp. 496-506.

Linos, E, Swetter, SM, Cockburn, MG, Colditz, GA & Clarke, CA 2009, 'Increasing Burden of Melanoma in the United States', *Journal of Investigative Dermatology*, vol. 129, no. 7, pp. 1666-1674.

Liu, J, Ericksen, SS, Besspiata, D, Fisher, CW & Szklarz, GD 2003, 'Characterization of substrate binding to cytochrome P450 1A1 using molecular modeling and kinetic analyses: case of residue 382', *Drug Metabolism & Disposition*, vol. 31, no. 4, pp. 412-420.

Liu, J, Ericksen, SS, Sivaneri, M, Besspiata, D, Fisher, CW & Szklarz, GD 2004, 'The effect of reciprocal active site mutations in human cytochromes P450 1A1 and 1A2 on alkoxyresorufin metabolism', *Archives of Biochemistry & Biophysics*, vol. 424, no. 1, pp. 33-43.

Loaiza-Perez, AI, Kenney, S, Boswell, J, Hollingshead, M, Alley, MC, Hose, C, Ciolino, HP, Yeh, GC, Trapel, JB, Vistica, DT & Saosville, EA 2004, 'Aryl hydrocarbon receptor activation of an antitumor aminoflavone: Basis of selective toxicity for MCF-7 breast tumor cells', *Molecular Cancer Therapy*, vol. 3, no. 6, pp.

Lohr, M, Hoffmeyer, A, Kroger, JC, Freund, M, Hain, J, Holle, A, Karle, P, Knofel, WT, Liebe, S, Muller, P, Nizze, H, Renner, M, Saller, RM, Wagner, T, Hauenstein, K, Gunzburg, WH & Salmons, B 2001, 'Microencapsulated cell-mediated treatment of inoperable pancreatic carcinoma', *Lancet*, vol. 357, no. 9268, pp. 1591-1592.

Long, L & Dolan, ME 2001, 'Role of cytochrome P450 isoenzymes in metabolism of O-6-benzylguanine: Implications for dacarbazine activation', *Clinical Cancer Research*, vol. 7, no. 12, pp. 4239-4244.

Loo, TL, Luce, JK, Jardine, JH & Frei, E 1968, 'Pharmacologic Studies, of the Antitumor Agent 5-(Dimethyltriazeno)imidazole-4-carboxamide', *Cancer Research*, vol. 28, no. pp. 2448-2453.

Lord, RS, Bongiovanni, B & Bralley, JA 2002, 'Estrogen metabolism and the diet-cancer connection: rationale for assessing the ratio of urinary hydroxylated estrogen metabolites', *Alternative Medicine Review*, vol. 7, no. 2, pp. 112-129.

Lowry, OH, Rosenbrough, NJ, Farr, L & Randall, RJ 1951, 'Protein Measurement with the Folin Phenol Reagent', *Journal of Biological Chemistry*, vol. 193, no. pp. 267-275.

Luce, J, Thurman, WG, Isaacs, BL & Talley, RW 1970, 'Clinical trials with the antitumor agent 5-(3,3-dimethyl-1-triazeno)imidazole-4-carboxamide(NSC-45388).' *Cancer Chemother Rep.*, vol. 54, no. 2, pp. 119-124.

Luirink, J, von Heijne, G, Houben, E & de Gier, JW 2005, 'Biogenesis of inner membrane proteins in Escherichia coli', *Annual Review of Microbiology,* vol. 59, no. pp. 329-355.

Manna, SK & Mazumdar, S 2006, 'Role of threonine 101 on the stability of the heme active site of cytochrome p450cam: Multiwavelength circular dichroism studies', *Biochemistry,* vol. 45, no. 42, pp. 12715-12722.

Matias, J, Scudiero, DA, Hite, KM, Monks, A, Sausville, EA, Waxman, DJ & Yu, LJ 2001, 'P450 enzyme expression patterns in the NCI human tumor cell line panel', *Drug Metabolism & Disposition,* vol. 29, no. 3, pp. 304-312.

McFadyen, MCE, Melvin, WT & Murray, GI 2004, 'Cytochrome P450 enzymes: Novel options for cancer therapeutics', *Molecular Cancer Therapy,* vol. 3, no. 3, pp. 363-371.

McLure, JA, Miners, JO & Birkett, DJ 2000, 'Nonspecific binding of drugs to human liver microsomes', *British Journal of Clinical Pharmacology,* vol. 49, no. 5, pp. 453-461.

McManus, ME, Burgess, WM, Veronese, ME, Huggett, A, Quattrochi, LC & Tukey, RH 1990, 'Metabolism of 2-Acetylaminofluorene and Benzo(a)Pyrene and Activation of Food-Derived Heterocyclic Amine Mutagens by Human Cytochromes-P-450', *Cancer Research,* vol. 50, no. 11, pp. 3367-3376.

Meer, L, Janzer, RC, Kleihues, P & Kolar, GF 1986, 'In vivo metabolism and reaction with DNA of the cytostatic agent, 5-(3,3-dimethyl-1-triazeno)imidazole-4-carboxamide (DTIC)', *Biochemical Pharmacology,* vol. 35, no. 19, pp. 3243-3247.

Meunier, B, de Visser, SP & Shaik, S 2004, 'Mechanism of oxidation reactions catalyzed by cytochrome p450 enzymes', *Chem Rev,* vol. 104, no. 9, pp. 3947-3980.

Miles, CS, Ost, TWB, Noble, MA, Munro, AW & Chapman, SK 2000, 'Protein engineering of cytochromes P-450', *Biochimica Et Biophysica Acta-Protein Structure and Molecular Enzymology,* vol. 1543, no. 2, pp. 383-407.

Miyake, Y & Takayama, N 1975, 'Spectral Intermediates during the Reduction of Hepatic Microsomal Cytochrome P-450.' *J Biochem.,* vol. 79, no. pp. 1077-1087.

Miyoshi, Y, Takahashi, Y, Egawa, C & Noguchi, S 2002, 'Breast cancer risk associated with CYP1A1 genetic polymorphisms in Japanese women', *Breast Journal,* vol. 8, no. 4, pp. 209-215.

Moult, J 1999, 'Predicting protein three-dimensional structure', *Current Opinion in Biotechnology,* vol. 10, no. 6, pp. 583-588.

Murray, GI, Foster, CO, Barnes, TS, Weaver, RJ, Snyder, CP, Ewen, SW, Melvin, WT & Burke, MD 1992, 'Cytochrome P450IA expression in adult and fetal human liver', *Carcinogenesis,* vol. 13, no. 2, pp. 165-169.

Nadler, SG & Strobel, HW 1991, 'Identification and Characterization of an Nadph-Cytochrome-P450 Reductase Derived Peptide Involved in Binding to Cytochrome-P450', *Archives of Biochemistry and Biophysics,* vol. 290, no. 2, pp. 277-284.

Nakajima, M, Tane, K, Nakamura, S, Shimada, N, Yamazaki, H & Yokoi, T 2002, 'Evaluation of approach to predict the contribution of multiple cytochrome P450s in drug metabolism using relative activity factor: effects of the differences in expression levels of NADPH-cytochrome P450 reductase and cytochrome b(5) in the expression

system and the differences in the marker activities', *Journal of Pharmaceutical Sciences,* vol. 91, no. 4, pp. 952-963.

Nebert, DW, Dalton, TP, Okey, AB & Gonzalez, FJ 2004, 'Role of aryl hydrocarbon receptor-mediated induction of the CYP1 enzymes in environmental toxicity and cancer', *Journal of Biological Chemistry,* vol. 279, no. 23, pp. 23847-23850.

Nebert, DW, McKinnon, RA & Puga, A 1996, 'Human drug-metabolizing enzyme polymorphisms: Effects on risk of toxicity and cancer', *DNA and Cell Biology,* vol. 15, no. 4, pp. 273-280.

Nebert, DW & Nelson, DR 1991, 'P450 Gene Nomenclature Based on Evolution', *Methods in Enzymology,* vol. 206, no. pp. 3-11.

Negishi, M, Uno, T, Darden, TA, Sueyoshi, T & Pedersen, LG 1996, 'Structural flexibility and functional versatility of mammalian P450 enzymes', *Faseb Journal,* vol. 10, no. 7, pp. 683-689.

Nelson, DR, Koymans, L, Kamataki, T, Stegeman, JJ, Feyereisen, R, Waxman, DJ, Waterman, MR, Gotoh, O, Coon, MJ, Estabrook, RW, Gunsalus, IC & Nebert, DW 1996, 'P450 superfamily: Update on new sequences, gene mapping, accession numbers and nomenclature', *Pharmacogenetics,* vol. 6, no. 1, pp. 1-42.

Nguyen, TA, Tychopoulos, M, Bichat, F, Zimmermann, C, Flinois, JP, Diry, M, Ahlberg, E, Delaforge, M, Corcos, L, Beaune, P, Dansette, P, Andre, F & de Waziers, I 2008, 'Improvement of cyclophosphamide activation by CYP2B6 mutants: From in silico to ex vivo', *Molecular Pharmacology,* vol. 73, no. 4, pp. 1122-1133.

Ogliaro, F, de Visser, SP & Shaik, S 2002, 'The 'push' effect of the thiolate ligand in cytochrome P450: a theoretical gauging', *Journal of Inorganic Biochemistry,* vol. 91, no. 4, pp. 554-567.

Olson, CF 1994, 'Time and space efficient pose clustering', *Computer vision and pattern recognition,* vol., no. pp. 251-258.

Omura, T & Sato, R 1964a, 'The carbon monoxide-binding pigment of liver microsomes: Evidence for its hemoprotein nature.' *J Biol Chem,* vol. 239, no. pp. 2370-2378.

Omura, T & Sato, R 1964b, 'The Carbon Monoxide-binding Pigmentof Liver Microsomes', *Journal of Biological Chemistry,* vol. 239, no. 7, pp. 2379-2385.

Ong, CE, Miners, JO, Birkett, DJ & Bhasker, CR 1998, 'Baculovirus-mediated expression of cytochrome P4502C8 and human NADPH-cytochrome P450 reductase: optimization of protein expression', *Xenobiotica,* vol. 28, no. 2, pp. 137-152.

Otyepka, M, Skopalik, J, Anzenbacherova, E & Anzenbacher, P 2007, 'What common structural features and variations of mammalian P450s are known to date?' *Biochimica Et Biophysica Acta-General Subjects,* vol. 1770, no. 3, pp. 376-389.

Palmer, T 1981, *Understanding enzymes / Trevor Palmer,* Ellis Harwood ; Halsted Press, Chichester : New York :.

Parikh, A, Gillam, EMJ & Guengerich, FP 1997, 'Drug Metabolism by Escherichia Coli Expressing Human Cytochromes P450', *Nature Biotechnology,* vol. 15, no. 8, pp. 784-788.

Parikh, A, Josephy, PD & Guengerich, FP 1999, 'Selection and characterization of human cytochrome P450 1A2 mutants with altered catalytic properties', *Biochemistry,* vol. 38, no. 17, pp. 5283-5289.

Patterson, LH & Murray, GI 2002, 'Tumour cytochrome P450 and drug activation', *Current Pharmaceutical Design,* vol. 8, no. 15, pp. 1335-1347.

Persson, I, Johansson, I & IngelmanSundberg, M 1997, 'In vitro kinetics of two human CYP1A1 variant enzymes suggested to be associated with interindividual differences in cancer susceptibility', *Biochemical and Biophysical Research Communications,* vol. 231, no. 1, pp. 227-230.

Peterson, JA & Prough, RA 1986, 'Cytochrome P-450 Reductase and Cytochrome b5 in Cytochrome P-450 Catalysis', in *Cytochrome P450,* eds PR Oritz de Montellano, Plenum Press, New York.

Petushkova, NA, Kanaeva, IP, Lisitsa, AV, Sheremetyeva, GF, Zgoda, VG, Samenkova, NF, Karuzina, II & Archakov, AI 2006, 'Characterization of human liver cytochromes P450 by combining the biochemical and proteomic approaches', *Toxicology in Vitro,* vol. 20, no. 6, pp. 966-974.

Polasek, TM, Elliot, DJ, Lewis, BC & Miners, JO 2004, 'Mechanism-based inactivation of human cytochrome P4502C8 by drugs in vitro', *Journal of Pharmacology and Experimental Therapeutics,* vol. 311, no. 3, pp. 996-1007.

Polasek, TM, Elliot, DJ & Miners, JO 2006, *Measurement of Human Cytochrome P4501A2 (CYP1A2) Activity In Vitro in Current Protocols in Toxicology*, Vol. 4.19, Supp. 27,

Polasek, TM, Elliot, DJ, Somogyi, AA, Gillam, EMJ, Lewis, BC & Miners, JO 2006, 'An evaluation of potential mechanism-based inactivation of human drug metabolizing cytochromes P450 by monoamine oxidase inhibitors, including isoniazid', *British Journal of Clinical Pharmacology,* vol. 61, no. 5, pp. 570-584.

Polasek, TM & Miners, JO 2006, 'Quantitative prediction of macrolide drug-drug interaction potential from in vitro studies using testosterone as the human cytochrome P4503A substrate', *European Journal of Clinical Pharmacology,* vol. 62, no. 3, pp. 203-208.

Poulos, TL, Finzel, BC, Gunsalus, IC, Wagner, GC & Kraut, J 1985, 'The 2.6-A crystal structure of Pseudomonas putida cytochrome P-450.' *J Biol Chem.,* vol. 260, no. 30, pp. 16122-16130.

Powell, MJD 1977, 'Restart Procedures for the Conjugate Gradient Method', *Mathematical Programming,* vol. 12, no. pp. 241-254.

Pritchard, MP, Glancey, MJ, Blake, JAR, Gilham, DE, Burchell, B, Wolf, CR & Fridberg, T 1998, 'Functional Co-Expression of Cyp2d6 and Human Nadph-Cytochrome P450 Reductase in Escherichia Coli', *Pharmacogenetics,* vol. 8, no. 1, pp. 33-42.

Pritchard, MP, Ossetian, R, Li, DN, Henderson, CJ, Burchell, B, Wolf, CR & Friedberg, T 1997, 'A general strategy for the expression of recombinant human cytochrome P450s in Escherichia coli using bacterial signal peptides: expression of CYP3A4, CYP2A6, and CYP2E1', *Archives of Biochemistry & Biophysics,* vol. 345, no. 2, pp. 342-354.

Provost, E, Rhee, J & Leach, SD 2007, 'Viral 2A peptides allow expression of multiple proteins from a single ORF in Transgenic zebrafish embryos', *Genesis*, vol. 45, no. 10, pp. 625-629.

Pugsley, AP 1993, 'The Complete General Secretory Pathway in Gram-Negative Bacteria', *Microbiological Reviews*, vol. 57, no. 1, pp. 50-108.

Queirolo, P & Acquati, M 2006, 'Targeted therapies in melanoma', *Cancer Treatment Reviews*, vol. 32, no. 7, pp. 524-531.

Reid, JM, Kuffel, MJ, Miller, JK, Rios, R & Ames, MM 1999, 'Metabolic activation of dacarbazine by human cytochromes P450: the role of CYP1A1, CYP1A2, and CYP2E1', *Clinical Cancer Research*, vol. 5, no. 8, pp. 2192-2197.

Rendic, S 2002, 'Summary of information on human CYP enzymes: Human P450 metabolism data', *Drug Metabolism Reviews*, vol. 34, no. 1-2, pp. 83-448.

Richardson, TH, Jung, F, Griffin, KJ, Wester, M, Raucy, JL, Kemper, B, Bornheim, LM, Hassett, C, Omiecinski, CJ & Johnson, EF 1995, 'Universal Approach to the Expression of Human and Rabbit Cytochrome P450s of the 2c Subfamily in Escherichia Coli', *Archives of Biochemistry & Biophysics*, vol. 323, no. 1, pp. 87-96.

Ridderstrom, M, Zamora, I, Fjellstrom, O & Andersson, TB 2001, 'Analysis of selective regions in the active sites of human cytochromes P450, 2C8, 2C9, 2C18, and 2C19 homology models using GRID/CPCA', *Journal of Medicinal Chemistry*, vol. 44, no. 24, pp. 4072-4081.

Roblin, S, Okey, AB & Harper, PA 2004, 'AH receptor antagonist inhibits constitutive CYP1A1 and CYP1B1 expression in rat BP8 cells', *Biochemical & Biophysical Research Communications*, vol. 317, no. 1, pp. 142-148.

Rooney, PH, Telfer, C, McFadyen, MC, Melvin, WT & Murray, GI 2004, 'The role of cytochrome P450 in cytotoxic bioactivation: future therapeutic directions', *Current Cancer Drug Targets*, vol. 4, no. 3, pp. 257-265.

Rooseboom, M, Commandeur, JNM & Vermeulen, NPE 2004, 'Enzyme-Catalyzed Activation of Anticancer Prodrugs', *Pharmacological Reviews*, vol. 56, no. 1, pp. 53-102.

Rowland, P, Blaney, FE, Smyth, MG, Jones, JJ, Leydon, VR, Oxbrow, AK, Lewis, CJ, Tennant, MG, Modi, S, Eggleston, DS, Chenery, RJ & Bridges, AM 2006, 'Crystal structure of human cytochrome P450 2D6', *Journal of Biological Chemistry*, vol. 281, no. 11, pp. 7614-7622.

Saitou, N & Nei, M 1987, 'The Neighbor-Joining Method - a New Method for Reconstructing Phylogenetic Trees', *Molecular Biology and Evolution*, vol. 4, no. 4, pp. 406-425.

Sambrook, J & Russell, DW 2001, *Molecular Cloning: A Laboratory Manual*, Cold Spring Harbor Laboratory Press, New York.

Sanada, M, Takagi, Y, Ito, R & Sekiguchi, M 2004, 'Killing and mutagenic actions of dacarbazine, a chemotherapeutic alkylating agent, on human and mouse cells: effects of Mgmt and Mlh1 mutations', *DNA Repair*, vol. 3, no. pp. 413-420.

Sandhu, P, Baba, T & Guengerich, FP 1993, 'Expression of Modified Cytochrome-P450-2c10-(2c9) in Escherichia-Coli, Purification, and Reconstitution of Catalytic Activity', *Archives of Biochemistry & Biophysics*, vol. 306, no. 2, pp. 443-450.

Sansen, S, Yano, JK, Reynold, RL, Schoch, GA, Griffin, KJ, Stout, CD & Johnson, EF 2007, 'Adaptions for the oxidation of polycyclic aromatic hydrocarbons exhibited by the structure of human P450 1A2', *The journal of Biological Chemistry,* vol. jbc.M611692200, no. pp. 1-16.

Schleinkofer, K, Sudarko, Winn, PJ, Ludemann, SK & Wade, RC 2005, 'Do mammalian cytochrome P450s show multiple ligand access pathways and ligand channelling?' *Embo Reports,* vol. 6, no. 6, pp. 584-589.

Schoch, GA, Yano, JK, Wester, MR, Griffin, KJ, Stout, CD & Johnson, EF 2004, 'Structure of human microsomal cytochrome P4502C8 - Evidence for a peripheral fatty acid binding site', *Journal of Biological Chemistry,* vol. 279, no. 10, pp. 9497-9503.

Schwartz, PS, Chen, CS & Waxman, DJ 2002, 'Enhanced bystander cytotoxicity of P450 gene-directed enzyme prodrug therapy by expression of the antiapoptotic factor p35', *Cancer Research,* vol. 62, no. 23, pp. 6928-6937.

Schwartz, PS & Waxman, DJ 2001, 'Cyclophosphamide induces caspase 9-dependent apoptosis in 9L tumor cells', *Molecular Pharmacology,* vol. 60, no. 6, pp. 1268-1279.

Scott, EE, He, YA, Wester, MR, White, MA, Chin, CC, Halpert, JR, Johnson, EF & Stout, CD 2004a, 'An open conformation of mammalian cytochrome P450 2B4 at 1.6-A resolution.' *PNAS,* vol. 100, no. 23, pp. 13196-13201.

Scott, EE, White, MA, He, YA, Johnson, EF, Stout, CD & Halpert, JR 2004b, 'Structure of mammalian cytochrome P4502B4 complexed with 4-(4-chlorophenyl) imidazole at 1.9-angstrom resolution - Insight into the range of P450 conformations and the coordination of redox partner binding', *Journal of Biological Chemistry,* vol. 279, no. 26, pp. 27294-27301.

Scripture, CD, Sparreboom, A & Figg, WD 2005, 'Modulation of cytochrome P450 activity: implications for cancer therapy', *Lancet Oncology,* vol. 6, no. 10, pp. 780-789.

Shaik, S, Kumar, D, de Visser, SP, Altun, A & Thiel, W 2005, 'Theoretical perspective on the structure and mechanism of cytochrome P450 enzymes', *Chemical Reviews,* vol. 105, no. 6, pp. 2279-2328.

Shealy, FY, Struck, RF, Holum, LB & Montgomery, JA 1961, 'Synthesis of Potential Anticancer Agents. XXIX. 5-diazoimidazole-4-carboxamide and 5-diazo-*v*-triazole-4-carboxamide.' *Journal of Organic Chemistry,* vol. 26, no. 7, pp. 2396-2401.

Shen, AL, Porter, TD, Wilson, TE & Kasper, CB 1989, 'Structural analysis of the FMN binding domain of NADPH-cytochrome P-450 oxidoreductase by site-directed mutagenesis', *Journal of Biological Chemistry,* vol. 264, no. 13, pp. 7584-7589.

Shet, MS, Fisher, CW, Arlotto, MP, Shackleton, CHL, Holmans, PL, Martinwixtrom, CA, Saeki, Y & Estabrook, RW 1994, 'Purification and Enzymatic Properties of a Recombinant Fusion Protein Expressed in Escherichia Coli Containing the Domains of Bovine P450 17a and Rat Nadph-P450 Reductase', *Archives of Biochemistry & Biophysics,* vol. 311, no. 2, pp. 402-417.

Shet, MS, Fisher, CW, Holmans, PL & Estabrook, RW 1993, 'Human cytochrome P450 3A4: enzymatic properties of a purified recombinant fusion protein containing

NADPH-P450 reductase', *Proceedings of the National Academy of Sciences of the United States of America*, vol. 90, no. 24, pp. 11748-11752.

Shimada, T & Fujii-Kuriyama, Y 2004, 'Metabolic activation of polycyclic aromatic hydrocarbons to carcinogens by cytochromes P450 1A1 and 1B1', *Cancer Science*, vol. 95, no. 1, pp. 1-6.

Shimada, T, Inoue, K, Suzuki, Y, Kawai, T, Azuma, E, Nakajima, T, Shindo, M, Kurose, K, Sugie, A, Yamagishi, Y, Fujii-Kuriyama, Y & Hashimoto, M 2002, 'Arylhydrocarbon receptor-dependent induction of liver and lung cytochromes P450 1A1, 1A2, and 1B1 by polycyclic aromatic hydrocarbons and polychlorinated biphenyls in genetically engineered C57BL/6J mice', *Carcinogenesis*, vol. 23, no. 7, pp. 1199-1207.

Shimada, T, Wunsch, RM, Hanna, IH, Sutter, TR, Guengerich, FP & Gillam, EM 1998, 'Recombinant human cytochrome P450 1B1 expression in Escherichia coli', *Archives of Biochemistry & Biophysics*, vol. 357, no. 1, pp. 111-120.

Sippl, MJ 1993, 'RECOGNITION OF ERRORS IN 3-DIMENSIONAL STRUCTURES OF PROTEINS', *Proteins-Structure Function and Genetics*, vol. 17, no. 4, pp. 355-362.

Sparfel, L, Huc, L, Le Vee, M, Desille, M, Lagadic-Gossmann, D & Fardel, O 2004, 'Inhibition of carcinogen-bioactivating cytochrome P450 1 isoforms by amiloride derivatives', *Biochemical Pharmacology*, vol. 67, no. 9, pp. 1711-1719.

Stevens, MF, Hickman, JA, Langdon, SP, Chubb, D, Vickers, L, Stone, R, Baig, G, Goddard, C, Gibson, NW & Slack, JA 1987, 'Antitumor activity and pharmacokinetics in mice of 8-carbamoyl-3-methyl-imidazo[5,1-d]-1,2,3,5-tetrazin-4(3H)-one (CCRG 81045; M & B 39831), a novel drug with potential as an alternative to dacarbazine', *Cancer Research*, vol. 47, no. 22, pp. 5846-5852.

Szczesna-Skorupa, E, Ahn, K, Chen, CD, Doray, B & Kemper, B 1995, 'The cytoplasmic and N-terminal transmembrane domains of cytochrome P450 contain independent signals for retention in the endoplasmic reticulum', *J Biol Chem*, vol. 270, no. 41, pp. 24327-24333.

Szczesna-Skorupa, E, Chen, CD, Rogers, S & Kemper, B 1998, 'Mobility of cytochrome P450 in the endoplasmic reticulum membrane', *Proc Natl Acad Sci U S A*, vol. 95, no. 25, pp. 14793-14798.

Szklarz, GD & Paulsen, MD 2002, 'Molecular modeling of cytochrome P450 1A1: enzyme-substrate interactions and substrate binding affinities', *Journal of Biomolecular Structure & Dynamics*, vol. 20, no. 2, pp. 155-162.

Szymczak, AL, Workman, CJ, Wang, Y, Vignali, KM, Dilioglou, S, Vanin, EF & Vignali, DAA 2004, 'Correction of multi-gene deficiency in vivo using a single 'self-cleaving' 2A peptide-based retroviral vector', *Nature Biotechnology*, vol. 22, no. 5, pp. 589-594.

Taly, V, Urban, P, Truan, G & Pompon, D 2007, 'A combinatorial approach to substrate discrimination in the P450CYP1A subfamily', *Biochimica Et Biophysica Acta-General Subjects*, vol. 1770, no. 3, pp. 446-457.

Tarner, IH, Muller-Ladner, U & Fathman, CG 2004, 'Targeted gene therapy: frontiers in the development of 'smart drugs'', *Trends Biotechnol*, vol. 22, no. 6, pp. 304-310.

Tassaneeyakul, W, Birkett, DJ, Veronese, ME, McManus, ME, Tukey, RH, Quattrochi, LC, Gelboin, HV & Miners, JO 1993, 'SPECIFICITY OF SUBSTRATE AND INHIBITOR PROBES FOR HUMAN CYTOCHROMES-P450 1A1 AND 1A2', *Journal of Pharmacology and Experimental Therapeutics,* vol. 265, no. 1, pp. 401-407.

Tassaneeyakul, W, Mohamed, Z, Birkett, DJ, McManus, ME, Veronese, ME, Tukey, RH, Quattrochi, LC, Gonzalez, FJ & Miners, JO 1992, 'Caffeine as a Probe for Human Cytochromes-P450 - Validation Using Cdna-Expression, Immunoinhibition and Microsomal Kinetic and Inhibitor Techniques', *Pharmacogenetics,* vol. 2, no. 4, pp. 173-183.

Teodorescu, O, Galor, T, Pillardy, J & Elber, R 2004, 'Enriching the sequence substitution matrix by structural information', *Proteins-Structure Function and Genetics,* vol. 54, no. 1, pp. 41-48.

Testa, B 2004, 'Prodrug research: futile or fertile?' *Biochem Pharmacol,* vol. 68, no. 11, pp. 2097-2106.

Thatcher, NJ, Edwards, RJ, Lemoine, NR, Doehmer, J & Davies, DS 2000, 'The potential of acetaminophen as a prodrug in gene-directed enzyme prodrug therapy', *Cancer Gene Therapy,* vol. 7, no. 4, pp. 521-525.

Tyndale, RF & Sellers, EM 2001, 'Variable CYP2A6-Mediated Nicotine Metabolism Alters Smoking Behavior and Risk', *Drug Metabolism and Disposition,* vol. 29, no. 4, pp. 548-552.

Udomuksorn, W, Elliot, DJ, Lewis, BC, Mackenzie, P, Yoovathaworn, K & Miners, JO 2007, 'Influence of mutations associated with Gilbert and Crigler-Najjar type II syndromes on the glucuronidation kinetics of bilirubin and other UDP-glucuronosyltransferase 1A substrates', *Pharmacogenetics and Genomics,* vol. 17, no. 12, pp. 1017-1029.

Venkatakrishnan, K, von Moltke, LL, Court, MH, Harmatz, JS, Crespi, CL & Greenblatt, DJ 2000, 'Comparison between cytochrome P450 (CYP) content and relative activity approaches to scaling from cDNA-expressed CYPs to human liver microsomes: ratios of accessory proteins as sources of discrepancies between the approaches', *Drug Metabolism & Disposition,* vol. 28, no. 12, pp. 1493-1504.

von Groll, A, Levin, Y, Barbosa, MC & Ravazzolo, AP 2006, 'Linear DNA low efficiency transfection by liposome can be improved by the use of cationic lipid as charge neutralizer', *Biotechnology Progress,* vol. 22, no. 4, pp. 1220-1224.

Wade, RC, Winn, PJ, Schlichting, E & Sudarko 2004, 'A survey of active site access channels in cytochromes P450', *Journal of Inorganic Biochemistry,* vol. 98, no. 7, pp. 1175-1182.

Wallner, B & Elofsson, A 2005, 'All are not equal: A benchmark of different homology modeling programs', *Protein Science,* vol. 14, no. 5, pp. 1315-1327.

Wargo, JA, Robbins, PF, Li, Y, Zhao, YB, El-Gamil, M, Caragacianu, D, Zheng, ZL, Hong, J, Downey, S, Schrump, D, Rosenberg, S & Morgan, R 2009, 'Recognition of NY-ESO-1+tumor cells by engineered lymphocytes is enhanced by improved vector design and epigenetic modulation of tumor antigen expression', *Cancer Immunology Immunotherapy,* vol. 58, no. 3, pp. 383-394.

Weisel, M, Proschak, E & Schnider, G 2007, 'PocketPicker: analysis of ligand binding-sites with shape descriptors', *Chemistry Central Journal*, vol. 1, no. 7, pp. 1-17.

Werck-Reichhart, D & Feyereisen, R 2000, 'Cytochromes P450: a success story', *Genome Biol*, vol. 1, no. 6, pp. REVIEWS3003.

Wester, MR, Johnson, EF, Marques-Soares, C, Dansette, PM, Mansuy, D & Stout, CD 2003a, 'Structure of a substrate complex of mammalian cytochrome P450 2C5 at 2.3 A resolution: evidence for multiple substrate binding modes', *Biochemistry*, vol. 42, no. 21, pp. 6370-6379.

Wester, MR, Johnson, EF, Marques-Soares, C, Dijols, S, Dansette, PM, Mansuy, D & Stout, CD 2003b, 'Structure of mammalian cytochrome P4502C5 complexed with diclofenac at 2.1 angstrom resolution: Evidence for an induced fit model of substrate binding', *Biochemistry*, vol. 42, no. 31, pp. 9335-9345.

Wester, MR, Yano, JK, Schoch, GA, Yang, C, Griffin, KJ, Stout, CD & Johnson, EF 2004, 'The structure of human cytochrome P4502C9 complexed with flurbiprofen at 2.0-angstrom resolution', *Journal of Biological Chemistry*, vol. 279, no. 34, pp. 35630-35637.

Williams, PA, Cosme, J, Sridhar, V, Johnson, EF & McRee, DE 2000a, 'Mammalian microsomal cytochrome P450 monooxygenase: Structural adaptations for membrane binding and functional diversity', *Molecular Cell*, vol. 5, no. 1, pp. 121-131.

Williams, PA, Cosme, J, Sridhar, V, Johnson, EF & McRee, DE 2000b, 'Mammalian microsomal cytochrome P450 monooxygenase: structural adaptations for membrane binding and functional diversity', *Molecular Cell*, vol. 5, no. 1, pp. 121-131.

Williams, PA, Cosme, J, Ward, A, Angove, HC, Matak Vinkovic, D & Jhoti, H 2003, 'Crystal structure of human cytochrome P450 2C9 with bound warfarin', *Nature*, vol. 424, no. 6947, pp. 464-468.

Woodard, SI & Dailey, HA 1995, 'Regulation of Heme-Biosynthesis in Escherichia-Coli', *Archives of Biochemistry and Biophysics*, vol. 316, no. 1, pp. 110-115.

Xu, G & McLeod, HL 2001, 'Strategies for enzyme/prodrug cancer therapy', *Clinical Cancer Research*, vol. 7, no. 11, pp. 3314-3324.

Yamazaki, H, Gillam, EM, Dong, MS, Johnson, WW, Guengerich, FP & Shimada, T 1997, 'Reconstitution of recombinant cytochrome P450 2C10(2C9) and comparison with cytochrome P450 3A4 and other forms: effects of cytochrome P450-P450 and cytochrome P450-b5 interactions', *Archives of Biochemistry & Biophysics*, vol. 342, no. 2, pp. 329-337.

Yamazaki, H, Nakajima, M, Nakamura, M, Asahi, S, Shimada, N, Gillam, EM, Guengerich, FP, Shimada, T & Yokoi, T 1999, 'Enhancement of cytochrome P-450 3A4 catalytic activities by cytochrome b(5) in bacterial membranes', *Drug Metabolism & Disposition*, vol. 27, no. 9, pp. 999-1004.

Yamazaki, H, Shimada, T, Martin, MV & Guengerich, FP 2001, 'Stimulation of cytochrome P450 reactions by apo-cytochrome b5: evidence against transfer of heme from cytochrome P450 3A4 to apo-cytochrome b5 or heme oxygenase', *Journal of Biological Chemistry*, vol. 276, no. 33, pp. 30885-30891.

Yang, S, Cohen, CJ, Peng, PD, Zhao, Y, Cassard, L, Yu, Z, Zheng, Z, Jones, S, Restifo, NP, Rosenberg, SA & Morgan, RA 2008, 'Development of optimal bicistronic lentiviral vectors facilitates high-level TCR gene expression and robust tumor cell recognition', *Gene Therapy,* vol. 15, no. 21, pp. 1411-1423.

Yano, JK, Hsu, MH, Griffin, KJ, Stout, CD & Johnson, EF 2005, 'Structures of human microsomal cytochrome P450 2A6 complexed with coumarin and methoxsalen. ' *Nat.Struct.Mol.Biol.,* vol. 12, no. pp. 822-823.

Yasukochi, Y & Masters, BS 1976, 'Some properties of a detergent-solubilized NADPH-cytochrome c(cytochrome P-450) reductase purified by biospecific affinity chromatography', *Journal of Biological Chemistry,* vol. 251, no. 17, pp. 5337-5344.

Yeo, KR, Rostami-Hodjegan, A & Tucker, GT 2004, 'Abundance of cytochromes P450 in human liver: a meta-analysis', *British Journal of Clinical Pharmacology,* vol. 57, no. 5, pp. 687-688.

Yu, JL, Paine, MJI, Marechal, JD, Kemp, CA, Ward, CJ, Brown, S, Sutcliffe, MJ, Roberts, GCK, Rankin, EM & Wolf, CR 2006, 'In silico prediction of drug binding to CYP2D6: Identification of a new metabolite of metoclopramide', *Drug Metabolism and Disposition,* vol. 34, no. 8, pp. 1386-1392.

Zhai, S, Dai, R, Friedman, FK & Vestal, RE 1998, 'Comparative Inhibition of Human Cytochromes P450 1A1 and 1A2 by Flavonoids', *Drug Metabolism and Disposition,* vol. 26, no. 10, pp. 989-992.

Zhao, YH & Halpert, JR 2007, 'Structure-function analysis of cytochrornes P4502B', *Biochimica Et Biophysica Acta-General Subjects,* vol. 1770, no. 3, pp. 402-412.

Zheng, L, Baumann, U & Reymond, JL 2004, 'An efficient one-step site-directed and site-saturation mutagenesis protocol', *Nucleic Acids Research,* vol. 32, no. 14, pp.

Zhou, D, Lu, Y, Steiner, MS & Dalton, JT 2000, 'Cytochrome P-450 2C9 sensitizes human prostate tumor cells to cyclophosphamide via a bystander effect', *Antimicrobial Agents & Chemotherapy,* vol. 44, no. 10, pp. 2659-2663.